TRANSIT DOSIMETRY BASED ON WATER EQUIVALENT PATH LENGTH MEASURED WITH AN AMORPHOUS SILICON ELECTRONIC PORTAL IMAGING DEVICE

KAVUMA AWUSI, BSc. MSc.

Submitted in fulfilment of the requirements for

the Degree of Doctor of Philosophy

University of Glasgow

College of Medicine, Veterinary and Life Sciences

Department of Clinical Physics and Bioengineering

Supervisors:

1) Prof. Alex Elliott

2) Martin Glegg

May, 2011

Abstract

Background and purpose:

In vivo dosimetry is one of the quality assurance tools used in radiotherapy to monitor the dose delivered to the patient. The digital image format makes electronic portal imaging devices (EPIDs) good candidates for in vivo dosimetry. Currently there is no commercial transit dosimetry module, which could facilitate routine in vivo dosimetry with the EPID. Some centres are developing their in-house packages, and they are under assessment before introduction into routine clinical usage. The main purpose of this work was to develop the EPID as an in vivo dosimetry device.

Materials and methods:

Knowledge of a detector's dose-response behaviour is a prerequisite for any clinical dosimetric application, hence in the first phase of the study, the dosimetric characteristics of eleven Varian a-Si500 EPIDs that are in clinical use in our centre were investigated. The devices have been in use for varying periods and interfaced with two different acquisition control software packages, IAS2 / IDU-II or IAS3 / IDU-20. Properties investigated include: linearity, reproducibility, signal uniformity, field size and dose-rate dependence, memory effects and image profiles as a function of dose. In the second phase, an EPID was calibrated using the quadratic method to yield values for the entrance and exit doses at the phantom or patient. EPID images for a set of solid water phantoms of varying thicknesses were acquired and the data fitted onto a quadratic equation, which relates the reduction in photon beam intensity to the attenuation coefficient and material thickness at a reference condition. The quadratic model was used to convert the measured grey scale value into water equivalent path length (EPL) at each pixel for any material imaged by the detector. For any other non-reference conditions, scatter, field size and MU variation effects on the image were corrected. The 2D EPL is linked to the percentage exit-dose for different thicknesses and field sizes, thereby converting the plane pixel values at each point into a 2D dose map at the exit surface of the imaged material. The off axis ratio is corrected using envelope and boundary profiles generated from the treatment planning system (TPS). The method was extended to include conformal and enhanced dynamic wedge (EDW)

fields. A method was devised for the automatic calculation of areas (to establish the appropriate scatter correction) from the EPID image that facilitated the calculation of EPL for any field, and hence exit dose. For EDW fields, the fitting coefficients were modified by utilizing the Linac manufacturer's golden segmented treatment tables (STT) methodology. Cross plane profiles and 2D dose distributions of EPID predicted doses were compared with those calculated with the Eclipse 8.6 treatment planning system (TPS) and those measured directly with a MapCHECK 2 device.

Results:

The image acquisition system influenced the dosimetric characteristics with the newer version (IAS3 with IDU-20) giving better data reproducibility and linearity fit than the older version (IAS2 with IDU-II). The irradiated field areas can be accurately determined from EPID images to within ± 1% uncertainty. The EPID predicted dose maps were compared with calculated doses from TPS at the exit. The gamma index at 3% dose difference (DD) and 3mm distance to agreement (DTA) resulted in an average of 97% acceptance for the square fields of 5, 10, 15 and 20 cm thickness solid water homogeneous phantoms. More than 90% of all points passed the gamma index acceptance criteria of 3% DD and 3mm DTA, for both conformal and EDW study cases. Comparison of the 2D EPID dose maps to those from TPS and MapCHECK shows that, more than 90% of all points passed the gamma index acceptance criteria of 3% dose difference and 3mm distance to agreement, for both conformal and EDW study cases.

Conclusions:

The quadratic calibration can effectively predict EPL and hence exit dose. Good agreement between the EPID predicted and TPS calculated dose distributions were obtained for open fields, conformal and EDW test cases. There were noteworthy deviations between EPID, TPS and MapCHECK doses on field edges. But it should be emphasised that, for practical in vivo dosimetry, these areas of reduced accuracy at the field edges are much less important. It is concluded that the EPID Quadratic Calibration Method (QCM) is an accurate and convenient method for online *in vivo* dosimetry and may therefore replace existing techniques.

Acknowledgements

Firstly, I owe an enormous debt of gratitude to my supervisor Prof. Alex Elliott for his commitment to help see this project through to its final completion, and his equally generous and wise guidance during its development. His efforts and willingness to travel between two centres to ascertain the progress, despite his hectic busy schedules. His constant encouragement to innovative thoughts was a great motivator.

My gratitude goes to my co-supervisor Martin Glegg, Consultant medical Physicist and deputy head of radiotherapy physics Department at Beatson West of Scotland Cancer Centre (BWoSCC). His knowledge, ideas, perceptiveness and analytical approach were vital to the completion of this thesis.

The acknowledgement would not be complete without the mention of Dr. Mohamed Metwally, consultant medical physicist, BWoSCC. He provided continual technical support in dosimetry and his integral view on research and strives for perfection, opened doors to a wealth of knowledge.

A warm thank you to a number of medical physics students that I shared office with. I am deeply indebted to Hugh Wallace, John Loveland and Kurian Oommen for their valuable inputs and suggestions during the tenure of the research, their willingness and continued support in resolving technical issues and for the endless discussions.

I express my sincere thanks to all the staff, Radiotherapy physics Department, BWoSCC, who made a significant contribution and gave encouragement for making this work possible. I highly appreciate their support and making the environment conducive for research. I particularly thank Garry Curry, the head of Radiotherapy Physics Department, BWoSCC, for helping to lay the foundation for the project and for his continual support.

I must thank my sponsor, the Islamic Development Bank, which granted me scholarship that facilitated my travel, living expenses and payment of the University tuition fees.

Last but not least, I would like to express my thanks to the Radiotherapy Department - Mulago Hospital, Kampala – Uganda, for their support and allowing me to go for further studies. My sincere thanks go to Dr.J.B. Kigula-Mugambe, Senior Consultant Oncologist and Head of Radiotherapy Department.

On a personal note, I would like to thank my family, for their patience and support thought this large undertaking, above all, to bear with me while I am away during the programme.

Finally, I would like to give thanks to those whose names are not mentioned here, for their direct or indirect assistance towards fulfilling this PhD programme.

To all of the above, I extend my deepest gratitude and appreciation. It is a pleasure to have all of you as a working team.

Kavuma Awusi

Table of Contents

Abstract ii
Acknowledgements iv
List of Tables xi
List of Figures xii
Abbreviations xxi
1 CHAPTER ONE: INTRODUCTION AND AIM OF THIS RESEARCH 1
1.1 Radiotherapy 1
1.2 Portal dosimetry and Equivalent Path Length 2
1.3 Major structural components of a medical Linear accelerator 2
1.3.1 The gantry and treatment couch 3
1.3.2 The treatment head 4
1.3.3 Electronic portal imaging device 4
1.3.4 On-board Imager 4
1.3.5 Support systems 5
1.4 Radiation beam production 6
1.5 Physical properties of radiotherapy beams 8
1.5.1 Electron beam properties 8
1.5.2 Photon beam properties 8
1.5.3 Interaction processes 9
1.5.3.1 Photoelectric absorption 10
1.5.3.2 Compton scattering 11
1.5.3.3 Pair production 11
1.5.4 Attenuation of photons 11
1.5.5 Photon dosimetry 12
1.5.5.1 Depth influence 13
1.5.5.2 Effect of field size 14
1.6 Objective of radiotherapy 15
1.7 Radiotherapy treatment planning 16
1.8 Treatment verification 17
1.8.1 Positional (Geometric) verification 19
1.8.2 Treatment parameter verification 19
1.8.3 Dosimetric verification: In vivo dosimetry 20
1.8.3.1 Entrance and exit dosimetry 21
1.8.4 Modalities of treatment verification 23

1.8.4.1 Film 23
1.8.4.2 Thermoluminescent dosimeters 23
1.8.4.3 Diodes 24
1.8.4.4 MOSFET 24
1.8.4.5 Ionisation Chambers 25
1.8.4.6 Electronic Portal Imaging Devices 25
1.8.5 Advantages of electronic portal imaging devices over other modalities 26
1.9 Portal Dosimetry Literature Review 27
1.9.1 History of EPID usage for dosimetry 27
1.9.2 Dosimetric characteristics of a-Si electronic portal imaging devices 29
1.9.3 Dose Verifications 31
1.9.4 In vivo dosimetry with electronic portal imaging devices 32
1.9.5 Portal dosimetry commercial Packages 34
1.9.5.1 Varian's portal dosimetry system 34
1.9.5.2 Dosimetry Check 35
1.9.5.3 EPIQA 35
1.9.5.4 EPIDose 36
1.9.5.5 Elekta iViewGT and Siemens Optivue 36
1.9.6 Current drawbacks for the wide use of electronic portal imaging devices as a dosimeter 37
1.10 Aims of this study 37
2 CHAPTER TWO: MEGA-VOLTAGE ELECTRONIC PORTAL IMAGING DEVICES: DEVELOPMENT 39
2.1 Introduction to electronic portal imaging devices 39
2.2 Types of electronic portal imaging devices 39
2.2.1 Direct and Indirect radiation detection electronic portal imaging devices 39
2.2.2 Matrix (Scanning liquid) Ion Chamber detectors 41
2.2.3 Camera-Based detectors 42
2.2.4 Flat panel detectors 44
2.2.4.1 Basic image formation theory for the indirect a-Si electronic portal imaging devices 44
2.3 General uses of electronic portal imaging devices 46

2.3.1 Treatment setup verification 47
2.3.2 Electronic portal imaging devices as a physics tool for routine linear accelerator QA 48
2.3.3 Dosimetric application 49
2.3.3.1 Electronic portal imaging devices calibration for dosimetry .. 49
2.3.3.2 Transit and Non-transit dosimetry 50
2.4 Overview of the Varian electronic portal imaging device detector system 52
2.4.1 Image detection unit 52
2.4.2 Image acquisition system 53
2.4.3 Acquisition computer control software 53
2.4.4 Electronic readout of a-Si detectors 54
2.4.4.1 Single (integrated) mode 54
2.4.4.2 Continuous mode - high dose imaging 55
2.4.4.3 Cone beam mode (only available on linacs with OBI system) . 55
2.4.5 Imager calibration 56
2.4.5.1 Dark field image 56
2.4.5.2 Flood field image 56
2.4.5.3 Main components of the Varian's portal dosimetry system 57
3 CHAPTER 3: MATERIALS AND METHODS 58
3.1 Dosimetric performance of a-Si500 EPIDs 58
3.1.1 Image acquisition 59
3.1.2 Detector reproducibility and responses to a reference beam 60
3.1.3 Dose-response behaviour / Linearity 61
3.1.4 Pixel uniformity-response across the entire detector panel 62
3.1.5 Electronic portal imaging device's relative dosimetry 63
3.1.6 Field size dependence 64
3.1.7 Doserate influence 64
3.1.8 Directional dependence 65
3.1.9 Further image profile analysis and memory effects 65
3.1.10 Electronic portal imaging devices ageing due to radiation 65
3.1.11 Electronic portal imaging devices, as a dosimeter 66
3.2 Water equivalent path length calculation from EPID images 67
3.2.1 Treatment unit and EPID detector 68
3.2.2 Measurements and Image acquisition for calibration 69

3.2.3 Measurement of correction factors 71
3.2.3.1 Field size and phantom thickness 71
3.2.3.2 Monitor unit effects 73
3.2.4 Open fields 75
3.2.4.1 Verification of equivalent path length from EPID images 75
3.2.4.2 Exit dose prediction for open fields from EPID images 76
3.2.4.3 Entrance dose prediction for open fields from EPID images ... 79
3.2.4.4 Verification of exit dose 80
3.2.5 Irregular fields 80
3.2.5.1 Equivalent path length from EPID images for irregular fields . 81
3.2.5.2 Exit dose from EPID images for irregular fields 85
3.2.6 Enhanced dynamic wedge fields 86
3.2.6.1 Equivalent path length from EPID images for EDW fields 86
3.2.6.2 Exit dose from EPID images for EDW fields 89
3.2.7 Dose comparison with treatment planning system 89
3.2.8 Further dose verification with MapCHECK 2 device 90
4 CHAPTER 4: RESULTS AND DISCUSSION 93
4.1 Dosimetric Performance 93
4.1.1 Detector reproducibility and response to a reference beam 93
4.1.2 Dose-response behaviour / Linearity 95
4.1.3 Pixel uniformity-response across the entire detector panel 99
4.1.4 Electronic portal imaging device's relative dosimetry 100
4.1.5 Field size dependence 101
4.1.6 Doserate influence 103
4.1.7 Directional dependence 106
4.1.8 Further image profile analysis and memory effects 108
4.1.9 Electronic portal imaging devices as a dosimeter 113
4.2 Water equivalent path length measured with an EPID 115
4.2.1 Variations of the fitting parameters A and B 115
4.2.2 The phantom scatter and field size correction factors 118
4.2.3 Monitor unit effects 119
4.2.4 Measured and calculated Percentage Exit Thickness Dose (PETD) 121
4.2.5 Verification of calculation of the equivalent path length 122
4.2.5.1 Equivalent path length for solid water phantoms 122

4.2.5.2 Equivalent path length for solid water phantoms with varying monitor units....124
4.2.5.3 Equivalent path length for solid water and non water phantoms 125
4.3 Dose comparison....127
4.3.1 Exit and entrance dose comparison for open fields....127
4.3.2 Irregular fields....138
4.3.3 Enhanced dynamic fields....149
4.3.4 Comparison of exit dose results with other literature....172
5 CHAPTER 5: CONCLUSIONS AND FUTURE WORK....175
5.1 Conclusions....175
5.2 Possible future direction....177
Appendix A: Solving Quadratic Equations....180
APPENDIX B: Relation between TPR and PETD....183
List of References....185
APPENDIX C: Peer reviewed publications arising from thesis....196

List of Tables

Table 2- 1. Specifications of the Varian imager (Varian PortalVisionTM aS500, 2001) 54
Table 3- 1. The different accelerator models with EPIDs, the EPID image acquisition system and their corresponding clinical use period in months. 58
Table 3- 2. Conversion process of EPL to dose using PETD table 76
Table 4- 1 Percentage signal short-term reproducibility for the different EPIDs: 93
Table 4- 2. Comparison of EPID J (System-II) response to a single 20 MU exposure to a series of lower-dose exposures with equivalent MU. 98
Table 4- 3. Detectors response at different points (figure 3-1) relative to their central position P_0. P_{avr} is the average of four points in the beam penumbra region. The subscripts I and II indicate whether the detector is a system-I or system-II respectively..... 100
Table 4- 4. Polynomial coefficients for different EPIDs described in equation 3.2 and the R^2 value for the field size fit. 102
Table 4- 5. Different EPIDs, their use period (months) and corresponding approximate dose (only corrected for inverse square law) from the Varis system database..... 112
Table 4- 6. EPL convergence for selected thicknesses (Th) and field sizes (FS) 123
Table 4- 7. Summary of the EPL results from figure 4-19 comparing calculated (equation 3.13) and those measured from EPID images..... 126
Table 4- 8. Percentage differences at exit and entrance central points between TPS and EPID for different field sizes and solid-water thickness (T) for 6 MV beam..... 129
Table 4- 9. Comparison of expected and EPID calculated areas for square fields and cases described in figure 3.7 139
Table 4- 10. Comparison of segmented treatment values calculated with the proposed algorithm using equation 3.24 and those printed out after EDW treatment from the linac..... 151

List of Figures

Figure 1- 1. Varian linear accelerator (Model ix) 3
Figure 1- 2. Block diagram, illustrating the major components of the accelerator needed for the generation of the radiation beam (Adapted from Khan, 2003). 7
Figure 1- 3. Primary photon interaction processes with their secondary emissions 10
Figure 1- 4. Attenuation of photon beam through an absorber..... 12
Figure 1- 5. Dose-response curves for tumour control probability (curve A) and normal tissue complication probability (curve B) (adapted from Podgorsak 2005)..... 16
Figure 1- 6. Steps in the radiotherapy treatment process, linked by a chain 18
Figure 1- 7. Illustration of the (a) entrance and (b) exit dose calculation planes22
Figure 1- 8. Typical depth dose curve in water phantom 22
Figure 2- 1. Types of radiation detectors. Figure (a) is the Indirect detector while figure (b) show the direct detector mechanism. 40
Figure 2- 2. Schematic of a SLIC EPID. 42
Figure 2- 3. Schematic of a video-based EPID..... 43
Figure 2- 4. Figure (a) is a schematic illustration of an a-Si photo diode coupled to thin film transistor (TFT). Figure (b) is a schematic arrangement of photodiodes and controls used in the flat panel imager (Reproduced from Varian document library). 45
Figure 2- 5. Figure (a) shows the main layers making up the detector (b) Functional cross-section of EPID..... 46
Figure 2- 6. Transit and non-transit 50
Figure 2- 7. Block diagram of the image detection unit (IDU) (Reproduced from Varian document library). 53
Figure 2- 8. Dark-field and Flood-field images..... 56
Figure 3- 1. Specific locations used to measure the uniformity with in a 20 x 20 cm^2 radiation field size in the EPID detector. Each of the positional points has an area of 13 x 13 pixels. Mean response for all the points were compared to the central axis (P_0) reading of each EPID detector. The response of the points (P_L, P_R P_G and P_T) in the penumbra region were averaged (P_{avr}) for each EPID. 63

Figure 3- 2. The geometrical setups for: (a) EPID image acquisition and (b) Ionisation chamber measurements. In both (a) and (b) the detectors (EPID and ion chambers) were kept at fixed SDD. The ion chamber was set with a 10.0 cm solid water backscatter and build-up equivalent to the beam d_{max} (1.5 cm). 67

Figure 3- 3. The experimental setup for EPID image acquisition. The solid water phantom thickness (T) was symmetrically set about the isocentre and the EPID kept at a fixed source to detector distance (SDD=140 cm)..... 69

Figure 3- 4. The experimental setups for (a) EPID and (b) ionisation chamber measurement of scatter and field size correction factors. The solid water phantom thickness (T) was symmetrically set about the isocentre and the detectors kept at fixed source to detector distances (SDD = 140 cm). The ion chamber was set with a 1.0 cm solid water backup and build-up equivalent to the beam d_{max} (1.5 cm and 2.5 cm for 6 MV and 16 MV respectively). 72

Figure 3- 5. Figures (a) and (b) are schematic cross sectional diagrams for different phantoms of varying electron densities..... 75

Figure 3- 6. The experimental setup used for ionisation chamber measurement of PETD 78

Figure 3- 7. Shows the lower torso phantom and the white central square in (a) shows the 20x20 cm^2 irradiated area. 80

Figure 3- 8. Irregular apertures of varying shapes and areas. The dimensions are in cm measured at the isocentre. 82

Figure 3- 9. Respective EPID images for the apertures shown in figure 3.7 above 83

Figure 3- 10. Respective field edges determined from the EPID images above .. 84

Figure 3- 11: MapCHECK 2 device (SUN Nuclear Corporation, Melbourne Florida, USA)..... 91

Figure 3- 12: The setup used for the simultaneous MapCHECK measurement and EPID image acquisitions. 92

Figure 4- 1. Long term (six months) reproducibility for three system-II detectors 94

Figure 4- 2. Pixel deviation from the mean for each EPID, after exposure to a reference beam (50 MU, 400 MU/Min doserate and 10x10cm^2 field size)..... 95

Figure 4- 3. Figure (a) shows Ionisation chamber response as a function of monitor units for different accelerators. Figures (b) and (c) show the signal to monitor units ratio (SMUR) variation with monitor units. The readings at various monitor units were normalised to 1000 MU for the ionisation chambers and EPIDs..... 97

Figure 4- 4. Figure (a) shows typical central profiles comparing an EPID acquired image (dashed line) and actual MapCheck transmission (straight line) with a four step-wedge. A relative signal of 100 indicates an open field transmission; creating a fifth step in the figure. The X and Y figures quoted in boxes of figure (b) and (c) are the numerical values on the horizontal and vertical axes for each point. 101

Figure 4- 5. EPID signal variations with field size. The data were normalised to a 10x10cm^2 field size for the two systems. The figure also includes a comparison with an ionisation chamber of accelerator B and I for system-I and system-II respectively. 103

Figure 4- 6. System-II EPIDs response to varying doserates. Figures (a) and (b) show pixel values variation with doserate for total doses of 20 MU and 100 MU respectively. The original data (points) were fitted to a power potential function in equation 3.3 and the lines show the best fit for each EPID. Figure (c) shows data normalised to 400 MU/Min. 104

Figure 4- 7. Figures (a) and (c) shows pixel responses at different gantry angles for EPIDs G and J respectively, while figures (b) and (d) show their data normalised to those at gantry angle zero. 107

Figure 4- 8. Central image profiles indicating post irradiation effect on the EPID. The image profile (continuous line) was acquired within 12 seconds after 50 MU to a 5x5 cm^2 field (dashed line) taken earlier. The profile in the inset is the difference between the image profiles. The double arrow shows the signal enhancement at the centre (5 x 5 cm^2) within the 20 x 20 cm^2 field size 108

Figure 4- 9. Typical integrated image profiles for different EPID detectors obtained at different MU, constant doserate of 400 MU/min and

10x10 cm^2 field size at isocentre. The images were analysed in their absolute sense without taking into consideration the averaged number of frames at each set MU. 110

Figure 4- 10. Cross profiles images of four EPIDs acquired at 5 and 50 MU in the transverse (L-R) and radial (G-T) planes of the linear accelerator20x20 cm^2 field size at isocentre. System-1 profiles (b and d) show dose (MU) dependence in the G-T direction.....111

Figure 4- 11. Comparison of EPID response with ion chamber as a function of MU 114

Figure 4- 12 EPID versus ion chamber response with solid water thickness 115

Figure 4- 13. Profiles extracted from the fitting parameter matrices A(i,j) and B(i,j) along the left-right direction of the EPID. Figures (a) and (b) show the symmetrical variations of B(i,j) and A(i,j) with off-axis distance for two 6 MV and 16 MV beams respectively. The X and Y (at each point, the Y value is either the A(i,j) or B(i,j) value) quoted in boxes are numerical values on the horizontal and vertical axes for each point. Figures (c) and (d) show a 3D visualisation of the B(i,j) and A(i,j) fitting parameters respectively. 117

Figure 4- 14. Correction factor variations as a function of field size for phantom thicknesses 5cm, 10cm, 15cm, 20cm, and 32 cm for 6 MV beam...119

Figure 4- 15. Figures (a), (c) and (e) show system-II linearity for thicknesses 10 cm, 20 cm and 32 cm measured at 400 MU/min respectively, while figures (b), (d) and (f) are their corresponding SMUR. Figures (g) and (h) show linearity and SMUR respectively for thickness 20 cm measured at 100 MU/min. 120

Figure 4- 16. Comparison of measured (meas) and calculated (cal) PETD at selected field sizes (FS) and depths.....122

Figure 4- 17. EPL profiles from EPID images for selected solid water phantom thicknesses and acquired at different field sizes. The X and Y (at each point, the Y value is the EPL) quoted in the boxes are numerical values at the centre on the horizontal and vertical axes for each point. 124

Figure 4- 18. Pre-MU (UnCorr) and post-MU (Corr) EPL (calculated before and after MU correction respectively) for 10 cm, 20 cm and 32 cm solid

water; and field sizes of (a) 5x5 cm^2, (b) 10x10 cm^2 and (c) 20x20 cm^2.....125

Figure 4- 19. Profiles extracted from centre of EPL maps for (a) slabs of solid water, bone and lung materials positioned in steps, as illustrated in figure 3-5 a. (b) cylindrical lung, solid water and cortical bone materials inserted between two 5cm slabs of solid water as illustrated in figure 3-5 b. The X and Y (at each point, the Y value is the EPL) quoted in boxes are the EPID measured values on the horizontal and vertical axes for each point, while P1, P2, P3 and P4 are corresponding calculated values.....126

Figure 4- 20. Dose profiles at the centre of the EPID images and TPS demonstrating the effect of flood field before and after correction for a 20x20 cm^2 field, to a 20cm thickness solid water material with 200 MU and 6 MV beam. Figure (a) compares TPS and EPID entrance dose profiles and figure (b) shows TPS and EPID exit dose profiles. 128

Figure 4- 21: Effect of resampling the MapCHECK data points 131

Figure 4- 22: Figures (a), (b) and (c) compare 2D absolute exit dose (cGy) distributions measured with MapCHECK device, calculated with TPS and those from EPID images respectively, for a 20x20 cm^2 field size and 100 MU. 132

Figure 4- 23. Exit dose comparison for case in figure 3.5(a) as described in section 3.2.1.1 Figures (a) and (c) are 2D TPS predicted colour maps and contour distributions, while (b) and (d) are their respective EPID calculated doses. Figure (e) shows horizontal EPL and dose profiles through the centre of their respective EPID images. Figure (f) is the corresponding gamma distributions between the TPS and EPID. ...133

Figure 4- 24. Exit dose comparison for the case in figure 3.5(b) as described in section 3.2.4.1 Figures (a) and (c) are 2D TPS predicted colour maps and contour distributions, while (b) and (d) are their respective EPID calculated doses. Figure (e) shows horizontal EPL and dose profiles through the centre of their respective EPID images. Figure (f) is the corresponding gamma distributions between the TPS and EPID. ...134

Figure 4- 25. Exit dose comparison for the case in figures 3-6 as described in section 3.2.4.4. Figures (a) and (b) are the 2D TPS predicted and

EPID calculated dose contours respectively. Figure (c) shows horizontal TPS dose (dashed) and EPID dose (dotted line) and EPL profiles through the centre of the EPID image. Figure (d) is the corresponding gamma distributions between the TPS and EPID. Figure (e) is a 2D dose difference map. Figure (f) is the EPID image of the irradiated 20x20 cm^2 field area of the phantom. 136

Figure 4- 26. Exit dose comparison for the case in figure 3-6, for 10x10 cm^2. Figures (a) and (b) are the 2D EPID predicted and TPS calculated dose contours respectively. Figure (c) is a 2D dose difference contour distribution. Figure (d) is the EPID image of the irradiated 10x10 cm^2 field area of the phantom. 137

Figure 4- 27. EPL profile (along the Y direction) calculated from the EPID image of figure 3.8 (d) 140

Figure 4- 28. Comparison of TPS (a) and EPID (b) exit doses for case of figure 3-7(a), where the doses in shielded areas are compared. Figures (a) and (d) are the same TPS doses but the dose data in shielded areas have been zeroed. Similarly, figures (b) and (e) are the same EPID doses but the dose data in shielded areas have been zeroed. Figures (c) and (f) are the corresponding gamma index maps.....141

Figure 4- 29: Figures (a) and (b) show EPID and TPS 2D absolute exit dose distributions for the irregular shaped apertures in figure 3.7 (c). Figure (c) demonstrates the gamma index map. Figure (d) is a histogram showing the gamma index values, computed from gamma map of figure (c).....143

Figure 4- 30:Figures (a), (b) and (c) show 2D absolute exit dose (cGy) distributions measured with MapCHECK device, calculated with TPS and those from EPID images respectively for the irregular shaped field in figure 3.7 (d). Figures (d), (e) and (f) demonstrate the respective 2D gamma maps, evaluated at 3% DD and 3 mm DTA...144

Figure 4- 31: Comparison of EPID and TPS for case of figure 3-7(e) 145

Figure 4- 32. Comparison of EPID and TPS for the cases of figure 3-7 (b) and (f) 146

Figure 4- 33. Exit dose comparison for the anthropomorphic phantom case in figure 3-7 as described in section 3.2.4.4, irradiated with an irregular field illustrated in figure 3-7 (c). Figures (a) and (b) are the

2D EPID predicted and TPS calculated dose contours respectively. Figure (c) shows the corresponding gamma index (3% DD and 3mm DTA) map between the TPS and EPID. Figure (d) is the acquired EPID image from which the dose distribution in figure (a) was calculated. 148

Figure 4- 34. Figures (a), (d) and (g) show EDW EPIDs acquired with different setups. Figures (b), (e) and (h) show their respective profiles, while figures (c), (f) and (i) are the corresponding field edges determined from the EPID image. 150

Figure 4- 35. EPL profiles in X and Y directions predicted from images obtained without any material between the source and imager for open field (solid lines), 30^0 (dash-dot lines), 45^0 (dot lines) and 60^0 (dash lines) EDW angles. 153

Figure 4-36. Comparison of measured (solid lines) and derived (dotted lines) profiles without any material in the beam $M_0^{\theta}(i,j)$ in the X and Y directions for EDW angles 30^0 (figure 4-36 (a) and (b)) and 45^0 (figure 4-36 (c) and (d)). Figures 4-36 (e) and (f) show the profiles for EDW angles 60^0. Figures 4-36 (g) and (h) show a 3-D visualization of the fitting parameter for the EDW 30^0 and 45^0 angles respectively.....155

Figure 4- 37. Figures (a) and (b) show the variations of fitting parameter matrices $B_{w\theta}(i,j)$ and $A_{w\theta}(i,j)$ along the Y direction of the EPID respectively for open field (θ=0), 30^0, 45^0 and 60^0 EDW fields. The results also compare the measured and derived profiles for the 30^0 and 45^0. Figures 4-37 (c) and (d) show a 3-D visualizations of the fitting parameters for 30^0 EDW field.....157

Figure 4- 38. Figures (a) and (b) are 2D exit dose distributions for EPD and TPS respectively for a 15^0 EDW with 20x20 cm^2. Figures (c) and (d) show their corresponding exit dose cross plane profiles in the X and Y direction respectively. Figures (e) and (f) show the percentage dose difference map and gamma index (3% DD and 3mm DTA) respectively.....158

Figure 4- 39. Figures (a) and (b) are 2D colourwash exit dose distributions for EPD and TPS respectively for a 30^0 EDW with 15x15 cm^2. Figures (c) and (d) show their corresponding exit dose cross plane profiles in the X and Y direction respectively. Figures (e) and (f) show the

percentage dose difference map and gamma index (3% DD and 3mm DTA) respectively. 160

Figure 4- 40. Figures (a) and (b) are 2D exit dose distributions for EPD and TPS respectively for a 30^0 EDW with 15x15 cm^2 and 200 MU. Figures (c) and (d) show their corresponding exit dose cross plane profiles and dose differences (dashed lines) in the X and Y direction respectively. 161

Figure 4- 41. Figures (a) and (b) are 2D exit dose distributions for EPD and TPS respectively for a 45^0 EDW with 10x10 cm^2. Figures (c) and (d) show their corresponding exit dose cross plane profiles in the X and Y direction respectively. Figures (e) and (f) show the percentage dose difference map and gamma index (3% DD and 3mm DTA) respectively.....162

Figure 4- 42. Figures (a) and (b) are 2D exit dose distributions for EPD and TPS respectively for a 60^0 EDW with 20x20 cm^2. Figures (c) and (d) show their corresponding exit dose cross plane profiles in the X and Y direction respectively. Figure (e) shows the percentage dose difference map.....163

Figure 4- 43. Figures (a) and (c) compare EPID image profiles for Y1-IN (solid lines) and Y2-OUT (dash lines) for 30^o and 45^o EDW respectively. Figures (b) and (d) show the same data superimposed onto each other by flipping the Y1-IN data.....165

Figure 4- 44. Figures (a) and (b) are 2D exit dose distributions for EPD and TPS respectively for a 30^0, Y2- OUT, EDW with 15x15 cm^2. Figure (c) shows their corresponding exit dose cross plane profiles and dose differences (dashed lines) in the Y direction. Figure (d) is the gamma map (3% DD and 3mm DTA) computed from figures (a) and (b). ...166

Figure 4- 45. Figures (a), (b) and (c) show 2D absolute exit dose (cGy) distributions measured with the MapCHECK device, calculated with TPS and those from EPID images respectively, for a 45^0, Y2- OUT, EDW with 15x15 cm^2. The image was acquired with 200 MU at collimator angle 90^0. Figure (d) shows the corresponding exit dose cross plane profiles and dose differences between EPID and MapCHECK profiles (dot-dashed line) in the X direction. Figures (e), (f) and (g) demonstrate the respective 2D gamma maps, evaluated

at 3% DD and 3 mm DTA.Figure (d) is the gamma map (3% DD and 3mm DTA) computed from figures (a) and (b).....168

Figure 4- 46. Exit dose comparison for the anthropomorphic phantom case in figure 3-7 as described in section 3.2.4.4, irradiated with 100 MU, 30^0 EDW, Y1- IN, collimator angle 0^0, with 15x15 cm^2 symmetric field. Figures (a) and (b) compare 2D TPS and EPID dose contours respectively. Figures (c) and (d) compare cross plane profiles in the X and Y respectively. Figure (e) shows the percentage dose difference map between the TPS and EPID doses. Figure (f) is the acquired EPID image from which the dose distribution in figure (b) was calculated. 170

Figure 4- 47. Exit dose comparison for the anthropomorphic phantom case in figure 3-7 as described in section 3.2.4.4, irradiated with 100 MU, 45^0 EDW, Y2- OUT, collimator angle 90^0, with 15x15 cm^2 symmetric field. Figures (a) and (b) compare 2D TPS and EPID dose contours respectively. Figures (c) and (d) compare cross plane profiles in the X and Y respectively. Figure (e) shows the percentage dose difference map between the TPS and EPID doses. Figure (f) is the acquired EPID image from which the dose distribution in figure (b) was calculated. 171

Abbreviations

A	Irradiation field area
AAPM	American Association of Physicist in Medicine
A(i,j)	Quadratic coefficient related to attenuation coefficient of material
a-Si	Amorphous silicon
B(s)	Correction factor for reduced back scatter proximal to the exit surface
B_p	Boundary profile
B(i,j)	Quadratic coefficient related to attenuation coefficient of material
CBCT	Coned beam computed tomography
CF	Correction factor
CT	Computed tomography
DD	Dose difference
D_{EPID}	Electronic portal imaging device dose
DF	Dark field
d_{max}	Depth of maximum dose
DQE	Detective quantum efficiency
DTA	Distance to agreement
D_{TPS}	Treatment planning system dose
EDW	Enhanced dynamic wedge
EM	Electromagnetic
E_p	Envelope profile
EPID	Electronic portal imaging device
EPL	Equivalent path length
FF	Flood field
FS	Field size
GSTT	Golden segmented treatment table
Gy	Gray
$h\nu$	Photon energy
IAS	Image acquisition software
IDU	Image detection unit
IGRT	Image guided radiation therapy
IMRT	Intensity modulated radiation therapy
KeV	Kilo electron voltage

MLC	Multi leaf collimator
$M_o(i,j)$	Image signal obtained without any material in the beam
MU	Monitor units
MV	Mega Voltage
NTCP	Normal tissue complication probability
OBI	On-board imager
OF	Output factor
PDD	Percentage depth dose
PETD	Percentage exit thickness dose
QA	Quality assurance
QCM	Quadratic calibration method
SAD	Source to axis distance
SDD	Source to detector distance
SF	Scatter factor
SLIC	Scanning Liquid Ionisation Chamber
SMUR	Signal to monitor units ratio
SPR	Scatter to primary ratio
SSD	Source to surface distance
STT	Segmented treatment table
T	Physical thickness
TCP	Tumour control probability
TFT	Thin film transistor
TLD	Thermoluminescent dosimeter
TMR	Tissue maximum ratio
TPR	Tissue phantom ratio
TPS	Treatment planning system
μ	Attenuation coefficient
ρ	Relative electronic density
2D	Two dimensional
3D	Three dimensional

CHAPTER ONE: INTRODUCTION AND AIM OF THIS RESEARCH

1.1 Radiotherapy

Radiation has been used in medicine for diagnostic and therapeutic purposes since the discovery of x-rays over one hundred years ago. Radiotherapy is the use of high energy x-rays and other ionising radiation such as gamma rays, electrons, protons, etc to treat diseases. The radiotherapy process is complex and involves a series of procedural steps beginning with patient diagnosis, disease staging and lastly the treatment of a specified target volume with predetermined radiation energies and beam parameters. Currently 80% of cancer patients will require radiotherapy as part of their treatment (Janaki et al, 2010), complementing other cancer treatment modalities like surgery, chemotherapy, hormonotherapy or immunotherapy.

Radiotherapy is subdivided into two major branches: internal (Brachytherapy) and external (Teletherapy). In internal radiotherapy the sources are placed in contact with the patient. Mainly sealed sources of radioactive nuclides such as Ir-192, Cs-137, Co-60, Au-198, I-125, etc with different characteristics are used in treatment. On the other hand is external beam radiotherapy, where the radiation source is at a distance from the patient. The most widely used external type of treatment is by photon beam. External photon beams fall into two categories depending on their origin, means of production and energy. The first categories are the gamma rays, which originate from radioactive nuclei such as Cobalt-60 radiocative sources units. The second categories are the X rays which originate in a target bombarded with energetic electrons. The X rays are produced either in an X ray tube (orthovoltage X rays) or in a linear accelerator (linac) (megavoltage X rays). Photon and electron beams produced by linacs are the most commonly used beams in cancer treatments. A very small fraction of treatments are carried out by particles such as protons, neutrons and other heavier ions, but many of these are still under investigation. This study was conducted with external photon beams, using a Linear accelerator.

1.2 Portal dosimetry and Equivalent Path Length

The principal focus of this study is on portal dosimetry, which is defined as the extraction of quantitative dosimetric information from a portal image (image taken behind the irradiated object). Portal dosimetry can be done mainly with a film and electronic portal imaging devices (EPID); limited information can be obtained from using TLDs, diodes, etc. Portal dosimetry is subdivided into transit (where photon beams pass through a phantom or patient) and non-transit dosimetry (where there is no attenuating material between the beam source and the imaging device). EPID portal dosimetry is achieved by the acquisition of grayscale images and conversion to 2D dose maps in the plane of the imager.

The presence in a patient's body of many different tissues each with its own density and chemical composition constitutes a big challenge in radiotherapy, since it would require simulating the ions traversals through all these materials. One possibility of approaching this problem is to apply the concept of water equivalent path length (EPL), defined as the radiological depth between a source and a any other point of interest or calculation point, as determined by the linear attenuation of each material in the path. In other words, if we consider a single radiation ray traversing several tissues of different thicknesses and densities, the EPL concept scales all these tissues to the depth of water which has the same attenuating effects. In this study we calibrated EPID images to determine the EPL, hence the term EPL is used to denote the water thicknesses at each EPID pixel location of the imaged phantom, measured via the transmission of mega voltage photon beams.

1.3 Major structural components of a medical Linear accelerator

Figure 1.1 shows a photograph of a Varian medical linear accelerator (Varian Medical Systems, Palo Alto, California, USA), showing the main structural components.

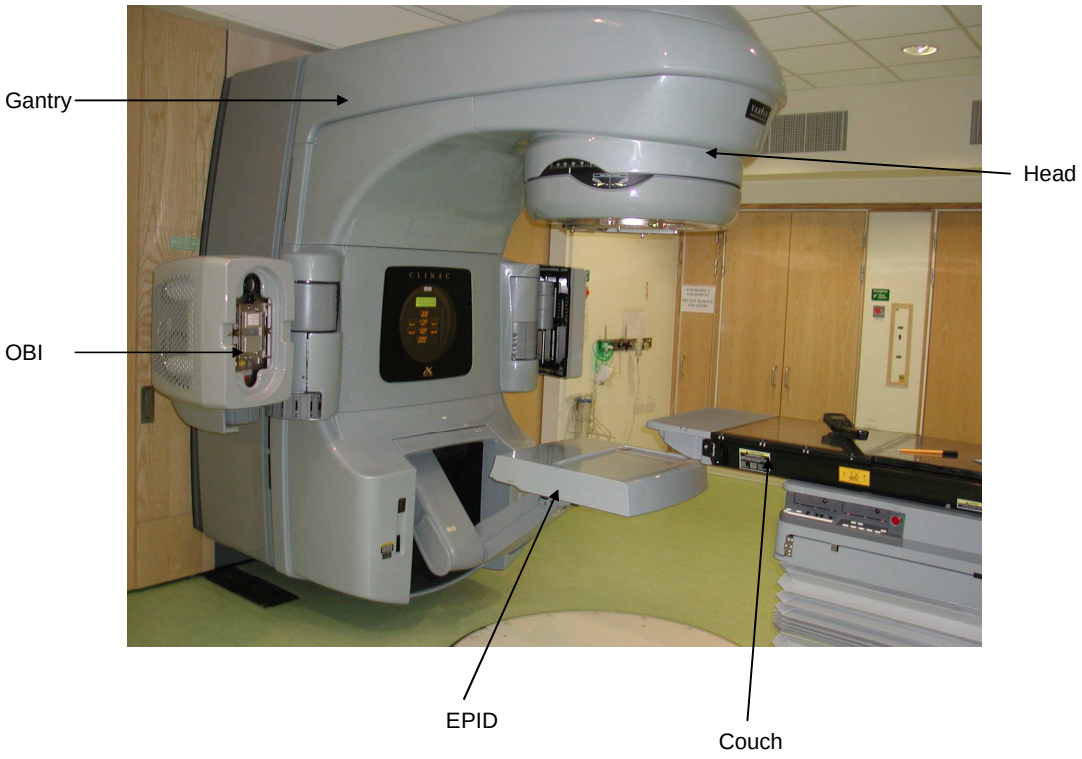

Figure 1- 1. Varian linear accelerator (Model ix)

1.3.1 The gantry and treatment couch

The beam is generated within the gantry, which rotates around the patient. The patient lies on a moveable treatment couch that can move in many directions including vertical (up / down), lateral (right / left) and longitudinally (in / out). Radiation can be delivered to the tumour from any angle by rotating the gantry and moving the treatment couch. Alignment and precision of the linear accelerator gantry and the treatment table are very important parameters in the quality of patient treatment. In operating a linear accelerator, the gantry and collimator rotate around the isocentre (a point in space where radiation beams intersect when the gantry is rotated), and laser (used to make sure the patient is in the proper position) alignment are important parameters for commissioning and quality assurance. The geometric gantry accuracy of 1.0 mm radius at the isocentre is required to deliver a precise dose distribution in conformal and advanced treatment techniques such as intensity modulated radiation therapy (IMRT) image guided radiation therapy (IGRT) and stereotactic treatments.

1.3.2 The treatment head

To make use of and control the produced radiation, all accelerators are designed with a treatment head which provides sufficient shielding against leakage radiation, consisting of a thick shell of high-density shielding material such as lead or tungsten. The treatment head contains many components and the major ones are: X-ray target, primary fixed collimator, scattering foils, flattening filter, ion chamber dosimetry system (two completely independent systems located directly under the x-ray flattening filter which monitor delivered dose, dose rate and beam symmetry), secondary adjustable jaws and the multi leaf collimator (MLC) system that provides mechanically variable collimation.

1.3.3 Electronic portal imaging device

A critical requirement in radiation therapy is accurate day-to-day treatment setup. The primary objective for the development of the electronic portal imaging devices (EPID) was to provide high quality portal images. A Portal image is obtained by positioning any 2D radiation detector such as film in the radiation beam, behind a patient while on treatment. The primary purpose is to verify patient position under actual conditions of treatment, which is an essential component of a patients' treatment. The EPID is mounted at the base of the treatment machine and controlled via a robotically controlled arm. The retractable arm allows quick and easy set up of the image detector during clinical operation and hence saves time. The EPID retractable arm has the capability of moving the radio-sensitive part of the detector to any desired vertical, horizontal or lateral position within its geometrical operating positions.

1.3.4 On-board Imager

The On-Board Imager (OBI) device is used for verification of correct patient position in relation to the isocentre and verification of the treatment fields in relation to assigned landmarks in radiotherapy treatments. The OBI is an automated system recently added to modern linacs, specifically to ease IGRT treatments by managing patient and target movement- both before and during

treatments. The OBI is a kilovoltage X ray imaging system that improves tumour targeting using high resolution, low dose digital imaging in the treatment room. The use of kV imaging means lower patient dose and provides better image quality than megavoltage imaging performed with an EPID. Similar to the EPID, the OBI is mounted on the treatment machine via robotically controlled arms which operate along three axes of motion so that they can be positioned for the best possible view of the tumour. The OBI provides the tools to manage both interfraction motion (changes in position caused by day-to-day set up conditions) and intrafraction motion (changes in position during a treatment session because of normal respiratory, organ motion and patient movement). The system allows a number of imaging choices including: 2D radiographic, fluoroscopic or 3D Cone beam CT imaging modalities.

1.3.5 Support systems

A medical accelerator has several ancillary systems that include: the power supply system, cooling water system, dielectric gas system, interlock and control systems.

- The power supply system: The external power supply delivers the power required to operate the entire unit.

- The cooling water system: Cooling is necessary in order to maintain a precise temperature control for stability of operation. The main parts which need cooling include: microwave generator, accelerating waveguide structure, radiofrequency isolators, pulse modulator, high power transformers, beam focusing and steering coils and X ray target. For convenience, the same cooling system is used for all components to be cooled, requiring water to be supplied at a fixed flow rate and temperature.

- The dielectric gas system: The transition section between the Klystron (on dual energy accelerators) and transmission waveguide needs to be gas filled and is operated at high pressure to prevent sparking. It is typically operated at twice atmospheric pressure and filled with Sulphur Hexafluoride (SF_6) gas. The circulating water provides surface cooling for

the dielectric load. Both gas filled sections of the microwave system are separated from the evacuated sections by the waveguide windows. The high pressure system is usually fitted with a gauge and pressure operated switch which provides an interlock, inhibiting the operation of the modulator if the pressure falls bellow a pre-set level.

1.4 Radiation beam production

Accelerators used in radiotherapy accelerate bunches of electrons either by travelling or stationary electromagnetic (EM) waves to high energies through a disc loaded tube at frequencies in the microwave (≈ 3000 MHz, wavelength ≈10 cm) region, in a vacuum. Radiotherapy accelerators accelerate electrons either by travelling or standing waves, and the main difference between the two is the design of the accelerator structure. Travelling wave structure requires a terminating load to absorb the residual power at the end of structure preventing backward reflected waves. The standing wave provides maximum reflection of the waves at both ends of the structure such that the combination of forward and reverse travelling waves will give rise to standing waves. Figure 1-2 shows the block diagram of the main components commonly used in a medical linear accelerator, adapted from Khan (2003). The accelerator structure is quite complex, but mainly consists of an evacuated copper tube with its interior divided by copper discs of varying aperture and spacing. Pulsed microwaves produced in the Magnetron or Klystron are injected into the accelerator structure via a wave guide system and at the same instant electrons produced from the electron gun are also pulse injected into the accelerator structure. As the electrons are injected into the accelerator structure with an initial energy of ≈ 50 KeV, the electrons interact with the EM field of the microwaves and the electrons gain energy from the sinusoidal electric field. After the electrons have been accelerated the full length of the wave guide, the electron energy will depend mainly on the wave guide design, power applied to it and the current in the wave guide.

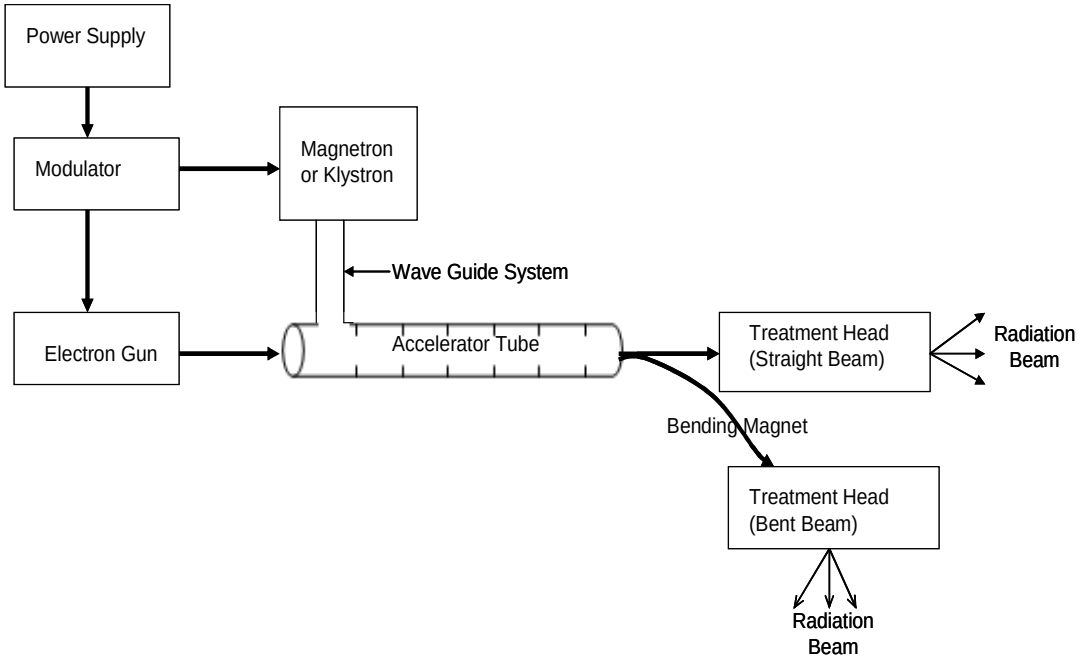

Figure 1- 2. Block diagram, illustrating the major components of the accelerator needed for the generation of the radiation beam (Adapted from Khan, 2003).

The high-energy electrons emerge from the exit window of the accelerator structure in a pencil beam ≈ 3 mm in diameter. In the electron mode, this beam is made to strike a scattering foil in order to spread the beam and to get uniform electron fluence across the treatment field. In the photon mode, after electrons have been accelerated to relativistic velocities, they strike a target and forward peaked photons with a broad energy spectrum are emitted due to bremsstrahlung production. As a result of the collisions, high-energy x-rays are produced from the target. In this case the collimated beam then passes through the flattening filter whose main function is to modify the forward peaked X-ray beam to a uniform beam and to filter the low energy X-rays. These high energy x-rays are directed to the patient's tumour and shaped as they exit the machine to conform to the shape of the patient's tumour. The beam may be shaped either by moving jaws that are placed in the head of the machine, by a multi-leaf collimator (MLC) that is incorporated into the head of the machine or a combination of both.

1.5 Physical properties of radiotherapy beams

1.5.1 Electron beam properties

A number of different types of particles e.g electrons, protons, neutrons and heavy ions are in use in radiotherapy and of these electrons and protons have gained wide spread use. The most clinically useful energy range for electrons is 4-22 MeV (Khan, 2003) and at these energies the electron beam can be used for the treatment of superficial tumours less than 5 cm deep. Because electrons are charged, they rapidly ionise the matter through which they are passing and therefore they are referred to as directly ionising radiation. In the process they lose energy, which falls off rapidly with depth in matter, hence their inability to deliver high dosages to deeper tissues. Typical applications for electron radiation include the treatment of skin cancers, chest wall irradiation for breast cancers, para-spinal lesions, some head and neck cancers and boosting dose to nodes. Although there are many similarities between the behaviour of electron and photon beams, there are also many differences and chief among the differences are summarised below (ICRU report 42, 1987):

1) One of the main features of the electron beam that makes it attractive for radiotherapy is the steep fall-off of the depth-dose curve beyond the dose maximum.

2) The broadening of the dose distribution with depth resulting in a bulged shape in the penumbra region.

3) The complex behaviour of electrons in and around tissue inhomogeneities due to multiple scattering.

4) The shape of the dose distribution particularly at depths greater than the electron beam range which is due to the bremsstrahlung produced mainly in the radiation head of the Linac and also irradiated material / patient.

1.5.2 Photon beam properties

Photons are often referred to as X-rays (generated as a result of atomic process) or γ-rays which is a result of decay of radioactive sources (nuclear process). X-radiation is mainly produced when fast moving electrons strike a high density target material and depending on the energy of incident electrons, either low or

high (or a combination of both) energy X-rays may be produced. Clinical X-ray beams typically range in energy between 10 kVp and 50 MV (Podgorsak, 2005). X-rays in the energy range between 10 – 50 kVp are used for diagnostic purposes. For therapeutic purposes the energy range is subdivided into superficial (50 -200 kVp), orthovoltage (200 to 500 kVp) and mega-voltage (0.5 to 50 MV). The most commonly used photon beams in radiotherapy range between 4 to 20 MV, produced from linear accelerators. Because photons have no charge, they are often referred to as indirectly ionising radiation and this physical property plays a fundamental role in their interaction mechanism. When photons interact with matter, ionisation is produced as a secondary effect, and this reaches a peak value at a certain depth from the surface, resulting in relatively less dose to the surface. This phenomenon leads to a skin sparing effect observed when patients are irradiated. An important consideration in the use of mega voltage photon beams for the treatment of cancer is the amount of surface dose delivered to the patient (Petti et al, 1983). One of the main characteristics of a high energy photon beam is its ability to penetrate deep into tissue while depositing energy in the form of radiation dose, and because of this, photons are mainly used for the treatment of deep seated tumours. Principal applications for photon radiation include the treatment of cancers of the prostate, cervix, oesophagus, lung, etc.

1.5.3 Interaction processes

The most important phenomena during interactions of radiotherapy photon beams are:

- Attenuation of photons by scattering and absorption
- Energy transfer to charged particles, i.e electrons and positrons
- Transport of charged particles
- Deposition of energy

The three most important photon interaction types relevant at energies used in radiotherapy (Metcalfe et al, 1997, Cherry et al 1998, Khan 2003) are photoelectric, Compton and pair production processes. Other interaction processes are the coherent (Classical or Rayleigh) scattering and gamma-n interactions, although their cross sections are small at radiotherapy energies. Figure 1-3 summarises the main interaction processes. The probability of each is

determined by a cross-section which depends on the photon energy and on the density and atomic number of the medium.

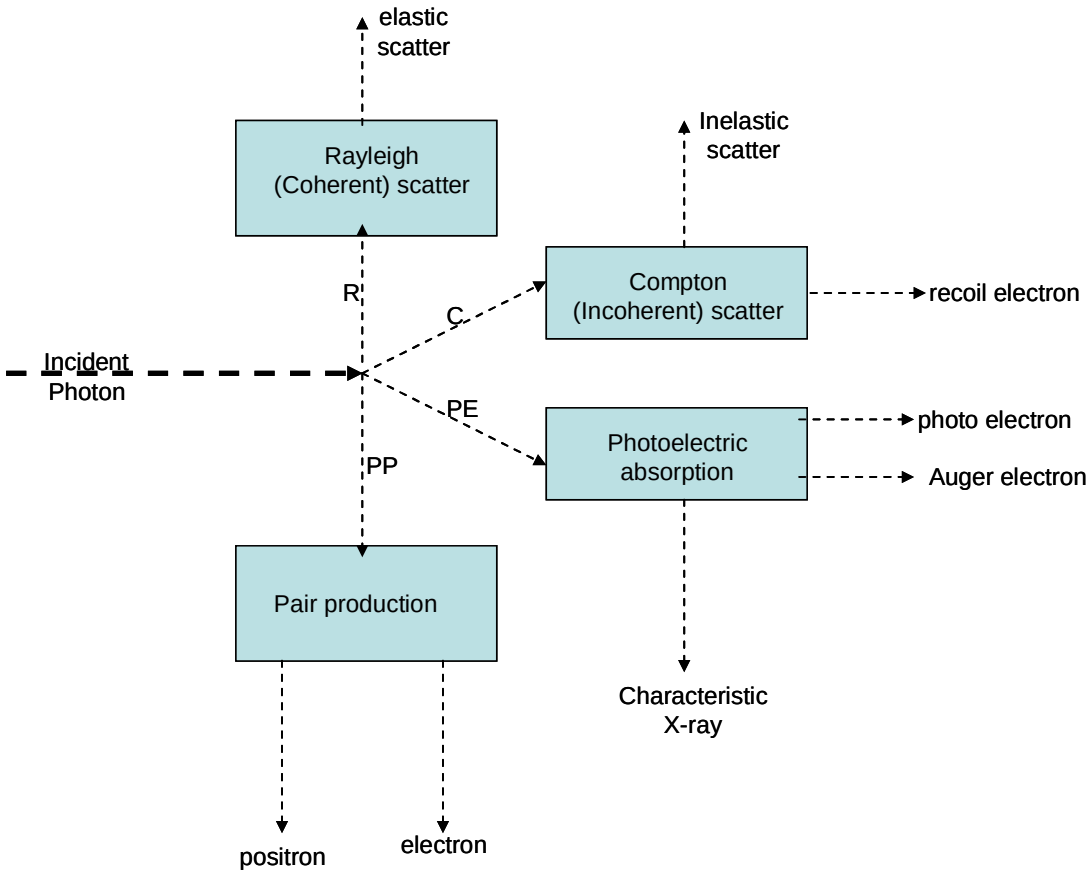

Figure 1- 3. Primary photon interaction processes with their secondary emissions

1.5.3.1 Photoelectric absorption

The photoelectric interaction is more probable at low photon energies and interactions occur with inner shell electrons e.g the K or L shells. All the energy of the incident photon ($h\nu$) is transferred to a bound electron, which is ejected from the atom with kinetic energy $E_e = h\nu - E_{b,}$ where E_b is the binding energy of the electron in the atom. A vacancy left in the shell after the ejection of the photoelectron is filled by electrons from outer orbits, and in the process characteristic x-rays are emitted. Auger electrons, which are mono-energetic, are emitted as a result.

1.5.3.2 Compton scattering

Compton scattering is the dominant photon interaction process at beam energies used in Megavoltage radiotherapy, replacing the photoelectric effect as the chief means of removing photons from the initial beam. It is the predominant interaction process in soft tissue at energies in the range of 200 kV to 2 MV. In these energy ranges, the energy of the incident photon is much greater than the binding energy of the atomic electrons. The interaction occurs with the outermost shell electrons that have negligible binding energies, resulting in the electron and scattered photon being ejected from the atom. By energy conservation, the incident photon energy ($h\nu$) is equal to the sum of the scattered photon energy and the kinetic energy of the ejected electron. The main outcome of the Compton scattering process is the ionisation of the atom.

1.5.3.3 Pair production

Pair production is most predominant at very high energies, with a threshold photon energy of 1.022 MeV (equivalent to $2m_oC^2$, where m_o is the electron rest mass and C is the speed of light) required to supply the rest energy of the two particles. At high energies, the incident photon escapes interaction with the electron cloud and enters the strong field surrounding an atomic nucleus. The photon disappears totally resulting in the formation of two oppositely charged ion particles, a positron and electron. The photon's energy in excess of the threshold is imparted to the ion pair as kinetic energy. That is, the total kinetic energy shared by the ion pairs is ($h\nu - 2m_oC^2$). Annihilation radiation occurs when the positron comes to rest and combines with an electron.

1.5.4 Attenuation of photons

Figure 1.4 shows an experimental arrangement for the study of photons attenuated through an absorbing material. A collimated mono-energetic photon beam is incident on an absorber of thickness Δt and a radiation detector is placed in the beam direction to measure the number of photons that pass through.

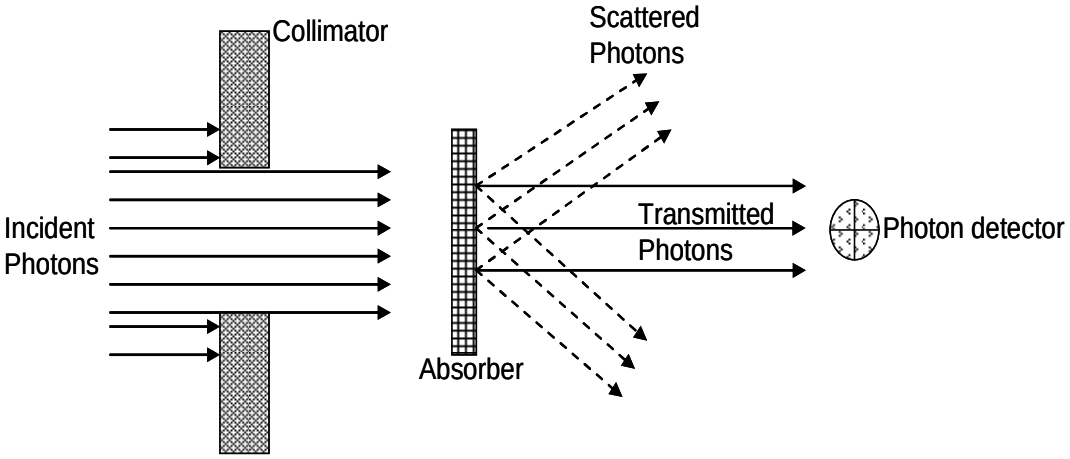

Figure 1- 4. Attenuation of photon beam through an absorber

It is assumed that if a photon interacts with an absorber atom, it is either absorbed or scattered according to the photoelectric, Compton and pair production processes. The intensity of the beam is reduced as the absorbing material thickness Δt is increased. Neglecting scatter, the reduction in photon intensity (ΔI) is proportional to incident photon intensity (I) and to the thickness of the absorber. Assuming a collimated beam where there are no scattered photons detected and also in the limit $\Delta t \rightarrow 0$, then $\Delta t \rightarrow dt$, thus

$$\Delta I \quad \alpha \quad I.\Delta t \Rightarrow dI = -\mu I dt \qquad (1.1)$$

Where the constant of proportionality μ is the linear attenuation coefficient and the minus sign indicates that the intensity of photons decreases as the absorber thickness increases. The solution of the equation is given by

$$I_t \quad = I_o e^{-\mu t} \quad or \quad \ln(I_t) \quad = \ln(I_o) - \mu t \quad or \quad \ln\left(\frac{I_t}{I_o}\right) \quad = -\mu t \qquad (1.2)$$

Where I_t is the intensity transmitted through thickness t and I_o is the incident. The equation indicates that the attenuation of a mono-energetic beam follows an exponential law and a plot of $\ln(I_t)$ versus t gives a straight line with a negative slope equal to μ. The total attenuation coefficient is the sum of the attenuation coefficients due to photoelectric, Compton, pair production and coherent processes.

1.5.5 Photon dosimetry

Dosimetry is a process of measuring radiation dosages. Conventional radiation dosimetry involves measuring doses resulting from ionising radiation and

modelling the particle interactions within tissue. Photons are indirectly ionising, that is they bring about their ionisation by a two-stage process. In the first stage, they interact with matter to produce electrons (and positrons) and these charged particles then produce ionisation along their tracks. The energy transferred from the photon beam to the irradiated material depends on the photon energy, interaction coefficients, atomic number of the material and electron density. The dose to a point in a medium is composed of the primary and scattered components. The primary dose component is composed of energy deposited by photons emitted from the source. The scattered dose component is the result of the scattered radiations from the collimator and irradiated phantom or material.

1.5.5.1 Depth influence

Several methods are available for calculating the absorbed dose to a point in a patient / phantom (Podgorsak, 2005 and Khan 2003). These methods utilise either the percentage depth doses (PDD) or tissue phantom ratios (TPR) or tissue maximum ratios (TMR).

The PDD distributions inside a phantom are usually normalised to D_{max}=100% at the depth of maximum dose (d_{max}), hence

$$PDD(d, A, f, E) = 100\frac{D_d}{D_{d\max}} = 100\frac{\dot{D}_d}{\dot{D}_{d\max}} \qquad (1.3)$$

where

- $PDD(d, A, f, E)$ is the percentage depth dose at depth d, due to field area A, source to surface distance (SSD) f and photon beam energy E.
- D_d and $\dot{D}_d$ are the dose and doserates respectively at a point at depth d
- $D_{d\max}$ and $\dot{D}_{d\max}$ are the dose and doserates respectively at a point at depth d_{max} on the central axis of the phantom.

However the dependence of PDD on SSD, makes the $PDD(d, A, f, E)$ method cumbersome for isocentric techniques. This limitation is overcome by using the TPR or TMR concepts that are nearly independent of SSD or SAD.

The TMR and TPR concepts are defined as

$$TPR(d, A_P, E) = \frac{D_d}{D_{dref}} = \frac{\dot{D}_d}{\dot{D}_{dref}} \text{ and } TMR(d, A_M, E) = \frac{D_d}{D_{d\max}} = \frac{\dot{D}_d}{\dot{D}_{d\max}} \quad (1.4)$$

where

- $TMR(d, A_M, E)$ and $TPR(d, A_P, E)$ are the tissue maximum ratio and tissue phantom ratio respectively at depth d , A_P and A_M are field areas defined at the isocentre for TPR and at a reference depth for TMR respectively and photon beam energy E.
- D_d and $\dot{D}_d$ are the dose and dose rates respectively in a phantom at an arbitrary point at depth d on the beam central axis.
- D_{dref} and $\dot{D}_{dref}$ are the dose and dose rates respectively in a phantom on the beam central axis, at a reference depth d_{ref} = 5cm or 10 cm (or any convenient depth) for the TPR and $d_{ref} = d_{max}$ for the TMR.
- The phantom position is varied such that the arbitrary measurement point and the reference point are the same distance from the source.

1.5.5.2 Effect of field size

For a photon beam with small field sizes, the central axis depth dose is delivered mainly by the primary beam component. For larger field sizes, photons are scattered to every location on and below the surface, including those along the central axis. The relative contribution of scattered radiation to the absorbed dose increases with depth because photon beams tend to be scattered in the forward direction. The radiation output for an accelerator then increases with increasing field sizes. Usually the outputs are measured for different field sizes ranging from the smallest to largest possible at a fixed depth for each field size. The obtained readings are normalised to that of the 10x10 cm^2 field area, and the resulting ratios are referred to as output factors OF(A,E), which are a function of field area A and photon beam energy E.

For isocentric setup, the dose $D(d, A)$ at a depth d for a field area A is then calculated according to the equation (Williams et al 2004)

$$D(d, A) = MUxOF(A)xD(d_{ref}, A_{ref})x\frac{TPR(d, A)}{100} \quad (1.5)$$

Where:

- MU is the number of monitor units given
- OF(A) is the output factor of field A relative to the reference field size (A_{ref} = 10x10cm^2)
- $TPR(d, A)$ is the tissue phantom ratio at depth d and field size A
- $D(d_{ref}, A_{ref})$ is the dose per MU (for linac, approximately 1cGy/MU)

1.6 Objective of radiotherapy

The main objective of radiotherapy is to deliver radiation that will maximize dose to the tumour and minimize dose to normal tissue and/or critical organs, thereby increasing the probability of cure and lowering normal tissue morbidity. Thus considerable effort is devoted to disease localisation, treatment planning, verification of patient setup and finally dose delivery to ensure that the most accurate treatment possible for the patient is provided. Due to the increased complexity of treatment planning and delivery techniques, verification of the dose before and during the actual patient treatment is necessary since the relationship between the absorbed dose and both tumour control probability (TCP) and normal tissue complication probabilities (NTCP) is steep (Podgorsak 2005, Metcalfe *et al* 1997). Figure 1-5 illustrates the relation between TCP and NTCP.

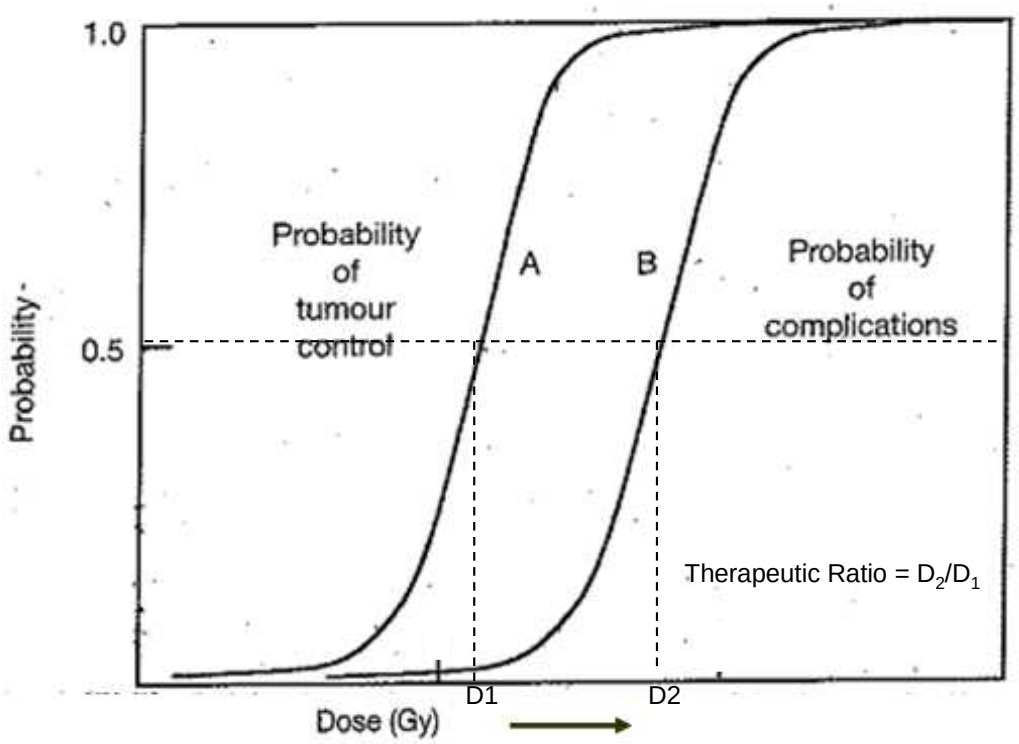

Figure 1- 5. Dose-response curves for tumour control probability (curve A) and normal tissue complication probability (curve B) (adapted from Podgorsak 2005).

The objective of radiotherapy is achieved by increasing the TCP while keeping NTCP to the minimum, a phenomenon known as the therapeutic ratio as defined in figure 1-5 above. There is a considerable amount of clinical evidence which indicates that a high degree of accuracy in dose delivery is essential for successful outcome of radiotherapy treatment (Wambersie et al 2001). A generally accepted criterion for dose accuracy which is developed on the basis of clinical and dosimetric experience is that the administered tumour dose should be within 5% of that specified by the oncologist (ICRU report 50 1993, ICRU report 62 1999). The striving for improved accuracy has led to tremendous developments in radiotherapy.

1.7 Radiotherapy treatment planning

Radiotherapy treatment planning is a process whereby sources of ionising radiation are suitably arranged and combined to give a desired dose distribution in a particular region of the body. The goal of treatment planning is to produce a high and uniformly distributed dose throughout the target volume while keeping the dose to the surrounding normal tissues / organs at risk as low as possible. It

is usually necessary to combine a number of external beams of radiation entering the body from different directions to obtain the desired distribution of absorbed dose in the target volume and to minimise unwanted exposures elsewhere. The combination of beams necessitates two important parameters in treatment planning and these are beam weighting and dose normalisation. Two sets of data are needed for the initialisation and accomplishment of treatment planning (ICRU report 24, 1987) and these are:

1. Beam data: These characterise the radiation and implies measurement at the therapy machine. The number and type of measurements depend on the model used for beam representation and the algorithm used to combine the information with patient data.
2. Patient data: These describe the patient's anatomy (geometry) in a form that can be combined with the beam data. These data include information on the external surface of the patient, the target volume, organ at risk and relevant tissue inhomogeneities.

The enormous amount of beam combination, dose distribution and patient information data necessitate the use of computers for planning. When a patient undergoes the necessary procedures involved in producing a treatment plan, including imaging e.g CT scan, MRI, etc, a computer plan is generated which is used as a tool for the accurate beam direction on the linac. Instructions from the plan have to be carried out in order to reproduce the correct arrangement of treatment fields. The plan specifies the gantry position, collimator positions and orientation, field sizes, shielding, wedge information and source to skin distance pertinent to an individual patient. The plan also provides a contour of the patient's anatomy giving a view of tumour and surrounding normal tissues / critical organs.

1.8 Treatment verification

Radiotherapy treatment is complicated and involves a series of processes that result in a dose distribution to a patient. It is a complex process involving many steps before the actual treatment begins. Figure 1-6 summarises the chain of processes involved before the patient is treated with radiotherapy (van Dyk 2005). A number of uncertainties are introduced at every step in the process of

planning and delivery of treatment, which makes treatment verification a crucial step in ensuring accurate treatment delivery.

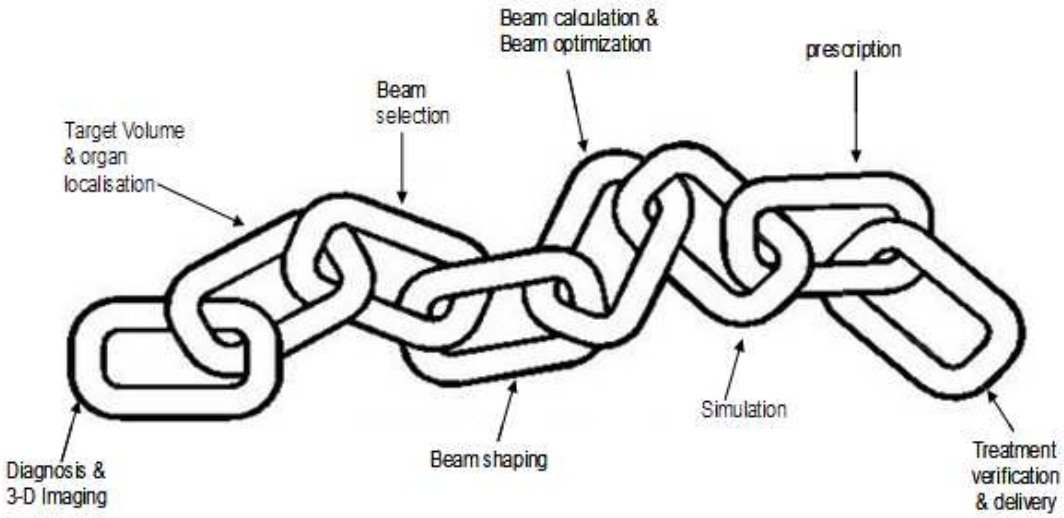

Figure 1- 6. Steps in the radiotherapy treatment process, linked by a chain

The process starts with the diagnosis and the decision to treat the patient with radiation therapy. This is followed by delineation of the target volume and organs at risk, usually from CT or MR scans. Next is dose calculation that includes beam energy selection, shaping and optimisation. Radiation fields are combined in an optimal manner to create a treatment plan for a particular patient to be given in one or an extended set of fractions. Each step in this treatment chain has one or more sources of error and it is therefore important that each single step is executed with the greatest accuracy possible. The uncertainty in each step will influence the accuracy of subsequent steps and, therefore impact on the overall treatment result. Uncertainties in the treatment process may include:

- Uncertainties in the position and extent of the target volume
- Inaccuracies in dose calculation algorithms
- Inaccuracies in treatment machine calibration, mechanical alignment and machine settings
- Inaccuracies in patient setup and/or inter-fractional patient movement
- Variability of patient's internal anatomy

The advancement and development of new procedures in radiotherapy demands a stringent verification procedure due to their complexity. The high dose

gradients in these complex treatments make single point-dose measurements inadequate in verifying the dose distribution. Radiotherapy treatment verification is the process that enables the tumour volume to be treated as planned. A comprehensive treatment verification programme is necessary that includes positional verification, treatment parameter verification and dosimetric verification to ensure that the right radiation dose is given to the correct place.

1.8.1 Positional (Geometric) verification

The aim of geometric verification is to ensure that the geometric accuracy of radiotherapy is within the limits set by the uncertainty margin allowed in the treatment plan. This is achieved by comparing information from the delivery against that planned. Verification is only one component of the treatment process. Accurate and reproducible planning procedures, including the acquisition of good quality reference images, are essential to successful verification. Geometric verification is achieved by comparing 2D or 3D images (data) of the treatment delivered with that planned. In many instances a reference image is obtained, which shows the planned geometry of the treatment field placement relative to internal or anatomical bones or markers. The reference image can be digitally reconstructed radiographs, simulator images or the entire volumetric planning data. Any of these may be used as the standard against which treatment images are assessed. Before the start of radiotherapy, a pre-treatment verification (process that compares the reference images with the planned treatment) is done.

1.8.2 Treatment parameter verification

There are several control mechanisms to evaluate the accuracy of the single steps in the treatment procedure. These checks are based on QA of the treatment equipment, including the Linac and treatment planning system, and on the data transfer among the various types of equipment, such as transfer of data from a CT-scanner to the TPS and from the TPS to the linear accelerator. However, human procedures are subject to error also and determine the

accuracy of the actual patient treatment. In practice, despite these control mechanisms random or systematic errors still may occur (Lavalle et al 2006). The dosimetric impact of these errors is unique for each case and depends on the proportion of fields in error and volume mistreated (Ramaseshan et al 2004). An additional check during the actual treatment delivery provides information about the actual dose delivery and gives the ability to correct the dose before the next treatment fraction, when dose errors occur.

1.8.3 Dosimetric verification: In vivo dosimetry

Dosimetric verification is as crucial as the field placement geometric verification, considering the complicated treatment protocols employed in modern radiotherapy. Verifying dose is the most obvious method of assessing the accuracy of a patient's treatment. Patient dose verification, *in vivo* dosimetry, serves as an important part of a QA programme in radiotherapy and has been recommended for quality improvement of patient care in radiation therapy by several organizations such as the European Society of Therapeutic Radiology and Oncology (Ferreira et al, 2000) and the Royal College of Radiologists (RCR) report No BFCO(08)1 "towards Safer Radiotherapy" (2008) . *In vivo* dosimetry is a tool to measure the radiation dose delivered to patients during radiotherapy. The aim of *in vivo* dosimetry is to compare dose measured at the time of treatment with the dose values specified by the radiation oncologist and the dose values calculated by the TPS, to ensure that the accuracy of the prescribed dose to the target volume is within acceptable limits. In addition to the use of *in vivo* dosimetry for assessing the dose delivered to an individual patient for the detection of various types of errors in the dose delivery process, it can also serve as a tool to verify new treatment techniques in the clinic, after the initial validation of the procedure using phantoms, or as an indicator to assess the dose in organs at risk. It is recommended that in vivo dosimetry should be carried out on all patients and that the treatment dose delivery should be accurate to within 5% (Huyskens, et al 2001, ICRU report 62 1999). For each individual patient the deviations between the delivered dose distribution and the distribution according to the treatment plan should be within the accepted tolerance limits. Radiation detectors that have been used for dose verification

include thermoluminescent dosimeters, diodes, films, and most recently electronic portal imaging devices (EPID).

1.8.3.1 Entrance and exit dosimetry

The most direct form of in vivo dosimetry is to physically place detectors inside the patient (Podgorsak, 2005), however this is only possible for treatments where there are cavities inside the body such as the mouth, vagina and rectum. The most common method is to measure the entrance or exit doses directly on the surface of the patient. Entrance dose measurements are performed in many centres during radiotherapy due to their simpler setup on the surface of the patient (Leunens et al 1990, Fiorino et al 2000). They are useful for identifying setup errors such as incorrect patient source to surface distance. Entrance dosimetry is commonly performed with single point dose devices such as diodes or Thermoluminescent detectors (TLDs) which unfortunately do not cover the entire radiation field, and possible errors may not be detected, more especially in IMRT treatments where there are numerous steep dose gradients occurring in the combined beam segments. In addition to the errors above that can be detected by entrance dose the exit dose, defined as the dose on the patient at the exit side of the beam, can be used to identify changes in tissue thicknesses and detect inhomogeneities via changes in dose transmitted through the patient (Broggi et al 2001).

Figure 1-7 illustrates the exit and entrance calibration planes used in the in vivo dosimetry calculations (Heukelom et al 1991) and also recommended by ESTRO (Huyskens et al 2001). The entrance point is defined at the dose plane a distance d_{max} from the entrance surface of the phantom. The exit dose is defined at the dose plane positioned at a distance d_{max}, from the exit surface of the phantom. It should be noted that the exit dose and entrance dose do not refer to the exit surface dose and entrance surface dose. Figure 1-8 shows a typical depth dose curve illustrating the main differences between entrance and exit doses and their respective surface doses. The lack of appropriate back scatter results in reduction of surface dose.

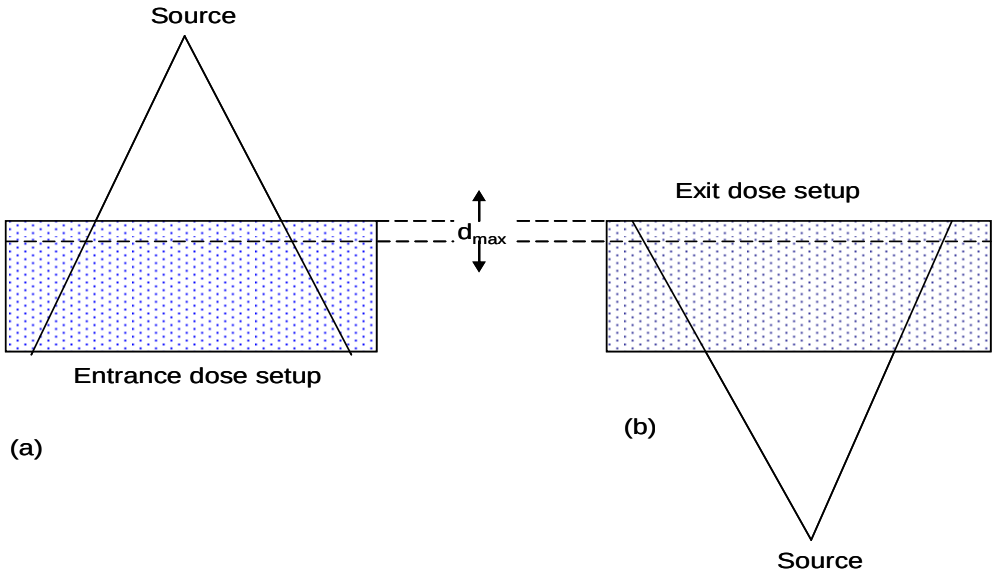

Figure 1- 7. Illustration of the (a) entrance and (b) exit dose calculation planes

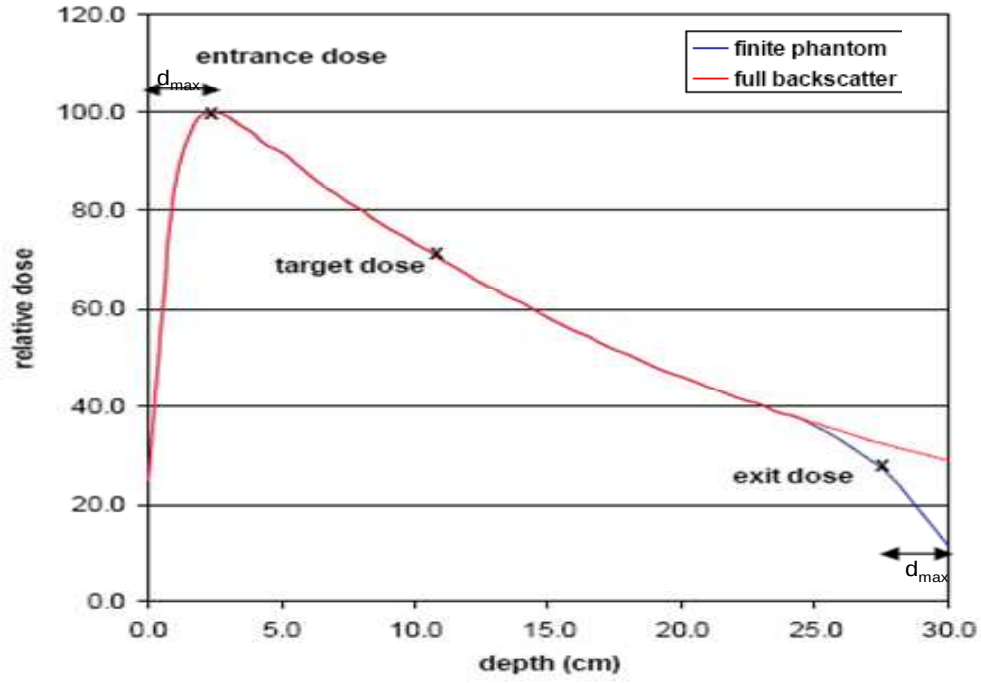

Figure 1- 8. Typical depth dose curve in water phantom

1.8.4 Modalities of treatment verification

1.8.4.1 Film

Film dosimetry can only be used for pre-treatment dose verification and typically employs high resolution radiographic film combined with film density digitisation to get a 2D dose distribution (Ezzell et al, 2003). The technique involves placing a film inside a solid water (dosimetrically water-equivalent plastic) flat phantom at the isocentre perpendicular to the beam axis. One film is used for each clinical field that is being verified. Film depth can vary from the depth of maximum dose (d_{max}) to any depth of interest in the treatment plan. Pinholes are placed in the film marking the location of the cross-hair or points of registration. To calibrate the film used for the clinical fields, a set of calibration films, taken from the same batch of film, are exposed with known radiation field sizes, depth and doses to generate a calibration curve or exposure of one film with step and shoot MLC controlled field beam. The calibration curve is then used to convert the optical densities of the test film to absolute dose. Advantages of using film are that 2D dose distribution is possible and that the required equipment is commonly available in most radiotherapy departments. However, film dosimetry suffers from several drawbacks (Warkentin et al 2003):

1) It is time consuming since it requires processing and scanning of the film, and needs a sensitometric curve to convert optical densities into absorbed doses.
2) The dose response may be affected by the production batch and processing conditions, which are difficult to control
3) Film verification of multiple fields is labour intensive
4) Film requires digitisation for quantitative comparison
5) Requires darkroom and processing facilities.
6) Storage and archiving of film are inconvenient and labour intensive

1.8.4.2 Thermoluminescent dosimeters

Thermoluminescence dosimeters (TLD) can be used to measure the dose at the entrance and/or the exit side of the patient. The fact that no cables are required during the measurement allows the use of TLDs inside tissue-equivalent phantoms to verify radiation doses delivered in new treatment techniques. These

features make TLDs a good *in vivo* dosimetry tool allowing dose assessments directly on patients during therapeutic procedures. A drawback of this approach is that dosimetric information is only obtained at a single or a few points. The major disadvantages of TLD are that there is no instant readout and that the signal is erased during readout and hence it is easy to lose dosimetric information.

1.8.4.3 Diodes

Diodes are semiconductor detectors which, when connected to a suitable electrometer, offer the unique combination of high sensitivity, immediate readout, simplicity of operation (no external bias voltage), small size and robustness against radiation damage. Silicon diodes can be made from either n-type or p-type silicon and in the boundary between two regions, one of p-type and another of n -type silicon, there is a depletion of free charge carriers. Irradiation induces charge flow and due to defects in the crystal lattice some electrons are trapped and will consequently not contribute to the diode signal. The charge can be amplified and measured with an electrometer. Diode signal depends on many factors (Huyskens et al 2001) including: photon beam energy, dose-rate, temperature, field size, source to surface distance, beam angulations and the presence of wedges or blocks. For this reason, diodes require many correction factors. Diodes are conventionally used for treatment verification. They are the most commonly used detector type for patient dose verification (van Elmpt et al 2008; Fiorino et al 2000). However, since they are usually placed on the patient's skin surface, they are used for point dose measurement and dose verification is usually limited to a number of superficial points.

1.8.4.4 MOSFET

Recently there has been an increased interest in the use of the metal oxide-silicon semiconductor field effect transistor (MOSFET) for *in vivo* dosimetry purposes (Ferreira et al 2000, Bloemen-van Gurp et al 2007). The system uses miniature non-intrusive MOSFET semiconductor radiation dosimeters (size less than 4 mm^2). Other characteristics of MOSFET devices are the direct and simple dose readout, the portability of the system and the recording of the accumulated dose of each detector. The output can be converted from mV to

cGy by entering a calibration factor in the reader for each single dosimeter. MOSFETs exhibit in addition a good linearity of their response (Ferreira et al 2000, Bloemen-van Gurp et al 2007). These studies determined important physical characteristics of the detectors to demonstrate the usefulness of MOSFETs as clinical dosimeters; and measurements were performed at different sites of the patient's body, with both photon and electron beams of various energies.

1.8.4.5 Ionisation Chambers

Ionisation chamber matrix detectors have been produced for measuring energy fluence or absorbed dose in two dimensions (Amerio et al 2004, Spezi et al 2005). These detectors consist of a large number of ionisation chambers placed in a regularly spaced array or at specific points in a phantom. Matrix detectors can be attached to the gantry of the linear accelerator or placed on the treatment couch. A quick verification of the beam is performed by comparing the output of these devices with a dose distribution predicted by the TPS. A drawback of these devices is that they have relatively few measuring points and therefore a low spatial resolution. This potentially limits their applicability to the verification of highly intensity-modulated fields.

1.8.4.6 Electronic Portal Imaging Devices

Currently electronic portal imaging devices (EPIDs) are mainly used for patient setup verification during treatment, but several other geometric properties like beam blocking shapes and leaf positions can also be determined. Recent literature indicates an increase in treatment verification with portal imaging (Topolnjak et al, 2010) and it is an effective means of reducing setup errors (Murthy et al 2008, Krengil et al, 2009). Furthermore, one of the most recent usages of EPIDs is portal dosimetry, which allows the possibility of dosimetric treatment verification. Pre-treatment monitor unit verification is possible with high accuracy and also geometric parameters can be verified using the same EPID image. The acquired images are available for on-line review before commencement of treatment. By combining geometric and dosimetric information, the data transfer between treatment planning system (TPS) and linear accelerator can be verified. The EPID dosimetric capability is based on the

presumption that the mean pixel value of the imager is dependent upon the photon fluence incident upon the corresponding area of the detector. This in turn is related to the dose at the exit surface of a patient or phantom. Thus, radiation dose measured at the detector is related to the attenuation through the patient and input dose. If the detector is far enough away from the patient to reduce scatter to a minimum, then the EPID image should produce an accurate estimate of the radiological thickness of the patient (Kairn et al, 2007), which can be related to dose (Kavuma et al, 2010).

1.8.5 Advantages of electronic portal imaging devices over other modalities

The EPIDs have several advantages over the other detectors used for dose verification, and the major ones are:

- The device is in most centres already attached to the accelerator
- Fast image acquisition
- No film processing and need of cassettes
- The image is in digital format with high resolution
- Point and 2D dose measurements
- Possibility of 3D dose verification, reconstructed by back projection of the 2D dose into a 3D image data from CT scan or cone beam CT
- Possibility of performing in-vivo dosimetry on linac-based treatments without the need for additional equipment
- Immediate image analysis is possible and review can be done at any workstation

The past 2-3 decades have yielded new clinical capabilities and substantial improvements in patient care. The greater complexity of today's radiotherapy practice creates considerable challenges for users. There is a general need to use a wide range of equipment features and clinical applications to improve the quality (e.g. reducing the radiation dose to patients' non-targeted areas) and effectiveness of the treatment. EPID has evolved because it provides real-time, fast image archiving, retrieval and automated image analysis. This has prompted

many research groups to study their use for radiotherapy dosimetry. However the current techniques are limited to pre-treatment verification, where the radiation fluence is only verified in the absence of a patient (non-transit). The actual day-to-day treatment verification of dose received by the patient is imperative to keep up with the pace of the increasing complexity of radiotherapy treatments. *In vivo* dosimetry using diode, TLD and/or MOSFET is commonly employed to verify the dose delivered during external beam radiotherapy (Nijsten et al 2007, Piermattei et al 2007). These measurement techniques, however, require considerable time and effort to implement routinely in busy radiotherapy departments and the amount of information gathered is limited to a single or a few selected points.

1.9 Portal Dosimetry Literature Review

1.9.1 History of EPID usage for dosimetry

One of the first uses of EPIDs for dose measurement was developed at the Netherlands Cancer institute and involved the scanning liquid-filled ionisation chamber (SLIC) EPID (Van Herk, 1991). Later in mid 1990's, this technological development led to PortalVision, a Varian (Palo Alto, CA, USA) commercial portal dosimetry software system. One of the main limitations of the SLIC was the relatively long read-out time (van Elmpt, 2008), such that the device could not measure dose directly, but was suitable for measuring dose rate. The measured dose rate was converted to absolute dose by recording a continuous readout of the monitor chamber signal of the linac during image acquisition and the number of MUs delivered for the measured dose image. Chang et al (2000) investigated dose verification using the liquid-filled ion chamber EPID by comparing profiles and dose measurement at the isocentre. The study reported an accuracy of 3% in central axis, better than the 5% requirement recommended by the Task Group 40 Report (Kutcher et al 1999) of the American Association of Physicist in Medicine (AAPM) for independent verification of the dose at the isocentre. Although this was sufficiently accurate for clinical QA, the slow response detector memory effect and beam hold-off effects (the withholding of linac beam pulses when MLC leaves are not in the correct positions), made the liquid-filled ionising chamber EPID usage impractical for clinical use (Chang et

al, 2002). Mohammadi et al (2007) used a scanning liquid-filled ionization chamber electronic portal imaging device (SLIC-EPID) and extended dose range (EDR2) films to evaluate transmitted dose profiles for homogeneous and inhomogeneous phantoms. Calibrated ionisation chamber measurements were used to convert the pixel values acquired from the electronic portal images to dose. For homogenous and inhomogeneous phantoms, more than 90% agreement was achieved using gamma criteria of 2% and 3 mm and 3% and 2.5 mm respectively.

In the mid 1990's, camera-based EPIDs were invented and developed into commercial products by various vendors, among which was iView^{TM}, marketed by Elekta Oncology Systems, Crawley, UK (Heijmen et al, 1995). The main advantages of these systems were that a large portion of the field could be imaged quickly due to the fast read-out of the camera and they had a high spatial resolution. The measured grey scale value was approximately linear with dose and did not depend on the absorber thickness placed in the beam (Pasma et al, 1998). The camera based EPID however, had a large field size dependence caused by scattered visible photons inside the optical system. Once the camera-based EPID was calibrated, mainly by removing the influence of the optical scatter effects, the device was suitable for performing portal dosimetry with deviations around 1–2% (van Elmpt, 2008). Pasma et al (1999) reported on the use of charged-coupled device (CCD) camera based system for pre-treatment dosimetric verification of IMRT beams produced with a dynamic MLC. EPID images were acquired for all beams and these images were then converted into 2D dose distributions and compared with the calculated dose distributions using a commercial TPS. The dose profile measured with the EPID was also compared with ionisation chamber measurements. The agreement between the EPID and ion chamber was within 2%.

The amorphous-silicon EPIDs (a-Si EPID) or flat-panel imagers were first described by Antonuk et al (1998) and currently are the most common type of EPID available. The panel consists of an X-ray converter, light detector, and an electronic acquisition system for receiving and processing the resulting digital image. The dose–response behaviour of the three commercially available a-Si EPIDs has been described; the Elekta iView GT system, the Siemens OptiVue and the Varian Portal Vision a-Si 500/1000 (McDermott et al 2004, McDermott et al 2006).

Munro et al (1998a, 1998b) investigated the dosimetric characteristic of a small (96x96 mm^2) a-Si indirect flat panel detector; they measured the linearity, spatial resolution, glare, noise and signal to noise characteristics. The results indicated that the response of the sensor was linear and did not suffer from the glare phenomenon associated with camera-based EPIDs. This study concluded that a-Si detectors are more suitable for dosimetric verification. El-Mohri et al (1999) studied linearity response, dose rate dependence, sensitivity, long and short term reproducibility of a-Si flat panel. This study investigated EPIDs in both the indirect and direct configuration modes. The direct detection mode was superior over the indirect mode in terms of linear response and good long term stability in pixel response.

1.9.2 Dosimetric characteristics of a-Si electronic portal imaging devices

The dosimetric characteristics of EPIDs have been studied by several investigators. McCurdy et al (2001) investigated dosimetric properties of a-Si detector such as linearity with dose (±0.5%), reproducibility (±2%) and response variations in gantry rotation and source to detector distance. Greer et al (2003) investigated the dosimetric properties of an a-Si EPID using continuous frame-averaging acquisition mode for 6 MV radiation beam. The properties investigated included effect of build-up, dose response, field size response, response to rapid MLC leaf speed, beam dose rate effect, memory effect and reproducibility. The dependence of response on EPID calibration and dead time in image frame acquisition occurring every after 64 frames was measured. The results of this study indicated that the response of the EPID with dose and dose rate was linear, and response to MLC motion (leaf speed of 2.5 cm/s) was also found to be linear. A field size deviation of ≈ 5% relative to d_{max} ion chamber measurement was found. Memory effect was negligible at ≈ 0.2% and reproducibility was good at ≈ 0.8%. This investigation also reported on the relative dosimetry of an a-Si EPID, where they measured the accuracy of the EPID in recording open and static wedge fields. EPID profiles through the central axis for the open field and in the wedged direction for the wedge field were compared to ion-chamber measurement and the agreement was within 3%.

Van Esch et al (2004) performed EPID detector saturation, linearity, reproducibility, ghosting, field size dependence and portal depth dose measurements. The results from this investigation indicated that detector saturation may result in dosimetric errors in the range 0.35 to 1.4%, though it can be worse than this depending on type of detector. The EPID response for depth dose (dose measurements as a function of absorbing material, normalised to their maximum value) was within 1% compared to an ion chamber in terms inverse square law behaviour. Short term and long term detector reproducibility was found to be within 2% for static as well as dynamic field delivery. Ghosting was below 1% for 6 MV and 18 MV. The field size dependence for EPID and ion-chamber measurements were similar for 6 MV and showed discrepancies of up to 9% for the 18 MV beam. The dose maximum plateau region is wider for the a-Si EPID with widths of ≈ 1.5 cm and ≈ 3 cm for 6 and 18 MV respectively.

Winkler and George (2006) carried out an inter-comparison of eleven Elekta iViewGT™ EPIDs from different institutions and reported on dose, dose-rate, and field-size responses among others. Chen et al (2006) and Nijsten et al (2007) reported the dosimetric properties for the Siemens EPID, mainly focusing on calibration methods for transit dosimetry. McDermott et al (2006) compared the ghosting effects for three (Varian, Elekta and Siemens) a-Si EPIDs and reported on their signal-to-MU ratios. Several articles have reported on the dosimetric characteristics of the Varian EPID (Greer et al 2003, Chang and Ling 2003).

One specific area where EPIDs have been successfully used for dosimetric purposes is in the pre-treatment verification of IMRT fields, by assessing the accuracy of the intended fluence as used in the treatment planning system (TPS) for dose calculation and the actually delivered fluence (Greer et al 2003, Van Esch et al 2004). These studies investigated the application of a-Si for pre-treatment dose verification by comparing clinical EPID IMRT images with fluence maps predicted by TPS. Van Esch et al (2004) developed and evaluated a portal dose prediction algorithm based upon the pencil beam dose calculation as implemented in the CadPlan TPS. Measured and predicted portal dose images were compared by means of line profiles and gamma index criteria. Over 90% of points in the IMRT fields passed the gamma criteria at 3% dose difference and 3 mm distance to agreement. Chang et al (2003) evaluated the use of a-Si 500 EPIDs for the verification of IMRT beam delivery using synchronous frame

averaging acquisition, which was evaluated on 25 prostate IMRT fields. The acquired EPID images for IMRT fields were converted to dose using a dose profile calibration curve. The measured dose profiles compared with the planned were in good agreement with a mean error of 1.9% and standard deviation of 0.5%. The central axis dose agreement was better than 2.0 %.

A major problem associated with a-Si EPIDs for transit dosimetry is the presence of a phosphor layer, which can introduce large deviations from water-equivalent behaviour due to energy-dependent response and visible light scattering, though the effect caused by the latter may be negligible. During the present work, Sabet et al (2010) modified an a-Si EPID to a direct detection configuration by removing the phosphor layer, and the accuracy of using it for transit dosimetry measurements was investigated for 6 and 18 MV treatment beams by comparison to ion-chamber in water measurements. This study concluded that the direct EPID could perform as an ion-chamber detector for transit dosimetry applications in all geometries. The major current limitation of the direct EPID is the poor image quality compared with the clinical configuration. This study suggested that the practicability of interchanging between imaging and dosimetry setups should be investigated.

1.9.3 Dose Verifications

Several authors have reported on different ways of using the EPID for dose verification. Leunens et al (1990) and Terron et al (1994) combined entrance and exit point dose measurements to determine a mid-plane dose inside the patients. This approach has been shown to be valuable for immediately identifying errors related to the inaccuracy of the TPS, especially for 2D dose calculation algorithms, setup errors, human errors and fluctuations in Linac output. The limitation of the approach has been the simplicity of the algorithms used to determine the midplane dose, which are only effective under certain geometric and symmetric (phantom) conditions (Leunens et al 1990). Algorithms for determining the midplane dose at a single point were later extended to 2D (Dam et al 1992, Ebert et al 1994), by correlating the 2D transmitted dose measured with film at a certain distance behind the phantom (patient) with a 2D dose at the exit surface of the patient. This was then used to predict 2D midplane dose distributions. These authors reported the agreement between

exit doses derived from transmitted film and diodes measurements to be within 5-8%. Discrepancies were attributed to scatter approximations for large phantom to detector distances and curvature in phantom geometry at the exit beam side. Under such conditions, the correlations in off-axis ratios at the midplane and transmitted dose plane deteriorated due to the decrease in contribution of scattered dose relative to the primary dose contribution. This was shown to overestimate the dose near the edges of the field calculated at the midplane relative to measurements or TPS calculations at the midplane (Dam et al 1992, Fiorino 2000).

For dosimetric use, portal images must be corrected for field size dependence, energy dependency and ghosting effects (Herman et al 2001). This idea was used by several investigators, e.g. comparison of the measured and predicted portal dose for each treatment field (Pasma et al 1998 and Van Esch et al 2004), verification of leaf positions for intensity modulated fields (Greer et al 2003 and Parent et al 2006), reconstructing the dose to the patient using the exit image acquired during treatment (Piermattei et al 2007 and Wendling et al 2006) and converting the image to a fluence distribution that is used as input to a dose algorithm to reconstruct a 3D dose to the patient (Renner et al 2005, Steciw et al 2005, Van Elmpt et al 2006 and Van Zijtveld et al 2007).

1.9.4 In vivo dosimetry with electronic portal imaging devices

The advancement of radiotherapy technology resulted in the transition from 2D film measurements described in section 1.8.4.1 to EPID acquired images as described in section 1.8.4.6. Kirby et al (1994) were one of the first authors to use an EPID for determining exit doses of phantoms and patients, using integrated images from a fluoroscopic EPID with 6 and 20 MV photon beams. They determined an empirical relationship between exit doses measured with diodes and transmitted doses measured with the EPID based on homogeneous phantom measurements for a variety of thicknesses and patient-to-EPID air gap distances. The empirical data were tested on a variety of irradiation geometries using an anthropomorphic phantom as well as on patients undergoing radiotherapy and the agreement was within ± 7%. The limitation of the method was its failure to accurately predict the exit dose under asymmetric scatter

conditions and also the ± 7% is out of tolerance compared to the ± 5% recommended by ICRU report 62.

The earlier 2D midplane dose calculation methods above were only accurate for small air gap distances ≈ 10 cm between the exit surface of the patient and the transmitted dose plane and did not take into account the decrease in scatter contributions for larger sized air gaps. Furthermore if EPIDs are to be used for exit and midplane dosimetry, such models need to be adjusted for the extended distances from the beam focus and patient for which EPIDs are installed. As a consequence, Boellaard et al (1997) developed a 2D back-projection-convolution model for converting transmitted doses to exit doses more accurately at larger phantom to detector air gaps of ≈ 50 cm. The idea was based on the separation of the total exit dose into the primary and scatter components. The scatter dose at the exit surface was calculated by convolving the primary exit dose with an exponential spread function, from which they derived the scatter to primary ratio transmissions. The agreement between exit doses calculated with the convolution model compared with exit dose measured with an ion chamber for an 8 MV photon beam under homogeneous and inhomogeneous phantoms was within 2.5% (Boellaard 1997).

Wendling et al (2006) extended the original convolution model of Boellaard et al (1997) for a-Si EPIDs. Additional kernels were applied to account for the unique response of the a-Si EPID, corrections for lateral scatter effects occurring within the EPID itself and improving accuracy in beam penumbra. More recent work focused on extension of 2D convolution models into a 3D dose reconstruction applied in different targets and organs at risk (Louwe et al 2007). Modifications such as the inclusion of patient contour information were included and were found to significantly improve the results.

Fidanzio et al (2010) used a generalized set of correlation functions F(TPR,w,L) and empirical factors f(TPR,d,L); where TPR is the Tissue Phantom Ratio, w is the phantom thickness, L is the square field side, and d is the distance between the phantom mid-plane and the isocenter to reconstruct the isocenter dose for 6, 10 and 15 MV photon beams. The in vivo dosimetry method was developed from previous work done by the same group (Piermattei et al 2006 and Piermattei et al 2007). The function F(TPR,w,L) is defined as the ratios between the transit signals per MU, obtained by an a-Si EPID positioned below a solid water phantom, and the dose per MU values measured along the beam

central axis at phantom mid-plane coincident with the SAD. In the experimental set-up they determined the mid-plane doses per MU, and the transit signals per MU for different phantom and field sizes measured at the Source to EPID Distance. They used these data to determine the empirical factors f(TPR,d,L) that take into account the variations of the scattered photon contributions on the EPID due to the different phantom position with respect to the SAD. They reported tolerance levels that ranged between ±5% and ±6% depending on the tumour body location.

Whilst EPIDs are in routine use in radiotherapy departments to verify the desired treatment geometry in relation to anatomical structures, their role as *in vivo* dosimeters is less common (van Elmpt et al, 2008). In the past decade, research and development has been undertaken which relates to their double utilisation as an in vivo dosimeter and field verification tool (Fiorino et al 2000, Broggi et al 2001, Piermattei at al 2007, McDerrmott et al 2007, van Zijtveld et al 2009). Within the last two decades, EPIDs based on amorphous silicon panels mounted on an accelerator gantry have been introduced for patient setup verification (Fielding et al 2002, Herman et al 2001) while more recently, dose verification became more possible (Chen et al 2006, Wendling et al 2006, Parent et al 2007). EPIDs offer the possibility of performing in-vivo dosimetry on linac-based treatments without the need for additional equipment. EPID in-vivo dosimetry is thus defined as the determination of a dose distribution inside the patient based on EPID images acquired during treatment, and is only possible with the transit method (Wending et al 2006, van Elmpt et al 2008). In vivo verification of the delivered dose is achieved by comparing the portal image acquired during treatment to a predicted transmission. Such comparison can reveal problems in dosimetric performance of the linear accelerator, errors in the treatment plan or beam modifying devices such as wedges and compensators, and changes in patient anatomy.

1.9.5 Portal dosimetry commercial Packages

1.9.5.1 Varian's portal dosimetry system

The current portal dosimetry package available, version 8.2.0, is a non-transit package; hence it is used for pre-treatment verification of IMRT plans only. The

averaged grayscale image is converted into a portal dose image in the Dosimetric Workspace by summing all images taken over the beam-on time. Commissioning of the portal dosimetry system starts with configuring the Varis / Vision system. The portal dose image prediction (PDIP) software algorithm first has to be configured in Beam Configuration before it can be used in Eclipse 8.6. Among other things, an image of a test pattern has to be measured with the imager, and output factor tables of the imager have to be measured. This is analogous to the beam data measurements (water-phantom) needed for configuration of 3D dose-calculation algorithms. The processes inside the amorphous silicon imager are rather complicated and not comparable to ionisation-chamber water dosimetry. Hence the terms "dose" and the corresponding unit "Gy" are avoided by Varian in the context of Portal Dosimetry. Instead they use Calibrated Units (CU), where 1 CU corresponds to 1 Gy at a reference depth.

1.9.5.2 Dosimetry Check

Math Resolution LCC (USA) developed an EPID dose verification package “Dosimetry Check”, which was initially dedicated to non-transit pre-treatment dose verification, but now is extended to transit verification. In the UK, the “Dosimetry Check” software was first tested at the Edinburgh Cancer Center, Western General Hospital and evaluation of its suitability in different conditions was presented at the Scottish Radiotherapy Physics meeting (Nichol et al, 2010). The analysis of the results of the presentation concluded that, “Dosimetry Check” can be used as either a pre-treatment verification or as a transit dosimetry tool with reasonable accuracy and that further studies are required in order to establish acceptable tolerances for different clinical sites. By the end of 2010, at the end of the present project, the Dosimetry Check software was commercially available. This system works with input from the Varian, Elekta, and Siemens EPID in integration mode.

1.9.5.3 EPIQA

EPIQA is also a non-transit commercial software that can convert a dosimetric image acquired by an EPID into a dose map, and to compare the dose map with a reference dose distribution. EPIQA was developed specifically for use with Varian a-Si500 mounted on a Varian 6EX linear accelerator. The software can be utilised

for verification of static as well dynamically modulated fields. The portal dosimetry image conversion to dose is based on the GLAaS algorithm (Nicolini and Fogliata 2006). It is a pre-treatment verification tool, hence incapable of *in vivo* verification. The main goal is to identify potential errors either in the calculation or in the delivery process.

1.9.5.4 EPIDose

EPIDose (Sun Nuclear, Melbourne, FL) is a tool designed for the use of EPIDs in IMRT QA that uses raw MV EPID images (no additional build-up and independent of gantry angle, but with dark and flood field corrections applied) to estimate absolute dose planes normal to the beam axis in a homogeneous media (i.e. similar to conventional IMRT QA methods) (Nelms et al 2010, Varatharaj et al 2010). EPIDose is a non-transit package used for pre-treatment verification of fluence by comparing the TPS and EPIDose dose distributions. EPIDose converts an EPID image to dose maps for analysis in the MapCHECK software (also a Sun Nuclear product), by performing a dose-to-dose comparison independent of TPS. Nelms et al (2010) evaluated its suitability by using the Varian EPIDs images (a-Si500 and a-Si1000) and Siemens EPIDs images (OptiVue500 and OptiVue1000).

1.9.5.5 Elekta iViewGT and Siemens Optivue

There is evidence in the literature suggesting that the Elekta iViewGT (Winkler et al 2007 and Cilla et al 2011) and Siemens Optivue (Fidanzio et al 2010) EPIDs were calibrated for transit and non-transit dosimetry. The purposes of these studies were to develop, implement and validate methods for portal dosimetry with amorphous silicon EPID for a wide energy range. Analytic functions were applied in order to correct for nonlinearities in detector response with dose rate, irradiation time and total dose. EPID scattering processes were corrected for by means of empirically determined convolution kernels. Unlike the known Varian PDIP, we did not find corresponding commercial portal dosimetry packages from Elekta and Siemens.

1.9.6 Current drawbacks for the wide use of electronic portal imaging devices as a dosimeter

Despite the positive characteristics of EPIDs over other modalities, there is limited usage of these devices for dosimetry and there is currently only one commercial transit dosimetry module (section 1.9.5 above): This became available only near the conclusion of this work. An appropriate calibration method for the conversion of the EPID image to dose is one of the main setbacks for using the devices dosimetricaly. Electronic portal imaging devices have been calibrated either by conversion of grey scale pixel value to dose value using an ion chamber or by using Monte Carlo simulation methods (prediction of the grey scale pixel value). The drawback is that these calibration models are not robust enough to cover all treatment techniques and irradiation configurations (van Elmpt et al 2008: see section 2.3.3.1). Some centres have developed in-house packages, which require assessment before induction into routine clinical usage. It is desirable to use a single piece of equipment for geometrical and dosimetrical verification to keep operational costs, treatment times and maintenance work to a minimum. The general aim for this study was therefore to develop techniques for integrated transit in vivo dosimetry verification using an EPID.

1.10 Aims of this study

As can be seen from section 1.9.4, there was no clinically usable system for transit dosimetry (either commercial or non-commercial) at the commencement of this project. The main aim of the study was to develop techniques for the transit dosimetric treatment verification using an a-Si EPID. The four sub-aims were:

- To investigate the dosimetric characteristics of Varian a-Si500 EPIDs by assessing a large number of clinically used devices, for consistency of performance and portal dosimetry implications.
- To develop a method to predict portal dose in different radiotherapy (clinical) settings based on equivalent path length, measured with an EPID

- To develop a method for dose verification by deriving the plane phantom / patient dose at the exit from the portal dose measured with the EPID which is compared with intended dose from TPS and MapCHECK device.
- To evaluate the developed techniques by comparing the predicted and measured patient doses in homogeneous / anthropomorphic phantoms.

CHAPTER TWO: MEGA-VOLTAGE ELECTRONIC PORTAL IMAGING DEVICES: DEVELOPMENT

2.1 Introduction to electronic portal imaging devices

For nearly 30 years, electronic portal imaging devices (EPIDs) have been under development by accelerator manufactures and individual investigators. In addition to the imaging system developments, there has been an extensive advancement in the means of extracting quantitative information from the images (Herman et al 2001, Antonuk 2002). These include extracting the treatment field edge to establish a known reference image and registration techniques to compare reference images with the newly acquired portal images. Despite the considerable development of imaging technology and image analysis techniques, the clinical role of this technology is still evolving. Initially touted as replacements for portal films, these systems have been used to reduce systematic errors in patient positioning for on-line (i.e., immediate) patient repositioning, to identify the location of radiopaque markers to account for organ motion, for megavoltage cone-beam CT and also for kilovoltage cone-beam CT. In addition to their use for imaging, these imaging systems are also being used for pre-treatment verification of IMRT fields and for transit dosimetry. Clinical acceptance of the imaging systems is increasing but much remains to be done. Improved methods of identifying errors in patient positioning and automated methods to correct these errors (e.g., moving the couch or changing the MLC pattern) will be required. Radiation therapy is becoming an image-guided therapy and portal imaging will become ever more important in the delivery process (van Elmpt et al, 2008).

2.2 Types of electronic portal imaging devices

2.2.1 Direct and Indirect radiation detection electronic portal imaging devices

Electronic portal imaging devices are designed to operate between 1 and 20 MV (Boyer et al 1992). Images from the EPID are the result of a high energy x-ray

beam passing through and interacting with the EPID sensitive layer. They detect low energy electrons resulting from Compton scattering of high energy photons. The differences in the attenuation of the photons due to varying densities and thicknesses in the object give rise to different grey scale or pixel values which form an image. The pixel value is proportional to the number of electrons or ions formed as a result of interactions of the attenuated x-rays beam with the sensitive medium of the EPID. With the technological advancement in electronics, the image quality of EPIDs of various types has improved significantly. Imaging devices can be classified into directly and indirectly detectors (Mayles et al, 2007), as illustrated in figure 2-1. Direct detection (figure 2-1 b) incorporates a buildup material (photodetector) to produce electrical charges on detection of an x-ray whereby the incoming photons are converted directly into secondary electrons for detection. Indirect detection (figure 2-1 a) incorporates a phosphor to produce visible wavelength photons on detection of an x-ray. The Indirect detector converts incident radiation into secondary electrons which are converted into visible light for detection. The process is indirect because the image information is transferred from the x-rays to visible light photons and then finally to electrical charge.

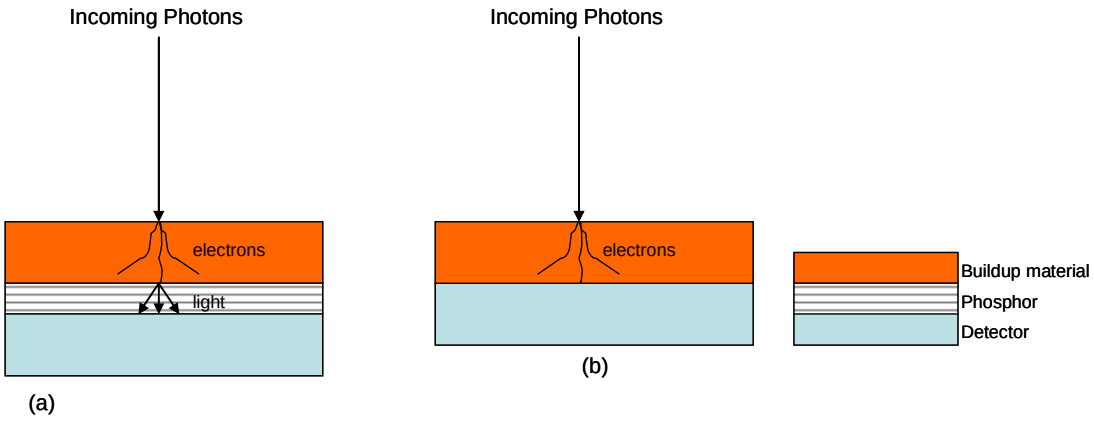

Figure 2- 1. Types of radiation detectors. Figure (a) is the Indirect detector while figure (b) show the direct detector mechanism.

Both detectors have a build-up layer, typically a piece of thin copper, to convert high energy photons to secondary electrons. This layer also serves to minimise the contamination electrons from the head of the linear accelerator treatment unit. In the indirect case, an additional phosphor layer is required to convert the secondary electrons to visible photons (figure 2-1a). Detectors are used to

detect the optical photons. For the direct detector EPID, detectors are placed directly beneath the build-up layers (figure 2-1b). Upon collecting the secondary particles in both the direct and indirect cases, a signal is generated and transferred for analysis via a set of peripheral electronics located around the device. For any imaging system, the most important physical quantity that must be determined is the signal-to-noise ratio (SNR). The detective quantum efficiency (DQE), which is defined as the square of output SNR divided by the input SNR, is the metric used to gauge the efficiency of imaging devices. DQE gives the SNR transfer characteristics of an imaging system as a function of spatial frequency. DQE gives a measure of how efficient the imaging system is, at transferring SNR (i.e. information) contained in the radiation beam on a 0 to 1 scale (Boyer et al 1992). Low optical conversion efficiency from one layer to the next may result in decreased DQE of the imaging system. Commercially available systems consist of scanning liquid ion chamber EPIDs, camera-based EPIDs and the active matrix flat panel imaging detectors (Munro et al 1998b, Antonuk 2002).

2.2.2 Matrix (Scanning liquid) Ion Chamber detectors

The matrix ion chamber device consists of two sets of electrodes that are oriented perpendicularly to each other separated by a 0.8-mm gap, which is filled with a fluid (2,2,4-trimethylpentane) that is ionized when the device is irradiated. Each set of electrodes consists of 256 wires spaced 1.27 mm apart to provide an active area of 32.5x32.5 cm^2. One set of electrodes is connected to 256 electrometers and the other set of electrodes is connected to a high-voltage supply that can apply a 300-V potential to each electrode individually. As illustrated in figure 2-2, the matrix ion chamber array is read out by applying a high voltage to each of the high-voltage electrodes in succession (for approximately 20 milliseconds) and measuring the signal generated in each of the 256 signal electrodes. The readings are read out via the electrometers which are multiplexed and sent to output via an amplifier.

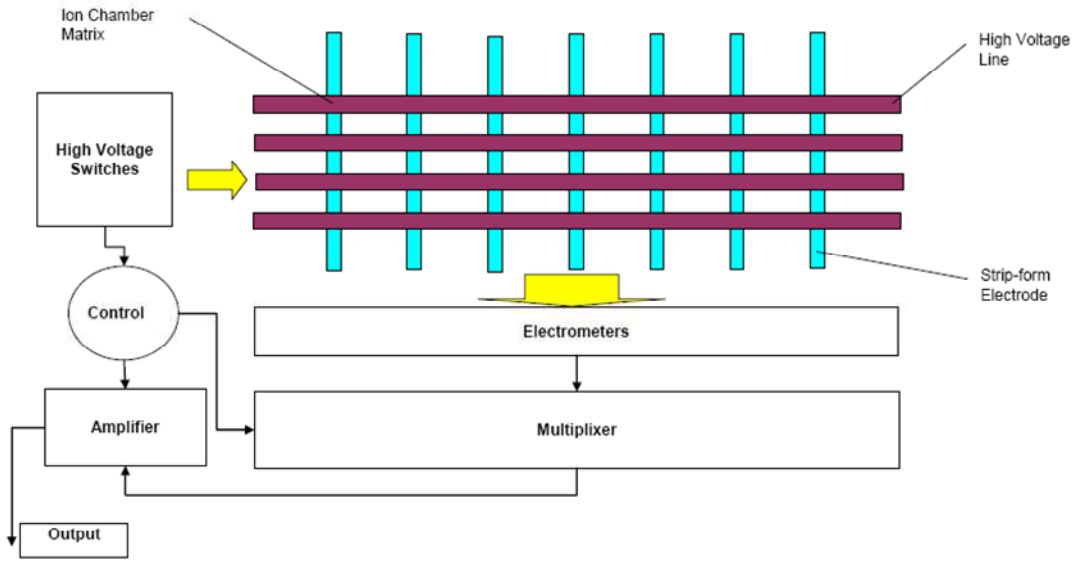

Figure 2- 2. Schematic of a SLIC EPID.

Several authors have investigated the use of SLIC EPID for dosimetry purposes Chang et al (2000), Mohammadi et al (2007). Advantages of these types of EPIDs are their compact sizes and their geometric reliability (images acquired with the system have no geometric distortions). The major limitation of a scanning radiation detector is quantum utilisation, since only one high-voltage electrode (out of 256) is active at any one time and the relatively long read-out time (van Elmpt, 2008).

2.2.3 Camera-Based detectors

Camera-based systems consist of a metal plate and a phosphor (gadolinium oxysulfide (Gd_2O_2S)) screen viewed by a camera using a 45° mirror. A metal/phosphor screen is used for converting x-rays to visible light which is directed to the camera via a mirror. When irradiated, high-energy electrons generated in the metal plate and the phosphor screen are converted into light in the phosphor screen and this light creates the video signal generated by the camera (figure 2-3). The video signal from the camera can be digitised and the digitised image can be viewed on a monitor located in the control area of the accelerator.

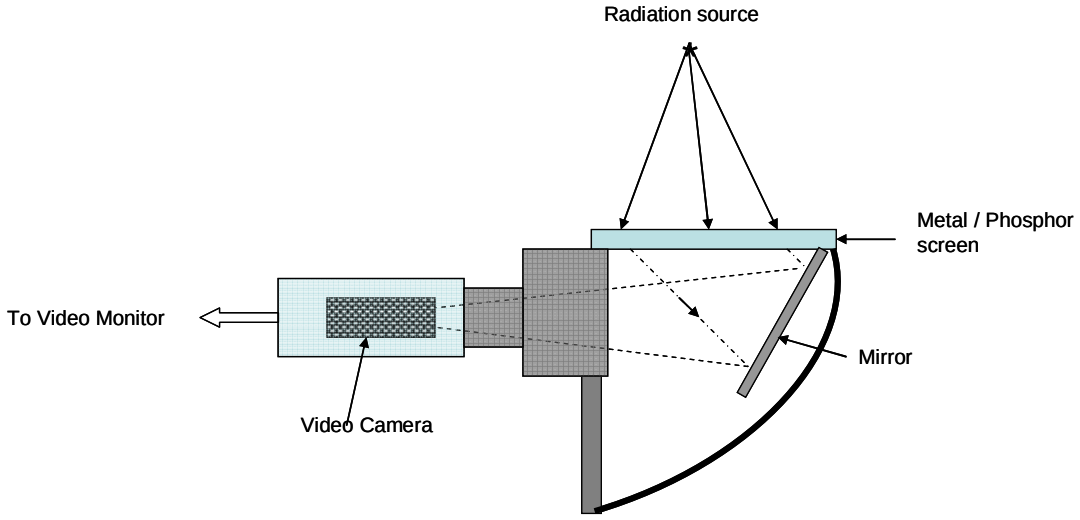

Figure 2- 3. Schematic of a video-based EPID

The main disadvantages of Video EPIDs are the poor light collection efficiency of the optical chain, which reduces the image quality, and optical glaring error which makes the use of these devices for dose verification difficult (Patridge et al 1999, Munro et al 1998). Since light is highly scattered within the phosphor screen, it is emitted from the rear of the screen in all directions with equal probability. Only those light photons that are emitted within a small cone subtended by the lens of the camera can generate a signal in the camera; typically only 0.1-0.01% of the light emitted by the phosphor screen reaches the camera. Two main reasons causing poor light collection efficiency (Herman et al 2001):

- If an x-ray photon interacts in the x-ray detector but none of the light generated by this interaction reaches the camera, then no measurable signal is produced
- If only a small signal is produced in the camera, then noise generated by the pre-amplifier and other electronics of the camera may be large compared to the signal.

As a result, the development of commercial camera-based EPIDs has focused on increasing light collection efficiency.

2.2.4 Flat panel detectors

Both the liquid-filled and camera-based types of EPIDs generally produced images of inferior contrast and spatial resolution to those obtained using film (Antonuk 2002). For this reason amorphous silicon (a-Si) flat panel EPID technology has replaced the liquid-filled and camera-based EPIDs due to their superior image quality. Flat panel detectors are currently divided into two types, Silicon or photodiode systems and Selenium or photoconductor systems. In either case, the image quality from the flat panel devices is superior to that of the liquid ion chamber or the video EPIDs. The most common type of EPID available today is the amorphous-silicon EPID (a-Si EPID) or flat-panel imager, first described by Antonuk et al (1998). The panel consists of an X-ray converter, light detector, and an electronic acquisition system for receiving and processing the resulting digital image. The underlying technology behind flat-panel a-Si EPIDs is large area integrated circuits called active-matrix arrays. Active-matrix technology allows the deposition of semiconductors, like amorphous silicon, across large-area substrates such that the physical and electrical properties of the resulting structures can be adapted for many different applications.

2.2.4.1 Basic image formation theory for the indirect a-Si electronic portal imaging devices

The amorphous silicon EPID consists of a copper plate, a gadolinium phosphor screen and an active-matrix array light sensor coupled to readout electronics. These devices have pixel resolution of less than 1mm. As illustrated in figure 2-4, each pixel in the flat-panel light sensor consists of a photodiode, which detects the light emitted by the phosphor screen, and a thin film transistor (TFT), which acts like a switch to control the readout of the signal. The data are read out through the data line and the timing is controlled by the control Field Effect Transistor (FET). The bias line is used to control the bias to the photodiode and the charge-up line is used to control the opening and closing of the control FET. The intensity of the light emitted from a particular location of the phosphor is a measure of the intensity of the x-ray beam incident on the surface of the detector at that point. During irradiation, each photodiode collects visible photons generated by the high energy x-rays; light that is

generated in the phosphor screen discharges the photodiode, which has a 5 V bias voltage applied. The TFT is non-conducting during this period. During readout, the TFT is made conducting and this allows current to flow between the photodiode and an external amplifier. The photodiode is recharged to its original bias voltage and the external amplifier records the necessary charge. This charge is proportional to the light reaching the photodiode during the irradiation. This charge is stored in the pixel until the active-matrix array is read out. By activating the TFT's one line at a time and by having all of the TFT's in one column connected to a common external amplifier, the signals generated in the flat-panel light sensor can be read out one line at a time with a modest number of electronic components. Readout frame rates of up to 30/s are achievable. This sequence continues while the x-ray exposure is occurring, allowing real-time images to be acquired.

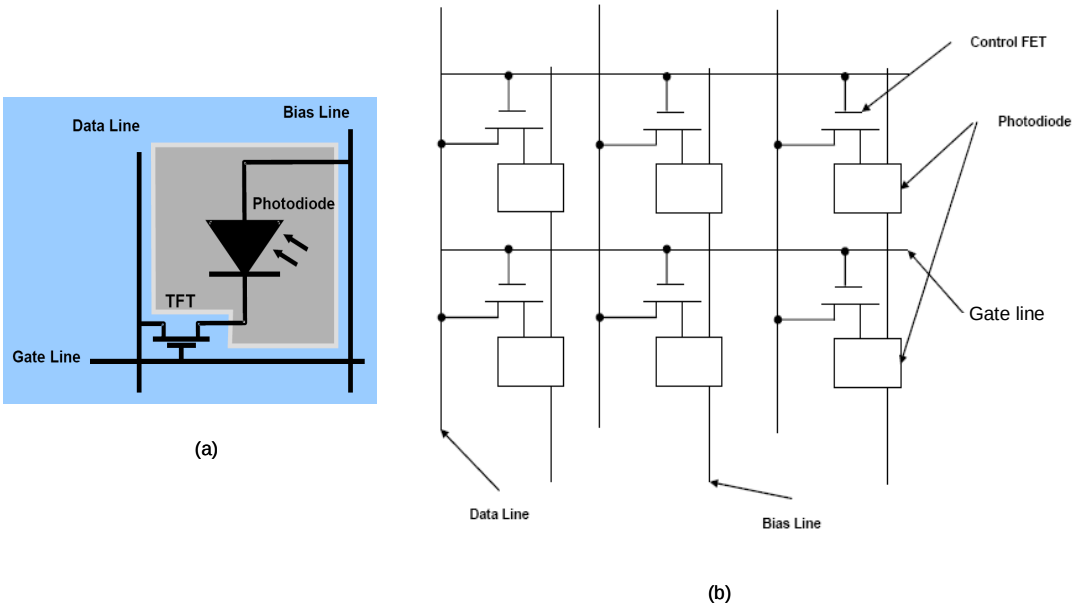

Figure 2- 4. Figure (a) is a schematic illustration of an a-Si photo diode coupled to thin film transistor (TFT). Figure (b) is a schematic arrangement of photodiodes and controls used in the flat panel imager (Reproduced from Varian document library).

The principle of operation of the a-Si-detector is shown schematically in Figure 2-5. The photodiodes have a very poor DQE for high-energy photons. To increase the DQE, there is an approximately 0.5 mm thick layer of gadolinium scintillator (Gd_2O_2S), and a 1mm thick copper build-up plate between the photo diodes and the radiation source (Varian Portal vision 2000 and McCurdy et al 2001). The

copper plate converts the high-energy photons into electrons, which produce optical light in the phosphor. These photons (Figure 2-5 b) are detected in the photodiode and stored as charge until the TFT is triggered to conduct the charge collected into the ADC in the readout electronics.

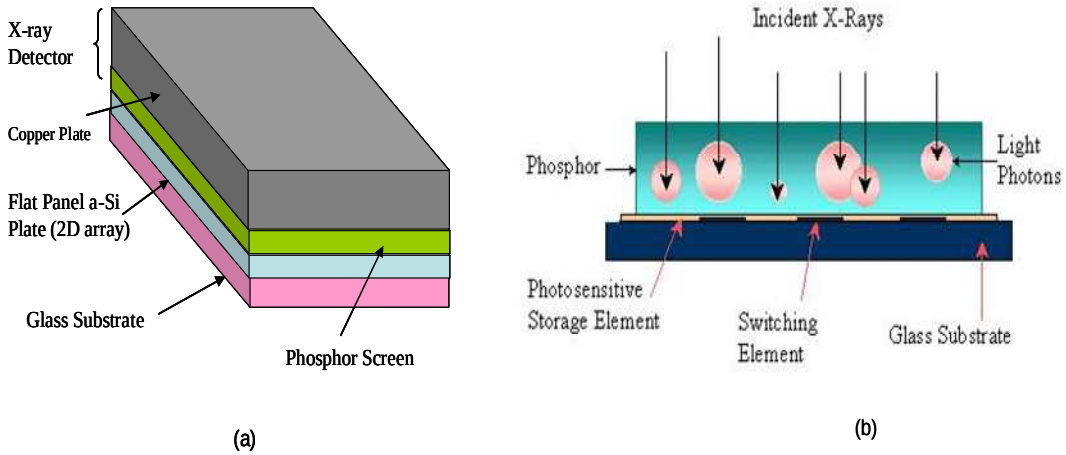

Figure 2- 5. Figure (a) shows the main layers making up the detector (b) Functional cross-section of EPID

The system efficiency is considered to be x-ray quantum limited. The size of the pixel, in addition to light spread in the phosphor screen and electron spread in the copper plate are the main factors affecting spatial resolution (Antonuk 2008, Munro 1998b). Glare, which is defined as light scatter, is insignificant for imaging suggesting that a flat panel EPID is capable of producing high image quality (Antonuk 2002). About 50% of the light emitted from the scintillator is used to produce the useful image which is orders of magnitude higher than the camera based and scanning liquid ion chamber EPIDs. For dosimetry purposes, a 1-2% deficiency in signal is significant enough to cause inaccuracy in dose verifications (Warkentin et al 2003).

2.3 General uses of electronic portal imaging devices

The current primary applications of EPIDs include treatment machine QA, patients' treatment-setup verification, assessment of target and organ motion,

patient dosimetry and compensator design and verification (Herman et al 2001, van Elmpt et al 2008).

2.3.1 Treatment setup verification

The goal of radiation therapy is to accurately deliver a prescribed radiation dose to the tumour and spare the surrounding healthy tissues. Treatment setup verification can be divided into verification of the geometric configuration of the treatment unit and verification of the patient and target position with respect to the treatment geometry. The geometric accuracy of patient positioning relative to the treatment beam is crucial and factors that could affect this accuracy include: incorrect patient alignment relative to the treatment beam, mis-alignment of the light field versus radiation field and the shift of skin markers and patient movement. Portal imaging is used to verify the accuracy of the patient positioning prior to treatment. Proper evaluation of treatment setup involves relating the information in a portal image to that extracted from a reference image (simulation film or DRR). Information compared may be the field border, the anatomic landmark or the 3D models of the patient from CT data.

Flat panel amorphous silicon (a-Si) detectors are now standard in the construction of electronic portal imaging devices (EPIDs) used for positional and dosimetric verification in external radiotherapy practice (McGarry et al 2007, Greer 2007, Berger et al 2006). With excellent image quality, patient setup verification and organ motion detection is readily achievable (Vetterli et al 2004). In addition, the convenience of EPID technology has led to growing interest in its role as a replacement for the laborious and time consuming methods of using x-ray film in dosimetric and quality assurance measurement (Menon and Sloboda 2004, Nijsten et al 2007).

2.3.2 Electronic portal imaging devices as a physics tool for routine linear accelerator QA

The digital format of the EPID image offers added advantages of using a-Si EPIDs for routine physics QA instead of the traditional ionization chambers, solid water stacks, and film. EPIDs can be calibrated to check photon beam field flatness and relative doses during routine machine QA. EPID results are used as "relative standards" to which later EPID results should be compared. EPID signal values are meaningless by themselves unless they are calibrated against another detector. EPID relative standards should be obtained after the treatment unit has been properly tuned, adjusted, and calibrated by using a conventional scanning water phantom and ionisation chambers. The major QA tests that can be done with EPIDs include:

- Verification of light field and radiation field coincidence or verification of light field and radiation field coincidence with field size dimensions
- Constancy check of radiation field flatness and symmetry
- Constancy check to compare day-to-day linac output
- Collimator isocentric accuracy check
- Cross-hair tray isocentric accuracy check
- Gantry Isocentric accuracy check
- Enhanced dynamic wedge (EDW) constancy check by comparing profiles in the direction of jaw motion
- Dynamic MLC QA, for example the popular Varian picket fence and complex tests
- Constancy check of electron beam energies, by comparing beam in-plane profiles (Beck et al, 2009).

The above QA procedures suggest that the EPID performance is a reliable medical physics tool. The main QA tests needed to be carried out on the EPID itself include:

- Positioning in the imaging plane
- Positioning perpendicular to the imaging plane
- Mechanical integrity and collision interlocks
- Spatial distortion and Noise
- On screen measurement tools of distances, angles and pixel resolution

- Contrast and Modulation transfer function
- Regular recalibration to ensure constant signal stability

2.3.3 Dosimetric application

Amorphous-silicon flat panel detectors are used to acquire digital portal images with excellent image quality. The efficiency in the use of detected signal and the improved spatial resolution makes the a-Si EPID better suited for dose verification compared to SLIC and camera based EPIDs (Warkentin et al 2003). Their ease of use also makes them attractive for dosimetry applications, but the images must be corrected for non-water equivalence of a-Si material, non-linear behaviour of the electronics, inhomogeneous pixel sensitivities, scattering in the detector and the panel's complex energy response.

The EPID image resulting from the whole radiation delivery may be calibrated to obtain a quantity that may be compared with a prediction based on the prescribed dose. This may be the total fluence reaching the detector or the dose delivered, in which case this image is calibrated using a dosimetric model and the resulting dose image is compared with a theoretical dose image based on prescription. Van Elmpt et al (2008) gave a comprehensive literature review of electronic portal imaging for radiotherapy dosimetry citing the advantages of EPIDs as: fast image acquisition; high resolution; digital format; potential for in vivo measurements; point dose measurement; and 3D dose verification. This has prompted many research groups to study their use for radiotherapy dosimetry.

2.3.3.1 Electronic portal imaging devices calibration for dosimetry

The use of any EPID for dosimetric verification requires implementation of a suitable calibration procedure to establish a relation between the pixel intensity and either fluence or dose distribution. Various authors have used different approaches to calibrate the EPID detectors for dosimetry purposes including analytical methods involving comparison of detector grey scale value with ionisation chamber response and Monte Carlo simulations. The first approach utilises empirical (measurement based) models by comparing grey scale pixel values to measured dose using a calibrated ionisation chamber inserted into a water phantom (Chen et al 2006, Chang et al 2000). The second approach uses

Monte Carlo simulations to predict the relation between the grey scale pixel values and dose (Siebers et al 2004, Chin et al 2003). However, a detailed model of the EPID is necessary for accurate simulations. Like many other Monte Carlo simulations, the calculation times are long and all the technical details regarding the construction and materials of the various layers are not always available. Hence the first method is simpler and faster than a Monte Carlo simulation and therefore more suited for implementation in clinical routine. The limitation is that empirical models need to be validated outside the reference conditions (van Elmpt et al 2008); in particular their robustness under various clinically encountered radiotherapy situations should be studied.

2.3.3.2 Transit and Non-transit dosimetry

Dosimetry verification techniques using EPIDs may be categorised according to whether the beams have passed through an attenuating medium e.g phantom or patient (transit); or not (non-transit) (Vial et al 2008, Elmpt et al 2008, Piermattei et al 2007). In both cases the dose can be reconstructed either inside or outside a phantom or patient.

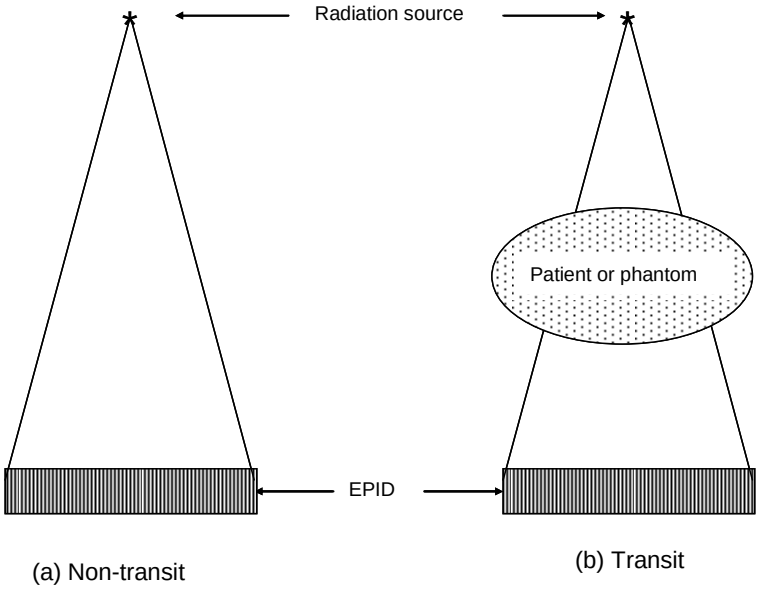

Figure 2- 6. Transit and non-transit

The non-transit (Figure 2-6(a)) approach is where the dose or fluence is acquired without any attenuating material (patient or phantom) in the beam. The method

involves the determination of the dose in the detector or patient (phantom) or determination of the incident energy fluence, based on measurements without an attenuating medium between the source and the detector. An image is acquired for each field without a patient (phantom) in the beam and compared with a predicted EPID response at the level of the imager. Alternatively the EPID image signal is reconstructed into dose inside the patients (phantom) as detailed above. The non-transit approach is mainly used as a pre-treatment dose verification method and hence is a valuable tool for performing quality control of treatment parameters related to dosimetric and geometric characteristics of the linac, independent of the patient.

Transit dosimetry (Figure 2-6(b)) or back projection is where the EPID is calibrated to predict dose based on the radiation transmitted through the patient or phantom. The technique involves the determination of the dose at the position of the detector or patient (phantom) or determination of the incident energy fluence, based on radiation transmitted through the patient or phantom. This approach is mainly used as a treatment dose verification method and offers the possibility of in-vivo dosimetry. An image is acquired for each field with the detector located behind the patient (phantom) and compared with predicted EPID response at the level of the imager or behind the patient/phantom. Alternatively the EPID image primary signal is back-projected and computed into dose inside the patient (phantom) CT scan by converting the image to energy fluence, using this as an input for the dose calculation algorithm and comparing to a plan calculated from the patient/phantom CT scan. The transit method has the potential of verifying both the treatment planning system (TPS) calculation of dose to the phantom or patient, and the delivery of dose by the Linac.

Nijsten et al (2007b) proposed a two-step global calibration model for a-Si EPIDs for transit dosimetry based on measurements and mathematical convolution methods. First, dosimetric EPID characteristics like long-term stability, build-up, ghosting effects, and field size dependence were investigated to implement a dosimetric calibration for open fields. Second, the model was extended for transit dosimetry application by including an energy spectrum correction model that corrects differences in EPID response between measurements with and without an object in the beam, field size dependence kernels, beam profile

correction derived for two photon energies and the conversion factor to absolute dose in water from EPID greyscale values.

2.4 Overview of the Varian electronic portal imaging device detector system

The EPID flat-panel used by Varian is an indirect detection system and comprises three main components, namely: Image detection unit, Image acquisition system and computer control software.

2.4.1 Image detection unit

The first component is the image detection unit (IDU). It has the shape and size of a standard film cassette and is positioned in the imaging plane using a robotic- controlled R-arm or exact-arm. It is connected by cables to the therapy control area from where image acquisition, processing and display are controlled. Within the detector, a phosphor scintillator converts incoming x-rays to visible photons which are sensed by an array of photodiodes implanted on the amorphous silicon panel. The photodiodes convert the incoming light to charge and the integrated charge is transferred to the read-out electronics to be counted as a pixel signal, proportional to incoming radiation intensity. The detector electronics allow the transfer of charges from the pixels to the read-out electronics by activating row after row of the pixel matrix while all the columns (data lines) are read-out thus forming an image. Radiation shielding of the electronics is required to avoid damage due to their close proximity to the detector (ie they are too near to the primary beam). Figure 2-7 shows a block diagram of a plan view of the IDU. Varian has two versions of IDUs, the older one is the IDU-II and the more recent is the IDU-20.

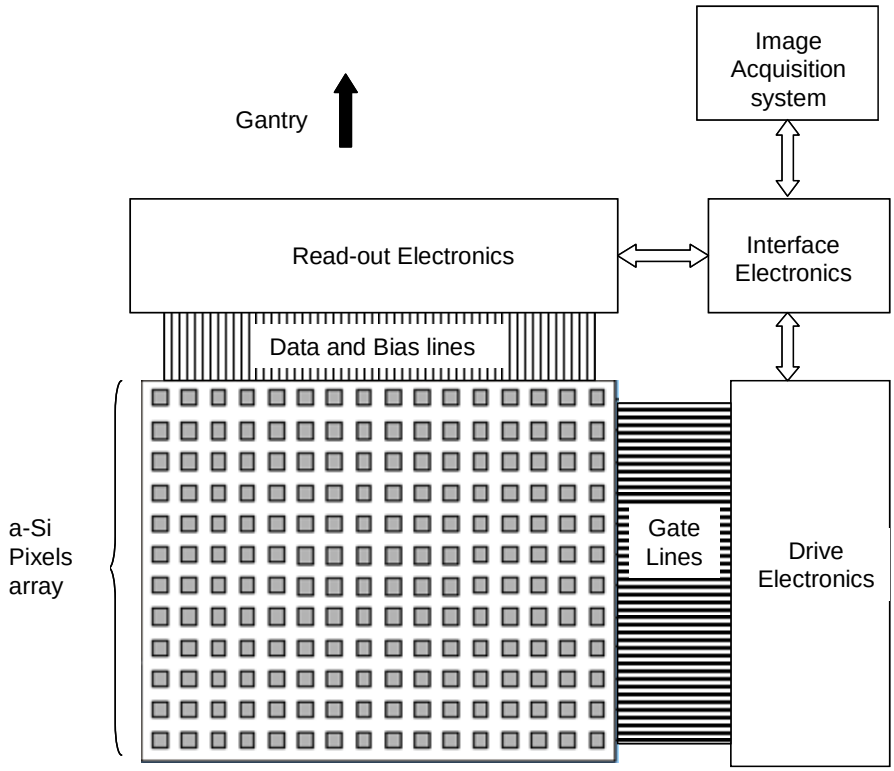

Figure 2- 7. Block diagram of the image detection unit (IDU) (Reproduced from Varian document library).

2.4.2 Image acquisition system

The image acquisition system (IAS) contains drivers and acquisition electronics for the image detection unit. The IAS interfaces to the IDU, the linac and the imager controller (the R-Arm or the exact-Arm). It is essentially a digital signal processor that provides frame averaging capabilities and image buffering. It controls and reads the image detector and performs image corrections. Varian has two versions of IAS, the older one is the IAS2 and the more recent is the IAS3.

2.4.3 Acquisition computer control software

The third component is the computer control software that maintains the interfaces and controls the communication between the IDU and the acquisition unit. Image correction data and acquisition parameters are stored on the hard disk of this computer. The EPID image is the average of acquired frames in the integration mode.

PortalVision™ is a Varian software system supporting the acquisition of electronic portal images before, during and after treatment and provides tools for quantitative portal image registration and review. Table 2-1 summarises the physical characteristics and specifications of the Varian imager.

Table 2- 1. Specifications of the Varian imager (Varian PortalVision™ aS500, 2001)

Detection Components	
Metal plate	0.6 mm copper
Phosphor screen	Gadolinium Oxy-sulphide
Photon detector	Amorphous-Silicon
Pixel	n-i-p photodiode
Pixel format	384x512 (a-Si 500) and 768x1024 (a-Si 1000)
Pixel pitch	784 μm (a-Si 500) and 392 μm (a-Si 1000)
Array dimensions	40x30 cm^2
Energy range	4-25 MV
Doserate range	100-600 MU/min
Image acquisition rate	3 frames / second
Image storage rate	2 images / second

2.4.4 Electronic readout of a-Si detectors

There are 3 modes for electronic readout schemes used for image acquisition with the a-Si EPID (Varian portal vision 2001). All three modes work towards a common goal of acquiring images with optimal Signal to Noise Ratio (SNR).

2.4.4.1 Single (integrated) mode

During single mode acquisition, the configured numbers of frames are readout prior to the start of irradiation. This cycle is called the refresh cycle; it clears the accumulated dark current and residual data. No readout occurs during the delivery of the radiation and the signal is integrated over the entire exposure period. The trailing edge of the Radiation-on signal generates one trigger pulse initiating one frame readout and also the accumulated data of the pixels during

the exposure interval. This readout scheme reduces the effects of readout noise and eliminates the pulsing effects of the linac on the final image. Since the signal is integrated during the exposure time and the readout is performed after the exposure, this improves the signal to noise ratio (SNR). The single mode acquisition is routinely used clinically and allows the acquisition of clinical images with exposures as low as 2 MU (Kirby et al 2006, de Boer et al 2000).

2.4.4.2 Continuous mode - high dose imaging

Continuous mode is primarily used for monitoring the patient during intensity modulated radiotherapy (IMRT) treatment. This acquisition mode includes movie images and the verification image (average of movie images). Implementation of this mode can be done with either the use of free running mode or external trigger mode. The external trigger continuous mode synchronises the frame readout with linac pulses thus eliminating the pulsing artefacts. This not only improves the image quality of movie images but also increases the accuracy of dosimetric verifications for applications such as IMRT. The external continuous mode can be further divided into two synchronisation modes; line synchronisation and frame synchronisation. In line synchronisation, each line can be triggered and readout individually. In frame synchronisation mode, the start of frame is synchronised with linac pulses. The sensors are forced to be discharged prior to the start of radiation-on to eliminate the dark current accumulation. The linac beam pulses are synchronised to the external trigger pulses which in turn are synchronised with the start of each frame scan. An offset correction image is used to correct the dark current of each pixel. During the gain correction, the median value of the pixel data of the whole sensor is evaluated and each individual pixel value is mapped to the median value. The final image is the average of the frame scan during radiation exposure.

2.4.4.3 Cone beam mode (only available on linacs with OBI system)

Cone beam acquisition mode is used to perform volume (multi-slice) kilovoltage CT (kVCT) or CBCT in the cone beam geometry to visualize 3D (three dimensional) anatomy during patient positioning. In this mode, image acquisition is synchronized with the linac enabling the imager to remove the pulsing artefacts from the image while also improving the SNR.

2.4.5 Imager calibration

The system requires a set of calibration images for each combination of acquisition mode, energy and dose rate parameters of the treatment machine used. An imager calibration set comprises two images, a dark-field image and a flood-field image. Each set is stored in the IAS database. Both images consist of up to 10 individual images taken in succession. PortalVision™ uses the averaged result of all images for correction.

2.4.5.1 Dark field image

In the dark-field image (DF), individual pixel-by-pixel values are measured by periodically acquiring an image without radiation. The DF correction is synchronised with linac pulses. An average of several images measured in quick succession is taken for minimum noise. Its contents reflect array imperfections and electrometer offsets. Figure 2-8 (a) displays a typical dark-field image exhibiting bright and dark vertical stripes.

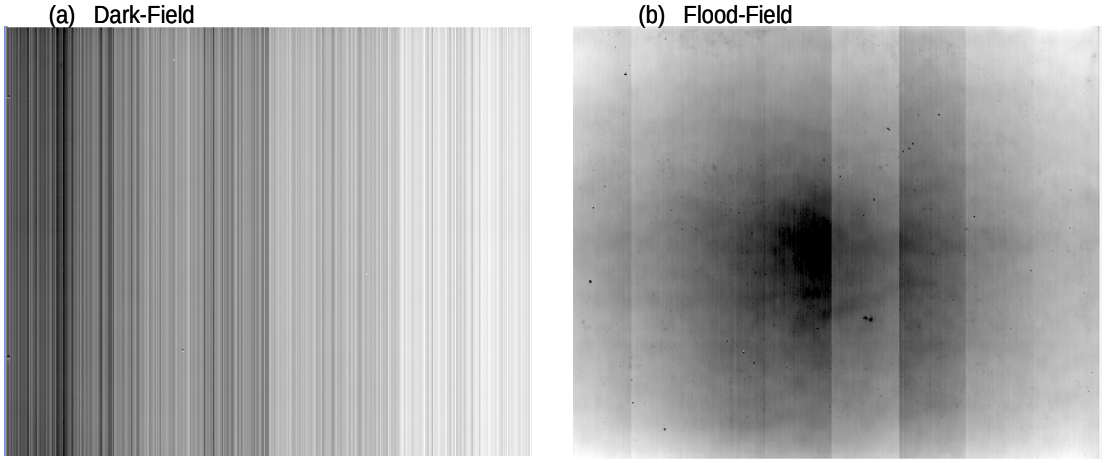

Figure 2- 8. Dark-field and Flood-field images

2.4.5.2 Flood field image

The flood-field (FF) image is also measured several times in quick succession and averaged for minimum noise. Its contents represent the field homogeneity, individual cell sensitivities and electrometer gains. The sensitivity of each pixel

is determined periodically by acquiring an image with radiation for a wide open field without an object. During the acquisition of the FF image, any interferences in the radiation field or the dose rate at which the EPID is being calibrated, will lead to a wrong FF correction file. The flood field image, illustrated in figure 2-8 (b) exhibits vertical bands of varying brightness.

These images are used to correct the beam-on raw object image according to the equation

$$\text{Corrected\_Image}(i, j) = \left[\frac{\text{Raw\_Image}(i, j) - \text{DF\_image}(i, j)}{\text{FF\_image}(i, j)} \right] * \text{FF}_{\text{mean}} \qquad (2\text{-}1)$$

Where the offset correction is equal to the stored dark field image subtracted from the acquired raw image. The gain correction is defined as the offset corrected image divided by the stored normalised flood-field image. FF_{mean} is the mean value of the flood field image. The *i* and *j* notations in the equation above represent the i^{th} - j^{th} pixel values in the X and Y directions of the image.

2.4.5.3 Main components of the Varian's portal dosimetry system

The Varian portal dosimetry system has three main requirements, namely:

1) The portal Imager (a-Si 500 or a-Si 1000): Portal dosimetry software in addition to the image acquisition system (IAS) is also required for the EPID to acquire dose maps. A special license is needed to activate the Dosimetry Workspace.
2) Portal dose prediction: Eclipse 8.6 treatment planning system algorithms are required to enable prediction of dose maps. These predicted dose images (PDI) are compared to the measured dose maps for dosimetric verification of treatment plans.
3) Portal dosimetry review workspace to evaluate the agreement between predicted and measured images. An evaluation module is required for the comparison of PDI and measured dose maps. The review workspace in Vision caters for this purpose. The software has tools for comparison and evaluation of dosimetric images e.g. gamma analysis, dose differences, etc. However, this is not a mandatory requirement as such analysis can be carried out using other analytical software.

CHAPTER 3: MATERIALS AND METHODS

3.1 Dosimetric performance of a-Si500 EPIDs

The department is equipped with eleven linear accelerators which are: 4 Clinac 600 C/EX, 4 Clinac 2100 C/CD/EX and 3 Clinac iX series with 6MV, 10MV and 16MV, all equipped with EPIDs as detailed in table 3-1. Six of the detectors (A, B, C, E, F and H) use hardware/software IDU-II/IAS2 while the other five detectors (D, G, I, J and K) use IDU-20/IAS3 (Varian Medical Systems, Palo Alto, California, USA). At the time of this study all the detectors were being used for clinical imaging only apart from detector I, which in addition had been configured / calibrated for dosimetric purposes. For simplicity we refer to hardware/software IDU-II/IAS2 as system-I and IDU-20/IAS3 as system-II (Table 3-1). Both system-I and system-II used in this study are a-Si500, though Varian has introduced a system-II fitted with an a-Si1000. The main difference between the a-Si500 and a-Si1000 is that the latter has a better pixel resolution compared to the former, as indicated in table 2-1.

Table 3- 1. The different accelerator models with EPIDs, the EPID image acquisition system and their corresponding clinical use period in months.

EPID	Hardware / Software	System	Accelerator Model	Months in use
A	IDU-II / IAS2	I	600 C/D	86
B	IDU-II / IAS2	I	600 C/D	86
C	IDU-II / IAS2	I	2100 C/D	82
D	IDU-20 / IAS3	II	21 EX	34
E	IDU-II / IAS2	I	6 EX	75
F	IDU-II / IAS2	I	21 EX	32
G	IDU-20 / IAS3	II	21 EX	32
H	IDU-II / IAS2	I	6 EX	32
I	IDU-20 / IAS3	II	iX	17
J	IDU-20 / IAS3	II	iX	17
K	IDU-20 / IAS3	II	iX	10

The manufacturer's technical specification suggests system-II has lower noise readout electronics, higher readout rates and faster data acquisitions compared to system-I. The EPID detectors in the two systems have active dimensions of 0.4m x 0.3m and a resolution of 512x384 pixels yielding an effective pixel size of 784μm. For system-I, readout of the EPID amorphous silicon array is synchronised with the beam pulses and a fixed integration time of 320 ms was used for image acquisition. System-II uses the asynchronous mode where the readout is controlled by an internal clock. This setup, specifically designed for IMRT fields' acquisition, is Varian's default mode for the system-II EPIDs, activated by setting the sync mode parameter to zero. For both systems portal images were acquired using AM maintenance (Varian portal imaging control software used to acquire EPID images) version 7.1.

Table 3-1 also shows the length of time each EPID had been in clinical use within our centre at the time this study was conducted. System-I detectors had been used for periods ranging from 32 to 86 (mean 66) months while system-II detectors had been used for a period ranging from 10 to 34 (mean 22) months. All measurements were performed in the evenings after the detectors had been in clinical use to ensure warm up. In this study a nominal photon energy beam of 6 MV was used in all measurements.

3.1.1 Image acquisition

For system-I, parameter settings in AM maintenance were kept constant for the 400 MU/min dose-rate, e.g number of rows acquired before next row synchronisation (Rows Per PVSYNC) = 9, synchronization delay = 350μs, IDU/ACPU Gain = 1, PV synchronisation frequency = 2400 Hz. For system-II, Varian uses a standard set of acquisition settings from their own optimisation experiments for each dose-rate. These parameters include the number of trigger pulses the system waits before acquisition begins, frame cycle time, number of rows to be acquired and subsequent number of frames between accelerator pulses.

To ensure uniform pixel response, EPIDs were calibrated for dark field (DF) to eliminate background and electronic noise. A flood field (FF) calibration was also used to correct for variations in sensitivity of individual pixels. While this eliminates variations in pixel sensitivity, it also has the effect of removing the characteristic horn-shape of the photon beam profile downstream of the

flattening filter. The number of frame averages for the DF and FF calibration fields for system-I were 60 and 30, while for system-II it was 30 and 30 respectively. Detectors were calibrated at the maximum effective field sizes of 28.6 x 21.4 cm^2 and 30.5 x 22.5 cm^2 for system-I and system-II respectively. Both detector systems have same area of 30x40 cm^2 at the isocenter, but due to mechanical positioning limitations vertically, all the system-I detectors could not attain the same effective field size at the imaging plane. All field sizes were defined at the source-to-isocenter distance of 100 cm, unless otherwise stated. The vertically downwards position of the accelerator-gantry was ensured with the help of a spirit level. The IDUs were positioned at lateral = 0, longitudinal = 0 and vertical = 40cm below the isocenter. For each EPID, the physical position of the detector was maintained on the central axis of the linear accelerator. The distance from the accelerator targets to the EPID surfaces was maintained at 138±0.5 cm aiming the distance to the sensitive layer to be at 140.0 for calibration and subsequent measurements. Van Esch et al (2004) and Greer et al (2003) reported negligible ghosting effects on Varian EPIDs. A minimum period of 1 minute was employed (Winkler et al, 2005) to minimise these memory effects even further since EPIDs of varying life periods were being investigated.

Images were acquired in the integrated mode, whereby the accumulated frames are displayed as a single image after irradiation is complete. At each setting, the measurement was repeated 3–4 times to derive the EPID integrated response (IR) which was calculated as the average of acquired number of frames (ANF).

$$[IR] = \frac{1}{n}\sum_{i=1}^{n}[MPV]_i \quad x \quad [ANF]_i \qquad (3.1)$$

Where n is the total number of measurements done and MPV is the mean pixel value.

3.1.2 Detector reproducibility and responses to a reference beam

Each detector was irradiated with a reference beam, defined as a 50 MU exposure, at a fixed field size of 10 x 10 cm^2, 400 MU/min doserate and at a fixed SDD of 138±0.5 cm. The average pixel value in the 13 x13 central pixel region was obtained for ten consecutive irradiations for each detector. The mean (of the average pixel values) for the ten consecutive readings was used to compare the detector's response to a reference beam and the percentage pixel

deviation from the mean value was calculated for each detector from [(MPV-Mean)/Mean] x 100%, where MPV is the mean pixel value for each detector (obtained as the average of ten consecutive measurements) and Mean is the average values for the detectors for each system. The responses for system-1 and system-II acquisition systems were analysed separately. Also the ten consecutive readings for each detector were used to calculate the short-term reproducibility. The long-term reproducibility was done by comparing the mean pixel value over a six month period.

3.1.3 Dose-response behaviour / Linearity

To assess the linearity of their dose response, each EPID was positioned at a fixed SDD of 138±0.5 cm and exposed at a constant dose rate of 400MU/min. Three integrated images of a 10x10 cm^2 open field were acquired. The linear accelerator monitor units used were 1, 2, 5, 10, 20, 50, 100, 200 500, and 1000. EPID response was assessed in a 13 x 13 pixel (approximately 1.0 cm^2 area) region of interest in the centre of the image. For all detectors, the signal-to-monitor units ratios (SMUR) in the range of 1–1000 MU were calculated by dividing the average EPID response by MU delivered. To ensure stability of the accelerators, MU variation measurements were monitored using an ion chamber (Wellhoffer Dosimetrie, Schwarzenbruck Germany) in a mini-water phantom at a depth of 1.5cm, prior to measurements with EPIDs. The phantom was placed on the couch in the centre of the beam and the source to water surface distance was maintained at the same level as for each EPID detector. Ionisation chamber measurements after temperature and pressure correction were compared with corresponding measurement with the EPIDs.

The effect of cumulative response was investigated by comparing an EPID's response to a single 20 MU exposure to a series of lower-dose exposures with equivalent MU. The total response given by $\left(\sum MPV \;\; x \;\; ANF\right)$ and the percentage deficit from the single 20 MU exposure were calculated.

3.1.4 Pixel uniformity-response across the entire detector panel

The EPID uniformity across each entire detector was investigated by comparing their response at specific positions relative to the central positions. The radiation beam uniformity for each accelerator was monitored as part of general quality assurance. The mean response in a 13x13 pixel region surrounding each of the positions P_0, P_1, …, P_8 was obtained for each detector in a 20 x 20 cm^2 (28 x28 cm^2 at the detector level) field size and P_L, P_R, P_G and P_T in the penumbra region as illustrated in figure 3-1. The penumbra region is known to be sensitive to detector and collimator positioning, a critical parameter in dosimetric applications. During irradiation, scatter in the imaging detector and over-response to lower energy photons, increases the pixel values in the periphery of the field. For each EPID, three images were acquired at the same monitor unit (50 MU) and doserate (400 MU/min). At the detector level, positional lengths are: $\overrightarrow{P_0P_1} = \overrightarrow{P_0P_2} = 7.0cm$ located at the EPID central axis along the left-right direction of the gantry. $\overrightarrow{P_0P_3} = \overrightarrow{P_0P_4} = 10.5cm$, located at the EPID central axis along the Gun-Target direction of the gantry. $\overrightarrow{P_0P_5} = \overrightarrow{P_0P_6} = \overrightarrow{P_0P_7} = \overrightarrow{P_0P_8} = 14.2cm$. Points P_5, P_6, P_7 and P_8 are 1.8 cm and 1.0 cm from the field edge in the left-right and the Gun-Target directions respectively. The four values in the penumbra regions were averaged (P_{avr}) for each detector such that any deviation/shift in one side is counterbalanced by the results in another. MATLAB (The MathWorks, Inc) was used to obtain the average of the three images and normalise the response to that of the central position P_0.

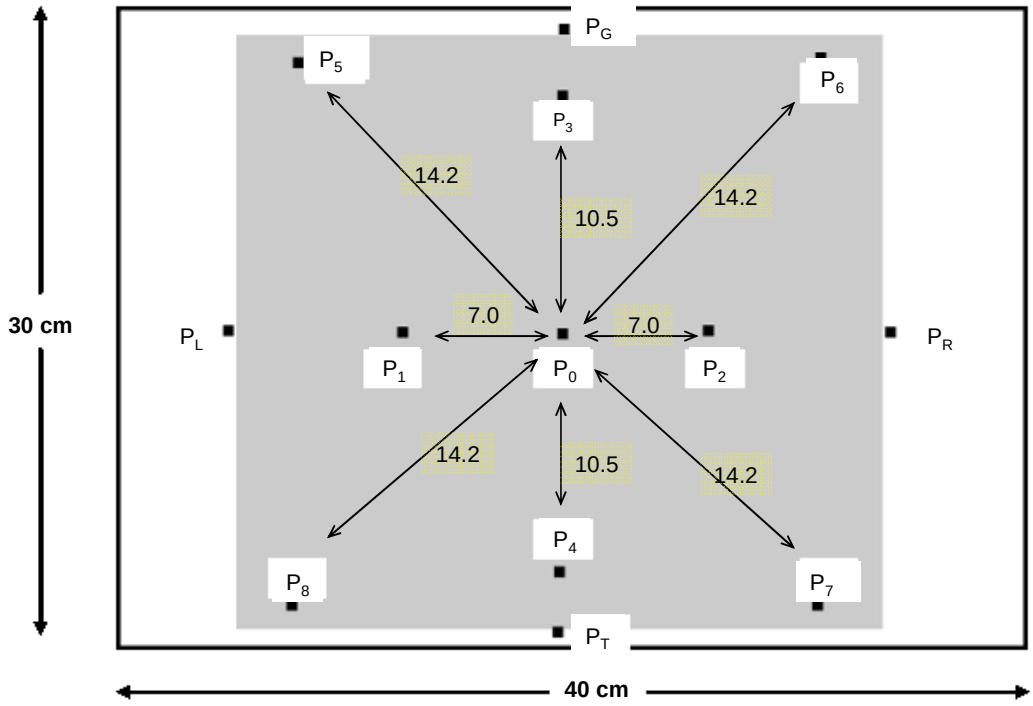

Figure 3- 1. Specific locations used to measure the uniformity with in a 20 x 20 cm^2 radiation field size in the EPID detector. Each of the positional points has an area of 13 x 13 pixels. Mean response for all the points were compared to the central axis (P_0) reading of each EPID detector. The response of the points (P_L, P_R P_G and P_T) in the penumbra region were averaged (P_{avr}) for each EPID.

3.1.5 Electronic portal imaging device's relative dosimetry

A physical step-wedge with relative thicknesses of 0.25, 0.50, 0.75 and 1.00 was used to assess relative response. The steps create steep dosimetric gradients similar to those encountered in IMRT. The step-wedge was positioned at the surfaces of the EPID detectors at the same source to surface distance of 140.0 cm. The centres of the EPID detectors and step-wedge were aligned using the isocentre lasers and checked with the central mechanical pointer of the accelerator. The field size was maintained at 1.0 x 7.5 cm^2. EPID images were obtained with 6 MV, 50 MU and 400 MU/Min in both Right-Left and Gun-Target directions relative to the accelerator. The signals were normalized to the open field reading and standard deviations at different steps calculated.

3.1.6 Field size dependence

With the EPID detectors at fixed distance of 138±0.5 cm, fields of various sizes were obtained at a constant doserate of 400 MU/min. Open field images were obtained at a fixed dose of 50 MU to field sizes of 2x2, 5x5, 10x10, 15x15 and 20x20 cm^2. For each field size, response was measured in a 13 x 13 pixel region of interest (approximately 1.0 cm^2 area) in the centre of the image. Each field size response was calculated as indicated in equation 3.1. Field size responses of the different EPID were compared to ionisation chamber measurements acquired in water with a fixed source=surface distance maintained to the corresponding level for each EPID detector. Both the EPID and ionization chamber data for different field sizes were normalised to that of a 10 x 10 cm^2 and fitted to a second order polynomial equation,

$$EF = A_0 + A_1(FS) + A_2(FS)^2 \qquad (3.2)$$

Where EF is the EPID field size dependence factor (defined on the central axis and assumed to be a constant for all pixels for a given field size), FS is the field size and A_0, A_1 and A_2 are polynomial coefficients.

3.1.7 Doserate influence

The EPIDs were calibrated at accelerator dose-rates of 100, 200, 300, 400, 500 and 600 MU/min utilising identical settings (field size/distances) and on the same day to minimise the day-to-day variations in pixel sensitivity, beam symmetry and accelerator outputs. For each dose-rate, the response of the EPIDs to 20MU and 100MU exposures at a 10x10cm^2 field size was evaluated. The EPID responses were obtained as described in the previous sections and readings normalised to those obtained at 400 MU/min. It is common practice to fit the doserate ($\dot{D}$) response to a power potential function of the form

$$S = k\dot{D}^{\Delta} \qquad (3.3)$$

(Fowler and Attix 1966, Pardo et al 2005, Muhammadi et al 2006, Winkler et al 2006). Where *S* is the detector read-out signal or detector relative read-out signal, *k* is a parameter for detector sensitivity and Δ is a parameter related to the non-linearity of the detector response. Equation 3.3 can be used with

absolute or relative (normalised) data. In particular Δ is less than one when the EPID shows an over-response and greater than one if the EPID shows an under-response.

3.1.8 Directional dependence

The EPIDs were exposed at varying gantry angles between 0^o to 360^o in 12 equal intervals, to assess the influence of mechanical stability on their response as a result of gantry rotation. Open beams of 10x10cm^2 field size, fixed SDD of 138±0.5 cm, 25 MU exposures and doserate of 400 MU/min were used for this analysis. At each gantry angle the EPID central response was evaluated as described in previous sections. Measurements were performed at collimator angles 0^o and 90^o. EPID response values for each collimator angle were normalised to that obtained at gantry angle 0^o.

3.1.9 Further image profile analysis and memory effects

Images for open field sizes 2x2, 5x5, 10x10, 15x15 and 20x20 cm^2 at different doses (MU) were obtained and analysed with MATLAB. Profiles through the central image axis both in the Gun-Target and Left-Right directions relative to the EPID were obtained and compared. For each EPID, a 5x5 cm^2 field size was irradiated with 50 MU followed by a 20x20cm^2 field size irradiated with 3 MU to evaluate memory effects. The time interval between the two exposures ranged from 12-15 seconds. Another 3 MU image for a 20x20cm^2 field size was obtained approximately 5 minutes later. The EPID ghosting effect response was characterised as the difference in the central axes profiles between the two 20x20cm^2 field size images expressed as the percentage increase in response at the centre of 5x5 cm^2.

3.1.10 Electronic portal imaging devices ageing due to radiation

Electronic portal imaging device's ageing due to radiation could be another factor that might cause degraded results. Hee et al. (2002) reported that

radiation damage affects the leakage current of photodiodes and the effect showed a linear dependence on absorbed dose. This may decrease the whole system performance, although it also depends on the ageing effects of other components. This effect was investigated further by extracting data from the "treatment field history" file of the Varis system for about 2.7 million treatment records of all our machines since 2001, when the first EPID was commissioned. The data were extracted using mySQL database software. The aim was to find out if there is correlation between the EPID cumulative dose/age and its performance. From the database, the actual linear accelerator monitor units delivered per treatment field when EPID images were acquired were obtained, from which the cumulative dose to the imagers could be calculated.

3.1.11 Electronic portal imaging devices, as a dosimeter

Electronic portal imaging devices were purposely developed for on-line patient setup verifications. The acquired image information is however related to the dose delivered to the EPID, and they are currently used as dosimeters as well. A study was conducted to evaluate the EPID as a dosimeter, by comparing its response with that of an ionisation chamber. Both detectors were positioned at the same source to detector distance (SDD) and same field size of 10x10 cm^2, as shown in figure 3-2. The ionisation chamber was positioned at depth of maximum dose (1.5 cm build up for 6 MV) with appropriate back scatter. Both detectors' signals were obtained at linear accelerator monitor units of 1, 2, 5, 10, 20, 50, 100, 200 500, and 1000; and at the same doserate of 400 MU/min. The EPID response was measured as the mean pixel value in a 13 x 13 pixel (approximately 1.0 cm^2 area) region of interest in the centre of the image.

The same setup was used to compare the EPID with the ion chamber in terms of photon beam-intensity reduction, by measuring the dose variation as a function of absorbing material. This was done by interposing solid water materials of increasing thicknesses between the source and the detectors. For each phantom thickness, both detectors were exposed to the same radiation conditions, (SDD = 140 cm, FS = 10x10 cm^2 and 100 MU). Similarly, the EPID response was measured as the mean pixel value in a 13 x 13 pixel region of interest in the centre of the

image. The data for each detector were normalised to that when there is no absorbing material (thickness = zero).

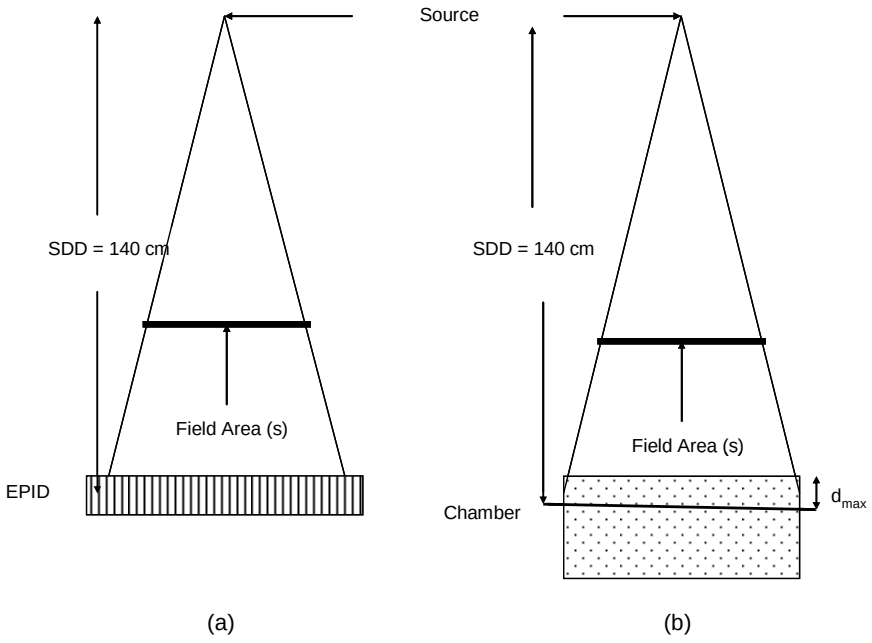

Figure 3- 2. The geometrical setups for: (a) EPID image acquisition and (b) Ionisation chamber measurements. In both (a) and (b) the detectors (EPID and ion chambers) were kept at fixed SDD. The ion chamber was set with a 10.0 cm solid water backscatter and build-up equivalent to the beam d_{max} (1.5 cm).

3.2 Water equivalent path length calculation from EPID images

The photon beam physical property of intensity reduction with increasing material thickness, as described in the last paragraph of section 3.1.11 above, was used to explore further the dosimetric capability of the EPID. The quadratic calibration method was used, a technique first proposed by Morton et al (1991) to convert any acquired EPID image into water equivalent path length (EPL).

3.2.1 Treatment unit and EPID detector

All measurements for the EPID calibration for equivalent path length (EPL) were performed using photon beams from the Varian linear accelerators (Clinac 2100 C/CD/EX and Clinac iX series) at 6MV and 16MV. The images were acquired with the Varian a-Si500 EPIDs, hardware/software IDU-20/IAS3 (Varian Medical Systems, Palo Alto, California, USA). Details regarding this imager design and calibration, image acquisition, and dosimetric characteristics have been described extensively in sections 2.5 and 3.1.1, and in the literature (McDermott et al 2006, van Esch et al 2004, Greer et al 2003, and Kavuma et al 2008). The EPID imager was kept at a fixed distance of 140 cm from the source for all images. Detectors were calibrated at fixed field sizes of 30.5 x 22.5 cm^2 (i.e this study was only done with system-II detectors) All field sizes were defined at the source-to-isocenter distance of 100 cm. Two approaches were used in portal image acquisitions:

- Using the Varian AM maintenance control software version 7.1 in the integrated mode where frames are acquired and integrated continuously giving a single image (the average) at the end of exposure. The acquired images were exported as DICOM files for analysis.

- In the second approach, test plans with desired field settings (i.e field size, monitor units, MLC shapes, etc) were created using the Varian RT chart software. The test patients were scheduled in the time planner, exported to the accelerator and treatments executed in the clinical mode, acquiring single integrated images at the end of each treatment. The acquired images were opened using the Varian portal dosimetry software and exported as ASCII files for analysis.

The second approach was mainly used because the images are automatically saved, test patients can be reused and image acquisition process is faster on the machine. Image processing and mathematical modelling were carried out using MATLAB v2008b (The MathWorks, Inc).

3.2.2 Measurements and Image acquisition for calibration

This study is based on the premise that the EPID image in the integrated mode is ideally dependent of the number of monitor units used to acquire the image. EPID images for a set of solid water phantoms of thicknesses 5, 10, 15, 20, 26 and 32 cm were acquired with a 21.5x21.5 cm^2 field size, for calibration. This is the reference field size and all irradiations were 100 monitor units (MU) at a doserate of 400 MU min^{-1}. Each phantom was positioned on the beam central axis on the treatment couch and the distance from the source to the centre of the phantom adjusted such that the source axis distance (SAD) was equal to 100 cm as shown in figure 3-3.

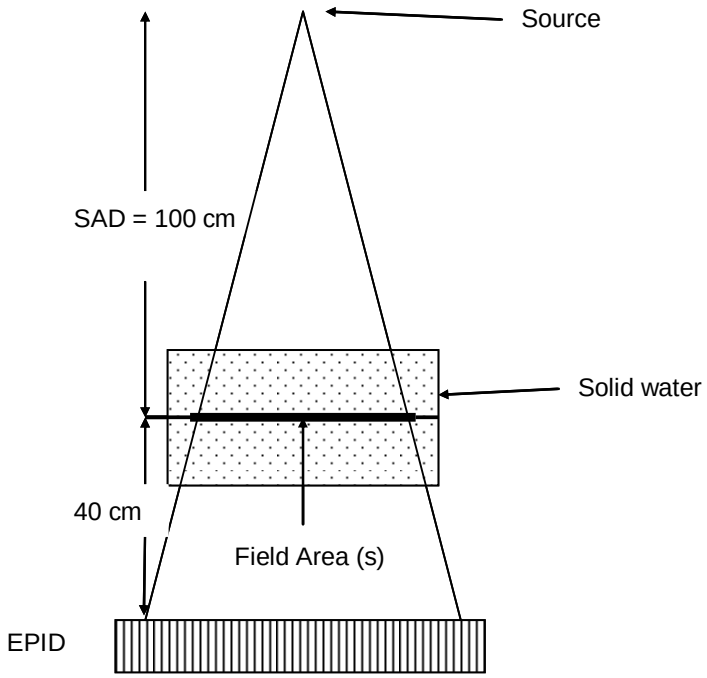

Figure 3- 3. The experimental setup for EPID image acquisition. The solid water phantom thickness (T) was symmetrically set about the isocentre and the EPID kept at a fixed source to detector distance (SDD=140 cm).

The photon beam has spectral variations due to the flattening filter, scatter and beam hardening in the object irradiated and hence the pixel intensity at any point in the detector will not follow exponential attenuation (equation 1.2) with object thickness. Equation 1.2 is modified by adding another term quadratic in thickness, and the data are fitted onto the resulting equation (Fielding et al 2002). The calculation of equivalent path length using the quadratic calibration

method was done following the same principle as above; and also described by Kairn et al (2008). In their work, they used Monte Carlo simulations to validate the use of EPID as gauge for patient or phantom radiological thickness, as an alternative to dosimetry.

The relationship between intensity and phantom thickness for a pixel at location (i,j) in the detector is assumed to be a quadratic function of thickness, given by

$$A(i,j)*T^2(i,j) + B(i,j)*T(i,j) + \ln\left(\frac{M(i,j)}{M_o(i,j)}\right) = 0 \qquad (3.4)$$

Where the $*$ symbol represents element-by-element matrix multiplication, M(i,j) is a 2D matrix of signals (i =1 to 384 and j =1 to 512) due to placing a thickness T(i,j) in the radiation beam and $M_o(i,j)$ is the matrix image signal obtained without any material in the beam for each pixel in the detector. T(i,j) at each pixel can be calculated from an expression related to the physical thickness of the material and setup / geometry of the unit and is given by

$$T(i,j) = \frac{T_o\sqrt{x(i,j)^2 + y(i,j)^2}}{SDD\sin\theta(i,j)} \qquad (3.5)$$

Where x and y denote the distance of the i^{th}-j^{th} pixel from the central axis, SDD and T_o are the source to detector distance and physical thickness of the material on the central axis respectively. $\theta(i,j)$ is the angle between the vertical axis and pixel (i,j) on the EPID is given by

$$\theta(i,j) = \tan^{-1}\left(\frac{\sqrt{x(i,j)^2 + y(i,j)^2}}{SDD}\right) \qquad (3.6)$$

The quadratic coefficients A(i,j) and B(i,j) are related to the attenuation coefficients of the material. All matrix multiplications and divisions are done element-by-element. The measured 2D signal array for each of the thicknesses above was fitted to equation 3.4 resulting in a set of 384x512x6 equations, linear in A(i,j) and B(i,j) of the form

$$A(i,j) * M_1(i,j) + B(i,j) * M_2(i,j) \quad = M_3(i,j) \qquad \textbf{(3. 7)}$$

Where $M_1(i,j)$, $M_2(i,j)$, $M_3(i,j)$ are the matrices resulting from the element-by-element squaring of T(i,j), T(i,j) and simplification of the logarithmic term of equation 3.4 respectively. These sets of equations were solved by means of the least square method to obtain matrices A(i,j) and B(i,j).

Any other material imaged by the detector resulting into matrix signal $M_4(i,j)$ can be solved by inverting equation 3.4 and substituting the values of fitting parameters A(i,j) and B(i,j) such that,

$$Th(i,j) \quad = \frac{-B(i,j) \pm \sqrt{B^2(i,j) \quad -4A(i,j)\ln[M_4(i,j)/M_o(i,j)]}}{2A(i,j)} \qquad \textbf{(3. 8)}$$

Where Th(i,j) is a two-dimensional matrix of thicknesses in cm which is equal to water equivalent path length (EPL) for the reference conditions. However if a patient / phantom is imaged at any other irradiation situation, other than the reference condition, the signal $M_4(i,j)$ has to be corrected for field size, phantom scatter and monitor unit changes to determine the (EPL). It was found that the solution given by evaluating the negative route of 3.8 was unrealistic, and thus discarded.

3.2.3 Measurement of correction factors

3.2.3.1 Field size and phantom thickness

Scatter correction factors (CF) due to phantom scatter and field size effects were used to correct for EPL calculations as described by Fielding et al 2002. These factors were determined experimentally for a range of field sizes with solid water phantoms of thicknesses 5, 10, 15, 20, 26 and 32 cm. Each phantom was positioned on the beam central axis on the treatment couch and the distance from the source to the centre of the phantom adjusted such that the SAD was equal to 100 cm. Figure 3-4 shows the setup used. The transit signals through the phantoms were detected either directly with the EPID (figure 3-4 a) or using an ionisation chamber positioned on the central axis at the EPID position

(figure 3-4 b). For the EPID, the response was measured as the mean pixel value in a 1 cm region of interest in the centre of the image. For the alternative method, the ionisation chamber was inserted in a 30x30cm^2 solid water phantom slab, with appropriate build-up (1.5 cm and 2.5 cm for 6 MV and 16 MV respectively) and 1 cm solid water phantom for back scatter to simulate the EPID. Using Monte Carlo simulations, Siebers et al (2004) established that 9.8 mm of water slab was optimum to model the equivalent EPID (Varian) backscatter material. Similarly, the phantom model used by Warkentin et al (2003) was ≈ 2.7 cm equivalent thickness for Monte Carlo simulation of the EPID.

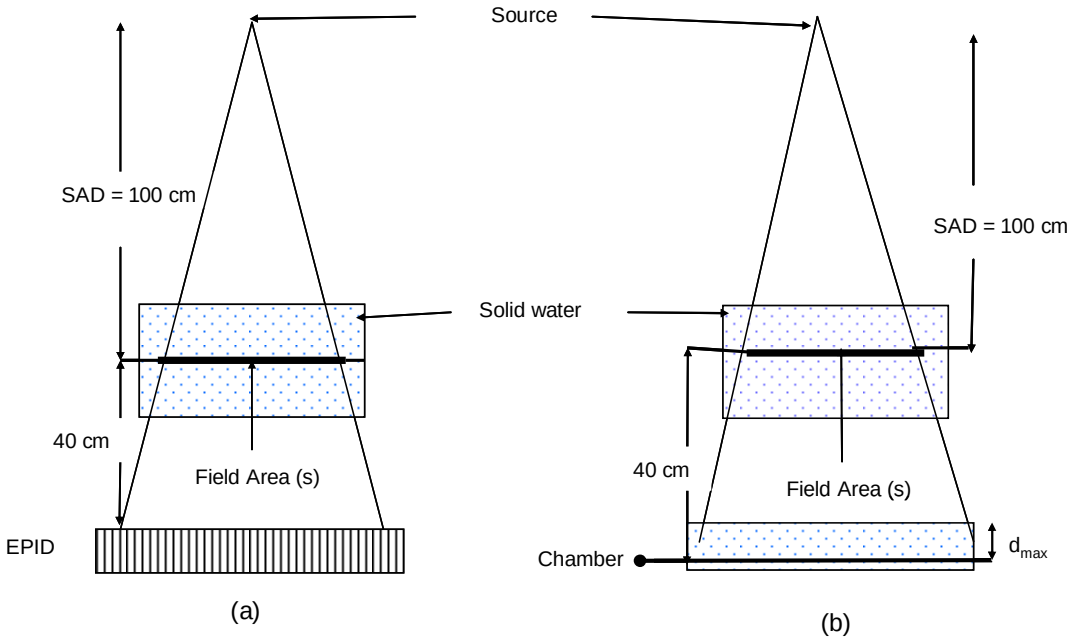

Figure 3- 4. The experimental setups for (a) EPID and (b) ionisation chamber measurement of scatter and field size correction factors. The solid water phantom thickness (T) was symmetrically set about the isocentre and the detectors kept at fixed source to detector distances (SDD = 140 cm). The ion chamber was set with a 1.0 cm solid water backup and build-up equivalent to the beam d_{max} (1.5 cm and 2.5 cm for 6 MV and 16 MV respectively).

The total radiation signal (dose) reaching the EPID detector is the sum of the primary and scatter components (Swindell et al 1996). The scatter factor, SF(s,z) due to field size (s) and physical thickness (z) is the ratio of the total signal (T_D) to the primary signal (P_D) and is defined by

$$SF(s,z) = \frac{T_D(s,z)}{P_D(z)} = 1 + SPR(s,z) \Rightarrow SPR(s,z) = \frac{T_D(s,z)}{P_D(z)} - 1 \quad (3.9)$$

Where SPR(s,z) is the scatter to primary ratio. The CF is related to the SPR (Mayles et al 2007, Kairn et al 2008), by

$$CF(s,z) = \frac{(1+SPR)_{ref}}{(1+SPR)_s} = \frac{\left[1+\frac{T_D(s,z)}{P_D(z)}-1\right]_{ref}}{\left[1+\frac{T_D(s,z)}{P_D(z)}-1\right]_s} = \frac{[T_D(s,z)]_{ref}}{[T_D(s,z)]_s} \quad (3.10)$$

Where ref is the reference field size (21.5x21.5 cm^2) and since the primary dose is independent of field size, then $P_D(z)_{ref} = P_D(z)_s$. Thus for either EPID or ionisation chamber measurements, the correction factor CF(s,z) due to field size (s) and solid water phantom thickness (z) were obtained as the signal ratios for the reference field and the field size of interest (s).

3.2.3.2 Monitor unit effects

The product of EPID pixel value and acquired number of frames has a linear relationship with the MU (McDermott et al 2006, Greer et al 2003 and Kavuma et al 2008). However, the preliminary results demonstrated significant differences between EPL for EPID images acquired with lower monitor units and those with higher monitor units. The effect of varying MU and the influence it has on the calculated EPL was studied by irradiating solid water materials of thicknesses 10, 20 and 32 cm for square field sizes of 5, 10 and 20 cm; at 20, 50, 100, 200, 300 and 500 MU; and doserates of 400 MU/min and 100 MU/min. The signal (average EPID response in a 13 x 13 pixel (approximately 1.0 cm^2 area) region of interest in the centre of the image) versus MU plots were generated for the three thicknesses. Another dosimetric parameter, the signal-to-monitor-units ratio (SMUR) was calculated by dividing the same EPID signal above by the delivered number of monitor units. The main purpose of the SMUR calculation is to take into consideration the non-linear response of EPID at lower MU. The data were normalised to those at 100 MU. From these results, correction factors dependent on the MU were determined and equation 3.8 above was modified to take into

consideration the varying effect of MU on EPL. Hence the overall correction due to phantom thickness, field area and monitor unit is given by

$$CF_{s,z,mu}(i,j) = \frac{CF_{s,z}(i,j)}{CF_{mu}} \quad (3.11)$$

This correction factor $CF_{s,z,mu}(i,j)$, becomes the coefficient of the $M_4(i,j)/M_0(i,j)$ term in equation 3.8 (Mayles et al 2007, Kairn et al 2008).

The calculation of the water EPL was accomplished using an iterative numerical method (Appendix A). An iterative algorithm was created to obtain a converged solution $x_{n+1}(i,j)$ and the thickness Th(i,j) calculated in equation 3.8 is the initial approximate solution $x_n(i,j)$ given by

$$x_{n+1}(i,j) = \frac{A(i,j)x_n(i,j)^2 - c(i,j)}{2A(i,j)x_n(i,j) + B(i,j)} \quad where \quad c(i,j) = \ln[CF_{s,z,mu}(i,j)\left(\frac{M_1(i,j)}{M_0(i,j)}\right)] \quad (3.12)$$

Matrices A(i,j), B(i,j) and the ratios $M_1(i,j)/M_0(i,j)$ are constants, but the correction is included in the loop which makes matrix c(i,j) a variable at each iteration. In other words after each iteration, a new correction is obtained depending on the previous solution. The solution $x_{n+1}(i,j)$ is the water equivalent path length or water equivalent thickness or radiological thickness. The solutions were tested for convergence for selected field sizes and thicknesses, i.e the solution x_{n+1} approached a steady value as n $\rightarrow$ large (see table 4.6, section 4.2.5.1). Convergence was obtained after two – three iterations; hence the algorithm was set to repeat itself five times. Bad pixels within the imager and at edges of the imager may cause imaginary roots or not a number (NAN) within the matrix. NANs were replaced by zeroes wherever they were in the matrix and imaginary roots were converted into the real numbers using Matlab. The stability of the fitting parameters A(i,j) and B(i,j) was investigated with a monthly repeat of image acquisition over a four month period for both 6 MV and 16 MV.

3.2.4 Open fields

3.2.4.1 Verification of equivalent path length from EPID images

EPID images were acquired for a range of field sizes and known thicknesses of water and non-water equivalent materials to verify the accuracy of calculated equivalent path length as described in equation 3.12. To investigate the influence of varying densities, materials of low, medium and high densities representing lung, water and bone respectively were used.

(a) Slabs of solid water, bone and lung materials were positioned in steps (figure 3-5 (a)). The dimensions of each slab were 30x30 cm^2 with thicknesses (relative electron densities) of 10cm (0.99) for solid water, 3 cm (1.3) for bone and 3 cm (0.34) for lung.

(b) In the second setup, cylindrical materials (diameter 3cm and height 7 cm) of lung, solid water and cortical bone with relative electron densities of 0.4, 0.99 and 1.66 respectively were sandwiched between two 5cm slabs of solid water. The cylinders were inserted into Styrofoam slab (relative electron density 0.05) as indicated in (figure 3-5 (b)). The relative electron densities quoted here are from the manufacture and were engraved on each phantom.

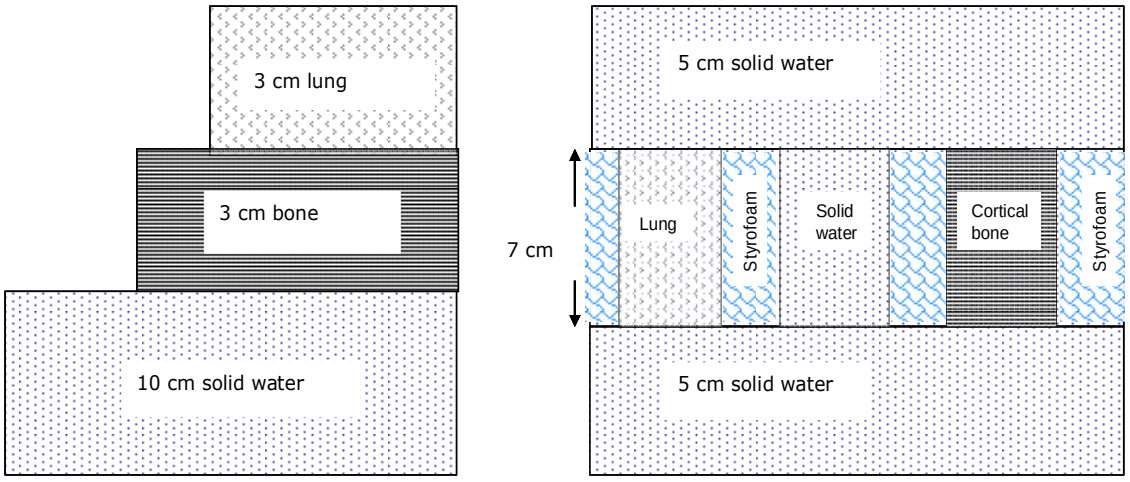

Figure 3- 5. Figures (a) and (b) are schematic cross sectional diagrams for different phantoms of varying electron densities.

The phantoms were positioned on the table in the center of the beam axis such that the SAD=100 cm to the phantom centres. EPID images of 20x20cm^2 field sizes were acquired with 6 MV exposures with 100 MU for both cases in figure 3-5. A theoretical formula by Broggi et al (2001) was used to compute the radiological thicknesses (EPL) for the cases in figure 3-5, whereby for any given material of physical thickness T_m and relative electronic density ρ_m, the EPL or radiological thickness is given by

$$EPL = T_m x \rho_m \quad (3.\ 13)$$

3.2.4.2 Exit dose prediction for open fields from EPID images

After the equivalent path length calculation from the EPID image had been carried out as described above, the method was extended to dose prediction. The exit dose is defined at the dose plane positioned at a distance d_{max}, from the exit surface of the phantom. In cases where the phantom / patient do not have a flat exit surface, the exit dose is similarly defined at irregular locations, with distances d_{max} from the exit surface. The dose at a depth for a particular field size can be calculated from the given number of monitor units, appropriate depth-dose data, output factor and off-axis correction (Williams et al 2004, Podgorsak et al 2005). For the 2D EPID image, an exit dose map (D_{ext}) was calculated by relating the calculated EPL to the percentage exit-thickness-dose (PETD), which is defined as the ratio of the exit dose at a depth of z-d_{max} to the dose at d_{max} (Appendix B), where z is the thickness of the phantom. Table 3-2 explains the conversion process for selected points in a 2D EPID image matrix obtained at 12 cm^2 FS. Each point in the EPID generated EPL matrix (3-2 a) is converted into a corresponding exit thickness dose (3-2 c) using the PETD(z,s) table (3-2b) by interpolation (look-up-table) between depths (d) and field sizes (FS).

Table 3- 2. Conversion process of EPL to dose using PETD table

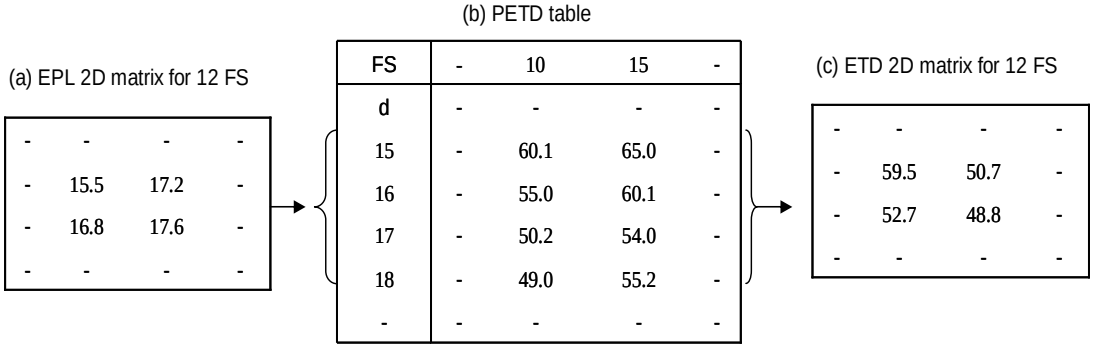

The PETD were derived from tissue phantom ratios (TPR) according to the equation

$$PETD(z,s) = \left(\frac{SAD}{SAD + z/2 - d_{\max}}\right)^2 TPR_{eff}(z,s) \qquad (3.\ 14)$$

Where SAD is the source to axis distance, TPR_{eff} is the TPR at an effective distance $z\text{-}d_{max}$ and d_{max} is the maximum depth dose for 6 MV photon beams. Similar to TPR, the field size (s) in PETD is defined at the isocenter. The TPR data generated from measured depth dose curves were imported from Eclipse 8.6 TPS (Varian Medical Systems, Palo Alto, California, USA). Equation 3.14 is theoretically justified in Appendix B and was experimentally verified by ionisation chamber measurements for selected field sizes and solid water phantom thicknesses, as illustrated in figure 3.6. This was done for square field sizes of 5, 10, 15 and 20 cm; at varying phantom thicknesses of 10, 15, 20 and 32 cm. At each setup, z/2 was always kept at SAD and the ionisation chamber was located at distance $z\text{-}d_{max}$ (z is the phantom thickness).

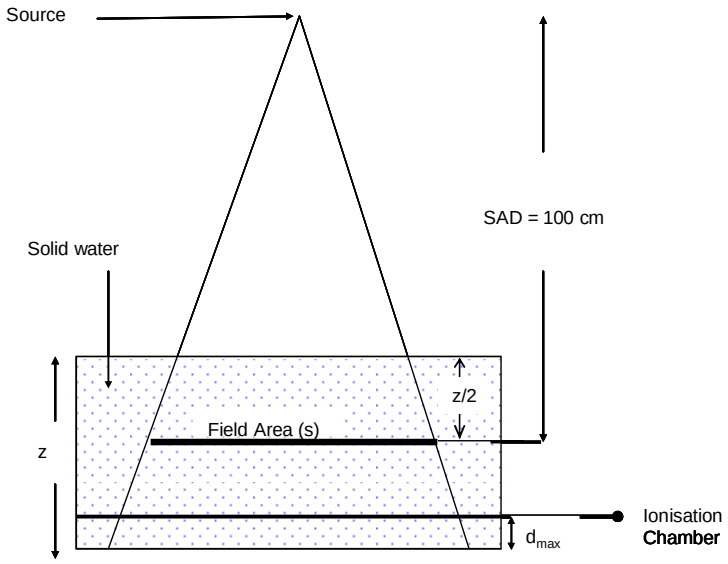

Figure 3- 6. The experimental setup used for ionisation chamber measurement of PETD

Flood field calibration of the EPID, required by the manufacturer's control software, has the effect of flattening the beam profile, thus improving imaging performance. However it has a deleterious effect on transit dosimetry because the process removes any in air / off-center ratio in the EPID image caused by the flattening filter (Van Esch et al 2004, Greer et al 2007). The off-axis doses were corrected by applying the open field envelope and boundary profiles (Storchi et al 1995, Storchi et al 1999). The envelope profile $E_p(r,z)$ is defined as the ratio of the dose at a point off-centre relative to the dose on the field central axis at the same depth and describes the off-axis ratio of each calculation point for an infinite uncollimated field. The boundary profile $B_p(x,z,s)$ is defined as the ratio of the dose at a point off-centre in a finite field relative to the dose at the same point in an infinite field and describes the effect of the edges of the collimator jaws for each field size. The data used in this study were imported from Eclipse 8.6 TPS's (Beam configuration work space) pencil beam algorithm that is generated from measured beam profiles.

The exit dose map is then calculated according to the equation

$$D_{ext}(i,j) = MUxOFxB(s)x\frac{PETD(i,j)}{100}xE_p(r,z)xB_p(x,z,s) \quad \textbf{(3. 15)}$$

Where:

- MU is the given monitor unit

- OF is the output factor of field s relative to the 10x10cm^2
- B(s) is a factor which corrects for reduced back scatter proximal to the exit surface (corrects dose in our setup to reference condition);
- $E_p(r,d)$ is the envelope profile, a function of radial distance (r) from the field central axis and the depth (z) of point
- $B_p(x,z,s)$ is the boundary profiles a function of distance (x) from the field central axis, depth (z) of point and field size(s).

3.2.4.3 Entrance dose prediction for open fields from EPID images

The entrance dose is the most commonly measured in vivo dosimetry parameter, which is usually compared to the expected dose predicted by the treatment planning system. The entrance dose is defined at the plane, a distance d_{max} from the entrance surface of the phantom. The entrance dose distribution was determined using back projection techniques based on the inverse square law and attenuation. The entrance dose (D_{ent}) was determined by projecting the exit dose maps back to the phantom entrance surface at depth of maximum dose (d_{max}) given by

$$D_{ent}(i,j) = \frac{D_{ext}(i,j)xE_p(r,d_{\max})xB_p(x,d_{\max},s)}{PDD_{corr}(i,j)xE_p(r,z)xB_p(x,z,s)} \quad (3.16)$$

Where $B_p(x,d_{max},s)$ and $E_p(r,d_{max})$ are the boundary and envelope profiles at the entrance respectively. PDD_{corr} is the percentage depth dose for each pixel's EPL, corrected for changes in SSDs using the Mayneord factor

$$\frac{pdd(d,A1,f1)}{pdd(d,A2,f2)} = \left\{ \frac{\frac{f1+d\max}{f1+d}}{\frac{f2+d\max}{f2+d}} \right\}^2 \quad (3.17)$$

Where d is set to be EPL- d_{max}.

3.2.4.4 Verification of exit dose

From the calculated EPL of the EPID images, exit doses were calculated as described in equation 3.15, and verified by comparison with corresponding doses calculated by the TPS. The exit doses were verified using the setup described in figure 3-5 (section 3.4.2.1) for verification of EPL. In addition, an anthropomorphic lower torso phantom shown in figure 3-7 (The Phantom Laboratory, Salem, New York, USA) was positioned on the treatment couch and anterior-posterior fields were delivered. The phantom consists of natural-human-skeleton lumbar vertebrae, pelvis, upper third of femur and a hollow cavity (reproduces the sigmoid flexure and rectum) cast into Urethane (material with same effective atomic number as the body soft tissue).

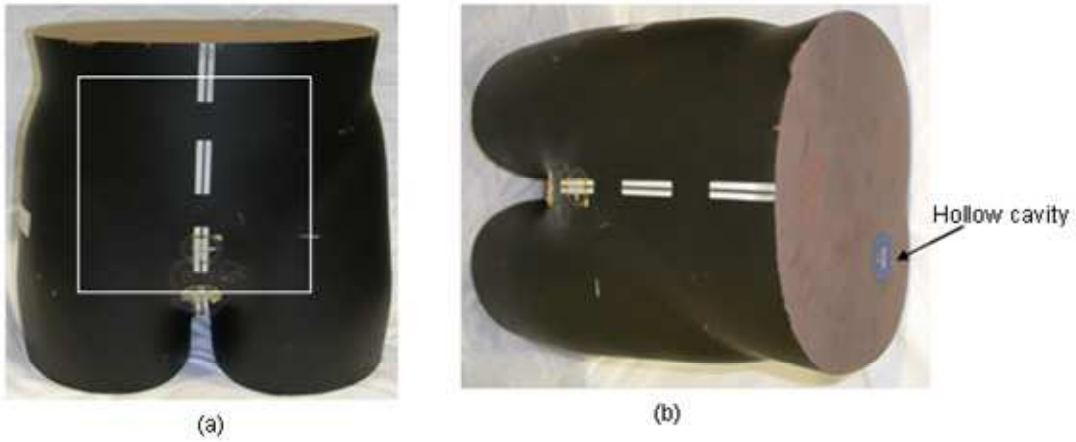

Figure 3- 7. Shows the lower torso phantom and the white central square in (a) shows the 20x20 cm^2 irradiated area.

The phantoms were positioned on the table in the centre of the beam axis such that the SAD=100 cm to the phantom centres. EPID images of 20x20cm^2 and 10x10cm^2 field sizes were acquired with 6 MV and 200 MU exposures.

3.2.5 Irregular fields

Radiation fields that are not square or rectangular or circular are termed irregular fields. An irregular field also has an equivalent square field that will

yield the same value of a given dose function as does the irregular field (Podgorsak 2005).

3.2.5.1 Equivalent path length from EPID images for irregular fields

The dose functions of interest are the scatter correction factor, $CF_{s,z}(i,j)$ as described in equations 3.10 and 3.11 above, and the output factor (OF) due to an irregular area. Field area and resulting phantom scatter are essential for predicting the EPL from an EPID image. In case of irregular fields, one option of determining area is to measure it from the EPID image. A range of irregular shaped fields of known field area were designed using the multi leaf collimators (MLC) in the Eclipse 8.6 (Varian Medical Systems, Palo Alto, California, USA) TPS. The fields were defined by the MLC leaves while the collimator jaws opening remained fixed at 25x25 cm^2. The plans were exported to the linac and all irradiations were done at 100 MU and dose rate of 400 MU/min. EPID images were acquired for these irregular shaped field apertures with 20 cm thicknesses of solid water materials to verify the accuracy of calculated equivalent path length and hence dose. The images for the computation of irregular fields were acquired using the RT chart fields, as described in section 3.2.1. Figures 3-8 (a-f) show some of the various aperture shapes used in the study. The shape in figure 3-8 (a) is commonly encountered whenever there is a need for partial blocking of the beam to shield a critical organ. The shape in figure 3-8 (e) was chosen because it is clinically similar to the anterior-posterior pelvic radiation fields used in the treatment of prostate and cervical cancers. The other shapes were chosen to test the abilities of the algorithm and the TPS. For the shape in figure 3-8 (d), the Eclipse 8.6 TPS has no problem with MLC abutting in open field (Varian solved this issue with the introduction of the Distributed Calculation Framework (DCF) in Eclipse 8.1).

A MATLAB code was written to read and detect the radiation field edges from the EPID acquired images shown in figures 3-9 (a-f) of the irregular shaped apertures. An edge detection algorithm based on searching the entire EPID image and computing the approximate gradients of the image intensity function was written. An edge is localised at those points where the gradient is a maximum. A mask image was derived in which pixels at the edge are characterised by ones and all other pixels elsewhere in the image are set to zero.

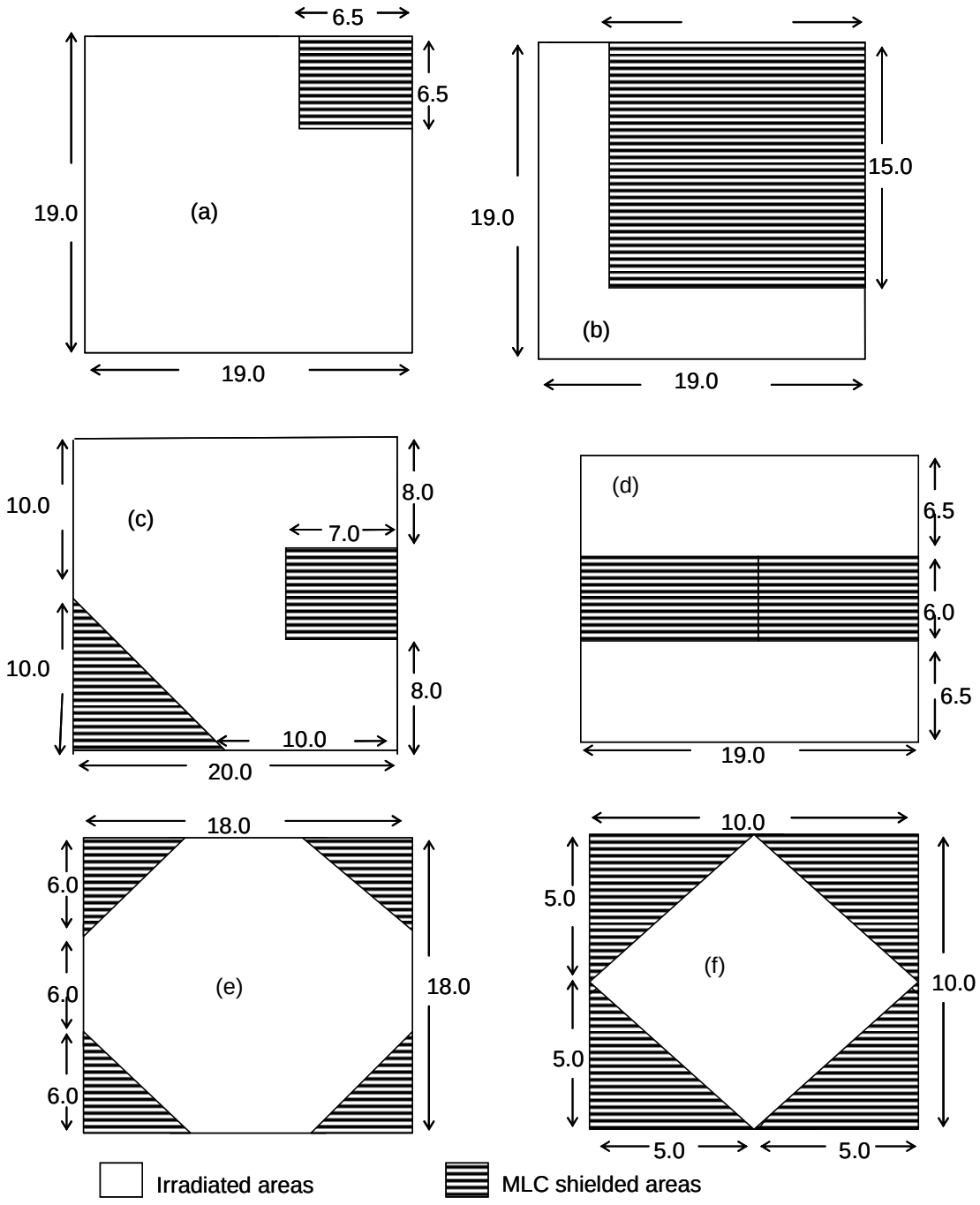

Figure 3- 8. Irregular apertures of varying shapes and areas. The dimensions are in cm measured at the isocentre.

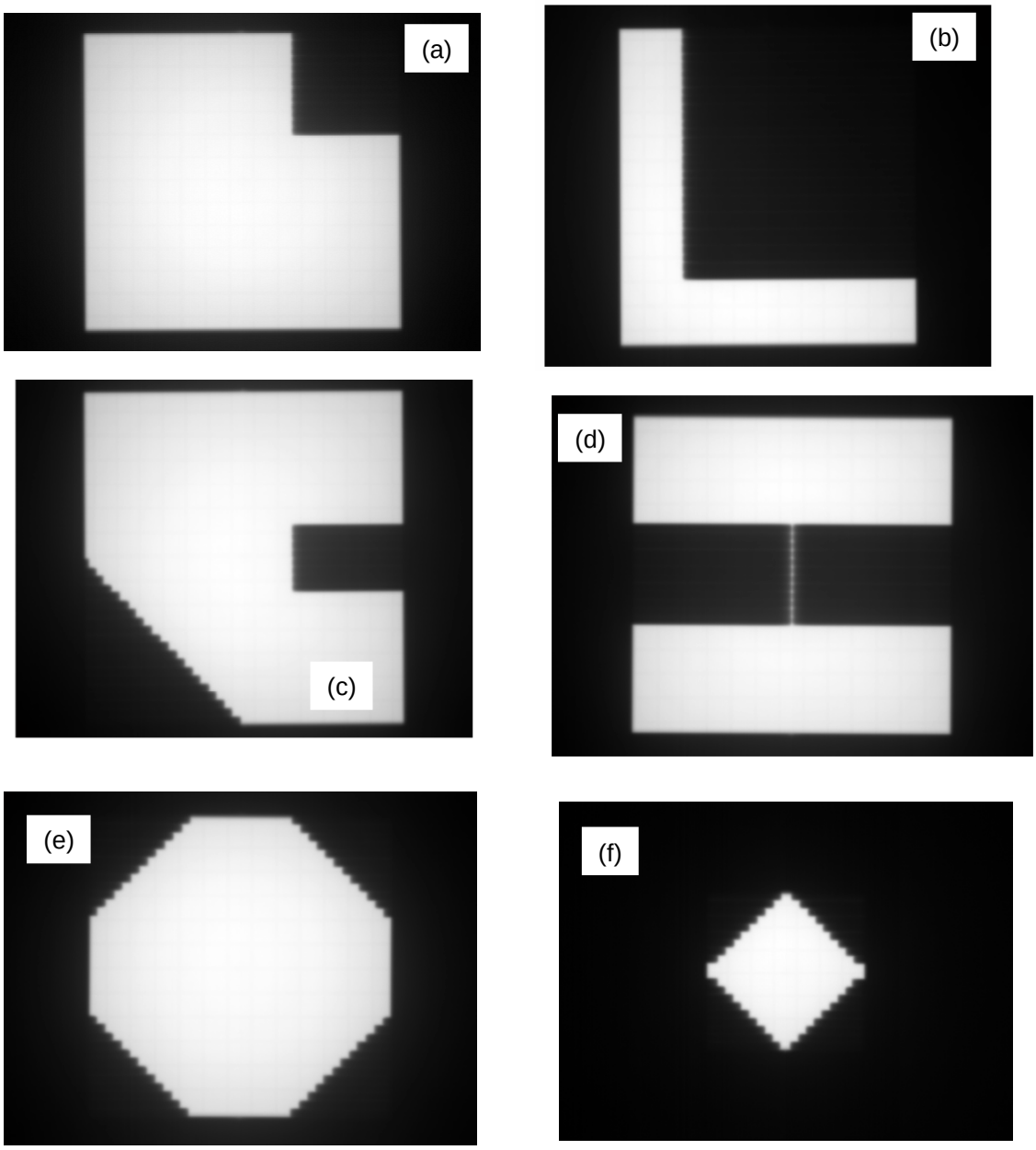

Figure 3- 9. Respective EPID images for the apertures shown in figure 3.7 above

By tracing the entire bounded region (irradiated area), edge polygons are formed as shown in figures 3-10 (a-f).

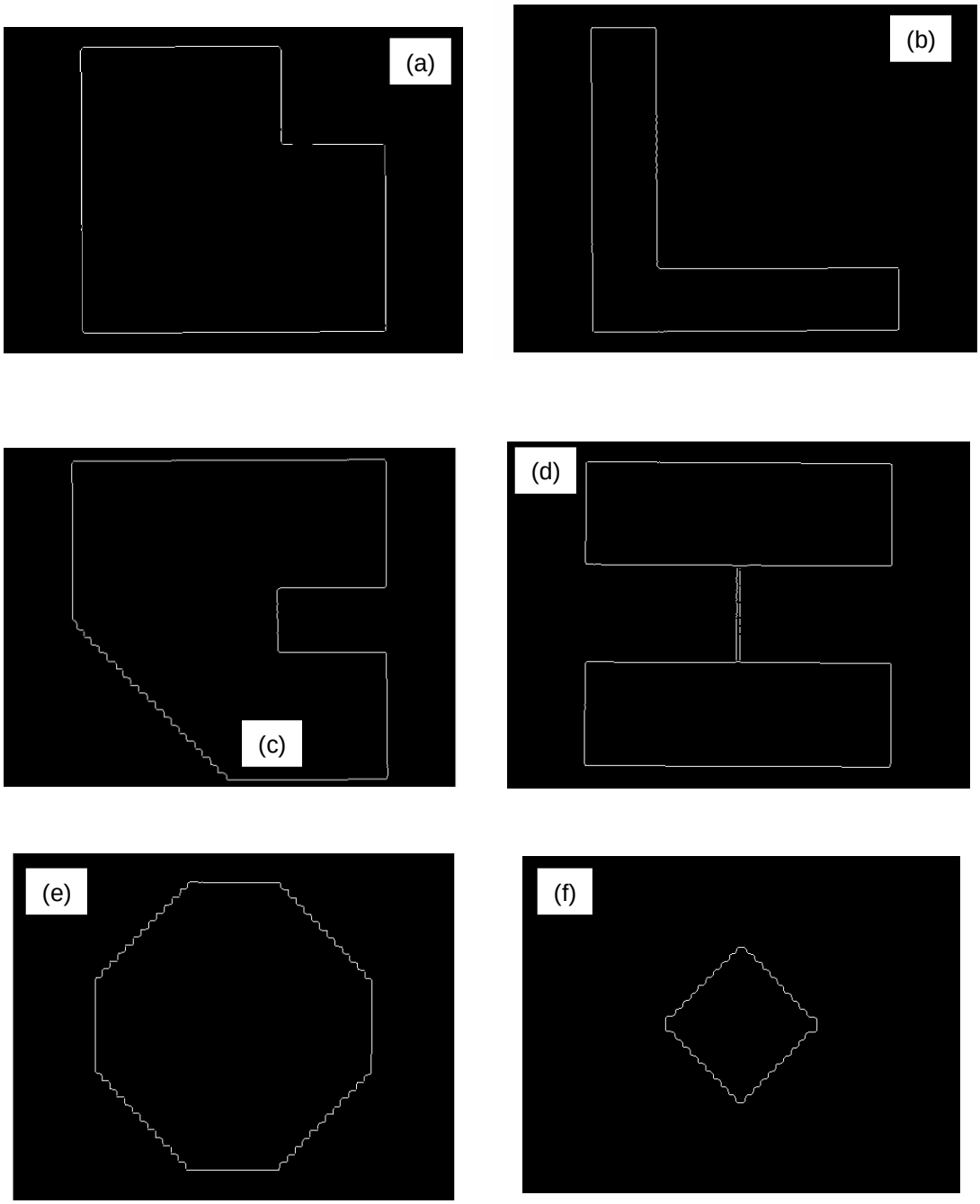

Figure 3- 10. Respective field edges determined from the EPID images above

The coordinates of the pixels of these polygons are searched and successively stored. If the *X* and *Y* coordinates of all vertices are known and entered in order of successive vertices, then the area of the polygon at the isocentre can be calculated (Beyer 1987) using the equation

$$Area = \frac{1}{2}\left((x_1 + x_2)(y_1 - y_2) + (x_2 + x_3)(y_2 - y_3) + \ldots + (x_n + x_1)(y_n - y_1)\right)\left(\frac{pix}{mag}\right) \quad (3.18)$$

Where,

- *n* is the total number of pixels forming the edge polygon,
- x_i and y_i ; i=1, 2, . . ., n are the x and y coordinates of each vertex pixel making the bound region;
- *pix* is the pixel size (resolution) = 0.784 mm and
- *mag* is the magnification.

The equivalent square areas are approximately obtained from taking the square roots of the area in equation (3.18). The area calculation was also tested with other images acquired for square, rectangular and wedged fields. The calculated areas using the equation above were compared with the expected area and percentage differences computed. The automatic calculation of area from the image facilitated the calculation of EPL, and hence dose for any irradiated field, including conformal shapes of unknown area. The calculated area is used to establish an appropriate scatter factor $CF_{s,z}(i,j)$, which is, together with the correction coefficients A(i,j), B(i,j) and the image signal obtained without any material in the beam $M_o(i,j)$ for open fields, used as described in equations (3.8) and (3.12) to predict the EPL.

3.2.5.2 Exit dose from EPID images for irregular fields

The area calculated above is used to establish an appropriate output factor (OF) and the exit dose calculated as described in equation (3.14). The EPL beneath the MLC shielded regions is too high (≈ 80 cm) compared to maximum depths for TPR table which was measured up to a depth of 40 cm. To facilitate calculation of doses in these regions, the TPR table was extrapolated to include values up to 50 cm. For all calculated EPL greater than 50 cm, the TPR was set to the MLC transmission factor. The images for the computation of MLC transmission were acquired using fields created in RT chart, as described in section 3.2.1. The MLC transmission is defined as the EPID dose (signal) ratio at the central axis of a closed MLC measurement to an open beam, for the same field size of 10x10cm^2 (Lorenz et al 2007). The mean pixel values in the 10x10cm^2 area were obtained for the open field and MLC closed field, that is

$$MLC\_Transimision = \frac{MeanPixelValue\_MLC\_Closed}{MeanPixelValue\_Open\_Field} = 0.013$$

To verify the accuracy of calculated equivalent path length and hence dose, corresponding doses calculated with the TPS were compared with those predicted by EPID.

3.2.6 Enhanced dynamic wedge fields

Enhanced dynamic wedge (EDW) dose profiles are computer controlled, created by sweeping one of the Y-jaw collimators from starting (open field) to closed position (0.5 cm from the opposite fixed Y-jaw), while both the X-jaws remain fixed during irradiation (Varian Medical systems 1996, Gibbons 1998, Prado et al 2002, Kuperman 2005). Because of the collimator motion, different parts of the field are exposed to the primary beam for different lengths of time, creating a wedged dose gradient across the field. The wedged dose distributions are generated by means of a single golden segmented treatment table (GSTT) for the 60^o wedge angle for each beam energy, and the GSTT is used to control the position of the moving jaw versus the proportion of the delivered monitor units. The dose distributions for the other wedged angles (10^o, 15^o, 20^o, 25^o, 30^o and 45^o) used clinically are reproduced by combining the open and 60^o wedged data beams, (Pasquino et al 2009) and are contained in a unique dose versus jaw position table called the Segmented Treatment Table (STT). EDW comprises of two parts: the open-field phase and a collimator-sweeping phase, both governed by the STT which specifies the moving jaw position in equally spaced steps as a function of the cumulative MU.

3.2.6.1 Equivalent path length from EPID images for EDW fields

The sweeping of the moving jaw across the radiated field modulates the radiation intensity passing through the phantom by varying the exposure time of any given point, hence the signal reaching the EPID. The images for the computation of EDW treatments were acquired using fields created in RT chart, as described in section 3.2.1.The edge detection and subsequent calculation of irradiated area method, described in section 3.2.5.1, was used for EDW fields.

There are two potential approaches for verification of dose for EDW - using either the same set of correction coefficients A(i,j), B(i,j) and $M_o(i,j)$ generated for open fields or generating another set of coefficients that involve the wedge motion in the field. The former approach has some limitations in predicting EPL especially for EDW angles above 30^0,(see section 4.3.3 in results and discussions) hence in this study, the latter approach was used. We tested the use of correction coefficients A(i,j), B(i,j) and $M_o(i,j)$ on EDW fields but because of the limitation described in section 4.3.3, the idea was dropped.

All the fitting parameter measurements were performed using the Y1-IN EDW orientation. The wedged image signal without any material in the beam $M_0^{\theta}(i,j)$ was calculated for the largest field size of 20x20 cm^2 used in this study with moving jaw Y1=-10 cm, fixed jaw Y2=10 cm, and fixed length X = 20 cm; using the MU fraction calculation methodology with GSTT (Gibbons 1998 and Kuperman 2005). For simplicity, the GSTT was represented analytically as an exponential function i.e

$$GSTT(Y) = a_0 + a_1 \exp(b_1 Y) \qquad (3.\ 19)$$

Where Y is the moving jaw position that ranges from -20 to 10 cm; the fitting coefficients a_0, a_1 and b_1 are determined from the Varian published values (Varian Medical Systems, 1996). The full-field segmented treatment table associated with wedge angle θ is given by (Kuperman 2005)

$$STT_{\theta}^{F}(Y) = MU\left(\frac{w_{\theta}GSTT(Y) + w_0 GSTT(0)}{w_{\theta}GSTT(Y=9.5) + w_0 GSTT(0)}\right)/K \qquad (3.\ 20)$$

Where MU is the applied monitor units; GSTT(0) and GSTT(Y=9.5) are the GSTT at Y=0 and Y=9.5 respectively (9.5 is due to the fact that the Varian wedge stops 0.5 cm from the fixed jaw position); K is a geometrical correction factor that scales the data from the isocenter to the EPID imager level;

$$w_\theta = \frac{\tan(\theta)}{\tan(60)} \quad and \quad w_0 = 1 - w_\theta \tag{3. 21}$$

The STT is a two-entry table composed of 20 segments (21 instances), which gives the positions of the moving jaw versus the proportion of the delivered monitor units for each field segment. To simplify data manipulation with the EPID, which is comprised of 384x512 pixels;

- First linear interpolation of the $STT_\theta^F(Y)$ table was used to create 384 points (in wedge direction), where all the points outside the desired field lengths are reduced to zeros.
- Secondly this row of 384 pixels is replicated 512 times to constitute matrix $M_0^\theta(i,j)$.
- Lastly the generated profiles present a slightly steep effect (Papatheodorou et al 1998) towards the end position of the moving jaw. Simple averaging of adjacent values was used to smooth the data.

To establish the appropriate coefficients for the wedged fields, an additional measurement and subsequent derivation of $A_{w60}(i,j)$ and $B_{w60}(i,j)$ for the 60° wedge was made. The correction coefficients for any other wedged angle θ ($A_{w\theta}(i,j)$ and $B_{w\theta}(i,j)$) were obtained from those of the 60° wedge and the open field ($A_{w0}(i,j)$ and $B_{w0}(i,j)$), using weighting factors obtained by the ratio of tangents in a way analogous to that applied to the GSTT (Prado et al, 2002). That is

$$A_{w\theta}(i,j) = (w_\theta)A_{w60}(i,j) + (w_0)A_{w0}(i,j) \quad and \tag{3. 22}$$

$$B_{w\theta}(i,j) = (w_\theta)B_{w60}(i,j) + (w_0)B_{w0}(i,j) \tag{3. 23}$$

With all the necessary factors established, the EPL for the irradiated material can be calculated as described in equations (3.8) and (3.12) above. The EPL predicted in this way is independent of wedge presence.

3.2.6.2 Exit dose from EPID images for EDW fields

The exit dose can then be calculated as in equation (3.14) and this dose will be independent of the wedge effect. The wedge effect in the dose is recovered using the STT methodology where Y in this case is truncated to the desired field length (in the wedge motion direction) according to the equation

$$STT_{\theta}(Y) = \left(\frac{w_{\theta} GSTT(Y) + w_0 GSTT(0)}{w_{\theta} GSTT(Y_{stop}) + w_0 GSTT(0)} \right) \quad (3.24)$$

In this case GSTT(Y_{stop}) is the GSTT at Y=Y_{stop}, where Y_{stop} = Y2-0.5. As described above $STT_{\theta}(Y)$ is converted into a 384x512 array to constitute a matrix $STT_{\theta}(i,j)$. It has been reported that EDW depth dose is almost identical to the open field depth dose (Papatheodorou et al 1999, Varian Medical Systems, 1996), hence the TPR for open fields can effectively be used in the conversion of EPL to dose. In the presence of an EDW of angle θ, the exit dose in equation (3.15) above is modified to

$$D_{ext}(i,j) = MUxSTT_{\theta}(i,j)xOFxB(s)x\frac{PETD(i,j)}{100}xE_p(r,z)xB_p(x,z,s) \quad (3.25)$$

Equation 3.25 above was tested by irradiating and subsequently acquiring EPID images for 20 cm solid water thickness with 15^0, 30^0 and 45^0 EDW at different field sizes. All irradiations were done at 100 MU. Corresponding plans were generated with the Eclipse 8.6 TPS for comparison.

3.2.7 Dose comparison with treatment planning system

Cross plane profiles, point dose differences and gamma index methods were employed in dose comparisons. The dose distributions obtained for different square, irregular and EDW field sizes were used in the evaluation of both the exit and entrance doses. All corresponding dose comparisons for TPS and EPID were absolute. Plane dose distributions at the exit (z-d_{max}) and entrance (d_{max}) were calculated in the Eclipse 8.6 (Varian Medical Systems, Palo Alto, California, USA) TPS for each of the fields. The calculated plane dose distributions from the

TPS were subdivided into a 512 x 384 matrix and imported into the Matlab software for comparison with those determined from EPID images. Point dose comparisons between the TPS dose (D_{TPS}) and EPID predicted dose (D_{EPID}) were calculated at the centres of homogeneous phantoms. For both the TPS and EPID, the point doses at the exit were assumed to be the mean of 13x13 pixels (~ 1 cm) at the central axis. The results were computed using the TPS as the reference and percentage differences were calculated as

$$(D_{TPS} - D_{EPID}) / D_{TPS} x100\% \qquad (3.\ 26)$$

In addition, TPS and EPID dose profiles (1D) were extracted from the centres of the irradiated fields and compared. Furthermore, the absolute dose-matrix (2D) datasets were evaluated quantitatively by calculating the gamma index, which is a measure of the percentage of points passing a selected criterion. The gamma index combines both the dose difference (DD) and distance-to-agreement (DTA) into a single quantity normalised by the acceptance criteria. With respect to the dose distribution in the high-dose gradient region, Low et al (1998) and Chen et al (2009) reported that the DTA is equally important to the differences between the measured and the calculated doses obtained from the TPS. The DTA is the distance between measured data points and the nearest point in the calculated dose distribution that exhibits the same dose.

3.2.8 Further dose verification with MapCHECK 2 device

To obtain additional independent verification of EPID calculated exit doses, MapCHECK 2 (SUN Nuclear Corporation, Melbourne Florida, USA) was calibrated and used to measure directly the exit doses for solid water phantoms. According to the manufacturer, MapCHECK 2 is a 2D array of 1527 uniformly spaced diodes, active detector resolution area of 0.64 mm^2, diode-diode spacing of 7.07mm and covering an area of 32x26cm at the isocentre. The device has a build up and backscatter to the active detectors region of 2.0 $\pm$ 0.1 and 2.75 $\pm$ 0.1 g/cm^2 respectively. Figure 3-11 shows a photo of the MapCHECK 2 device. For measurements, the device is connected to computer software, which is controlled from the operators' room. During exposure, each diode generates a

charge which is proportional to the dose received at that location. The charge is integrated, converted from analog to digital form and sent to the computer that applies the necessary correction factor and stores the data. The MapCHECK device was first calibrated by positioning it on the couch, aligning its detector level with the isocenter. It was then irradiated with a direct anterior (gantry angle zero) beam of 100 MU to a 10x10 cm^2 field size. The software allows the entry of a specified factor (dose corresponding to a given number of MU at specific depth and field size) which is used to normalise the data to create a calibration file that was used to correct the dose maps for all subsequent measurements.

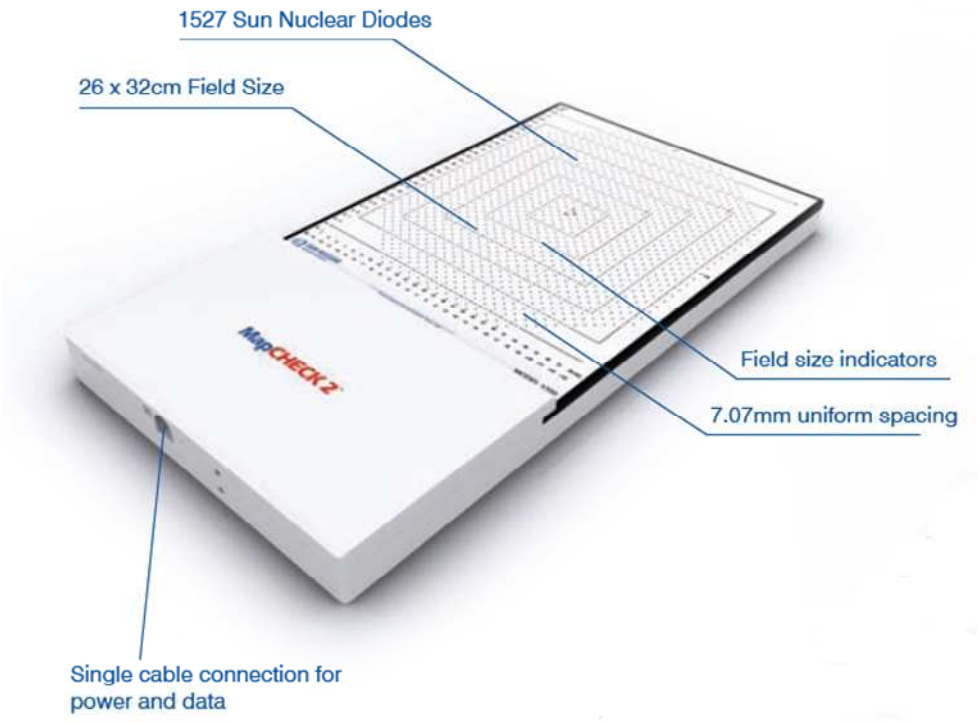

Figure 3- 11: MapCHECK 2 device (SUN Nuclear Corporation, Melbourne Florida, USA)

To avoid heavy weight above the MapCHECK device, it was positioned upside-down; on top of 15 cm thickness of homogeneous solid water (total water equivalent material of MapCHECK and solid water is ≈ 20 cm). The gantry was rotated to 180^0, such that the sensitive side of the MapCHECK device faced the

beam direction, as illustrated in figure 3-12. The setup enabled simultaneous measurement with MapCHECK and EPID image acquisition.

Figure 3- 12: The setup used for the simultaneous MapCHECK measurement and EPID image acquisitions.

The MapCHECK and solid water were CT scanned and images exported to the TPS. Corresponding plans were generated with the Eclipse 8.6 TPS for exit dose comparison. The above setup was used for selected open, conformal (MLC shaped) and EDW fields. The plans were exported to the Linac and exposures taken, acquiring EPID image and MapCHECK measurements at the same time. To compare the dose distributions from the MapCHECK device (sensitive region is 2.75 cm) with the EPID exit dose (calculated at 1.5 cm), the doses from the former were adjusted. The MapCHECK dose map was resized to the same number of 2D data points as those used for the EPID and TPS. The effect of resampling the MapCHECK data points was initially investigated to see if it had any adverse effect on the 2D dose map. All doses for EPID, MapCHECK and TPS are absolute, measured in cGy.

CHAPTER 4: RESULTS AND DISCUSSION

4.1 Dosimetric Performance

4.1.1 Detector reproducibility and response to a reference beam

Table 4.1 shows that system-II detectors have better short-term reproducibility. Repeated exposure of system-II EPIDs showed a standard deviation ranging between 0.13% - 0.71% compared to system-I that ranged between 2.74%- 4.93%.

Table 4- 1 Percentage signal short-term reproducibility for the different EPIDs:

EPID	Hardware/software	System	Reproducibility (% ST.DEV)
D	IDU-20/IAS3	System-II	0.13
G	IDU-20/IAS3	System-II	0.20
I	IDU-20/IAS3	System-II	0.13
J	IDU-20/IAS3	System-II	0.71
K	IDU-20/IAS3	System-II	0.14
A	IDU-II/IAS2	System-I	4.93
B	IDU-II/IAS2	System-I	2.74
C	IDU-II/IAS2	System-I	4.47
E	IDU-II/IAS2	System-I	4.07
F	IDU-II/IAS2	System-I	3.42
H	IDU-II/IAS2	System-I	3.39

Figure 4-1 shows the long-term stability of pixel response over a six-month period for three system-II EPID detectors. For each detector, the pixel responses at the central axis for the first month were compared for the readings in the next five subsequent months. The results show that the short-term and long-term reproducibility for system-II detectors is within ±1.5%, in agreement with McCurdy et al (2001).

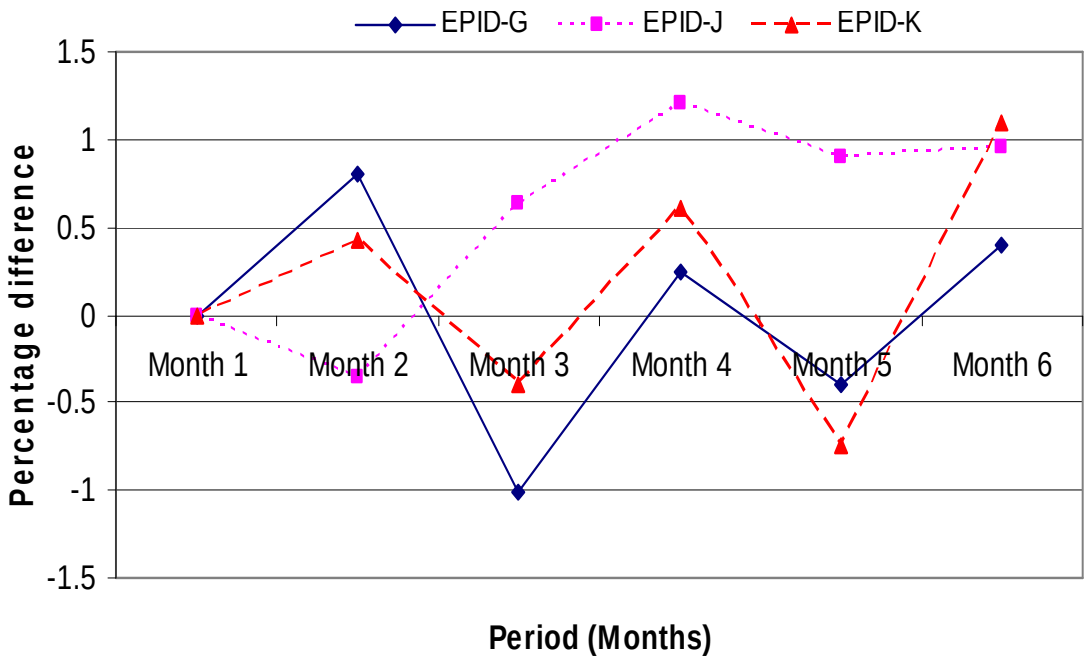

Figure 4- 1. Long term (six months) reproducibility for three system-II detectors

Figure 4-2 shows the EPIDs' responses to a reference beam. System-I EPIDs' showed a significantly wider pixel deviation of 17% compared to 8% for system-II. The error bars in figure 4-2 represent a fixed value of 0.22, which is the standard error of the mean.

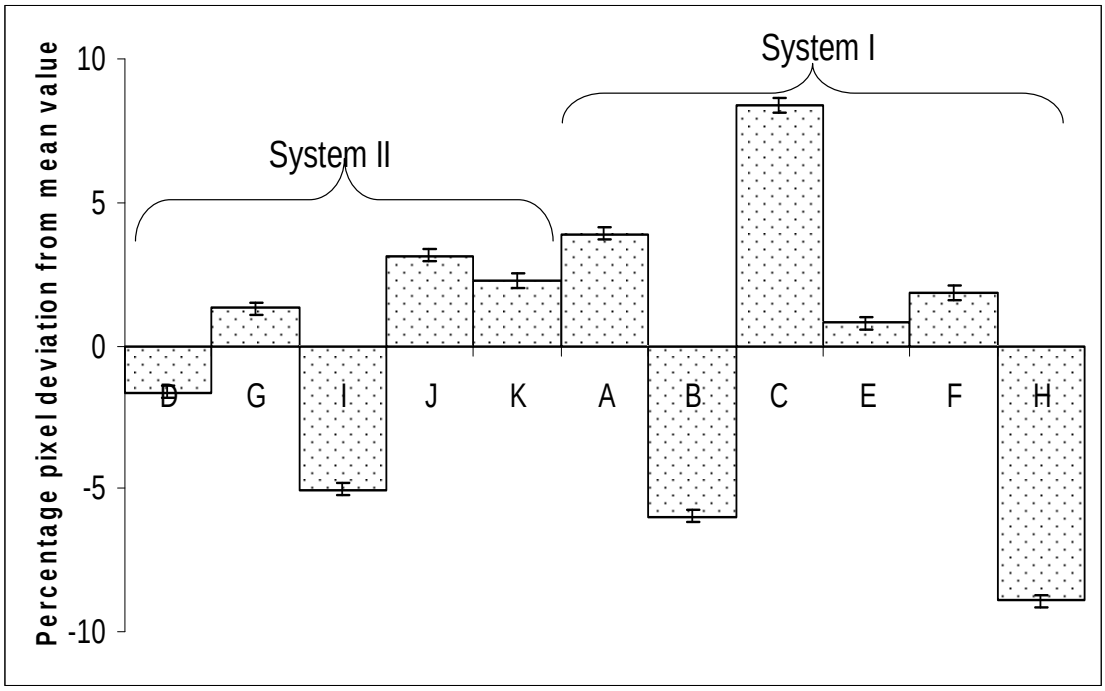

Figure 4- 2. Pixel deviation from the mean for each EPID, after exposure to a reference beam (50 MU, 400 MU/Min doserate and 10x10cm^2 field size).

The signal outputs from the central pixel region (≈ 1.0 cm) for the reference beam showed considerable variation from one detector to another, with system-I EPID's having wider pixel deviation of ±9% compared to ±5% for system-II. Comparing the responses in figure 4-2 and the period in months each EPID has been in clinical use (table 3.1) indicates that individually the EPIDs' responses to the test beam are age independent. Winkler and George (2006) reported variations of up to ± 10% on Electa iView^{GT} EPIDs and observed no relationship with age.

4.1.2 Dose-response behaviour / Linearity

In the integrated mode setup, pixel intensity increased linearly with applied monitor units. Figure 4-3 (a) shows typical accelerator output measurements using an ionisation chamber. Measurements were done at 140 cm source to detector distance. The results indicate that all accelerator outputs were stable prior to measurements with EPID's. The linearity varied with system-II detectors showing a better fit with measured data compared to system-I. Figure 4-3 (b) and (c) shows the signal to monitor units ratio (SMUR) of the

detectors normalized to 1000 MU as a function of MU. Ideally the SMUR should be unity (100%) regardless of how many MU are used at each exposure. System-II detectors showed a response that ranged between 95% - 97% at 5 MU and progressively increased with increasing MU. We found that the normalised SMUR for system-II EPID deviated from unity by 3-5% for ≤ 10 MU. The linearity was within 2% for 20 MU and practically 1% for 50 MU and above. At 1000 MU the SMUR is about 1%–1.2 % higher than that at 50 MU for system-II EPID's. Generally the SMUR varied between 3%-5% in the system-II group of EPID's within the 5-1000 MU range. System-I detectors show a wider inconsistency in the SMUR response. Detectors B,C and F show a gradual increase in SMUR with increasing MU. However the SMUR for detectors B and F at 5 MU of 52% and 38% respectively are too low compared to the expected values. Similarly their SMUR response at 1000 MU is 8% and 7% higher than that at 50 MU. The ionisation chamber responses were within 3% in the 5-1000 MU settings for these system-I detectors.

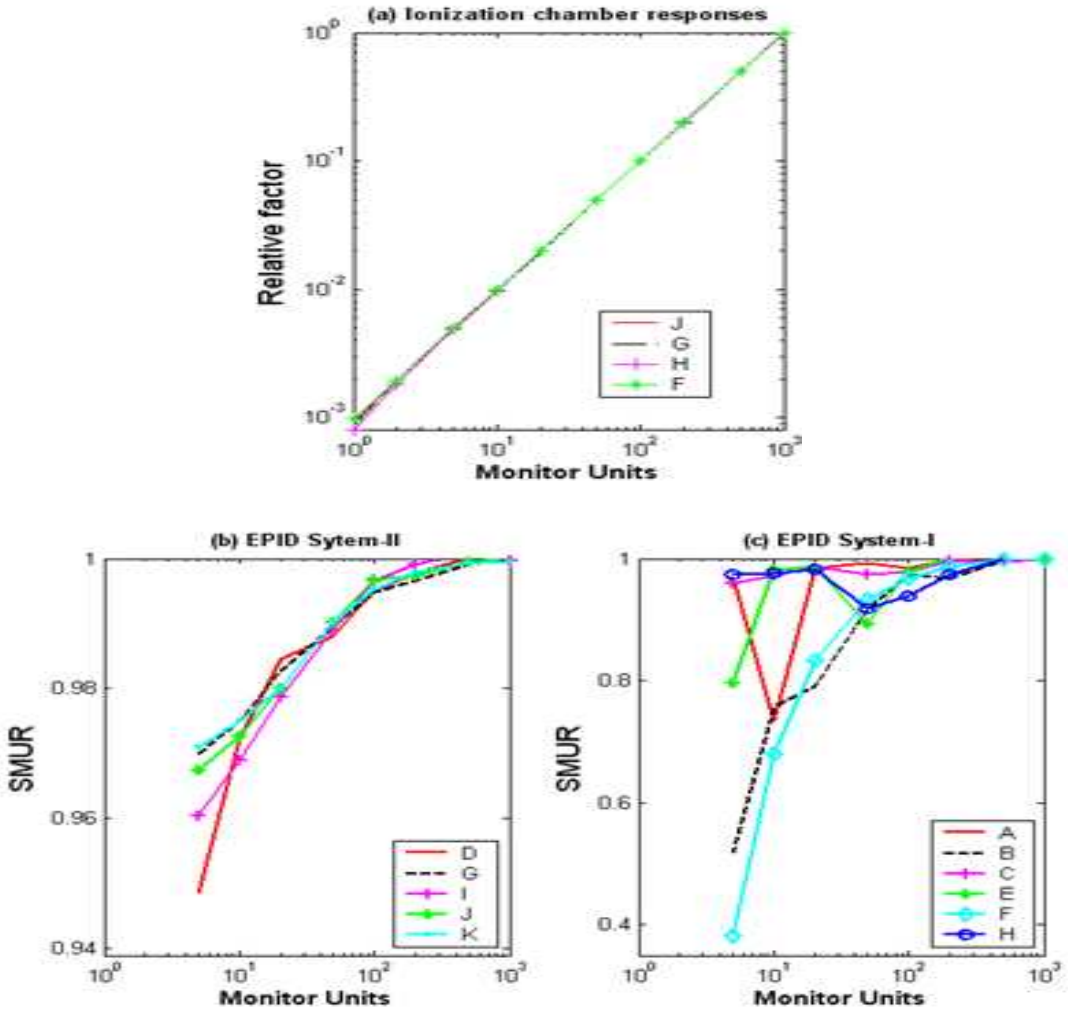

Figure 4- 3. Figure (a) shows Ionisation chamber response as a function of monitor units for different accelerators. Figures (b) and (c) show the signal to monitor units ratio (SMUR) variation with monitor units. The readings at various monitor units were normalised to 1000 MU for the ionisation chambers and EPIDs.

Ideally the dosimeter reading (M) should be proportional to the incident fluence (Q) and the ratio $\left(M/Q\right)$ should be constant regardless of MU settings. System-II EPID response across the panel became stable (within 0.2%) for MU greater than 200 MU, in agreement with Greer (2007). The system-II SMUR responses are similar to previous studies reported by Greer (2007) and McDermott et al (2006) for the Varian a-Si EPIDs and Winkler et al (2005) for Elekta iView^{GT}. The results directly show that there is much more variation for the system-I EPIDs compared to system-II.

Winkler and George (2006) reported an increase in detector sensitivity of 1.7 – 2.8% for the Elekta iView^{GT} in the MU range from 30 to 500. At lower MU (< 20),

all EPIDs had reduced sensitivity attributable to instability in the accelerator doserate and energy during start-up (Winkler et al, 2005). McDermott et al (2004) indicated that EPID frames within the first few seconds of irradiation miss dose and that the longer the irradiation time, the smaller the deficit. This is illustrated in table 4-2, that compares an EPID's response to a single 20 MU exposure to a series of lower-dose exposures with equivalent MU. The results indicate variations in the cumulative response for multiple exposures compared to a single exposure. The cumulative response for 20 exposures of 1 MU each, is 3% lower compared to a single 20 MU exposure.

Table 4- 2. Comparison of EPID J (System-II) response to a single 20 MU exposure to a series of lower-dose exposures with equivalent MU.

Number of exposures	20	10	4	2	1
Monitor units per exposure	1	2	5	10	20
Total response (Σ MPV x ANF)	113760	114200	115280	116100	117179
Deficit from single exposure (20 MU)	2.92%	2.54%	1.62%	0.92%	-

The slow rise in EPIDs signal (McDermott et al 2004), together with doserate instability during accelerator start-up, accounts for the under-response at shorter irradiation times.

Inconsistencies in the SMUR for system-I were much more significant than for system-II. Dead time corrections as indicated by McDermott et al (2006) due to frame saturation after every 64 frames could not rectify all the results nor could it account for discrepancies at the lower MUs. Chang et al (2003) indicated that there is dead time of 0.27 sec every 7.10 sec (the time for acquiring 64 frames) when accelerator operated at 400 MU/min. The deficit in performance in relation to system-II is demonstrated clearly in the pixel reproducibility results: system-I EPIDs averaged 3.8 % compared to 0.3% for system-II as shown in table 4-1. The pixel sensitivity reproducibility of the Varian EPID has been reported to be within 1% (Menon et al 2004, Greer et al 2003, Greer et al 2007). However the image detection-hardware / acquisition-software combinations and periods of the EPIDs in clinical use could not be established from these studies.

4.1.3 Pixel uniformity-response across the entire detector panel

Table 4-3 shows the relative pixel response across the EPID detectors, based on their locations as illustrated in figure 3-1. There are no significant differences between the two acquisition systems in measured pixel uniformity within the radiation field. Because of the Dark-field and Flood-field corrections, the beam profile is expected to be flat within the irradiated region. All the detectors show that the intensity is slightly high at the inner beam (P_1–P_4) and gradually decreasing towards the outer beam of the field (P_5–P_8), with the exception of EPID I whose central response is lower than at the field edges because it had been configured for dosimetry and hence the typical horn-shape in its beam profile. The trend in all other EPIDs is expected since a large field is used for the flood field. The 20x20 cm^2 field used in this experiment suffers a reduced scatter and therefore rolls off faster than the large field. Variations from the centre ROI of 1.0%, 2.2% and 4.5% for square field sizes of 5.0 cm, 7.5 and 10.1 cm were found. Assessments in the penumbra region (P_{avr}) show wider variations in response between different detectors with system-I having an average response of 28.3% compared to 13.5% for system-II.

Table 4- 3. Detectors response at different points (figure 3-1) relative to their central position P_0. P_{avr} is the average of four points in the beam penumbra region. The subscripts I and II indicate whether the detector is a system-I or system-II respectively

Position / EPID	P_1	P_2	P_3	P_4	P_5	P_6	P_7	P_8	P_{avr}
D_{-II}	0.998	0.994	0.987	0.997	0.959	0.957	0.967	0.957	0.164
G_{-II}	0.996	0.997	0.997	0.991	0.955	0.962	0.970	0.962	0.191
I_{-II}	1.036	1.034	1.045	1.050	1.020	1.021	1.032	1.020	0.022
J_{-II}	0.995	0.997	0.978	0.997	0.955	0.959	0.970	0.959	0.145
K_{-II}	0.994	0.994	0.986	0.993	0.957	0.957	0.966	0.957	0.153
A_{-I}	1.005	0.993	0.992	1.005	0.982	0.971	0.985	0.971	0.271
B_{-I}	0.997	0.996	1.001	0.994	0.973	0.971	0.974	0.971	0.362
C_{-I}	0.999	0.990	0.990	0.989	0.963	0.955	0.957	0.955	0.425
E_{-I}	0.998	0.994	0.993	1.003	0.961	0.983	0.979	0.983	0.160
F_{-I}	0.996	0.998	0.997	0.992	0.962	0.965	0.969	0.965	0.192
H_{-I}	0.996	0.997	1.001	0.990	0.975	0.968	0.968	0.968	0.290

The variations in relative pixel uniformity across the EPID detectors were less than 5% within the irradiated field. The effect of over response to low energy x-rays by the indirect a-Si EPID (Vial et al 2008, McCurdy et al 2001) is observed in the penumbra regions of the field, though it is twice as pronounced in system-1 than system-II.

4.1.4 Electronic portal imaging device's relative dosimetry

Figure 4-4 shows a typical step profile acquired from an EPID image with a step-wedge compared to the actual transmission measured with the MapCheck device. For system-I, the standard deviation in relative signal measured by all detectors in the step cross plane profiles beneath the 0.25, 0.50, 0.75, and 1.0 relative thickness in the Right-Left (Gun-Target) direction were 0.4 (0.9), 0.7 (1.2), 0.8 (1.4), and 1.0 (1.5) respectively, while for system-II, they were 0.3 (0.4), 0.5 (0.6), 0.5 (0.9) and 0.6 (1.0) respectively. Theoretically, the EPID and MapCheck results should be the same because they are relative values. The agreement between the EPID and MapCheck measurements was within 2% in the flat area of each step for both systems. In areas of steep dose gradient, at

transitions in the step depth, the maximum distance to agreement of the EPID to MapCheck is 2 mm. The residual longitudinal, vertical, lateral and rotational misalignment of the wedge with the EPID detector/MapCheck and the primary beam direction cannot be ignored. Together, these may account for the observed differences.

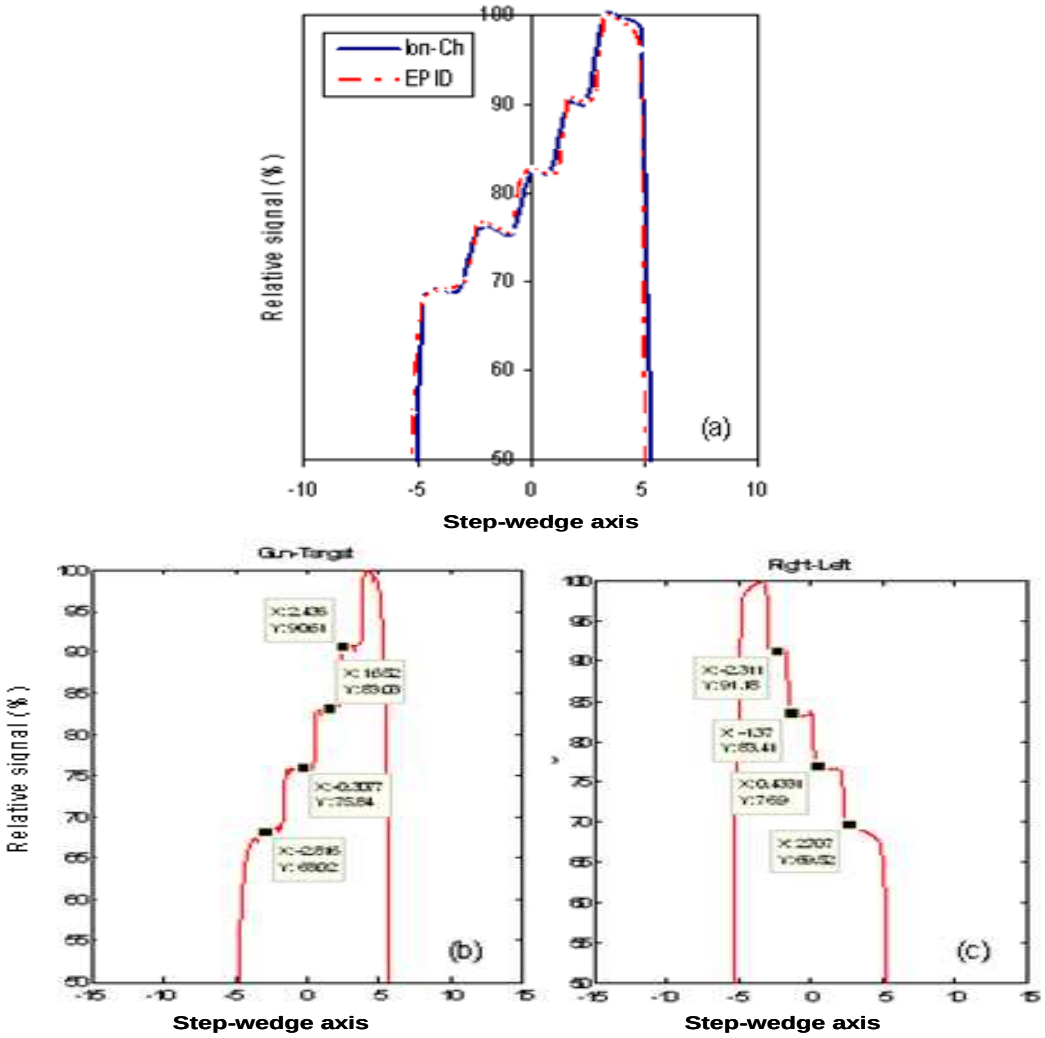

Figure 4- 4. Figure (a) shows typical central profiles comparing an EPID acquired image (dashed line) and actual MapCheck transmission (straight line) with a four step-wedge. A relative signal of 100 indicates an open field transmission; creating a fifth step in the figure. The X and Y figures quoted in boxes of figure (b) and (c) are the numerical values on the horizontal and vertical axes for each point.

4.1.5 Field size dependence

A systematic increase in the average pixel intensity was observed when increasing the field size from 2x2 cm^2 to 20x20 cm^2. For system-I, the relative

increase in detector responses ranged from 13.6% to 24.4% while system-II ranged from 23.0% - 23.4%. This pixel value dependence on field size is also reflected by the variation in the EPID scatter factors for the two systems. System-II EPID's had almost identical values of coefficients (equation 3.2) and exhibited better data fit to the second order polynomial compared to system-I that showed large variability. Table 4-4 shows the polynomial coefficients A_0, A_1 and $A_{2,}$ and the R^2 values for the different EPIDs.

Table 4- 4. Polynomial coefficients for different EPIDs described in equation 3.2 and the R^2 value for the field size fit.

EPID	System	A_0	A_1	$A_2 x(-10^{-4})$	Field size polynomial fit (R^2 value)
D	System-II	0.787	0.027	6	0.999
G	System-II	0.791	0.027	6	0.999
I	System-II	0.789	0.027	6	0.999
J	System-II	0.787	0.027	6	0.999
K	System-II	0.788	0.027	6	0.999
A	System-I	0.836	0.019	3	0.931
B	System-I	0.743	0.037	12	0.975
C	System-I	0.760	0.036	10	0.977
E	System-I	0.830	0.022	7	0.890
F	System-I	0.777	0.029	7	0.994
H	System-I	0.815	0.037	13	0.877

Figure 4-5 illustrates the relative signal variation with field size. For small field sizes, the EPID readings were slightly lower than the ion chamber readings, and when the field sizes is increased, the EPID readings were higher than the ion chamber readings, as illustrated in figure 4-5 (a). This effect is due to changes in scatter with increased field size. Scatter has a low energy component; its effect on the EPID's phosphor response is enhanced (due to presence of high atomic number component in the phosphor material) compared to an ionisation chamber (Van Esch et al 2004, Greer et al 2003). The results in figure 4-5 (b) for system-I are affected by the poor detector reproducibility of pixel signal.

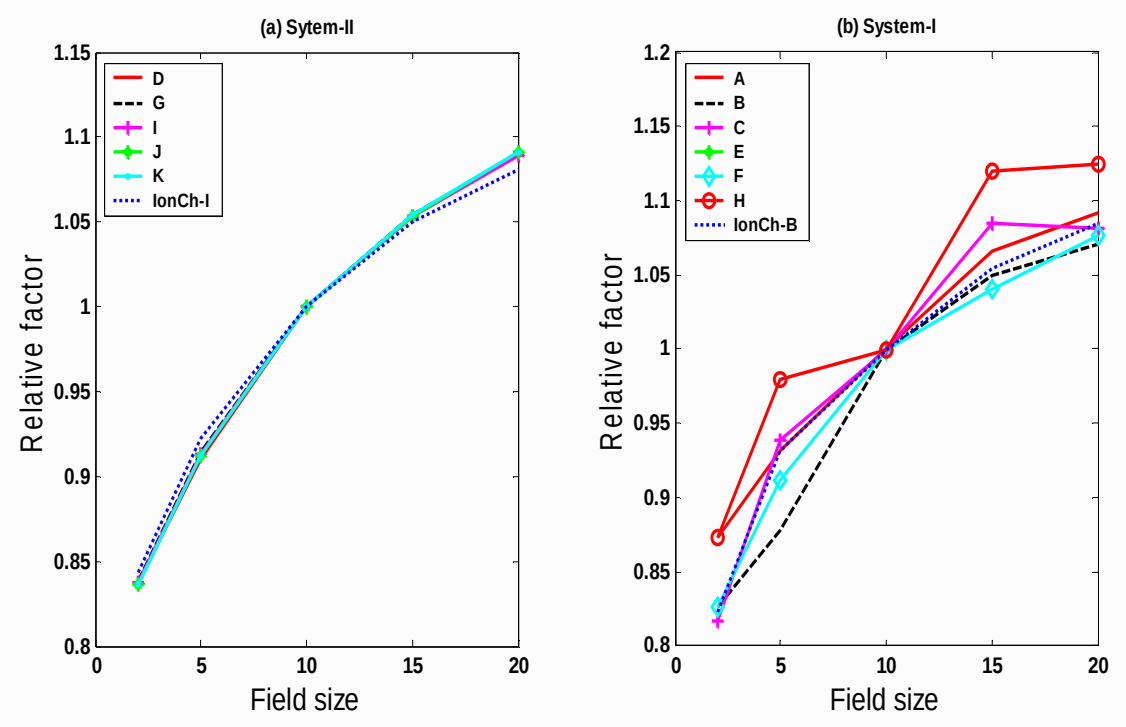

Figure 4- 5. EPID signal variations with field size. The data were normalised to a 10x10cm^2 field size for the two systems. The figure also includes a comparison with an ionisation chamber of accelerator B and I for system-I and system-II respectively.

4.1.6 Doserate influence

The system-II EPIDs show a general decrease in response to increasing doserates at both total monitor units values (20 and 100) used in the investigation. Figure 4-6 (c) shows that the system-II EPID's sensitivity decreased by between 1.0% - 1.8% with increasing the doserates in the range 100-600 MU/min.

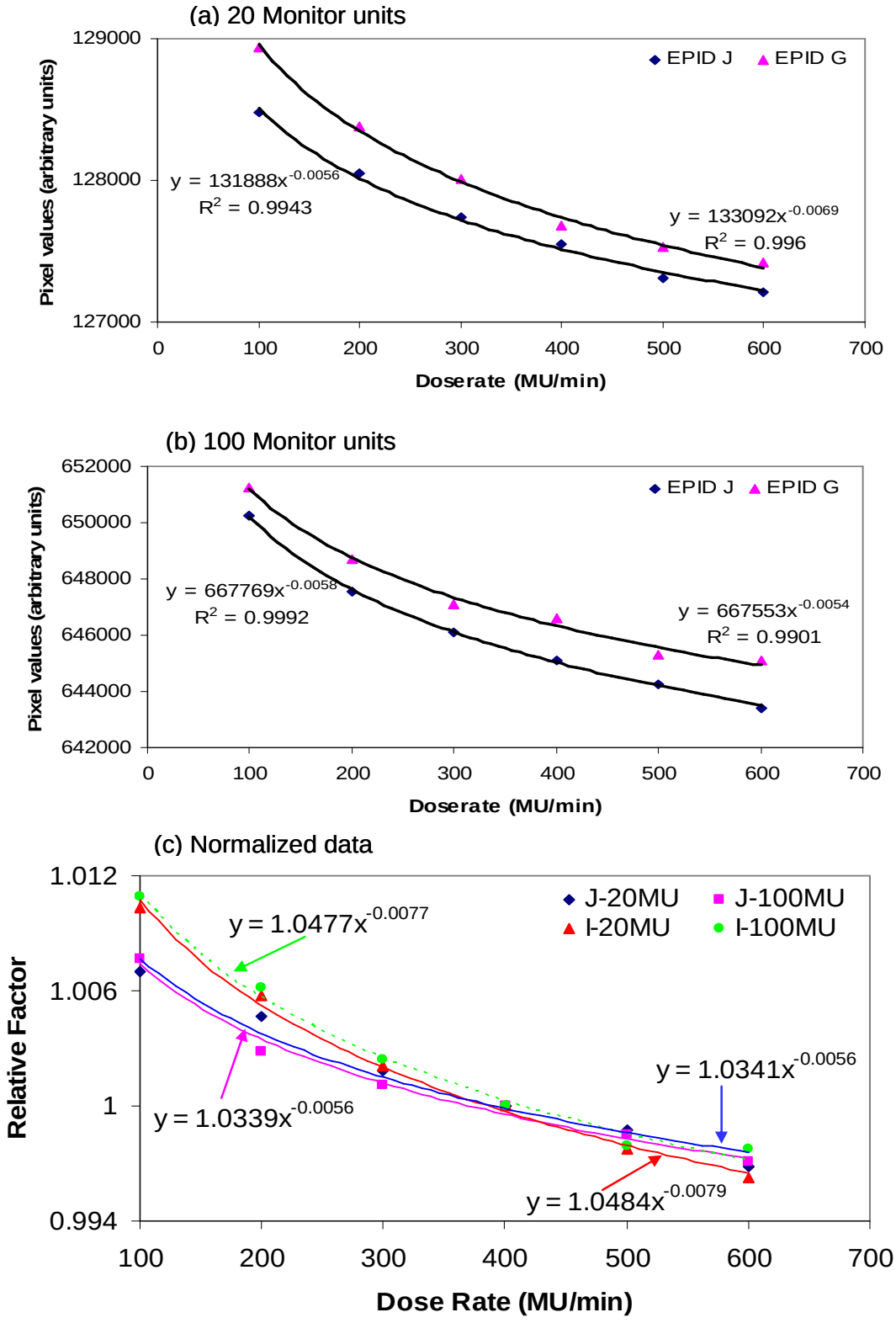

Figure 4- 6. System-II EPIDs response to varying doserates. Figures (a) and (b) show pixel values variation with doserate for total doses of 20 MU and 100 MU respectively. The original data (points) were fitted to a power potential function in equation 3.3 and the lines show the best fit for each EPID. Figure (c) shows data normalised to 400 MU/Min.

The doubling of the dose rate decreased the EPID's response by 0.2% to 0.5%. After fitting the data to equation 3.3, it was established that the EPIDs' non-linearity parameter Δ were within -0.006±0.002 at both 20 MU and 100 MU for all detectors. Figures 4-6 (a) and (b) show typical pixel value variation with doserate, obtained for system-II detectors. Using the normalised data (figure 4-6(c)), the EPIDs sensitivity parameter *K* were 1.048 and 1.034 for EPIDs I and J respectively, independent of monitor unit used. System-I EPIDs did not show any consistent doserate response.

Ideally, the response of any dosimeter $\left(M/Q\right)$ at two different dose rates $\left(dQ/dt\right)_1$ and $\left(dQ/dt\right)_2$ should remain constant (Podgorsak 2005). In reality, the doserate may influence the dosimeter readings and appropriate corrections may be necessary if the detector is to be used for absolute measurements. By increasing the doserates from 100 MU/min to 600 MU/min the sensitivity decreased by up to 1.8% for the system-II detectors. This is due to the synchronisation of the linear accelerator pulses and several preset parameters (described in section 3.1) in the IDU-20/IAS3 systems. The EPID response as a function of dose rate should be accurately determined especially in dynamic treatments. Therefore, the use of a single dose rate calibration curve cannot yield completely accurate results. Although it is well known that during IMRT delivery the accelerator doserate may vary and the EPID response will vary accordingly, in reality, there is very little variation in dose rate at 400 MU/min. Beam hold-offs that relate to the mobility of the MLC leaves to keep up with the beam should not be seen. Other studies assessing doserate effects on EPID have yielded varying results, suggesting that the response is dependent on individual vendor, detector and model. The Varian system-II EPIDs studied here show less doserate dependency than has been reported for the Elekta iView^{GT} (Winkler et al 2006). They reported changes in detector sensitivity of between 5%-11% in the doserate range 50-540 MU/min. The work done by Mohammadi and Bezak (2006) on the Varian SLIC EPID indicated that EPID response increased with increasing doserates, in the range 50 – 600 MU/min, in contrast to the results described in this work for the Varian system-II, that shows a decrease in response with increasing doserates. Similar to the Varian system-II detector, the Siemens Perkin-Elmer XRD EPID exhibited response variations of ≈ 1% measured between 50 MU/min and 300 MU/min doserates (Chen et al, 2006).

4.1.7 Directional dependence

Figures 4-7 (a) and (c) show typical pixel responses at different gantry angles and collimator angles of 0^0 and 90^0 for two system-II EPIDs. Figures 4-7 (b) and (d) show their respective data normalised to those at gantry angle zero. The relative sensitivity normalised to gantry angle zero ranged between 0.99 – 1.01 (within 2%). These departures from the values at gantry angle 0^0 are sufficiently small, that they may be considered insignificant. The insignificant variation in sensitivity with gantry angle shown in the two cases was exhibited by all system-II detectors. The work done by Parent et al (2007) and Moore and Seibers (2005) reported on how the mechanical parameters relative to the gantry can affect the response of the Varian a-Si EPID. The variations were associated with the mechanical response of the EPID to changes in the accelerator gantry angle. Clarke et al (2008) used a similar approach to measure MLC defined field sizes at varying gantry angles using an a-Si EPID. All these studies indicated that the deviations from those at 0^0 were not differentiable from the short term variations and may be considered insignificant.

(a)

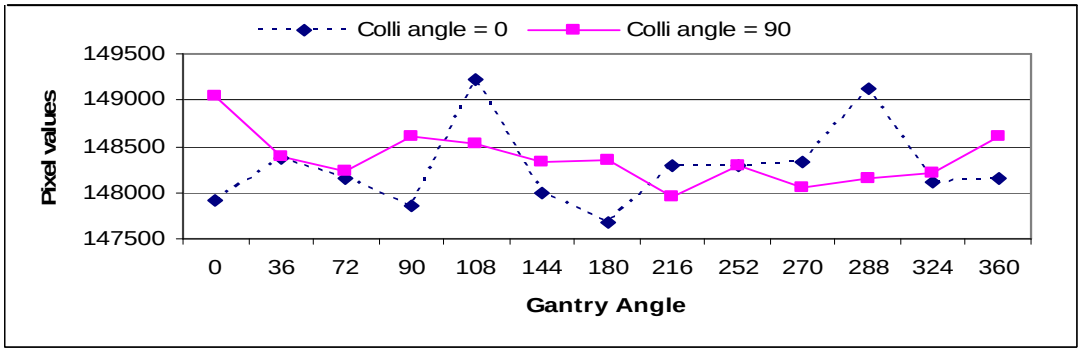

(b)

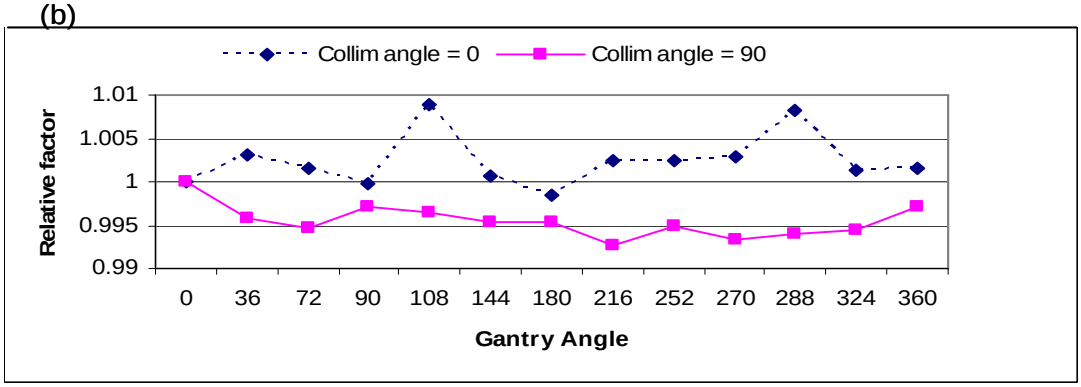

(c)

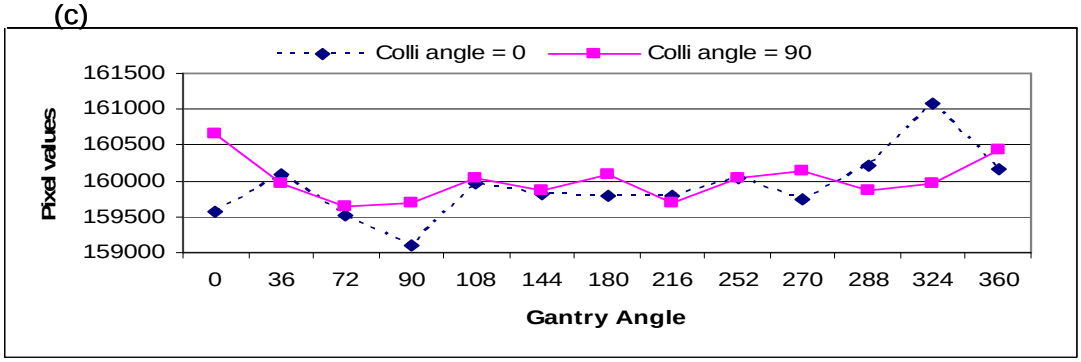

(d)

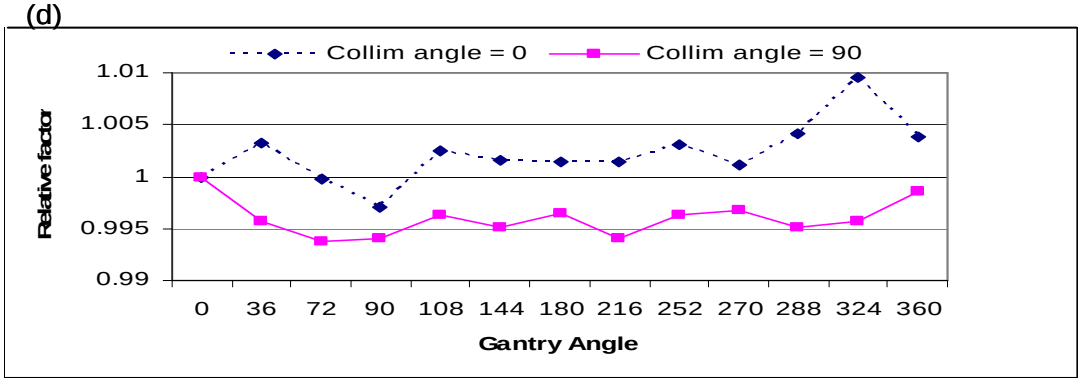

Figure 4- 7. Figures (a) and (c) shows pixel responses at different gantry angles for EPIDs G and J respectively, while figures (b) and (d) show their data normalised to those at gantry angle zero.

4.1.8 Further image profile analysis and memory effects

Figure 4-8 shows typical post irradiation effect on the EPID image profiles indicating the memory effect of the EPID, which manifests itself as an increase in pixel value for the 20 x 20 cm^2 field size in the region of a previous 5 x 5 cm^2 irradiation field. The percentage difference for each EPID was calculated as the signal enhancement at the centre (5 x 5 cm^2) within the 20 x 20 cm^2 field size compared to the signal for a 20 x 20 cm^2 taken after five minutes. Measurement of the EPID detector memory effect for system-I ranged from 1.1% to 1.8% with a mean of 1.4% while system-II ranged from 0.3% to 1.4% with a mean of 1.0%.

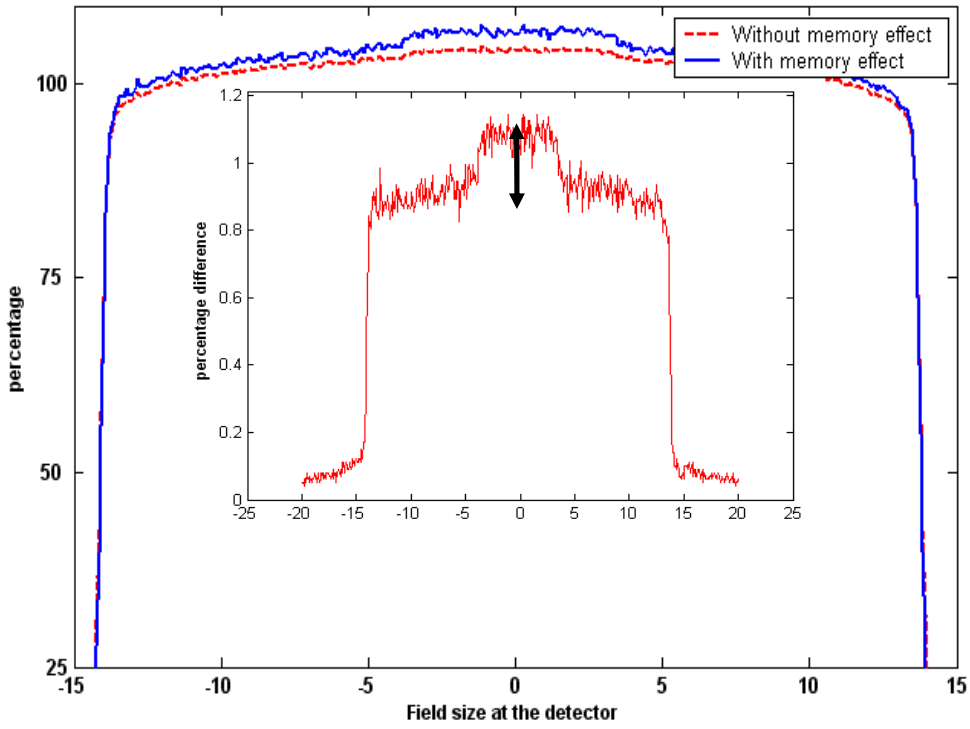

Figure 4- 8. Central image profiles indicating post irradiation effect on the EPID. The image profile (continuous line) was acquired within 12 seconds after 50 MU to a 5x5 cm^2 field (dashed line) taken earlier. The profile in the inset is the difference between the image profiles. The double arrow shows the signal enhancement at the centre (5 x 5 cm^2) within the 20 x 20 cm^2 field size

The EPID memory effect results were independent of the two acquisition systems and in agreement with previous studies performed on Varian EPIDs by Greer et al (2003) and Van Esch et al (2004). These studies indicated a residual increase in the central irradiated region of about 1%. Winkler et al (2005) used similar settings (doses, energy, field sizes and time interval) on the Elekta

iView^{GT} to those we used. They indicated a local modification of EPID response of up to 6% that may rise up to 16% with increase in photon energy.

Figure 4-9 shows integrated image profiles for different EPID detectors obtained at various monitor units, constant doserate of 400 MU/min and 10x10 cm^2 field size. The images were analysed by obtaining the mean of the two central pixel arrays in the Left-Right direction of the detectors. It should be noted that the profiles shown in this figure are related to the mean pixel value parameter reported by the EPID system in its un-calibrated state, and are thus not directly related to the SMUR data in figure 4-3. The SMUR is dependent on both mean pixel value and on the acquired number of frames. All the EPID profiles showed varying dependencies on MU accelerator settings. System-I images showed wider variations compared to system-II images. These varying image responses emphasise the necessity of individualised calibrations for each EPID if they are to be used for dosimetry purposes in agreement with previous studies (Winkler and George 2006).

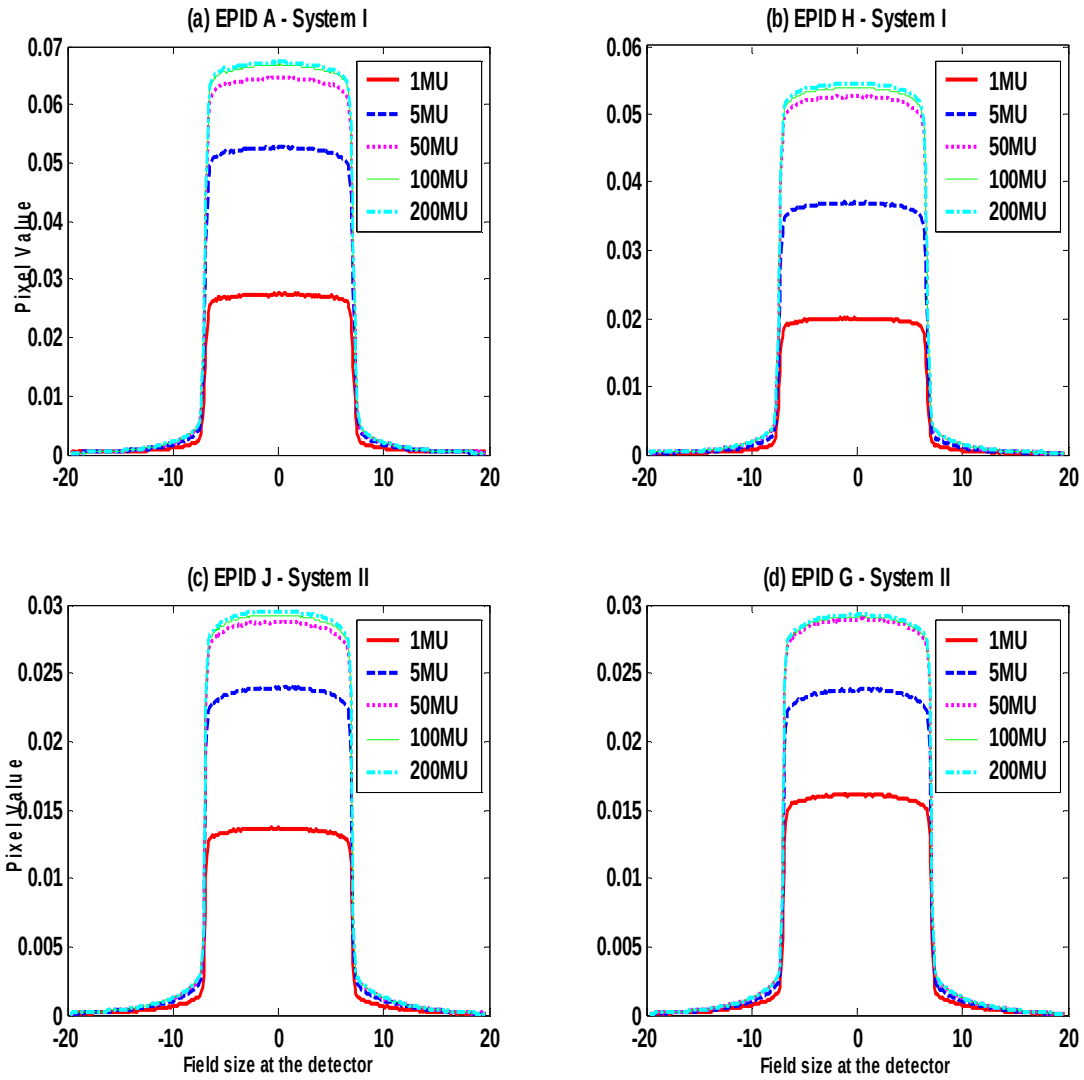

Figure 4- 9. Typical integrated image profiles for different EPID detectors obtained at different MU, constant doserate of 400 MU/min and 10x10 cm^2 field size at isocentre. The images were analysed in their absolute sense without taking into consideration the averaged number of frames at each set MU.

There are some differences in EPID response visible for the low MU fields for both systems in figure 4-9. The root cause is the under response at shorter irradiation times together with ghosting effects. Other possible causes are the nonlinearity of the electronics and sensitivity variations between different EPID panels and differences in accelerator outputs.

Figure 4-10 illustrates profiles of images acquired by the two systems at 5 and 50 MU. Figure 4-10(b) shows a 15-25% tilt in the T-G direction cross plane profiles at

5MU for system-I which is absent at 50 MU for the same detectors (figure 4-10d) or completely absent for system-II, as illustrated in figures 4-10(a) and 4-10(c).

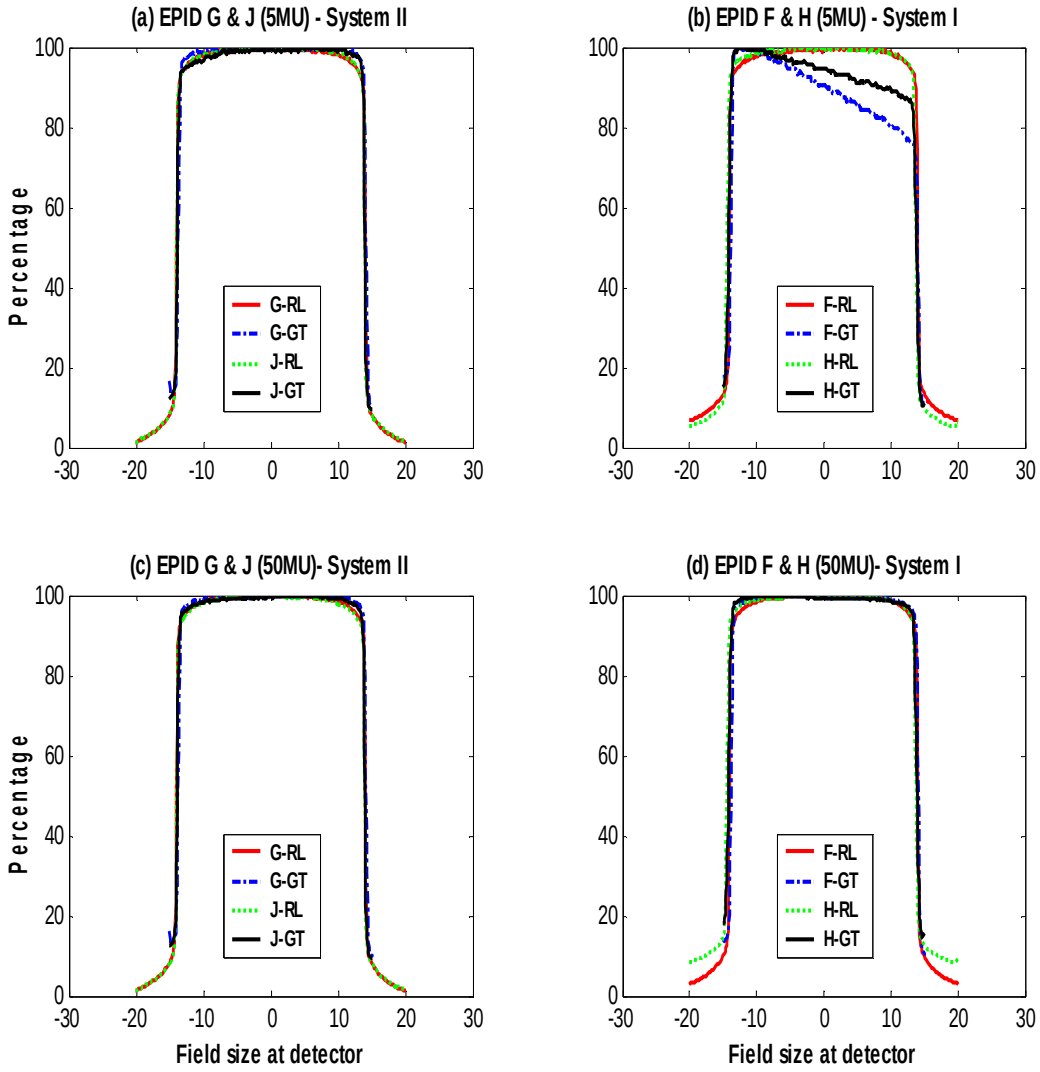

Figure 4- 10. Cross profiles images of four EPIDs acquired at 5 and 50 MU in the transverse (L-R) and radial (G-T) planes of the linear accelerator20x20 cm^2 field size at isocentre. System-1 profiles (b and d) show dose (MU) dependence in the G-T direction

The results indicate limitations of system-I in terms of dose linearity. The systems acquire data rows sequentially starting from the gun side scanning towards the target direction. At lower MU, the pulsed nature of the radiation delivered causes significant fluctuations from one frame to another. Accelerators start off at lower doserate and for lower MU; the start side of the readout frame (gun side) will read less dose accounting for the gradients in figure 4-10. It is possible that the acquisition speed of system-I and the exposure

duration at lower MU enhance the effect. Figure 4-10 suggests that the older (system-I) EPIDs may not be suitable for step-and-shoot IMRT verification (an important application of portal dosimetry) that frequently contains low MU segments.

The inconsistencies in SMUR (figure 4-3) and the imager effect demonstrated in figures 4-10 were investigated further by extracting data from the "treatment field history" file of the Varis system for about 2.7 million treatment records of all our machines since 2001, when the first EPID was commissioned. The aim was to find out if there is any correlation between the EPID cumulative dose/age and its performance. From the database, the actual linear accelerator monitor units delivered for each treatment field when an EPID image was acquired were obtained, from which the cumulative dose to the imagers could be calculated. Table 4-5 summarises EPID dose related data extracted from the "treatment field history" file of the Varis system. As expected the Linac and imager doses increase proportionally to the period the accelerator has been in clinical use. The percentage of dose delivered with the imager out, ranged between 12.2 – 18.7% with mean 14.2%.

Table 4- 5. Different EPIDs, their use period (months) and corresponding approximate dose (only corrected for inverse square law) from the Varis system database

EPID	EPID use (Months)	Linac Dose (KGy)	Imager Dose (KGy)	Imager Dose (corr. ISL)	Imager Dose/ Month
A	86	212.9	39.8	25.5	0.30
B	86	222.3	36.7	23.5	0.27
C	82	188.1	17	10.9	0.13
E	75	137.4	17.6	11.3	0.15
F	32	56.9	7.7	4.9	0.15
H	32	70.7	8.6	5.5	0.17
D	34	78.8	10.5	6.7	0.20
G	32	44.9	6.2	4.0	0.12
I	17	25.4	3.8	2.4	0.14
J	17	32.8	4.9	3.1	0.18
K	10	16.5	2.7	1.7	0.17

System-I EPIDs ageing due to radiation could be another factor causing degraded results. Hee et al (2002) reported that radiation damage affects the leakage current of photodiodes and the effect showed a linear dependence on absorbed dose. This may decrease the whole system performance, although it also depends on the aging effects of other components. However the results for the imager dose and imager dose per month were inconsistent with the EPID's reproducibility and SMUR and no conclusion could be drawn.

The overall results indicate the superiority of system-II, due to its lower noise readout electronics, higher readout rates and faster data acquisitions compared to system-I. The differences in the system synchronisation between the two systems may also contribute to the observed differences in the dosimetric characteristics and performance, especially for the lower MU. Greer (2007) studied the effects of the two Varian acquisition modes at different MU. This study indicated that the EPID image profiles were similar at higher monitor units and differences were noted in profiles acquired with less than 10 MU.

4.1.9 Electronic portal imaging devices as a dosimeter

A prerequisite for any clinical dosimetric application is a detailed understanding of the detector's dose-response behaviour. Figure 4-11 shows one of the system-II EPIDs (J), comparing the pixel value response with ionisation chamber measurements at varying monitor units. Results in figure 4-11 (a) are presented on linear scale where the abscissa represents the accelerator MU. The left and right ordinates represent the EPID pixel and ionisation chamber responses respectively. Figure 4-11 (b) shows the same data on a logarithmic scale, including the relative response (ratio of Ionisation chamber signal to that of the EPID). The EPID and ionisation chamber responses are parallel to each other and the relative response is practically constant at all monitor units, which re-affirms that the EPID image signal, if calibrated correctly, can be matched to that of the ionisation chamber. The ionisation chamber is the gold standard radiation detector for measurement of absorbed dose.

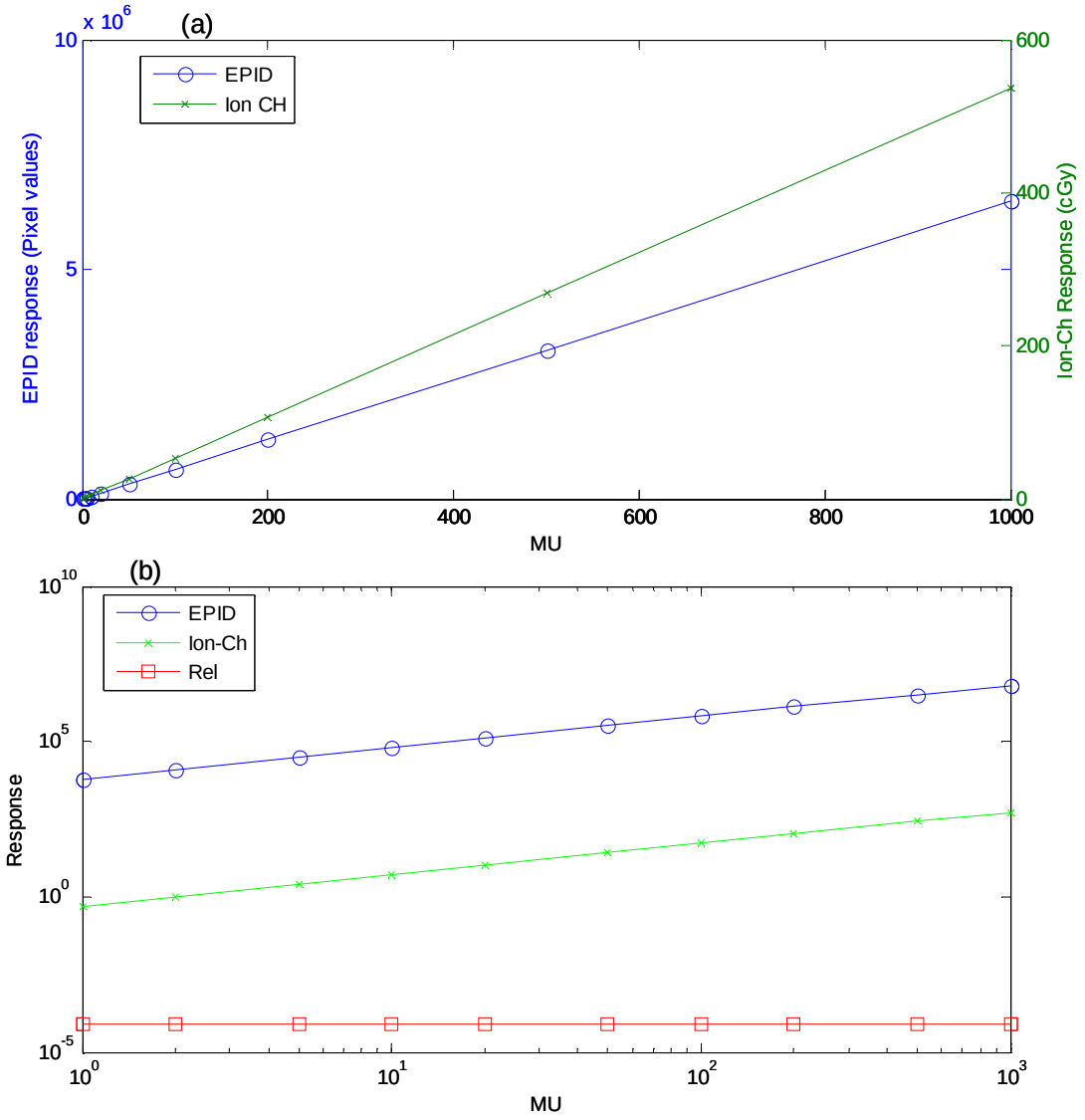

Figure 4- 11. Comparison of EPID response with ion chamber as a function of MU

The intensity of a photon beam is reduced as the absorbing material thickness is increased. Figure 4-12 shows the reduction in photon intensity measured with the EPID and ion chamber responses when solid water phantom materials of various thicknesses were placed between the source and the detectors (EPID and ion chamber). At each phantom thickness, both detectors were exposed at same radiation conditions. Both the EPID and ion chamber signals were acquired on the central axis, and the data for each detector normalised to those when there is no absorbing material (thickness = zero).

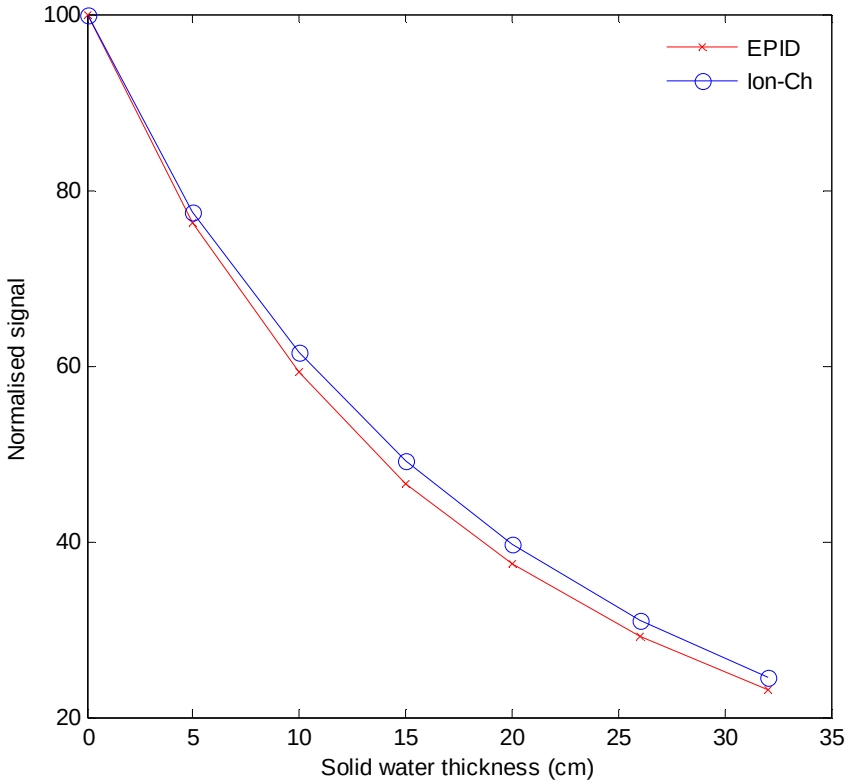

Figure 4- 12 EPID versus ion chamber response with solid water thickness

Increasing the solid water thickness both attenuates and hardens the beam. Because the EPID is more sensitive to lower energy photons, its response decreases more rapidly than the ion chamber as a function of attenuator thickness. Another possible explanation for this effect could be that low-energy scatter (secondary photons) is generated in the attenuating material, affecting the EPID response.

4.2 Water equivalent path length measured with an EPID

4.2.1 Variations of the fitting parameters A and B

Figure 4-13 shows profiles extracted from the fitting parameter matrices A(i,j) and B(i,j) along the left-right direction of the EPID. The results in figures 4-13(a) and (b) show the symmetrical variations of B(i,j) and A(i,j) with off-axis distance for two 6 MV and 16 MV beams respectively. The figures show that the

parameters are almost the same (within 1%) for two accelerators at the same 6 MV beam energy and decrease when the beam energy is increased to 16 MV. The B(i,j) parameter, which is theoretically the linear attenuation coefficient, has minimum values of 0.052±0.001 cm^{-1} and 0.024±0.0005 cm^{-1} for 6 MV and 16 MV beams respectively. These minima occur in the centre of the field, with values of B(i,j) gradually increasing with increasing distance from the centre up to a relative value of 1.2 and 1.3 of their minima for both energies respectively. On the other hand, the parameter A(i,j) has its maximum values of -3.0±0.2 $x10^{-4}$ cm^{-2} and -0.2±0.03 $x10^{-4}$ cm^{-2} for 6 MV and 16 MV beams respectively in the centre of the field, gradually decreasing with increasing distance from the centre.

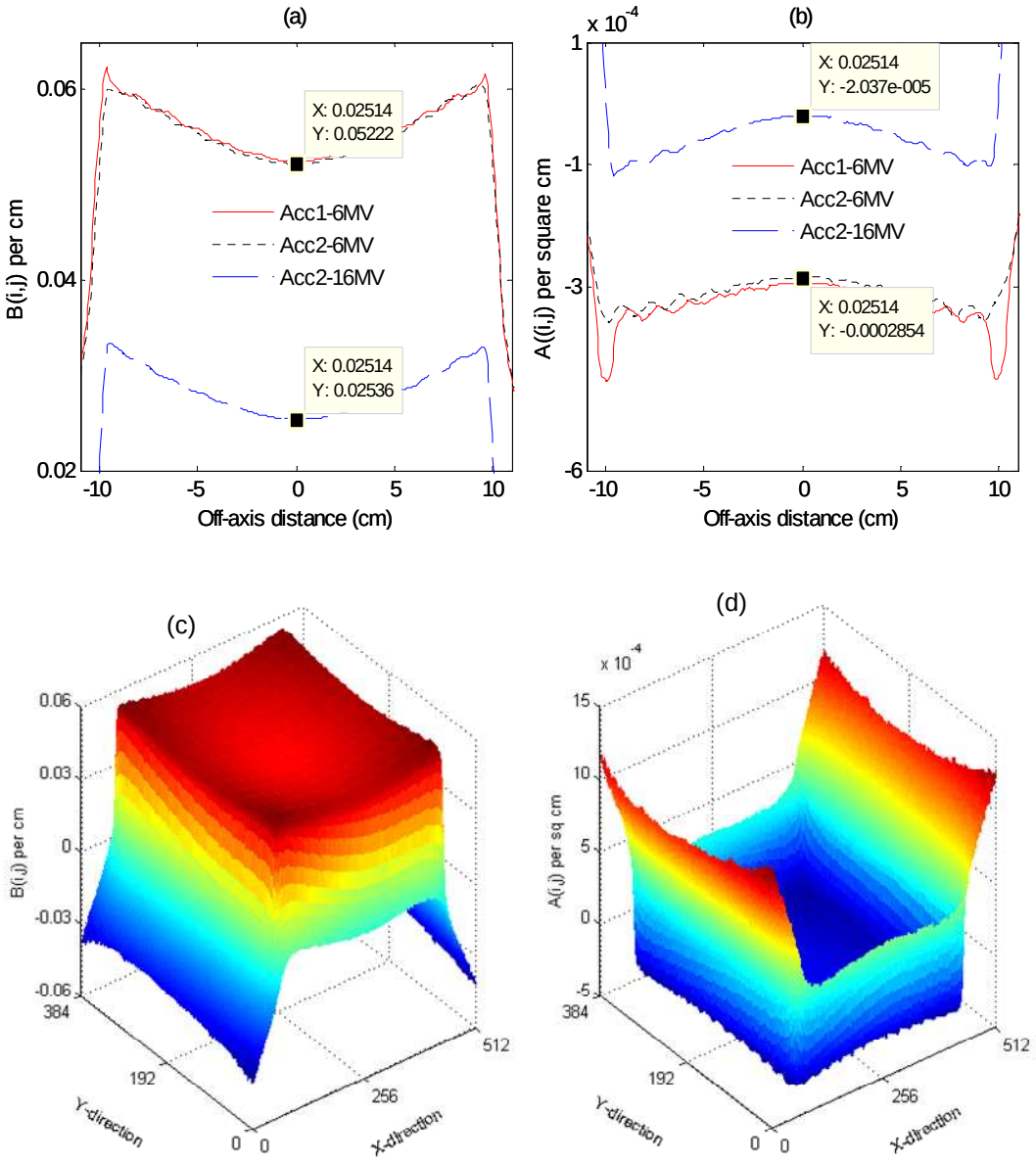

Figure 4- 13. Profiles extracted from the fitting parameter matrices A(i,j) and B(i,j) along the left-right direction of the EPID. Figures (a) and (b) show the symmetrical variations of B(i,j) and A(i,j) with off-axis distance for two 6 MV and 16 MV beams respectively. The X and Y (at each point, the Y value is either the A(i,j) or B(i,j) value) quoted in boxes are numerical values on the horizontal and vertical axes for each point. Figures (c) and (d) show a 3D visualisation of the B(i,j) and A(i,j) fitting parameters respectively.

The parameter B(i,j) is the linear exponent of the expression describing the attenuation of the photon beam as it traverses material upstream. It increases as the distance from the centre of the EPID orthogonal to the beam central axis increases. The trend of parameter B(i,j) is caused by the flattening filter being cone shaped. The central part of the beam travels through more material and is more filtered than the edges of the beam. Therefore the average photon energy through the centre is higher. The results indicates that B(i,j)

decreases with increasing beam energy from 6 MV to 16 MV. This is because of the attenuation coefficient components due to photoelectric and Compton (dominant interaction processes at radiotherapy beam energies) effects being inversely proportional to energy (Khan 2003). Monthly repeat of imager recalibration over a four-month period indicated that A(i,j) and B(j,j) could be reproduced to within 2%, in agreement with Kairn et al (2008). The value of the attenuation coefficient, B(i,j) in our case at the centre of the EPID is within ±3% compared to other studies (Allen 1999, McDonough et al 1999 and Vanetti de' Palma et al 2005). Backscatter from components of the EPID support arm downstream from the detector have been found to influence the signal by up to 5% (Greer et al 2007, Ko et al 2004). In the derivation of the fitting coefficients A(i,j) and B(i,j) (equation 3.4), the EPID signals M(i,j) obtained after imaging solid water phantoms are divided by the image signal obtained without any material in the beam $M_0(i,j)$. Also in equation (3.12), the image signals $M_1(i,j)$ whose EPL are to be established are divided with $M_0(i,j)$ term. This pixel by pixel division should theoretically eliminate the support arm effect; Figure 4-13 shows that the calibration coefficient profiles in both directions are not distorted due to the support arm; hence the support-arm-backscatter correction is not required when using the quadratic calibration technique for EPID dosimetry.

4.2.2 The phantom scatter and field size correction factors

As discussed in section 3.2.3 above, scatter and field size corrections are required for the EPID to predict thickness at any other field other than the reference field. Figure 4-14 shows the variation of correction factor CF with field size and thickness, measured with an EPID for a 6 MV beam. For any field other than the reference field size, CF increases with increasing phantom thickness. This study is limited to field size of 21.5x21.5 cm^2, as the maximum that can be imaged with EPID imager positioned 40.0 cm below the isocentre, without irradiating the electronic components of the IDU.

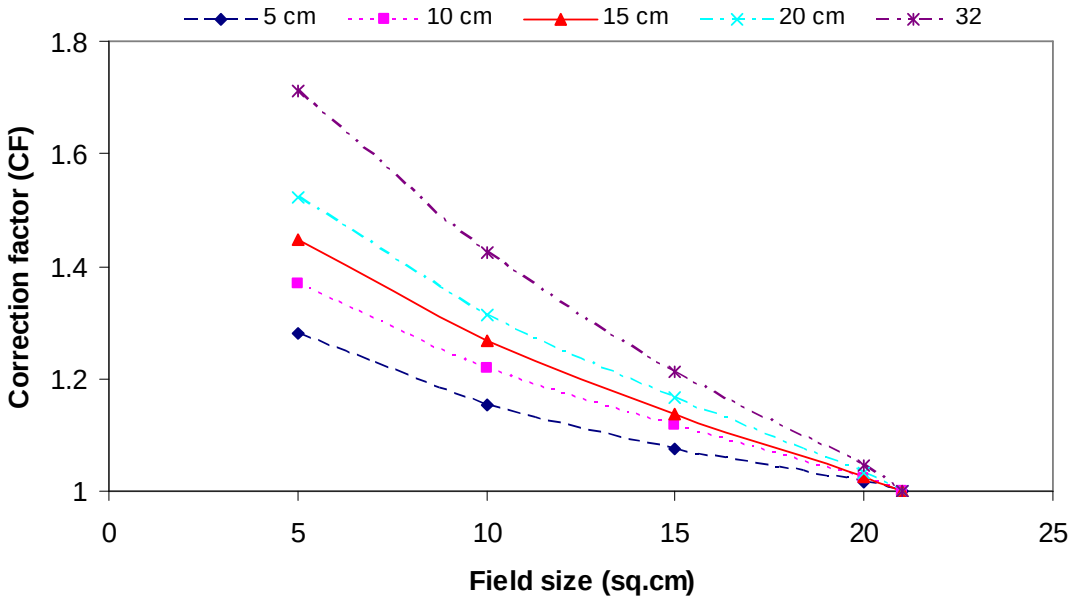

Figure 4- 14. Correction factor variations as a function of field size for phantom thicknesses 5cm, 10cm, 15cm, 20cm, and 32 cm for 6 MV beam

4.2.3 Monitor unit effects

Figures 4.15 (a), (c) and (e) show the variation of applied MU with system-II EPID response (linearity) for square field sizes of 5, 10 and 20 cm, measured at 400 MU/min dose rate and thicknesses of 10, 20 and 32 cm respectively. The results indicate the generally expected trend, where at any particular thickness the response increased with increasing field size, and decreased with increasing phantom thicknesses. Figures 4.15 (b), (d) and (f) show SMUR variations computed for the same data used in figures 4.15 (a), (c) and (e) respectively that exposes significantly reduced values at lower MU. Figures 4.15 (g) and (h) show a repeat of linearity and SMUR but measured at a reduced dose rate of 100 MU/min for solid water thickness of 20 cm. The linearity response at 100 MU/min as expected remained unchanged because the total delivered doses are independent of doserates, but the SMUR significantly increased for lower MU by about 3% and remained practically the same at higher MU.

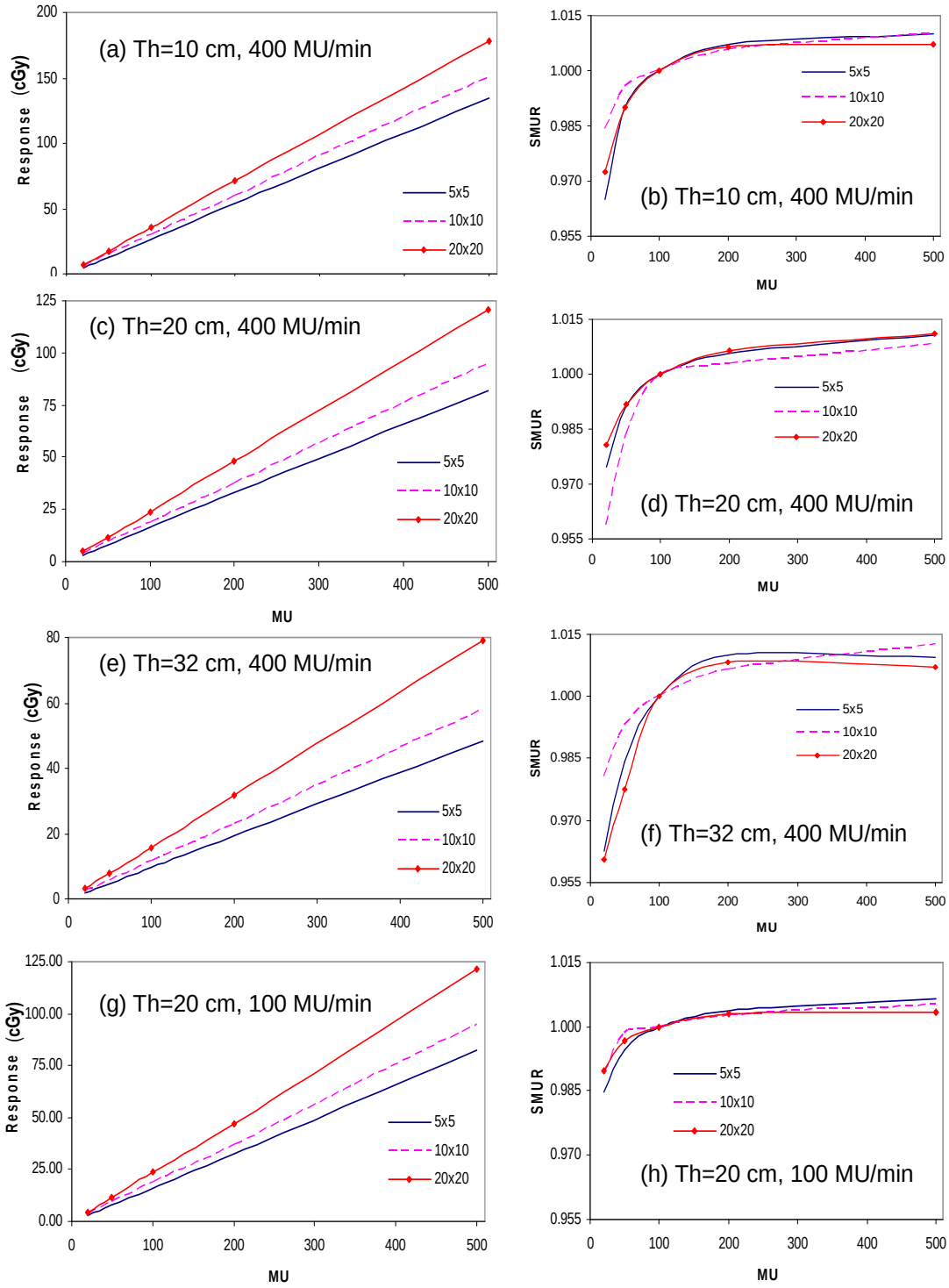

Figure 4- 15. Figures (a), (c) and (e) show system-II linearity for thicknesses 10 cm, 20 cm and 32 cm measured at 400 MU/min respectively, while figures (b), (d) and (f) are their corresponding SMUR. Figures (g) and (h) show linearity and SMUR respectively for thickness 20 cm measured at 100 MU/min.

The accurate determination of EPL is essential in the prediction of dose by EPID. For the EPID to predict dose effectively, it is desirable for the EPL to be precise and independent of delivered number of monitor units. Ideally the response of any radiation detector should be proportional to MU for both open and MLC blocked beams (Podgorsak 2005). The concept of linear relationship suggests that two quantities are directly proportional to each other for all situations, such that the ratios between corresponding entities are practically the same. However analysis of the SMUR for the same data used for the linear relationship results, revealed lower values at MU below 50, in agreement with McDermott, et al (2006). This implies that at lower MUs, the EPID response and MU variations are not perfectly proportional. These results can be correlated with that in figure 4-9, explained by under response at shorter irradiation times together with ghosting effects. The SMUR at a lower dose rate (100 MU/min) was found to be more consistent than that at 400 MU/min, indicating that the effect may be due to dead time within the imager system. Dead time in frame acquisition can result in reasonable loss of signal (Greer et al 2003). The imager has start-delay which is fixed and will cause a greater dead-time effect at low exposures. Under practical consideration the SMUR measured at 400 MU/min dose rate was only dependent on MU but not field size and phantom thickness. Hence a single look-up table depending on image MU was included in the EPL determination.

4.2.4 Measured and calculated Percentage Exit Thickness Dose (PETD)

Figure 4.16 shows a comparison of the measured and calculated (equation 3.13) PETD for square field sizes of 5, 10 and 20 cm and depths of 10, 15, 20 and 32 cm. As expected PETD decreases with increasing depth and decreasing field sizes. The results indicate that the differences between the measured and calculated are within 2%.

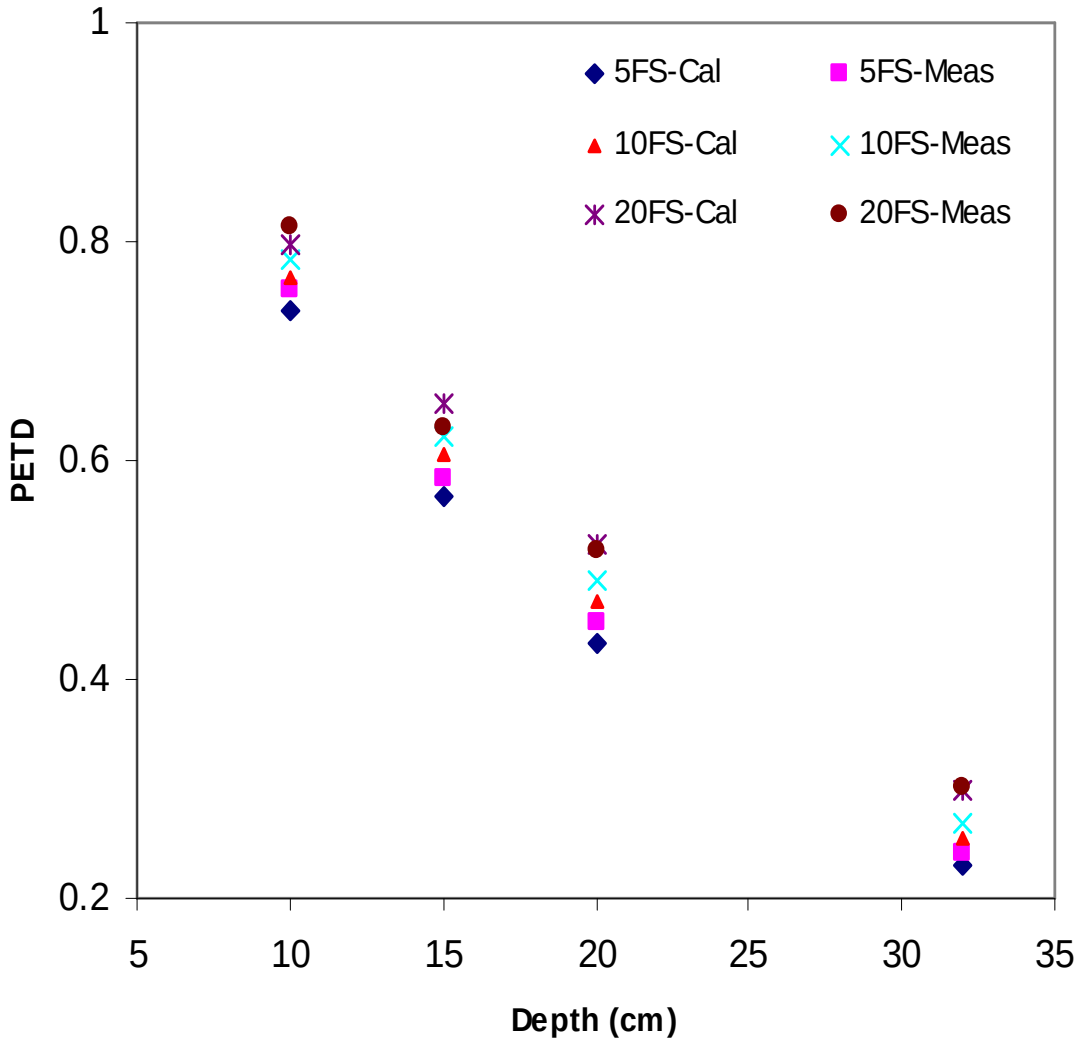

Figure 4- 16. Comparison of measured (meas) and calculated (cal) PETD at selected field sizes (FS) and depths.

4.2.5 Verification of calculation of the equivalent path length

4.2.5.1 Equivalent path length for solid water phantoms

Table 4-6 shows EPL convergence for selected thicknesses and field sizes after 20 iterations. The first item in each column is the initial solution obtained by solving equation 3.8. The values in the tables are the mean pixel value in a 1.0 cm^2 region of interest at the center of image, stored after each iteration. Using equation 3.13, the expected EPL for solid water thicknesses of 10 cm, 20 cm and 32 cm are 9.9 cm, 19.8 cm and 31.7 cm respectively. The results show that convergence to within ± 2mm of the final 20 iteration value was obtained after three – four iterations; hence the algorithm was set to repeat itself five times.

Previous authors (Fielding et al 2002 and Kairn et al 2008) reported convergence in thicknesses after three – five iterations.

Table 4- 6. EPL convergence for selected thicknesses (Th) and field sizes (FS)

Th10_5x5FS	Th10_10x10FS	Th10_20x20FS	Th20_5x5FS	Th20_10x10FS	Th20_20x20FS	Th32_10x10FS
17.7030	14.8072	10.6473	31.8328	27.5960	20.6745	44.0011
7.2775	8.7809	9.8814	14.5356	17.4274	19.8686	29.7312
10.6351	10.2140	9.9055	20.9465	20.1876	19.8907	32.0745
9.6628	9.8602	9.9038	19.3310	19.5832	19.8900	31.6787
9.9465	9.9401	9.9040	19.8477	19.7252	19.8901	31.7408
9.8602	9.9199	9.9040	19.7096	19.6923	19.8901	31.7291
9.8864	9.9249	9.9040	19.7471	19.7000	19.8901	31.7313
9.8784	9.9236	9.9040	19.7370	19.6982	19.8901	31.7309
9.8808	9.9240	9.9040	19.7397	19.6986	19.8901	31.7310
9.8801	9.9239	9.9040	19.7390	19.6985	19.8901	31.7310
9.8803	9.9239	9.9040	19.7392	19.6985	19.8901	31.7310
9.8802	9.9239	9.9040	19.7391	19.6985	19.8901	31.7310
9.8802	9.9239	9.9040	19.7391	19.6985	19.8901	31.7310
9.8802	9.9239	9.9040	19.7391	19.6985	19.8901	31.7310
9.8802	9.9239	9.9040	19.7391	19.6985	19.8901	31.7310
9.8802	9.9239	9.9040	19.7391	19.6985	19.8901	31.7310
9.8802	9.9239	9.9040	19.7391	19.6985	19.8901	31.7310
9.8802	9.9239	9.9040	19.7391	19.6985	19.8901	31.7310
9.8802	9.9239	9.9040	19.7391	19.6985	19.8901	31.7310
9.8802	9.9239	9.9040	19.7391	19.6985	19.8901	31.7310

Figure 4-17 shows the EPL profiles calculated from EPID images for selected thicknesses of solid water phantoms. The images were acquired at same 100 MU at various field sizes. The profiles in figure 4-17 (a-d), extracted in both the X-direction (solid lines) and Y-direction (doted lines), were acquired with solid water of thicknesses 5.0, 10.0, 20.0 and 32.0 cm; and field sizes of 10x10 cm^2, 15x15 cm^2, 20x20 cm^2 and 15x15 cm^2 respectively. From equation 3.13, the EPL for these thicknesses would be 4.95, 9.90, 19.80 and 31.68 cm respectively. The results in this figure indicate that EPID-measured EPL agrees with that calculated using the known physical thickness and electron density (equation 3.13) to within +/- 2mm. Monthly repeat of imager recalibration and subsequent EPL recalculation over a four-month period indicated that for a homogeneous solid water phantom, EPL could be reproduced to within +/- 2mm (80% of the central field). Towards the field edges, the EPL tends to increase due to the beam penumbra. The sharp increase in EPL at the field edges, results in the expected decrease in exit dose in these regions.

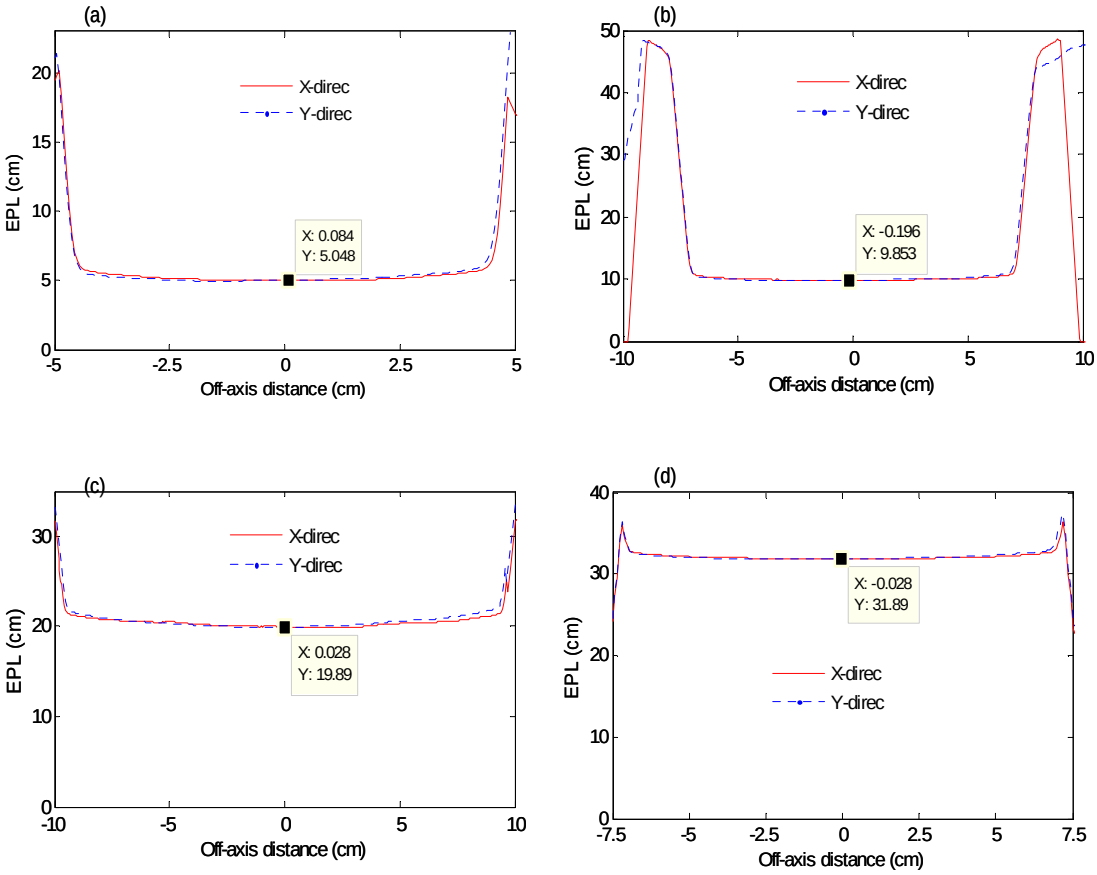

Figure 4- 17. EPL profiles from EPID images for selected solid water phantom thicknesses and acquired at different field sizes. The X and Y (at each point, the Y value is the EPL) quoted in the boxes are numerical values at the centre on the horizontal and vertical axes for each point.

4.2.5.2 Equivalent path length for solid water phantoms with varying monitor units

Figure 4-18 demonstrates the EPL for different thicknesses of solid water calculated before and after MU corrections, at different field sizes. The results show that at 20 MU, variations in EPL of up to 12 mm can occur between the corrected and uncorrected values.

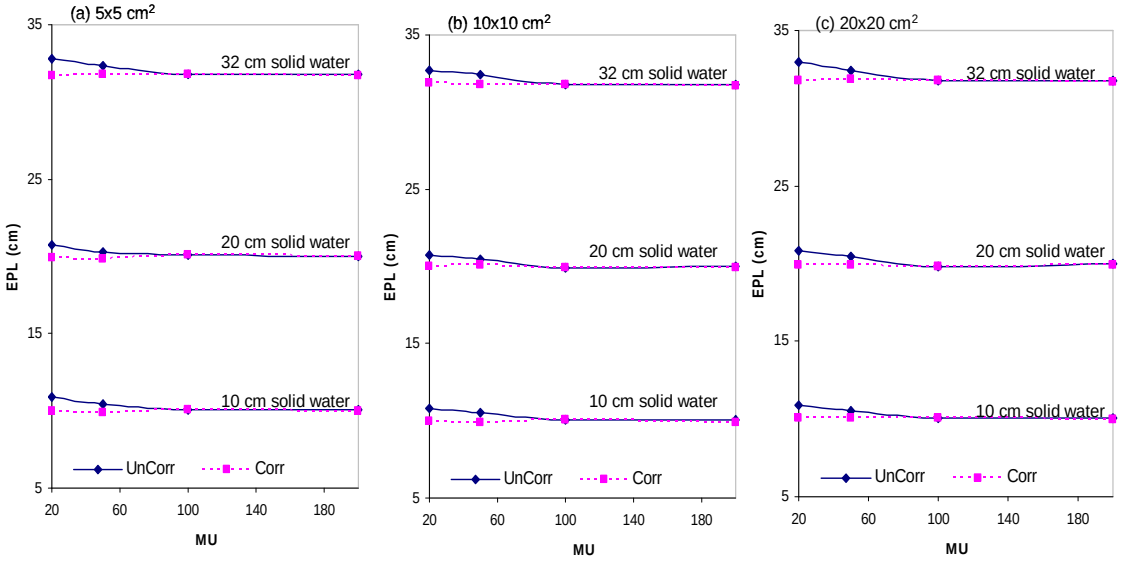

Figure 4- 18. Pre-MU (UnCorr) and post-MU (Corr) EPL (calculated before and after MU correction respectively) for 10 cm, 20 cm and 32 cm solid water; and field sizes of (a) 5x5 cm^2, (b) 10x10 cm^2 and (c) 20x20 cm^2.

Comparison of the pre-MU and post-MU EPL (EPL calculated before and after MU correction respectively) in figure 4-18, revealed that the latter gave better conformity with the expected EPL and were independent of both MU and field size. A deviation in EPL of ≈10 mm may result in an uncertainty in PETD of ≈ 3-5% depending on field size, and hence a discrepancy ≈ 3-5% in the exit dose.

4.2.5.3 Equivalent path length for solid water and non water phantoms

Figure 4-19 shows profiles from the calculated EPL of various materials of known thicknesses and relative electron densities for which EPID images were acquired, as described in figures 3-5 (a) and (b), section 3.2.4.1.

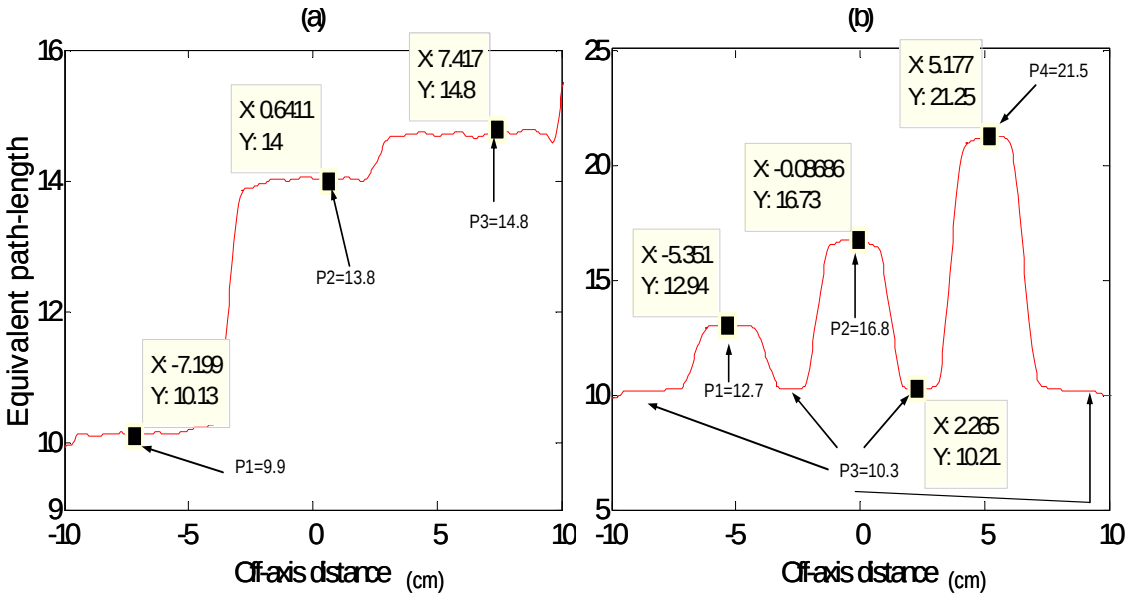

Figure 4- 19. Profiles extracted from centre of EPL maps for (a) slabs of solid water, bone and lung materials positioned in steps, as illustrated in figure 3-5 a. (b) cylindrical lung, solid water and cortical bone materials inserted between two 5cm slabs of solid water as illustrated in figure 3-5 b. The X and Y (at each point, the Y value is the EPL) quoted in boxes are the EPID measured values on the horizontal and vertical axes for each point, while P1, P2, P3 and P4 are corresponding calculated values.

Table 4-6 summarises the results from figure 4-19 obtained after the EPID calibration in comparison to the calculated EPL using equation 3.17. From these results, the calculated and the measured EPL are within ± 3 mm, equivalent to 2% or less in all cases.

Table 4- 7. Summary of the EPL results from figure 4-19 comparing calculated (equation 3.13) and those measured from EPID images

Figure	Position	Material	T_m (cm)	ρ_m	EPL (cm)	Total EPL Calculated (cm)	Measured EPL (cm)
a	P1	Solid water	10	0.99	9.9	9.9	10.1
	P2	Solid water	10	0.99	9.9	13.8	14.0
		Bone	3	1.3	3.9		
	P3	Solid water	10	0.99	9.9		
		Bone	3	1.3	3.9	14.8	14.8
		Lung	3	0.34	1.02		
b	P1	Solid water	10	0.99	9.9	12.7	12.9
		Lung	7	0.4	2.8		
	P2	Solid water	10	0.99	9.9	16.8	16.8
		Solid water	7	0.99	6.93		
	P3	Solid water	10	0.99	9.9	10.3	10.2
		Styrofoam	7	0.05	0.35		
	P4	Solid water	10	0.99	9.9	21.5	21.2
		Cortical bone	7	1.66	11.62		

Calculated and measured EPL are within ± 3 mm for all phantom materials and thicknesses. The uncertainty is comparable to Kairn et al's (2008) Monte Carlo simulated results, where they validated radiological thicknesses measured with an EPID. The accurate determination of EPL is crucial in the prediction of dose by EPID. An increase or decrease in EPL by ~ 1 cm results in a decrease or increase in PETD of ~ 3% and ~5% for field sizes 20cm^2 and 5cm^2 respectively in the thickness-range 10-32 cm. Hence such variations in EPL may result in ~ 3-5% discrepancy in the exit dose (Kavuma et al, 2010).

4.3 Dose comparison

4.3.1 Exit and entrance dose comparison for open fields

Figure 4-20 shows dose profiles for the homogeneous phantom extracted from the centre of the TPS calculated dose and EPID measured dose distributions, demonstrating the effect of PETD, envelope and boundary corrections. The figure shows a comparison of TPS's and EPIDs, entrance (figure 4-20 (a)) and exit (figure 4-20 (b)) dose profiles for a 20x20 cm^2 field, after a 20cm thick solid water phantom is irradiated with 200 MU of a 6 MV photon beam. The uncorrected EPID profiles indicate that the dose at the centre of the field is predicted to within 1%, but remains flat in the entire irradiated region. This is expected experimentally because the EPL for the homogeneous phantom is also flat, but does not reflect the actual dosimetric situations as shown by the TPS profile.

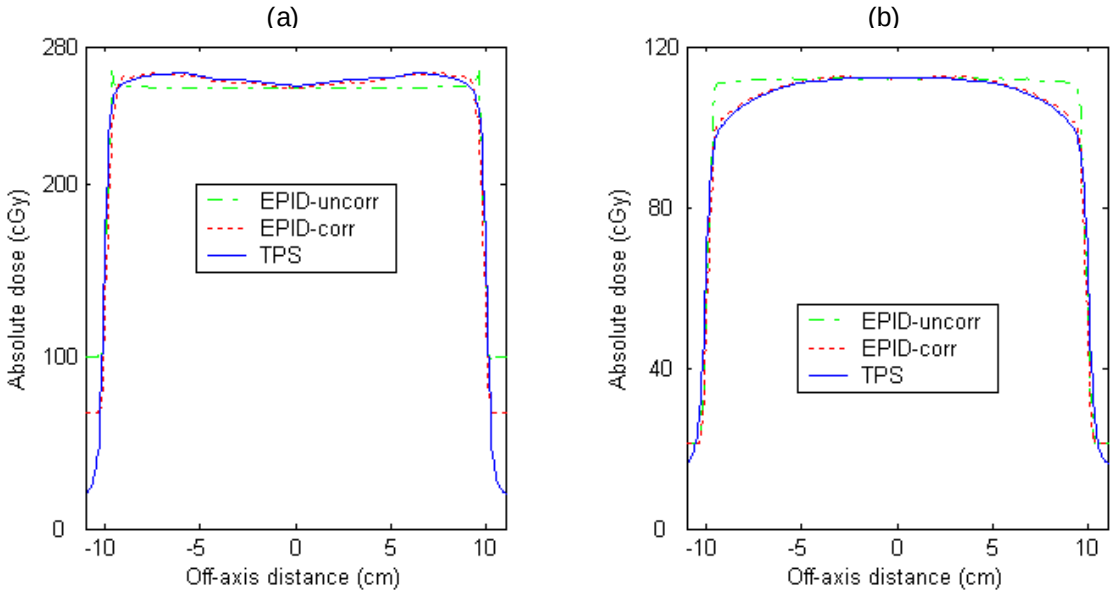

Figure 4- 20. Dose profiles at the centre of the EPID images and TPS demonstrating the effect of flood field before and after correction for a 20x20 cm^2 field, to a 20cm thickness solid water material with 200 MU and 6 MV beam. Figure (a) compares TPS and EPID entrance dose profiles and figure (b) shows TPS and EPID exit dose profiles.

Figures 4-20 (a) and (b) indicate that the EPID predicts a higher dose outside the treatment field compared to the TPS. This is consistent with previous investigations, though the effect is more significant for the entrance than for the exit doses. Vieira et al (2003) indicated that EPID dose deviations of up to 10% can occur in penumbra regions. For smaller fields, the EPID doses in the penumbra regions were still higher but the differences were within 3%. The penumbra dose difference for large field (20x20 cm^2) irradiations could have been increased because of the field size nearing the reference field size of 21.5x21.5 cm^2. One of the limitation of the method is that it cannot predict dose beyond the reference field size, because the fitting parameters A(i,j), B(i,j) and the open fields are not modelled in these areas. This possibly explains the observed spikes and unexpected discontinuities at the field edges of figure 4-20 for the EPID predicted dose. Another possibility could be that the a-Si EPID detectors are known for their over response to low energy x-rays which are common at field edges and penumbra regions (Vial et al 2008, McCurdy et al 2001). On the other hand, the method we used for the scatter and field size correction may also have an influence on the results. The CF correction is measured on the central axis and applied everywhere in the EPID. This would miscalculate the dose received by the EPID at the edge of a phantom where there is less scatter.

Table 4.7 shows a summary of the point dose percentage differences between the TPS dose (D_{TPS}) and EPID predicted dose (D_{EPID}) calculated at the centres of the homogeneous phantom for a range of field sizes (FS) and thicknesses (T) at 6 MV. The differences between TPS and EPID, at the exit appear to be increasing with field size. For small field size, the EPID predicted a higher dose compared to the TPS for all thicknesses while the trend is reversed at large field sizes. This is in contrast to the entrance dose differences, which appear to be unsystematic, except for the 5x5 cm^2.

Table 4- 8. Percentage differences at exit and entrance central points between TPS and EPID for different field sizes and solid-water thickness (T) for 6 MV beam

	Exit					Entrance				
FS/Th	10	15	20	26	32	10	15	20	26	32
5x5	-1.11	-1.26	-0.71	-1.62	-1.10	0.05	-0.46	-0.64	-0.72	-2.67
10x10	-0.50	-0.32	-0.10	0.08	-0.56	-0.14	-0.69	-0.28	0.15	-1.47
15x15	0.36	0.30	0.37	0.43	0.33	0.30	-0.30	-0.10	0.01	-0.70
20x20	0.70	0.57	0.50	1.40	1.24	0.48	-0.08	0.51	0.07	-0.54

The in vivo determination of entrance and exit doses are useful in clinical QA programs because the former aim to check the accuracy of MU calculations and delivery, while the latter serve in addition to check the influence of the patient (presence of inhomogeneities) on the dose calculation. Comparison of central axis point doses in table 4-7, at the exit and entrance showed that the TPS and EPID predicted values agreed to within 3%. These results show that the EPID doses were generally higher and lower than those of TPS at square field sizes of 5 cm and lower than those of TPS at square field sizes of 20 cm. This was related to a noticeable trend that the EPID's predicted EPL at 5x5cm^2 and 20x20cm^2 were respectively lower and higher than expected values by ~ 1-2mm. This could possibly be due to a weakness in a field-size dependent correction in our method.

A further comparison of the EPID-calculated and TPS dose distributions was carried out using a gamma analysis. Two dimensional measurements in

homogeneous phantoms show that the in-vivo dose at the exit and entrance could be predicted to within 3% dose difference (DD) and 3 mm distance to agreement (DTA) criteria. The results of our in vivo exit dose prediction are consistent with previous investigation (Zijtveld et al 2009, McDermott et al 2007, Nijsten et al 2007). The failed area (gamma index > 1) for square fields of 5, 10, 15 and 20 cm was about 3.1 % (average) of all the points in the irradiated regions and for all thicknesses. In 90 % of the irradiated field, a gamma map comparison between the measured and calculated dose maps showed failed area < 1.5%. The proportion of points within tolerance was higher for exit dose than for entrance dose. In conventional in vivo dosimetry where direct entrance dose are taken, the reverse might be expected, however because the algorithm uses the exit doses to predict the entrance doses, then any systematic errors in the calculation of the former will manifest in the latter. Hence this supports the notion that the use of exit doses is better than using entrance doses.

Figure 4-21 compares the effect of data-points resampling on the results. Figure 4-21 (a) is the original (53x65) dose map and figure 4-21 (b) shows the same central dose map covering an area of 26x26 cm^2 resampled to 356x356 data points. Figure 4-21 (c) shows cross-plane profiles through both dose maps, indicating that the magnitude of the values are insignificantly affected by resampling the data.

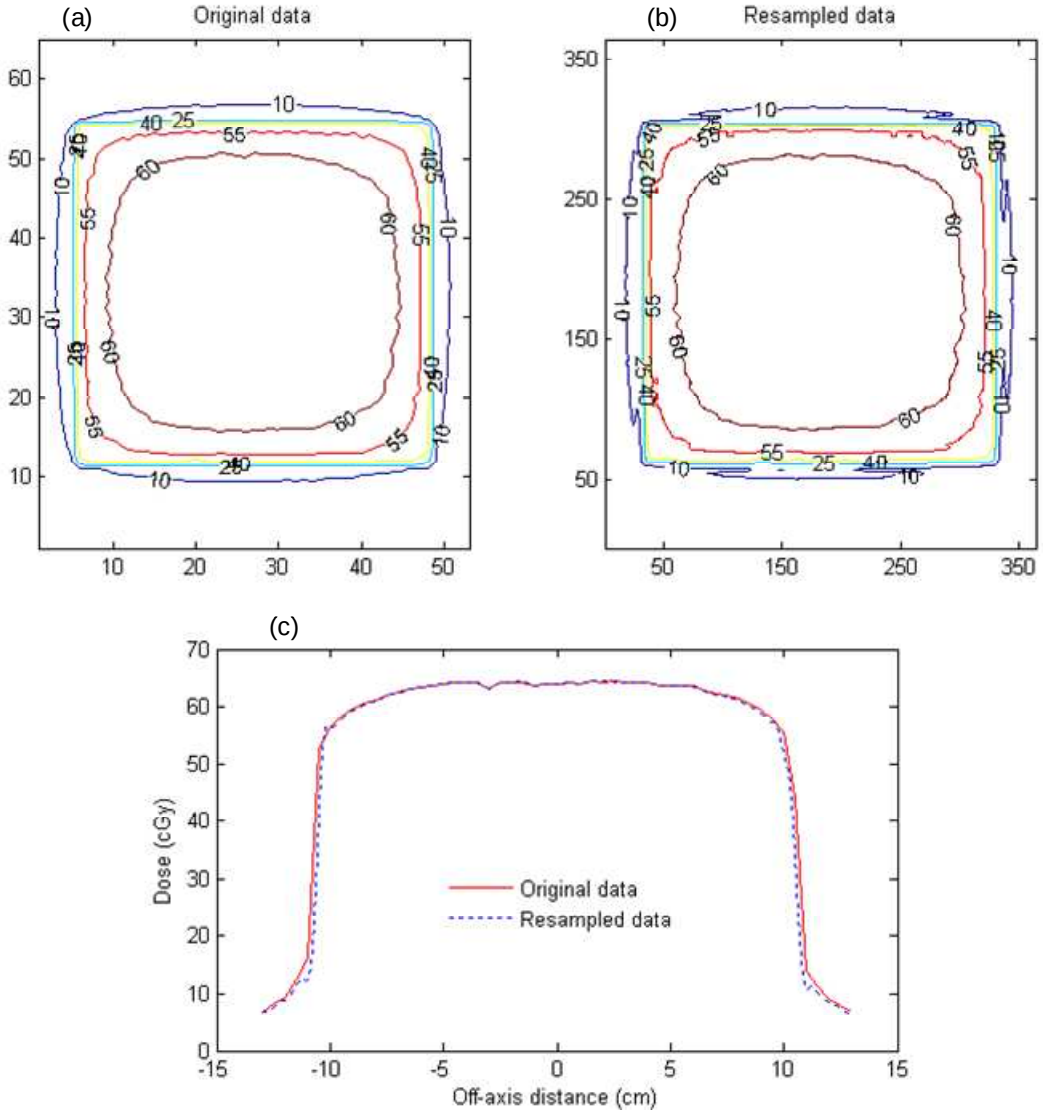

Figure 4- 21: Effect of resampling the MapCHECK data points

Figure 4-22 compares the exit dose, as illustrated in section 3.2.8 (figure 3-11), between the MapCHECK device measurement and EPID image acquired at the same time. The results in this figure shows MapCHECK (a), TPS (b) and EPID image (c) dose distributions, acquired with 20x20 cm^2 field size and 100 MU. The percentage of area in figure (4-22) where the gamma index (3% DD and 3mm DTA) failed were 2.5, 3.2 and 2.8 for the TPS vs MapCHECK, EPID vs MapCHECK and TPS vs EPID respectively.

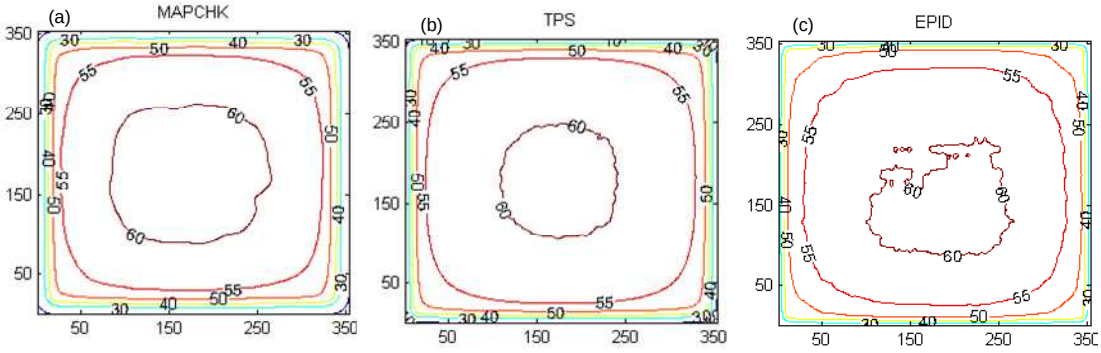

Figure 4- 22: Figures (a), (b) and (c) compare 2D absolute exit dose (cGy) distributions measured with MapCHECK device, calculated with TPS and those from EPID images respectively, for a 20x20 cm^2 field size and 100 MU.

Figures 4-23 and 4-24 show exit dose comparisons for the step and cylindrical phantom cases respectively as described in section 3.2.4.1. Figures 4-23 (a & c) and 4-24 (a & c) are TPS predicted dose while figures 4-23 (b & d) and 4-24 (b & d) are their respective EPID calculated dose. Figures 4-23 (e) and 4-24 (e) are horizontal EPID (dotted lines) and TPS (dashed lines) dose profiles, and EPL (solid lines) profiles computed from their respective EPID images. Figures 4-23 (f) and 4-24 (f) are their respective gamma evaluation between the TPS and EPID predicted, calculated at 3% and 3mm DTA tolerance criteria.

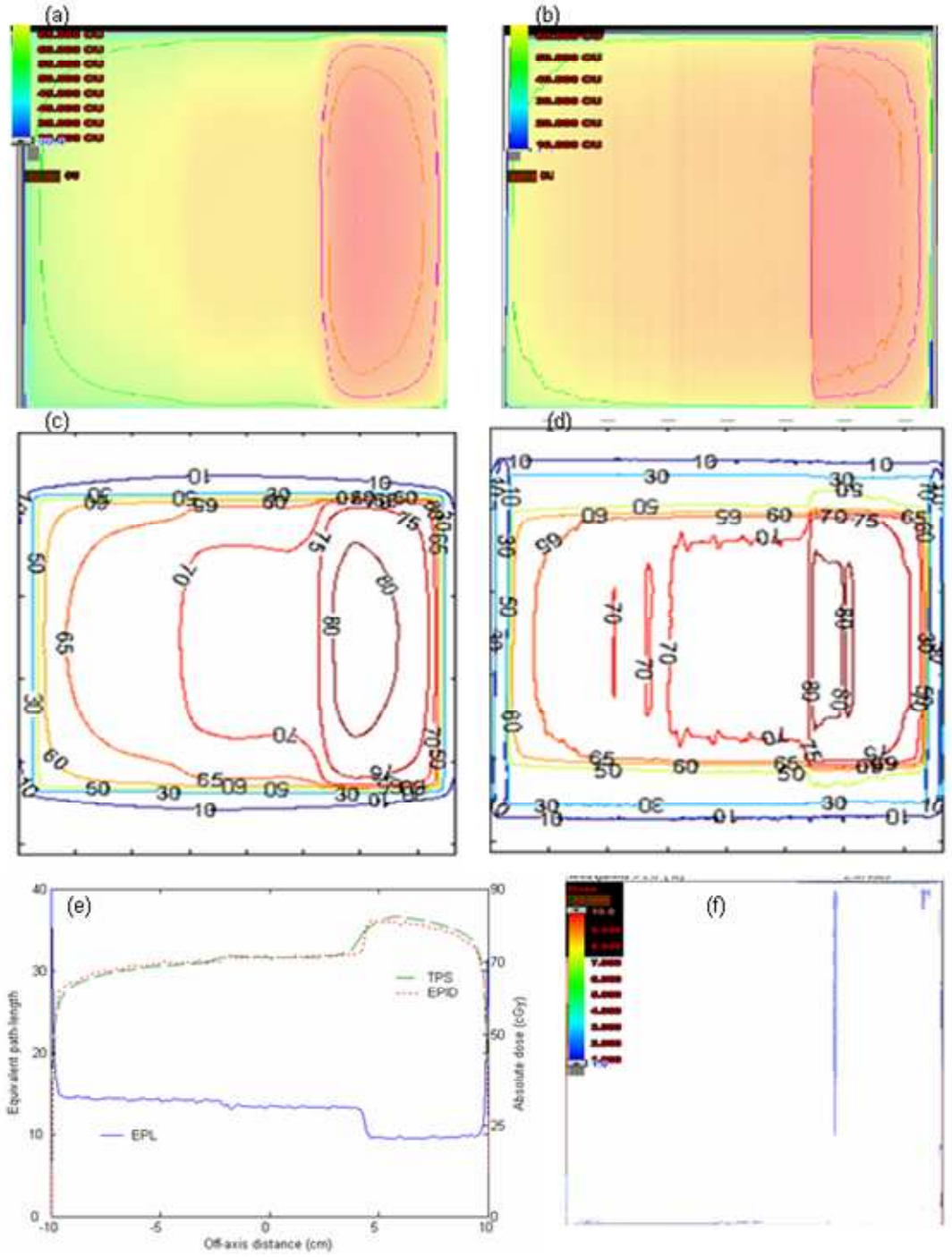

Figure 4- 23. Exit dose comparison for case in figure 3.5(a) as described in section 3.2.1.1 Figures (a) and (c) are 2D TPS predicted colour maps and contour distributions, while (b) and (d) are their respective EPID calculated doses. Figure (e) shows horizontal EPL and dose profiles through the centre of their respective EPID images. Figure (f) is the corresponding gamma distributions between the TPS and EPID.

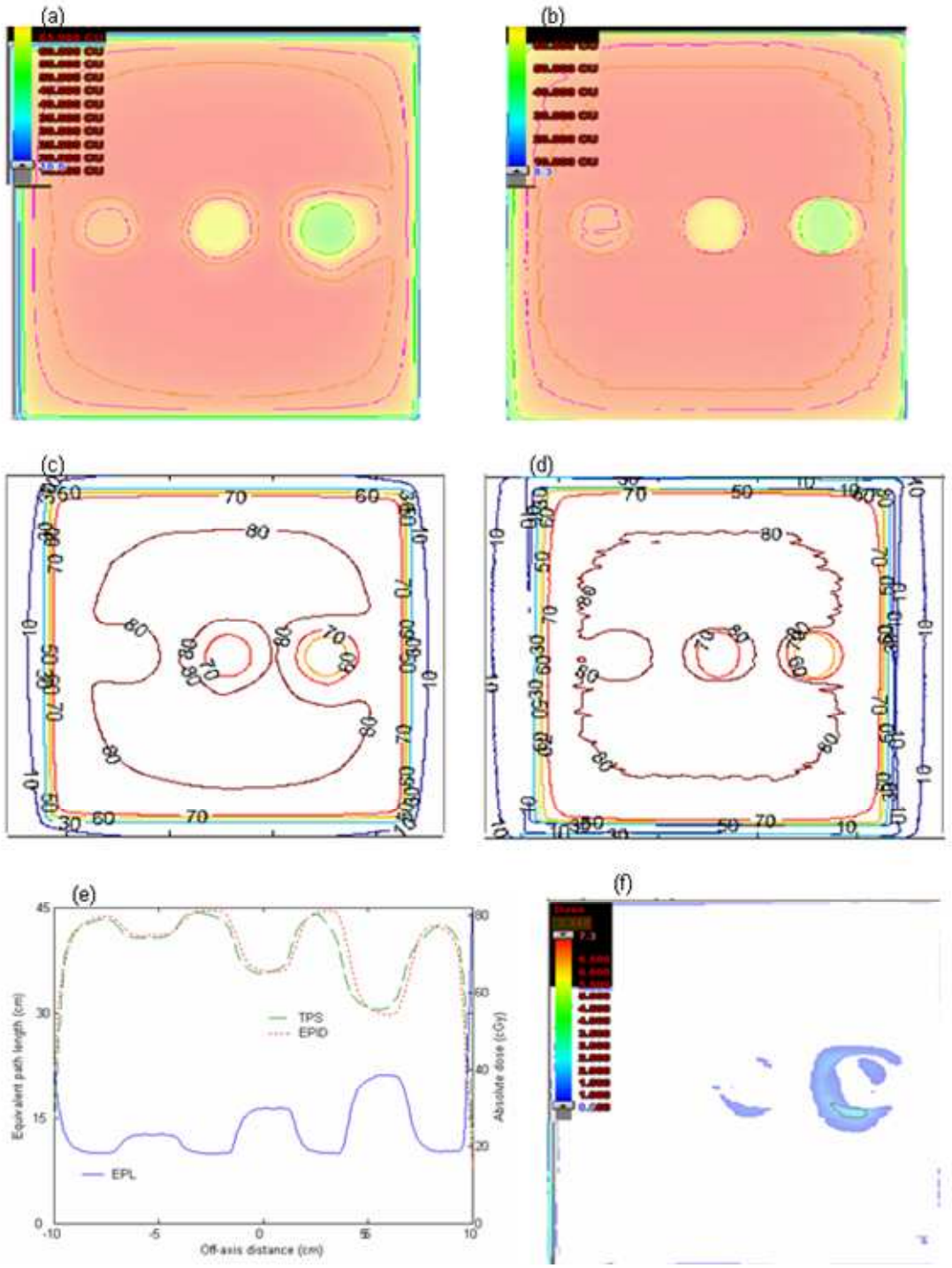

Figure 4- 24. Exit dose comparison for the case in figure 3.5(b) as described in section 3.2.4.1 Figures (a) and (c) are 2D TPS predicted colour maps and contour distributions, while (b) and (d) are their respective EPID calculated doses. Figure (e) shows horizontal EPL and dose profiles through the centre of their respective EPID images. Figure (f) is the corresponding gamma distributions between the TPS and EPID.

The comparison of dose (right ordinate) and EPL profiles (left ordinate) in figures 4-23 (e) and 4-24 (e) clearly depicts the inverse relationship between the two. Both these figures show discrepancies between the TPS and EPID in regions

where there is a steep increase or decrease in dose due to a respectively steep decrease or increase in EPL. Gamma index failures are correspondingly seen in those areas as indicated in figures 4-23(f) and 4-24(f).

Figure 4-25 shows exit dose comparisons for the anthropomorphic lower torso phantom as described in figure 3-6. Figure 4-25(f) is the EPID image of this phantom obtained with 20x20 cm^2 field size and 200 MU. Figures 4-25 (a) and (b) are TPS predicted and EPID calculated dose distributions. Figure 4-25 (c) shows horizontal dose profiles from the TPS (dashed lines), EPID (dotted lines) and EPL (solid lines) profiles computed from the EPID image. Figure 4-25 (d) shows the gamma evaluation between the TPS and EPID predicted, calculated at 3% and 3mm DTA tolerance criteria. Figure 4-25 (e) shows the dose difference (D_{EPID}-D_{TPS}) map.

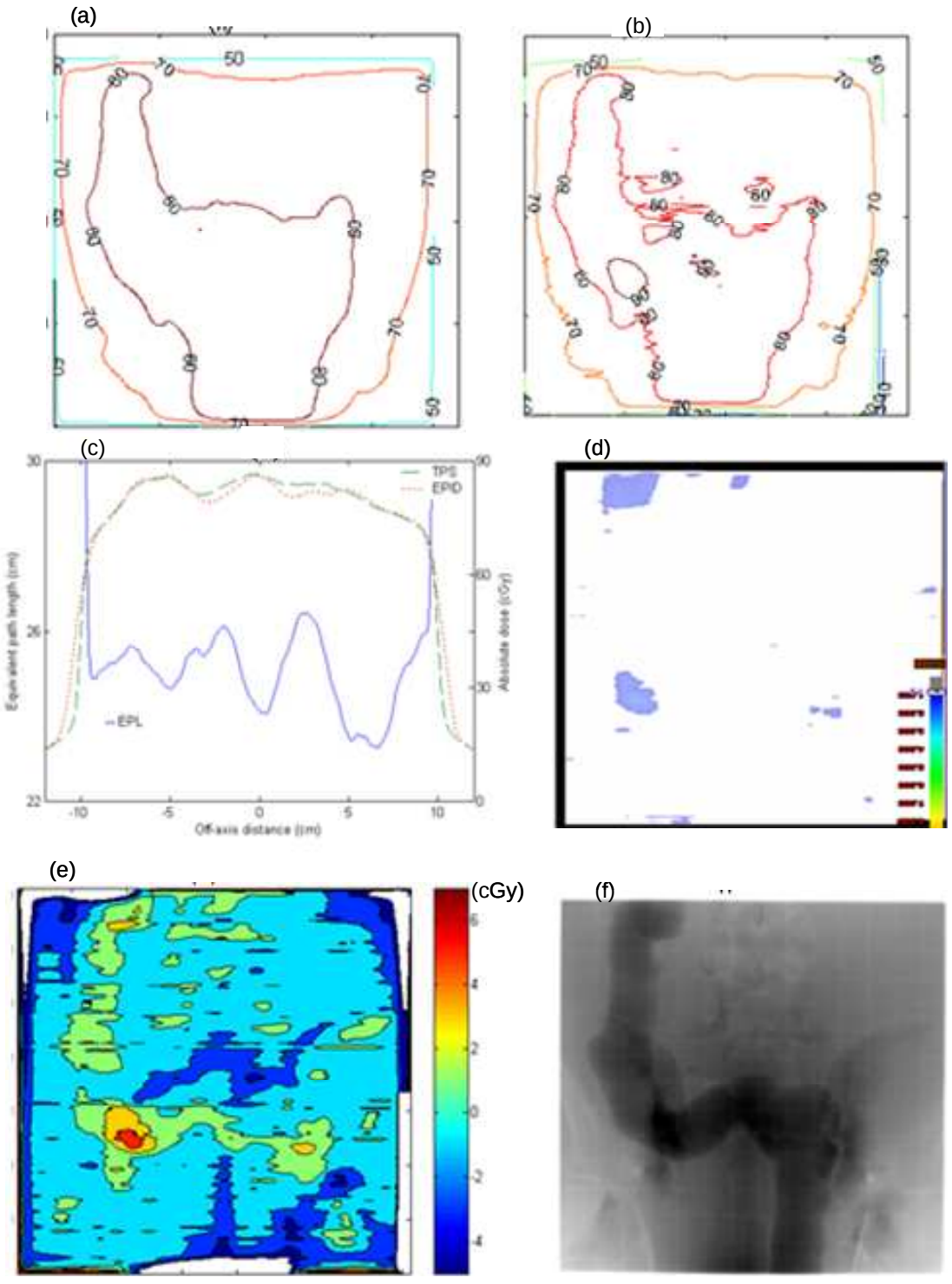

Figure 4- 25. Exit dose comparison for the case in figures 3-6 as described in section 3.2.4.4. Figures (a) and (b) are the 2D TPS predicted and EPID calculated dose contours respectively. Figure (c) shows horizontal TPS dose (dashed) and EPID dose (dotted line) and EPL profiles through the centre of the EPID image. Figure (d) is the corresponding gamma distributions between the TPS and EPID. Figure (e) is a 2D dose difference map. Figure (f) is the EPID image of the irradiated 20x20 cm^2 field area of the phantom.

Figure 4-26 shows exit dose comparisons for the same anthropomorphic lower torso phantom as described in figure 4-24 above, but for a 10x10 cm^2 field size. Figures 4-26 (a) and (b) are EPID predicted and TPS calculated dose distributions. Figure 4-26 (c) shows the dose difference (D_{EPID}-D_{TPS}) map. Figure 4-26 (d) is the EPID image of this phantom obtained with 200 MU.

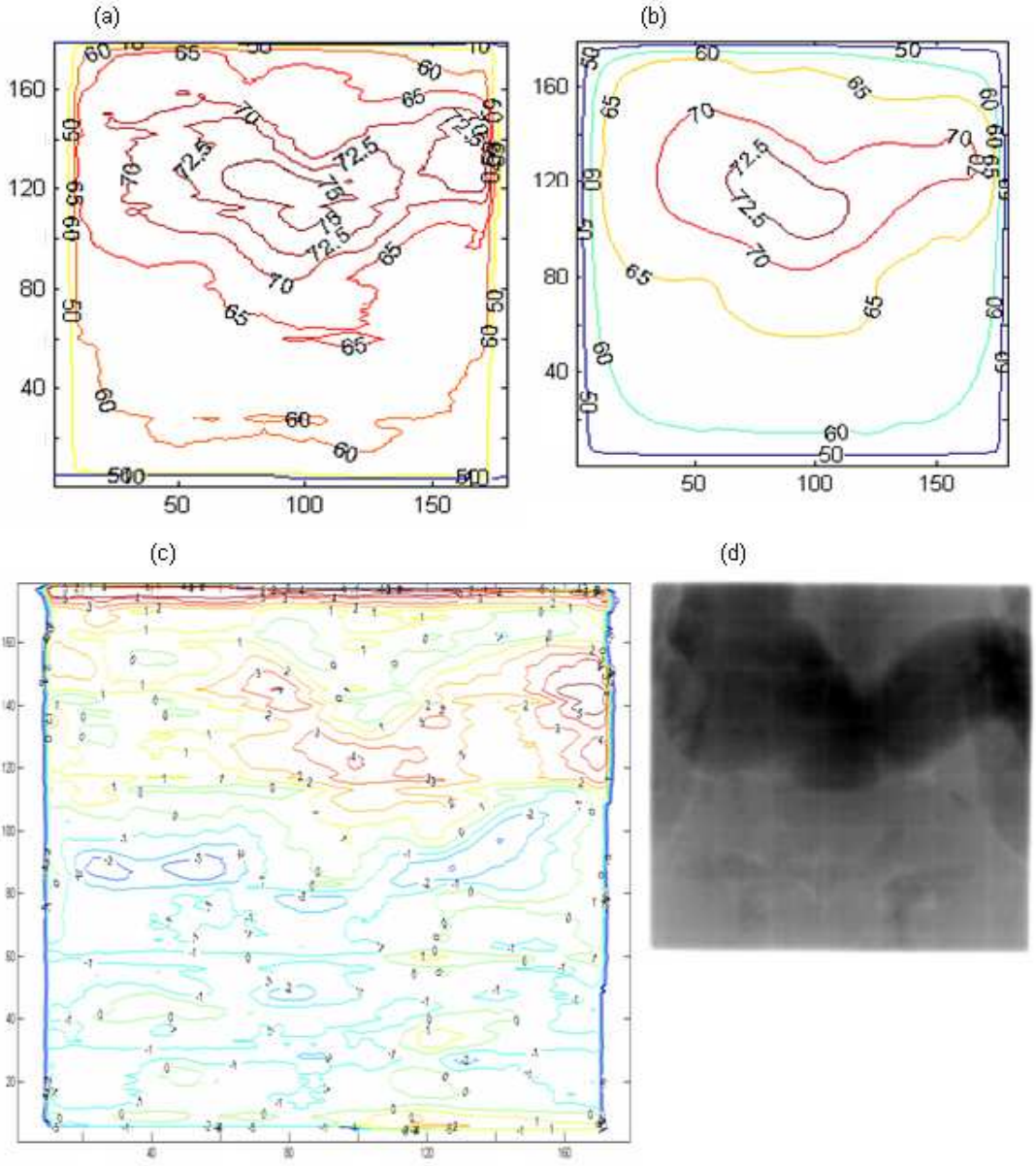

Figure 4- 26. Exit dose comparison for the case in figure 3-6, for 10x10 cm^2. Figures (a) and (b) are the 2D EPID predicted and TPS calculated dose contours respectively. Figure (c) is a 2D dose difference contour distribution. Figure (d) is the EPID image of the irradiated 10x10 cm^2 field area of the phantom.

Similar to results in figures 4-20 (a) and (b), figure 4-25 (c) indicates that the EPID predicts a higher dose outside the treatment field compared to the TPS. The air in the hollow cavity representing sigmoid colon and rectum of the anthropomorphic phantom (figures 3-7 and 4-24(f)) results in an increased dose along its path and both the TPS (figures 4-25 (a)) and EPID (figures 4-25 (b)) demonstrate this effect. The gamma index map in figure 4-25 (d) shows failures in the transverse-descending and descending-sigmoid colon junctions. The EPID predicted a higher dose than the TPS in the failed areas as demonstrated by the dose difference map (figure 4-25 (e)). A similar trend, i.e discrepancies in dose distribution is observed in figure 4-26, for a smaller field size. This variation is most likely due to increased air spaces in this colon-like structure. As much as our EPID dosimetry algorithm takes into account inhomogeneities at the conversion to EPL, it does not take into account the effects caused by irregular and sharp-edged surfaces on dose. This could be the main cause of discrepancies in some areas observed in figures 4-25 and 4-26. The case scenarios in this study may not be identical to those encountered clinically, but they do indicate that in some patient anatomies potential dose discrepancies may occur. This is supported by the findings of Mcdermott et al (2007) who indicated that gas pockets in the rectum may increase the failure percentage when comparing the planned and the EPID generated dose of prostate treatments.

4.3.2 Irregular fields

As mentioned in section 3.2.7 above, the irradiated field area and resulting phantom scatter are essential for predicting the EPL from an EPID image and hence dose. Table 4-8 shows a summary of the areas calculated from the EPID images for the test cases of figure 3-7, compared to their respective expected areas. The percentage dose differences were calculated as

$$\left(\frac{Expected\_Area - Calculated\_Area}{Expected\_Area}\right)x100\%$$

The deviations between EPID predicted and the geometrically expected areas for all images used in the study including squares and wedged fields were within ±1%.

Table 4- 9. Comparison of expected and EPID calculated areas for square fields and cases described in figure 3.7

Case	Expected Area	Calculated Area	Deference (%)
10x10 sq	100.0	99.5	0.5
20x20 sq	400.0	401.7	-0.4
21.6x20 (60º EDW)	432.0	433.5	-0.3
Case a	318.8	319.2	-0.1
Case b	136.0	135.1	0.7
Case c	322.0	323.6	-0.5
Case d	247.0	245.4	0.6
Case e	252.0	249.5	1.0
Case f	51.5	51.8	-0.6

The irradiated field areas can be accurately determined from the EPID image to within ± 1% uncertainty in all cases. Scattered radiation in portal images depends on beam energy, phantom/ patient thickness and field area (Swindell et al 1995, Mayles et al 2007, Kairn et al 2008). Accurate determination of field area, which is one of the paramount factors required in the establishment of phantom / patient scatter correction and hence EPL and dose, is essential. Because there are no simple means to determine the equivalent square for an irregularly shaped field, the most commonly used technique to predict the scatter / output factor correction is the sector-integration method (Sanz et al 2001, Podgorsak 2005), where the irregular field is resolved into sectors of circular beams originating at the point of interest in the phantom or patient. In the proposed method, the EPID image pixel resolution is less than 1.0 mm, hence the irradiated areas can be calculated to a high degree of accuracy. However, the sector integration method has an additional advantage that it accounts for the distances to the point of interest whereas the area calculation method used in this study does not. The use of area alone for scatter correction could be another source for the discrepancies in our results.

The EPL beneath the MLC shielded regions is too high compared to the maximum depths for TPR table which was measured up to a depth of 40 cm. Figure 4-27

shows the EPL profile calculated from EPID image of figure 3-8 (d) (MLC aperture 3-7 (d)). The figure shows that the EPL in the open beam is ≈ 20 cm and rises to over 100 cm in the shielded regions. With MLC height (physical thickness) of ≈ 6.5 cm and electron density of Tungsten ≈ 19.3 g/cc, then according to equation 3.17, the EPL in the shielded region should be much higher than 100 cm. This indicates that the EPL equation is not accurate at such large values, due to the A(i,j) and B(i,j) fitting parameters being optimized for the range 0 – 35 cm. In addition, it will be inappropriate to use A(i,j) and B(i,j) due to spectral changes and scattering caused by the MLC. Another factor is the difference in pair production probability between tungsten and water.

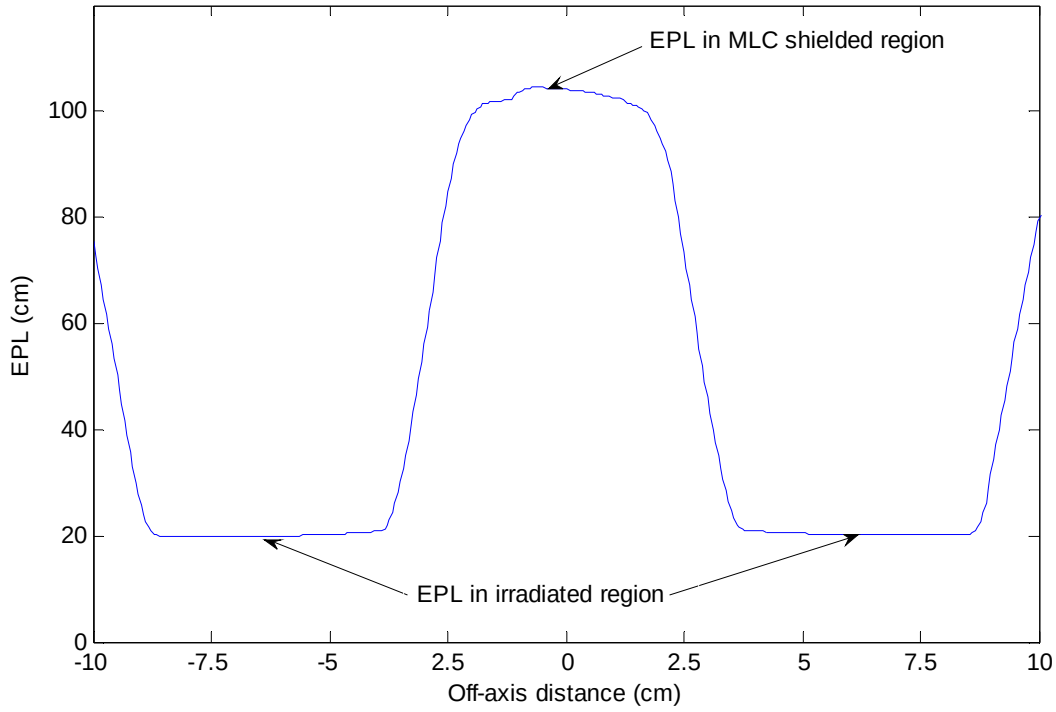

Figure 4- 27. EPL profile (along the Y direction) calculated from the EPID image of figure 3.8 (d)

To facilitate calculation of doses in these regions, the TPR was set to the MLC transmission factor. $MLC\_Transimision = \frac{MLC\_Closed\_EPID\_Signal}{Open\_Field\_EPID\_Signal} = 0.013$

The value of the MLC transmission factor measured with the EPID agrees with that of Lorentz et al 2007. They indicated that the MLC transmission varies

across the irradiated field ranging between 0.016 at the central axis to 0.012 towards the field edges.

Figure 4-28 shows the EPID and TPS exit dose comparison for the case of figure 3-7 (a). Figures 4-28 (a) and (b) show the TPS and EPID dose distribution where the EPID doses in the shielded regions are calculated as described in previous sections. The gamma index (figure 4-28 c) computed from figures 4-28 (a) and (b) at 3% DD and 3mm DTA criterion, indicates that 5.8% of the points failed. This gamma map shows that most of the discrepancies between the EPID and TPS doses are in the shielded regions. Figures 4-28 (d) and (e) and corresponding gamma index (f) show the same case, but the doses in the shielded regions have been zeroed. This was achieved by: first a matrix is created from the edge polygon, (say figure 3-10 (a) for this case) whereby all the enclosed pixels are filled with "ones" and "zeros" elsewhere. Secondly, the created matrix is multiplied (element by element) with the exit dose matrices. This automatically zeroes the doses outside the irradiated fields and the gamma index map (figure 4-28 f) shows a decrease in number of points failing the criterion.

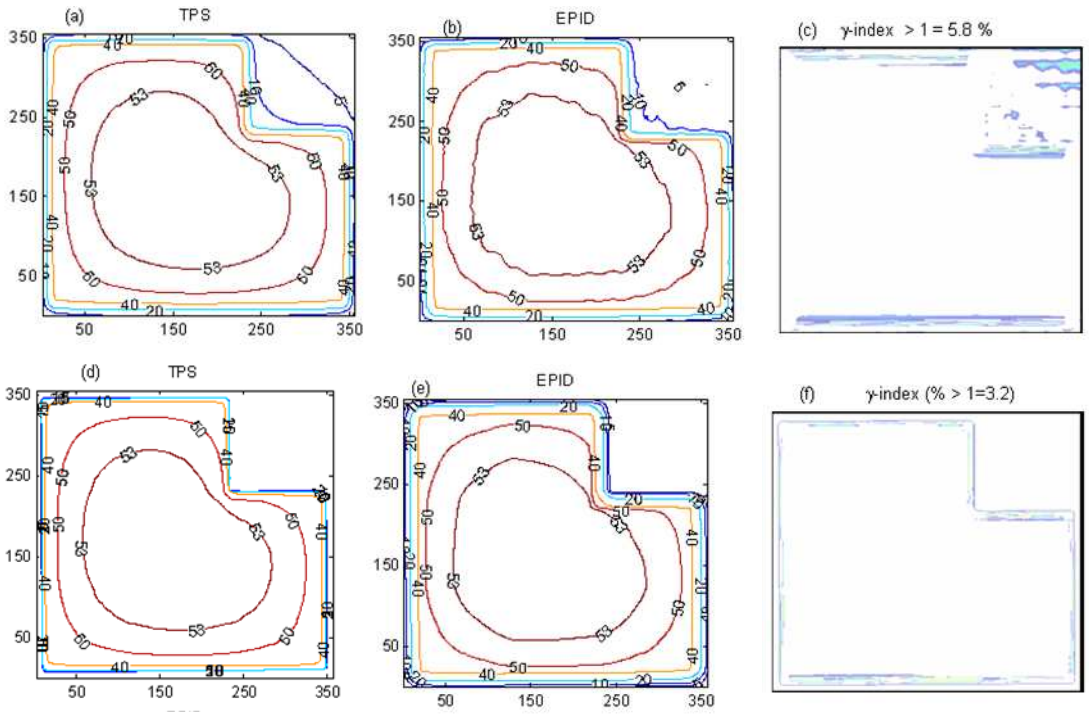

Figure 4- 28. Comparison of TPS (a) and EPID (b) exit doses for case of figure 3-7(a), where the doses in shielded areas are compared. Figures (a) and (d) are the same TPS doses but the dose data in shielded areas have been zeroed. Similarly, figures (b) and (e) are the same EPID doses but the dose data in shielded areas have been zeroed. Figures (c) and (f) are the corresponding gamma index maps.

Figures 4-29 (a) and (b) show the absolute 2D EPID predicted and TPS exit dose distributions respectively, for the cases of figures 3-7 (c). For the MLC-shaped field in this figure, the difference between the EPID and TPS doses within the in-field region was very small. Hence, the percentage of areas in this test case where the gamma index (figures 4-29 (c)) evaluated at 3% DD and 3mm DTA criterion, was greater than 1.0, was 4.5%. This is well illustrated in a histogram figure 4-29(d) showing the actual gamma indices distribution computed from the 2D gamma index maps of figures 4-29. About 50% of the total points in this figure have gamma value less than 0.3, with maximum gamma index of 9.9. The observed errors at the edges of the MLC might be partially corrected in the same way that the Varian Eclipse 8.6 TPS corrects their MLC delivery, by slight adjustment of the field edges when defined by MLC (Vial et al, 2006). This leaf offset is about 1.5-2.0 mm (Varian MLC). The effect this leaf offset might cause on the field edge dosimetry, need to be investigated.

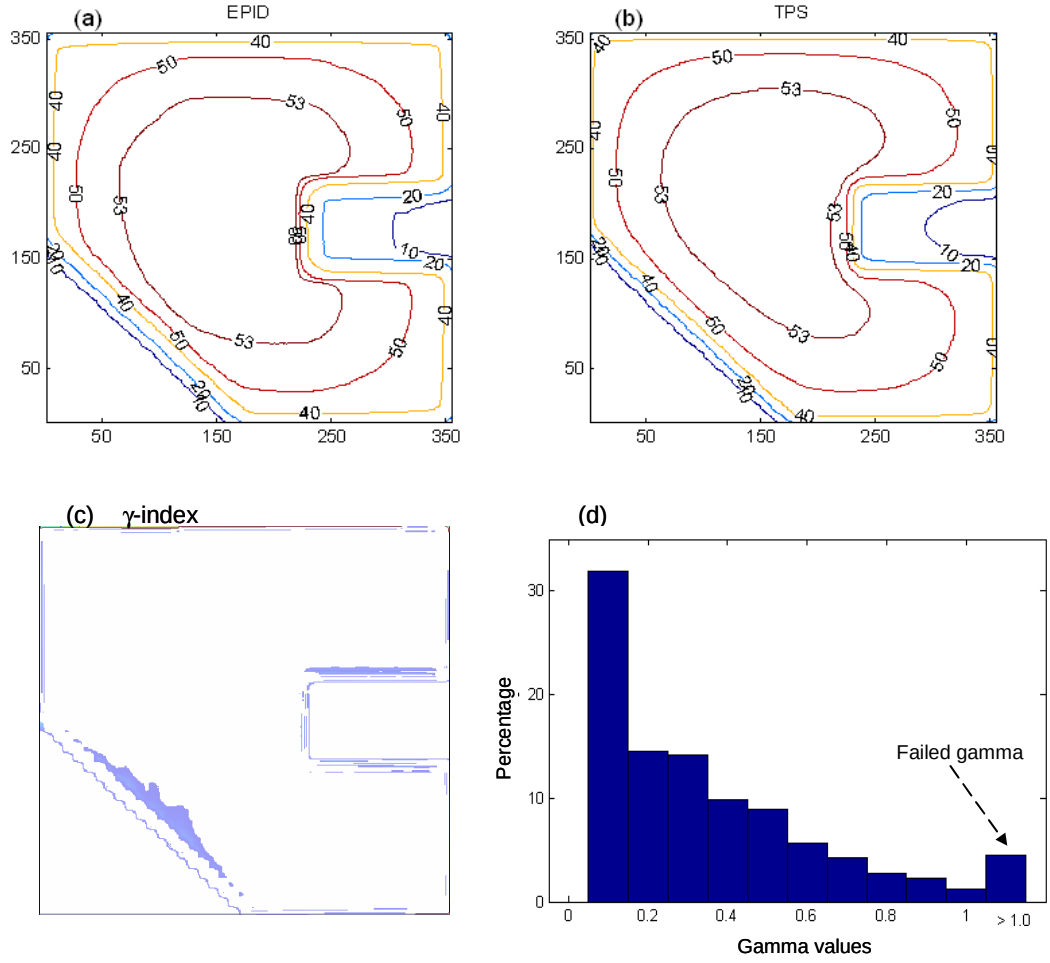

Figure 4- 29: Figures (a) and (b) show EPID and TPS 2D absolute exit dose distributions for the irregular shaped apertures in figure 3.7 (c). Figure (c) demonstrates the gamma index map. Figure (d) is a histogram showing the gamma index values, computed from gamma map of figure (c).

Figure 4-30 compares the absolute 2D dose distributions at the exit for the MLC shaped field in figure 3.7 (d) measured by MapCHECK (a), TPS predicted (b) and that calculated from EPID image (c). The percentage of areas where the gamma index (figures (d), (e) and (f)) evaluated at 3% DD and 3mm DTA criterion, was greater than 1.0, were 3.2%, 8.2% and 7.6% for TPS vs MapCHECK, EPID vs MapCHECK and TPS vs EPID respectively.

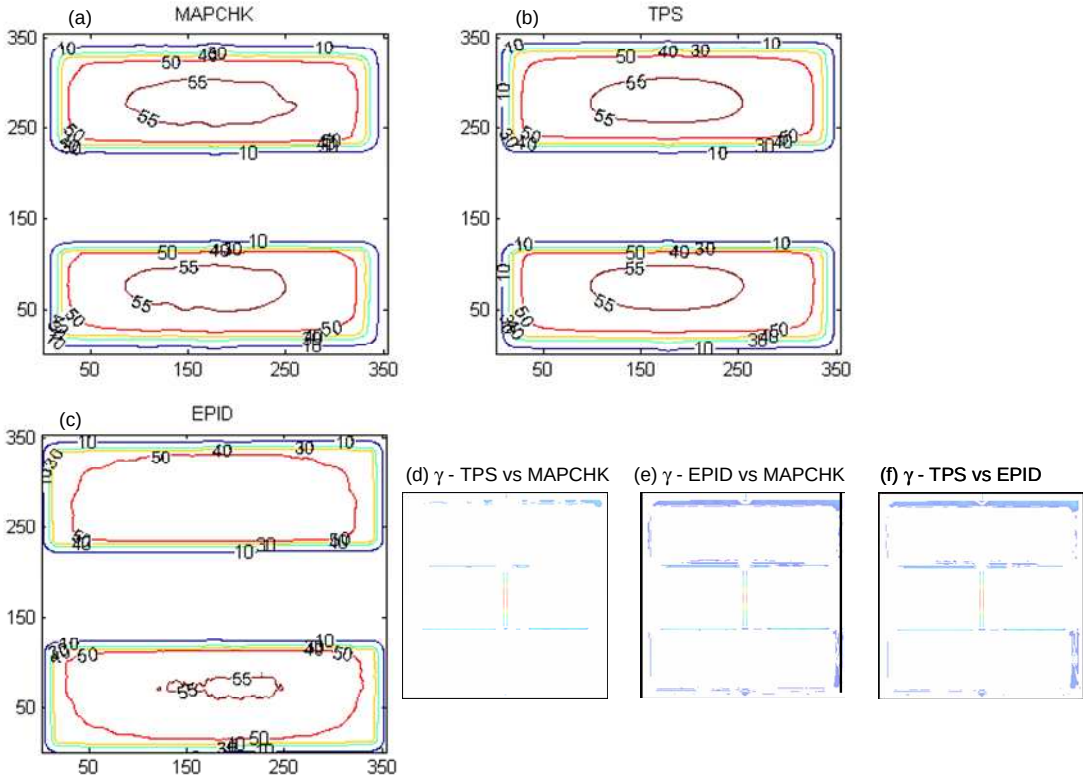

Figure 4- 30:Figures (a), (b) and (c) show 2D absolute exit dose (cGy) distributions measured with MapCHECK device, calculated with TPS and those from EPID images respectively for the irregular shaped field in figure 3.7 (d). Figures (d), (e) and (f) demonstrate the respective 2D gamma maps, evaluated at 3% DD and 3 mm DTA.

In figures 4-30, the dose differences between the EPID, MapCHECK and TPS at the centre, where the left and right MLC banks intersect, is much higher, resulting in higher gamma values as shown in figure 4-30 (d-f). Most of the discrepancies are at the MLC defined edges as illustrated in the 2D dose and gamma index distributions of figure 4-30 (d-f). More than 90% the points in the test cases for figure 3.7 (c) and (d) passed the gamma index evaluated at 3% DD and 3mm DTA criterion.

Figures 4-31 (a) and (b) show the absolute 2D EPID predicted and TPS calculated exit dose distributions respectively for the case of figure 3-7 (e). The doses under the MLC shielded areas have been zeroed in this figure. Figures 4-31 (c) and (d) compare dose profiles extracted from the dose distribution in the X and Y directions respectively. The matching between these profiles in the irradiated field was within 1%, indicating little or no systematic error. Figure 4-31 (e) shows a 2D percentage dose-difference map between the EPID and TPS predicted

doses, which demonstrates that most of the discrepancy is towards the field edges, also indicated by the gamma index map, figure 4-31 (f). The differences between EIPD and TPS towards the radiation field edge are high, ranging from -30% to 35%.

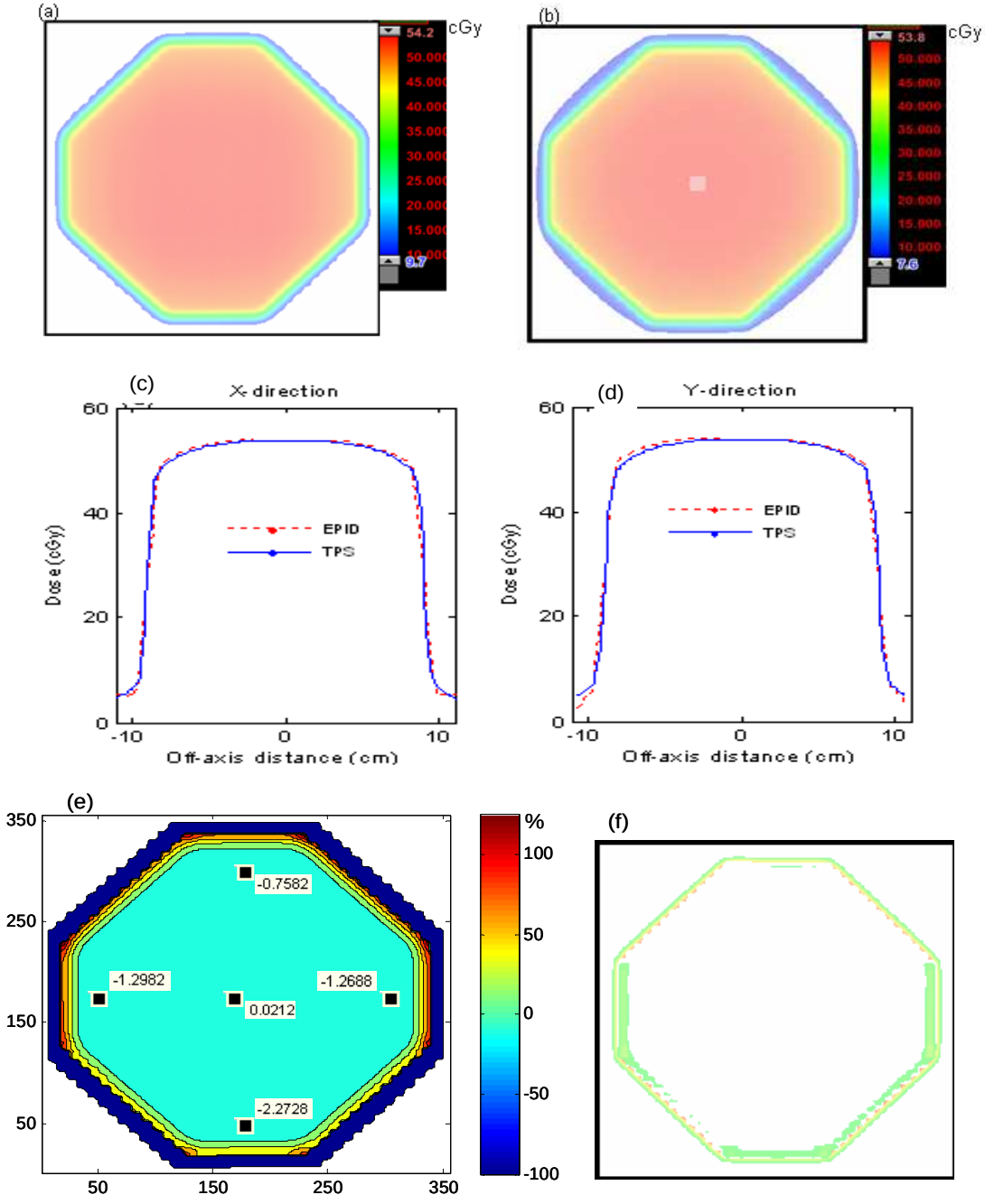

Figure 4- 31: Comparison of EPID and TPS for case of figure 3-7(e)

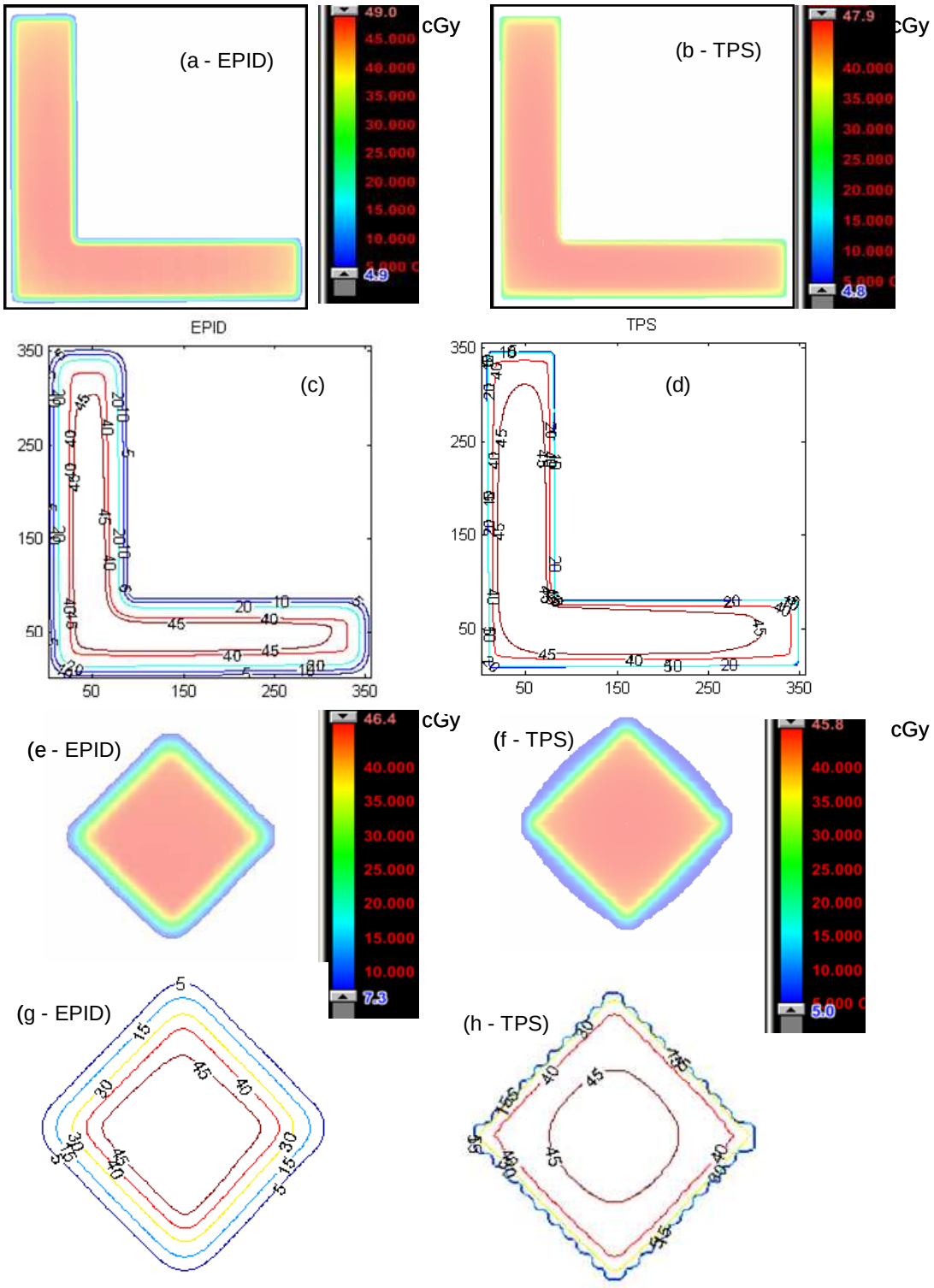

Figure 4- 32. Comparison of EPID and TPS for the cases of figure 3-7 (b) and (f)

Figures 4-32 (a) and (b) compare 2D exit doses in colour-wash predicted from EPID images and TPS respectively for the case in figure 3-7 (b). Figures 4-32 (c) and (d) show the same data as dose contours. Figures 4-32 (e) and (f) compare

2D exit doses in colour-wash predicted from EPID images and TPS respectively for the case in figure 3-7 (f). Figures 4-32 (g) and (h) show the same data as dose contours. Similar to previous cases, the dose matching between the two is excellent.

The doses in the centres of the irradiated fields for all the irregular cases are proportional to the areas indicated in table 4-8. In other words, the MLC shielding of certain areas within a radiation field not only reduces the dose behind the MLC shield, but also reduces the doses in the unshielded areas, in agreement with Boesecke et al (1985). Both the EPID and TPS doses convey this clearly.

Figure 4-33 shows the exit dose comparison for the anthropomorphic phantom case in figure 3-6 as described in section 3.2.4.4, irradiated with an irregular field illustrated in figure 3-7 (c), to a dose of 200 MU. Figures 4-33 (a) and (b) are the 2D EPID predicted and TPS calculated dose contours respectively. Figure (c) shows the corresponding gamma index map and 91.7% of points passed the 3% DD and 3mm DTA criteria. Figure (d) is the acquired EPID image from which the dose distribution in figure (a) was calculated. The air in the hollow cavity representing sigmoid colon and rectum of the anthropomorphic phantom results in an increased dose along its path, as demonstrated by both the EPID and TPS (figures 4-33 (a) and (b) respectively) dose distributions.

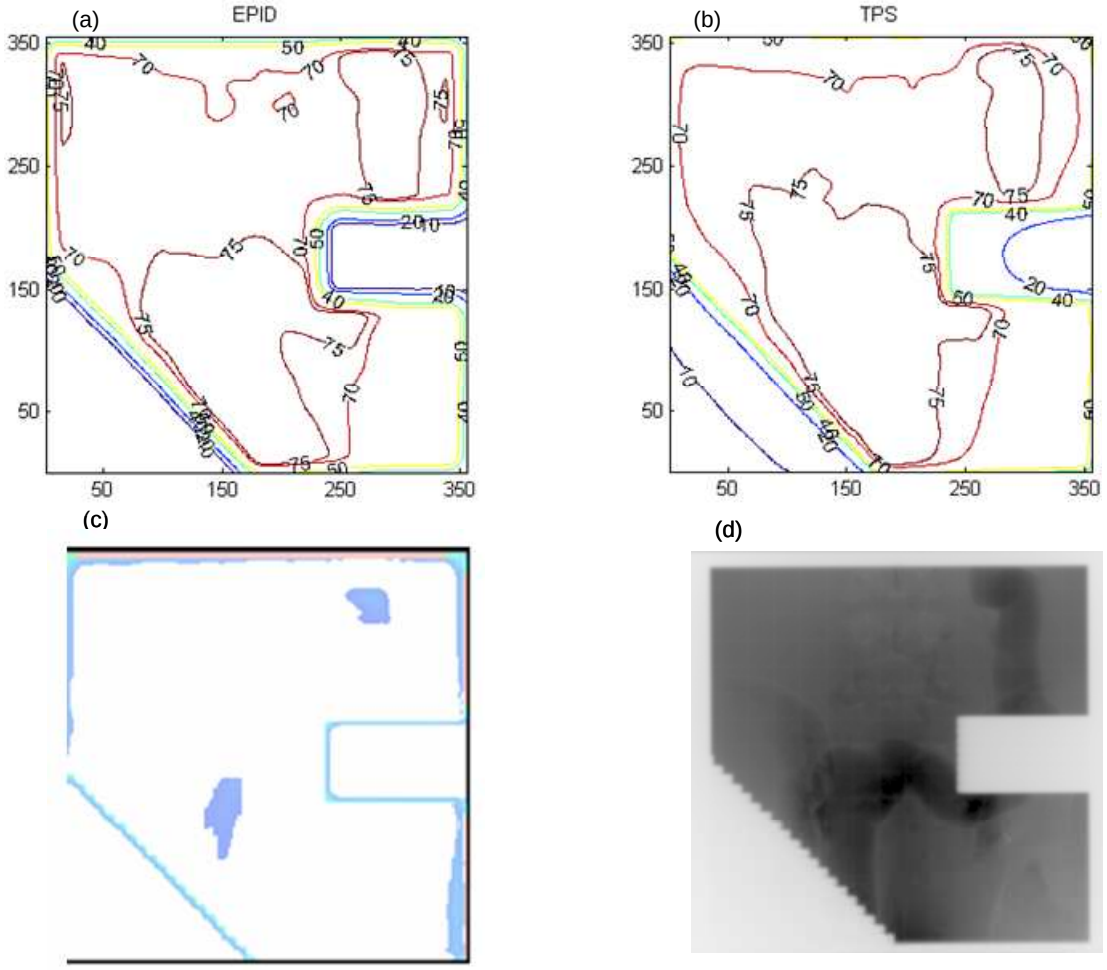

Figure 4- 33. Exit dose comparison for the anthropomorphic phantom case in figure 3-7 as described in section 3.2.4.4, irradiated with an irregular field illustrated in figure 3-7 (c). Figures (a) and (b) are the 2D EPID predicted and TPS calculated dose contours respectively. Figure (c) shows the corresponding gamma index (3% DD and 3mm DTA) map between the TPS and EPID. Figure (d) is the acquired EPID image from which the dose distribution in figure (a) was calculated.

Within the shielded regions and at the field edges, the percentage differences between the calibrated EPID and TPS calculated doses were much greater than in the in-field regions. Observed percent differences ranged from −15% to as much as 35%. This was partially due to the low EPID signal level in these regions compared to TPS. However, the differences in these regions were still small in an absolute sense. Similar to the previous example for the square field, the air in the hollow cavity representing sigmoid colon and rectum of the anthropomorphic phantom results in an increased dose along its path, as demonstrated by both the EPID and TPS (figures 4-33 (a) and (b) respectively) dose distributions. The error at the edges of the MLC profile might be at least

partially corrected the way that the Varian Eclipse planning system corrects their MLC delivery for the rounded leaf edge, by a slight adjustment of the field edge when defined by the MLC. This leaf offset is usually around 1.5-2.0 mm for the Varian MLC. The effect, this leaf offset might cause on field edge dosimetry, need to be investigated.

4.3.3 Enhanced dynamic fields

The edge detection and subsequent calculation of irradiated-area method, described in section 3.2.5.1 is similarly effective with EDW fields. Figures 4-34 (a-f) show 60^0 EDW EPID images, acquired for 20x20 cm^2 (X = 20.0 cm, Y1 = Y2 = 10.0 cm) field size, total delivered MU of 100. Figure 4-34 (a) was acquired without any material and figure 4-34 (d) was acquired with 20 cm of solid water. Figures 4-34 (b) and (e) show their corresponding profiles extracted in the wedge motion direction, while figures 4-34 (c) and (f) show the field edges deduced from their respective EPID images. Figures 4-34 (g), (h) and (i) were acquired with same setup as figure 4-34(d), but with a 30^0 EDW. Despite the variations in beam intensities and scattering effect reaching the imager (due to different EDWs, with and without solid water phantom), the calculated areas were the same. The areas calculated from figures 4-34(c), (f) and (i) were 401.70, 401.89 and 401.83 respectively, which is within 0.5% uncertainty compared to the expected value.

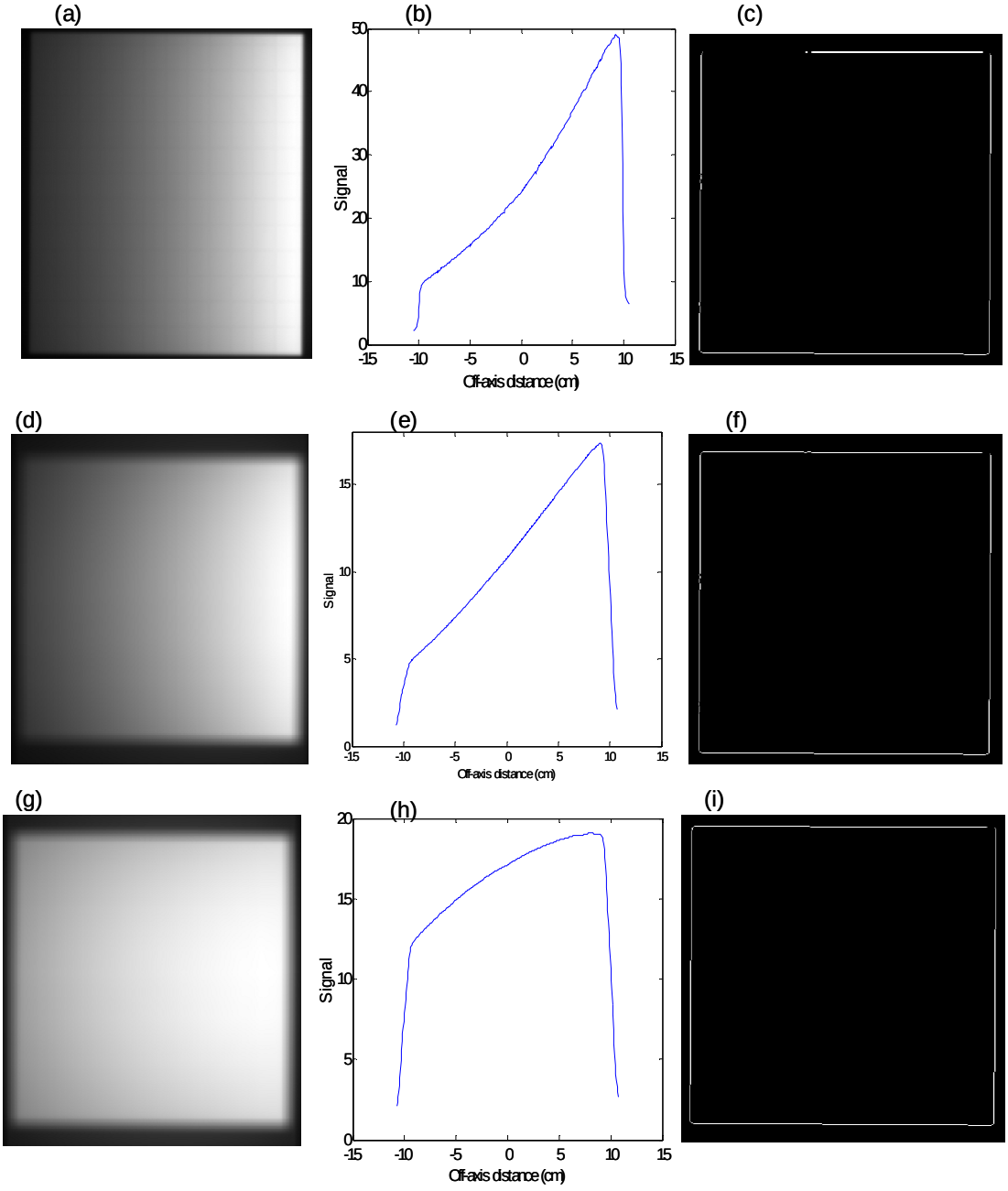

Figure 4- 34. Figures (a), (d) and (g) show EDW EPIDs acquired with different setups. Figures (b), (e) and (h) show their respective profiles, while figures (c), (f) and (i) are the corresponding field edges determined from the EPID image.

Table 4-9 compares segmented treatment tables calculated with the proposed algorithm using equation 3.24 and those printed out after EDW treatment at 100 MU exposures. The system's dynalog viewer files were retrieved after delivery, where the actual Y1 jaw (moving jaw) position and cumulative monitor units are recorded. The two tables on top were obtained using 30^0 EDW and field size

20x20 cm^2 (X=20 cm, Y1=10 and Y2=10). The two bottom tables were for 45^0 EDW and field size 15x15 cm^2 (X=15 cm, Y1=7.5 and Y2=7.5). The exposure to the first open field calculated for 30^0 EDW, with the algorithm is 53.75 MU, which is equal to that from the dynalog viewer. For the 45^0 EDW, the exposure to the first open field with the algorithm is 45.89 MU, compared to 45.77 MU from the dynalog viewer.

Table 4- 10. Comparison of segmented treatment values calculated with the proposed algorithm using equation 3.24 and those printed out after EDW treatment from the linac.

Derived using equation 3.24 — 30 degree EDW STT Table

Seg_no	Dose(MU)	Y1 (cm)	Y2 (cm)
1	0.000	10.00	10.00
2	53.752	10.00	10.00
3	54.681	8.97	10.00
4	55.702	7.95	10.00
5	56.821	6.92	10.00
6	58.050	5.89	10.00
7	59.398	4.87	10.00
8	60.877	3.84	10.00
9	62.501	2.82	10.00
10	64.283	1.79	10.00
11	66.238	0.76	10.00
12	68.383	-0.26	10.00
13	70.738	-1.29	10.00
14	73.321	-2.32	10.00
15	76.157	-3.34	10.00
16	79.268	-4.37	10.00
17	82.682	-5.39	10.00
18	86.428	-6.42	10.00
19	90.539	-7.45	10.00
20	95.050	-8.47	10.00
21	100.000	-9.50	10.00

Dynalog Viewer – 30^0 EDW

INSTANCE#	DOSE (MU)	COLL Y1 (cm)	COLL Y2 (cm)	Diff (%)
1	0.00	10.00	10.00	0.00
2	53.75	10.00	10.00	0.00
3	54.68	8.98	10.00	0.00
4	55.69	7.95	10.00	0.02
5	56.81	6.93	10.00	0.02
6	58.04	5.90	10.00	0.02
7	59.40	4.88	10.00	0.00
8	60.89	3.85	10.00	-0.02
9	62.52	2.83	10.00	-0.03
10	64.31	1.80	10.00	-0.04
11	66.28	0.78	10.00	-0.06
12	68.49	-0.28	10.00	-0.16
13	70.86	-1.30	10.00	-0.17
14	73.46	-2.33	10.00	-0.19
15	76.30	-3.35	10.00	-0.19
16	79.42	-4.38	10.00	-0.19
17	82.83	-5.40	10.00	-0.18
18	86.56	-6.43	10.00	-0.15
19	90.65	-7.45	10.00	-0.12
20	95.12	-8.48	10.00	-0.07
21	100.00	-9.50	10.00	0.00

Derived using equation 3.24 — 45 degree EDW STT Table

Seg_no	Dose(MU)	Y1 (cm)	Y2 (cm)
1	0.000	7.50	7.50
2	45.886	7.50	7.50
3	47.308	6.74	7.50
4	48.821	5.97	7.50
5	50.472	5.21	7.50
6	52.236	4.45	7.50
7	54.114	3.68	7.50
8	56.112	2.92	7.50
9	58.278	2.16	7.50
10	60.607	1.39	7.50
11	63.086	0.63	7.50
12	65.724	-0.13	7.50
13	68.566	-0.89	7.50
14	71.640	-1.66	7.50
15	74.914	-2.42	7.50
16	78.398	-3.18	7.50
17	82.127	-3.95	7.50
18	86.185	-4.71	7.50
19	90.507	-5.47	7.50
20	95.107	-6.24	7.50
21	100.000	-7.00	7.50

Dynalog Viewer – 45^0 EDW

INSTANCE#	DOSE (MU)	COLL Y1 (cm)	COLL Y2 (cm)	Diff (%)
1	0.00	7.50	7.50	0.00
2	45.77	7.50	7.50	0.25
3	47.21	6.73	7.50	0.21
4	48.70	5.98	7.50	0.25
5	50.39	5.20	7.50	0.16
6	52.13	4.45	7.50	0.20
7	54.05	3.68	7.50	0.12
8	56.03	2.93	7.50	0.15
9	58.24	2.15	7.50	0.07
10	60.55	1.40	7.50	0.09
11	63.08	0.63	7.50	0.01
12	65.69	-0.13	7.50	0.05
13	68.59	-0.90	7.50	-0.03
14	71.63	-1.65	7.50	0.01
15	74.97	-2.43	7.50	-0.07
16	78.40	-3.18	7.50	0.00
17	82.19	-3.95	7.50	-0.08
18	86.18	-4.70	7.50	0.01
19	90.56	-5.48	7.50	-0.06
20	95.06	-6.23	7.50	0.05
21	100.00	-7.00	7.50	0.00

The comparisons of the MU exposures at different Y1 jaw positions for both cases are in very good agreement. The last column in the table shows that the percentage differences between the derived MU at different jaw positions and those from the dynalog file are within ± 0.5%. Results from this table indicate that the proposed algorithm can very well replicate the exposure-versus-jaw position for the EDW.

The sweeping of the collimator jaw across the irradiated field generates an EPL that varies with the EDW angle. Figure 4-35 shows the EPL cross plane profiles for EPID images obtained without any material between the source and detector at 100 MU and 400MU/min. The EPLs were computed using the set of correction coefficients A(i,j), B(i,j) and $M_o(i,j)$ (only for figure 4-35) generated for open fields. As indicated in section 3.2.6.1, using parameters for open fields has limitations for calculation EPL for EDW fields; hence the main purpose for the results in figure 4-35 is to clarify on these drawbacks. For the open field, i.e. zero wedge (open in figure 4-35), the EPL measured across the entire field in the X and Y direction was 0±0.3 cm. For wedged beams, the EPL profiles in the Y (wedge motion) direction are higher at the start of the field and decrease gradually as collimator jaw sweeps across the field. For the zero-wedge field the entire 100 MU is delivered to the entire field, while the EDW comprises of the open-field phase and a collimator-sweeping phase. From the STT calculation when a total 100 MU is given, the proportions delivered to the open-field segments are 53.8MU, 35.2MU and 15.6 MU for the 30^0, 45^0, and 60^0 EDW respectively. For the EDW fields, as the cumulative MU increases, the EPL gradually decreases. EDW treatments are optimised such that the intended total MU is delivered by the end of treatment field, explaining why the EPL in the Y direction are nearly the same. These results clearly depict the inverse relationship between EPL and MU (dose).

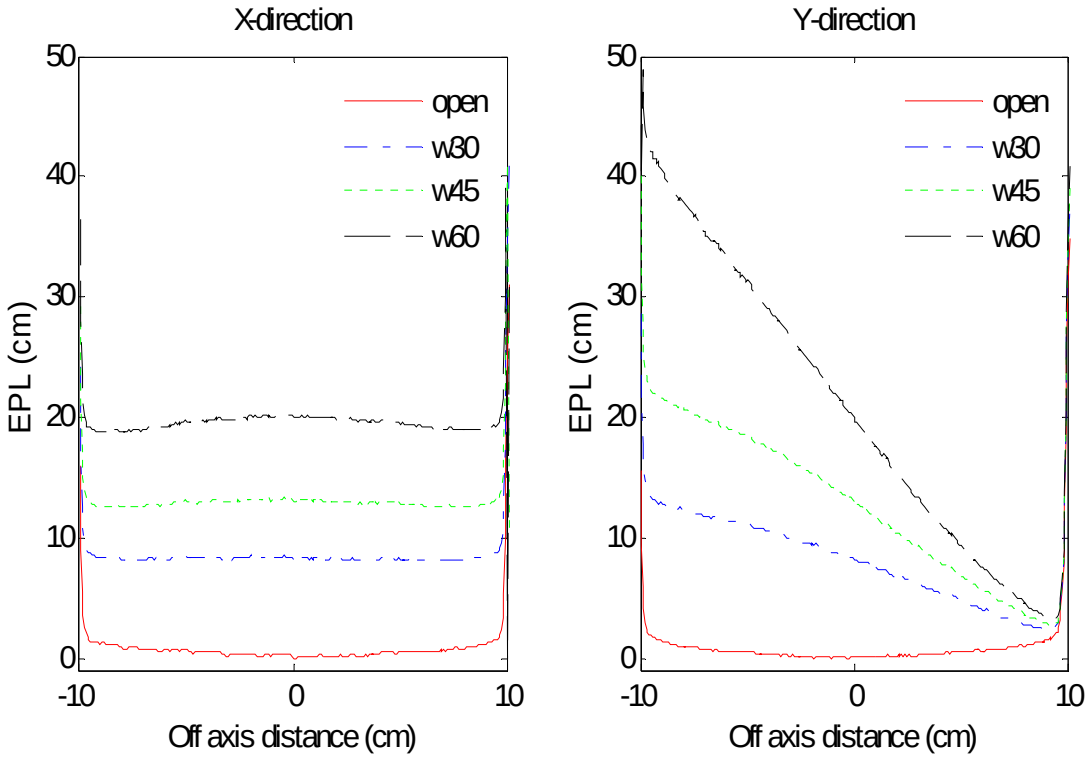

Figure 4- 35. EPL profiles in X and Y directions predicted from images obtained without any material between the source and imager for open field (solid lines), 30^0 (dash-dot lines), 45^0 (dot lines) and 60^0 (dash lines) EDW angles.

The EPL computed for EDW using the correction coefficients A(i,j), B(i,j) and $M_o(i,j)$ generated for open fields from EPID images is not due to the irradiated image alone, but also the influence of the sweeping jaw across the field. Cross plane profiles in figure (4-35) illustrate that EPL may rise beyond 20 cm across field for 45^0 EDW. The limitation with these open field coefficients is that, for EDW angles above 30^0, the combined EPL contribution from the EDW and irradiated material (~ 20 cm solid water) is high, reaching levels beyond the optimised range of calibration values (0-35 cm). Hence EPL in such cases may be calculated inappropriately. In addition to that, if the combined EPL goes beyond the maximum depths for the TPR table, which was measured up to depths of 40 cm, then the conversion of EPL to dose may be inaccurate as well.

Figure 4-36 shows measured and derived (equation 3.20) profiles without any material in the beam $M_0^{\theta}(i,j)$ in the X and Y directions for 30^0 (figures (a) and (b)) and 45^0 (figures (c) and (d)) EDW angles. These profiles are compared to the measured 60^0 EDW shown in figures 4-36 (e) and (f). As expected the signal at

the start of the moving jaw is much lower for the 60^0 EDW field and continues to increase with decreasing EDW angles. Figures 4-36 (g) and (h) show a 3-D visualization of the fitting parameters, for the EDW 30^0 and 45^0 angles respectively. The main reason why we derived the parameters is analogous to the methodology of the Eclipse TPS whereby, during EDW commissioning, only the 60^0 EDW and open field measurements are done. The rest of the EDW angles i.e 10^0, 15^0, 20^0, 25^0, 30^0 and 45^0 are generated from the 60^0 EDW and open field measurements (Varian medical Systems, 1996).

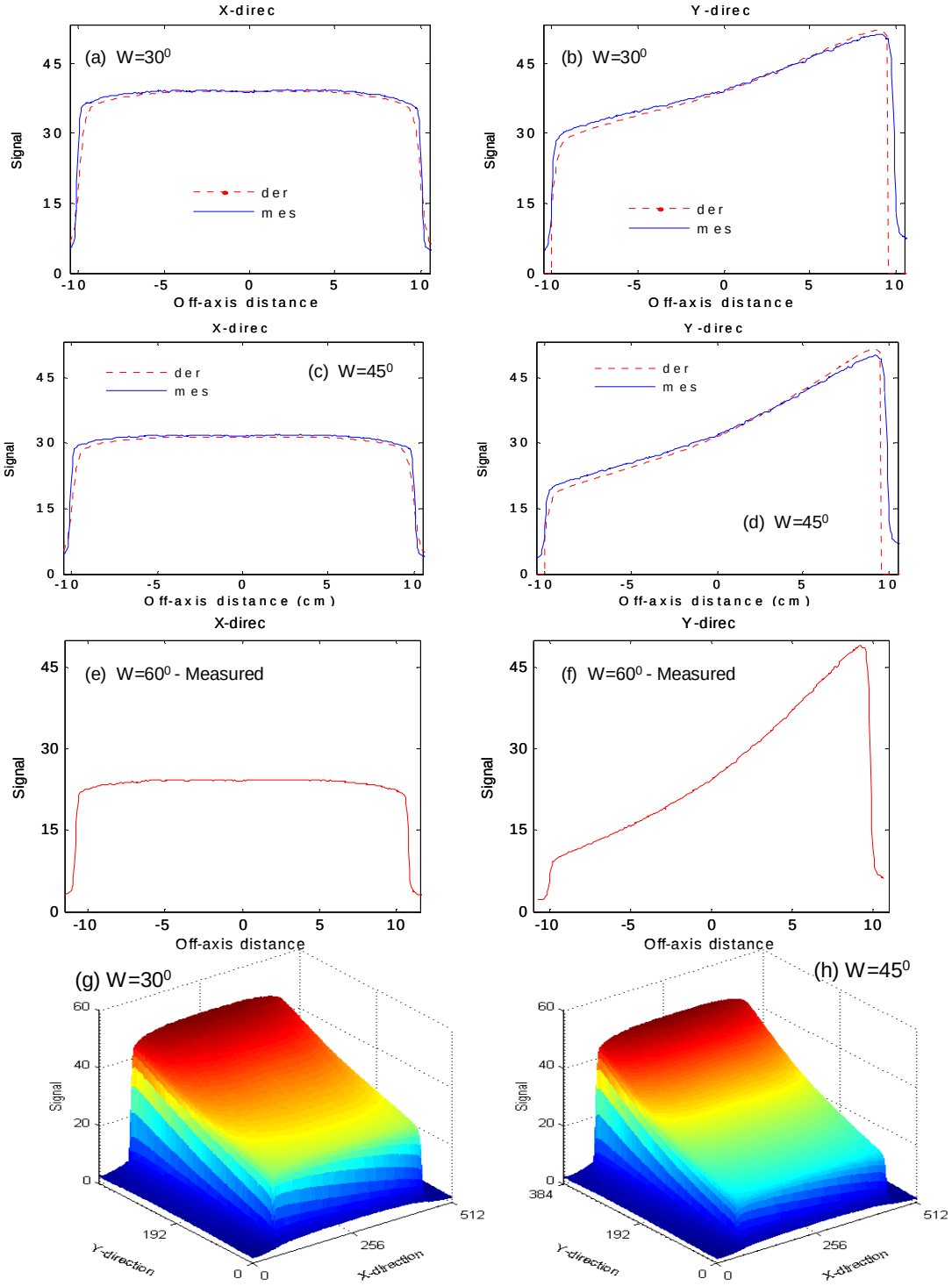

Figure 4-36. Comparison of measured (solid lines) and derived (dotted lines) profiles without any material in the beam $M_0^{\theta}(i,j)$ in the X and Y directions for EDW angles 30⁰ (figure 4-36 (a) and (b)) and 45⁰ (figure 4-36 (c) and (d)). Figures 4-36 (e) and (f) show the profiles for EDW angles 60⁰. Figures 4-36 (g) and (h) show a 3-D visualization of the fitting parameter for the EDW 30⁰ and 45⁰ angles respectively.

The results were for a symmetric field size of 20x20 cm^2 (X=20 cm, Y1=10 cm and Y2=10 cm). The comparison between measured and calculated profiles

shows that, in general, a good agreement has been achieved. The deviations near the fields' edges were less than 3%.

Figures 4-37 (a) and (b) show the variations of fitting parameter matrices $B_{w\theta}(i,j)$ and $A_{w\theta}(i,j)$ along the Y direction of the EPID respectively for open field (θ=0), 30^0, 45^0 and 60^0 EDW fields. It should be reiterated here that the $B_{w\theta}(i,j)$ and $A_{w\theta}(i,j)$ parameter for 60^0 EDW (W60-meas in figure 4-37) were only experimentally determined; they were used to determine $B_{w\theta}(i,j)$ and $A_{w\theta}(i,j)$ parameter for other EDW angles (i.e 45^0, 30^0 and 15^0). The results were for a symmetric field size of 20x20 cm^2 (X=20 cm, Y1=10 cm and Y2=10 cm).The results also compare the measured and derived data profiles (equations 3.22 and 3.23) of $B_{w\theta}(i,j)$ and $A_{w\theta}(i,j)$ for the EDW angles 30^0 and 45^0. As illustrated in the results, there are significant variations in $B_{w\theta}(i,j)$ and $A_{w\theta}(i,j)$ for open field and EDW fields. Unlike the open field data, which are symmetric about the central axis, the wedged parameters tend to reflect the slope of the wedge. This is a direct consequence of applying equations 3.22 and 3.23 to recalculate the parameters for wedged fields.

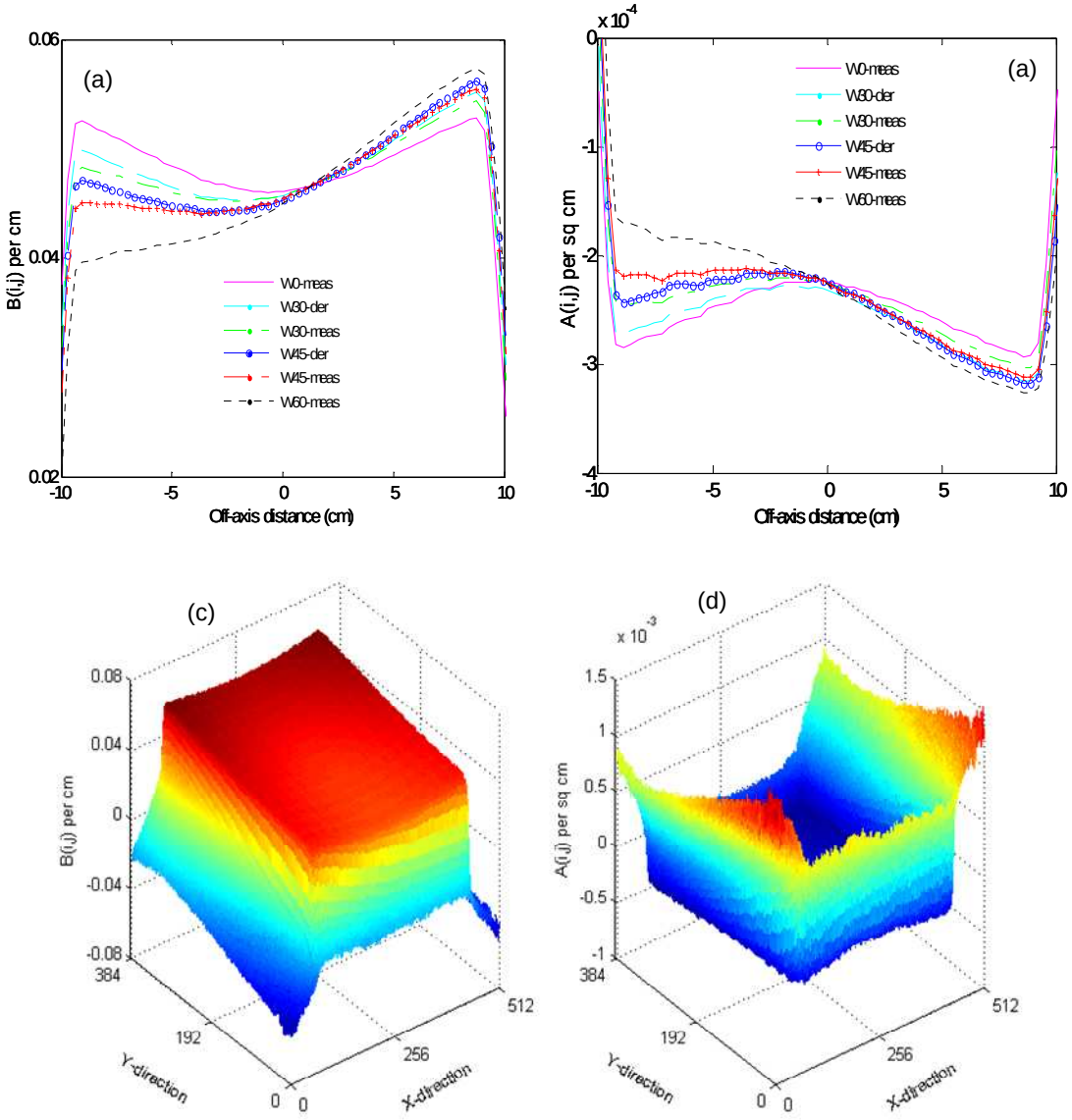

Figure 4- 37. Figures (a) and (b) show the variations of fitting parameter matrices $B_{w\theta}(i,j)$ and $A_{w\theta}(i,j)$ along the Y direction of the EPID respectively for open field (θ=0), 30^0, 45^0 and 60^0 EDW fields. The results also compare the measured and derived profiles for the 30^0 and 45^0. Figures 4-37 (c) and (d) show a 3-D visualizations of the fitting parameters for 30^0 EDW field.

The derived data using equations (3.19) – (3.24) were used for the exit dose (equation 3.25) calculations of EDW fields. Figures 4-38 (a) and (b) are 2D exit dose distributions for EPD and TPS respectively for a 15^0 EDW with 20x20 cm^2 (X=20cm, Y1=10 cm, Y2=10cm) field size. Figure 4-38 (c) shows the gamma index map, calculated at 3% dose difference and 3 mm distance to agreement criteria. The percentage area (points) that failed gamma criteria was 4.2%. Figure 4-38 (d) shows a 2D pixel-by-pixel percentage dose difference between the EPID and TPS exit dose distributions. The percentage dose differences were calculated as

$(\frac{D_{TPS} - D_{EPID})}{D_{TPS}} x100\%$. Figures 4-38 (e) and (f) are their corresponding exit dose cross plane profiles in the X and Y direction respectively.

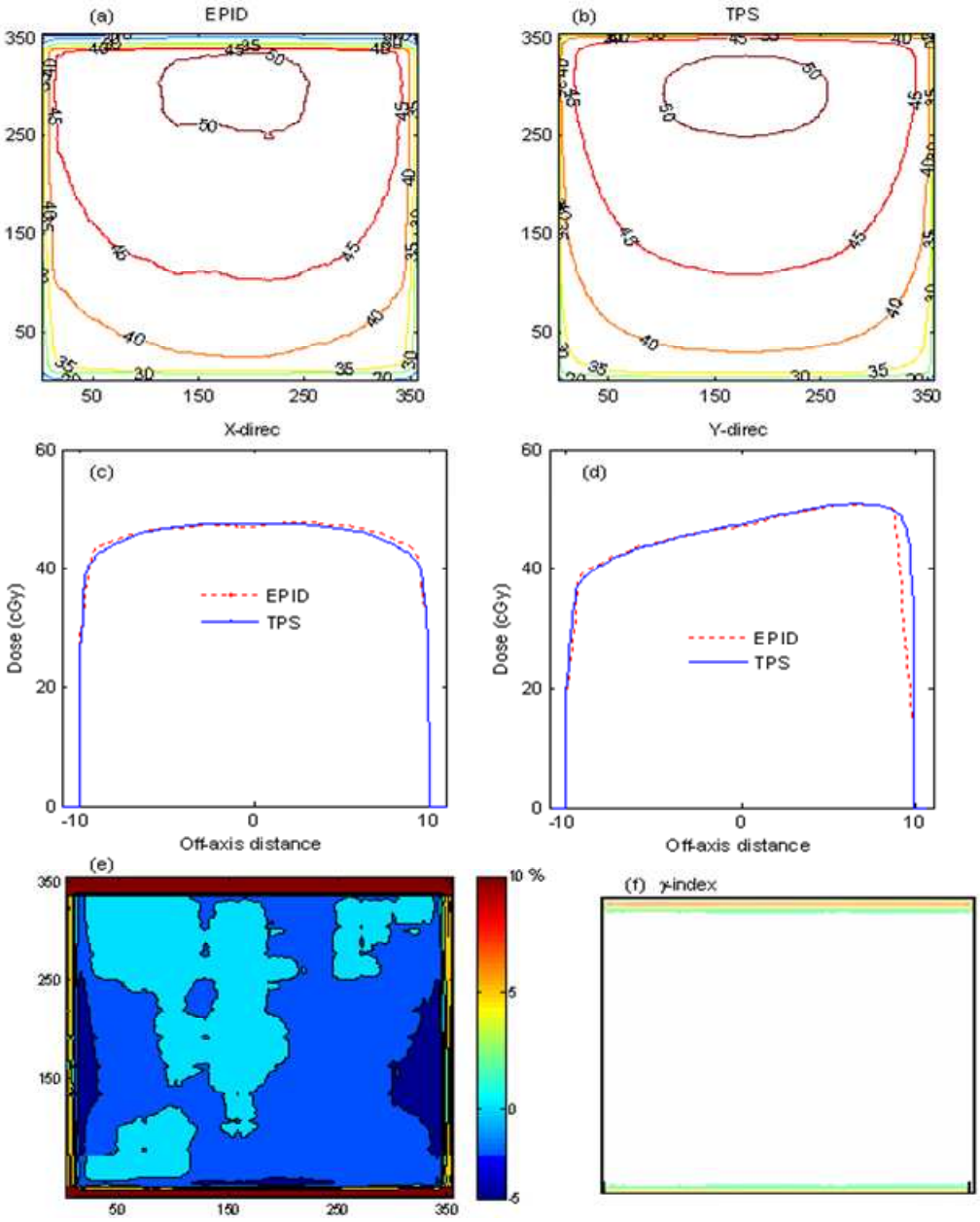

Figure 4- 38. Figures (a) and (b) are 2D exit dose distributions for EPD and TPS respectively for a 15^0 EDW with 20x20 cm^2. Figures (c) and (d) show their corresponding exit dose cross plane profiles in the X and Y direction respectively. Figures (e) and (f) show the percentage dose difference map and gamma index (3% DD and 3mm DTA) respectively.

The truncation of the GSTT profile to reduce it to a desired field size results in the automatic zeroing of EPID doses outside the irradiated region; hence for

comparison purposes the TPS doses are similarly zeroed outside the irradiation field.

Figures 4-39 (a) and (b) illustrate colourwash 2D exit dose distributions for EPID and TPS respectively for a 30^0 EDW with 15x15 cm^2 (X=15cm, Y1=7.5 cm, Y2=7.5cm) field size. Figures 4-39 (c) and (d) are their corresponding exit dose cross plane profiles in the X and Y direction respectively. Figure 4-39 (e) shows a 2D pixel-by-pixel percentage dose difference between the EPID and TPS exit dose distributions. Figure 4-39 (f) shows the gamma index map, calculated at 3% dose difference and 3 mm distance to agreement criteria. The percentage area (points) that failed gamma criteria was 5.5 %.

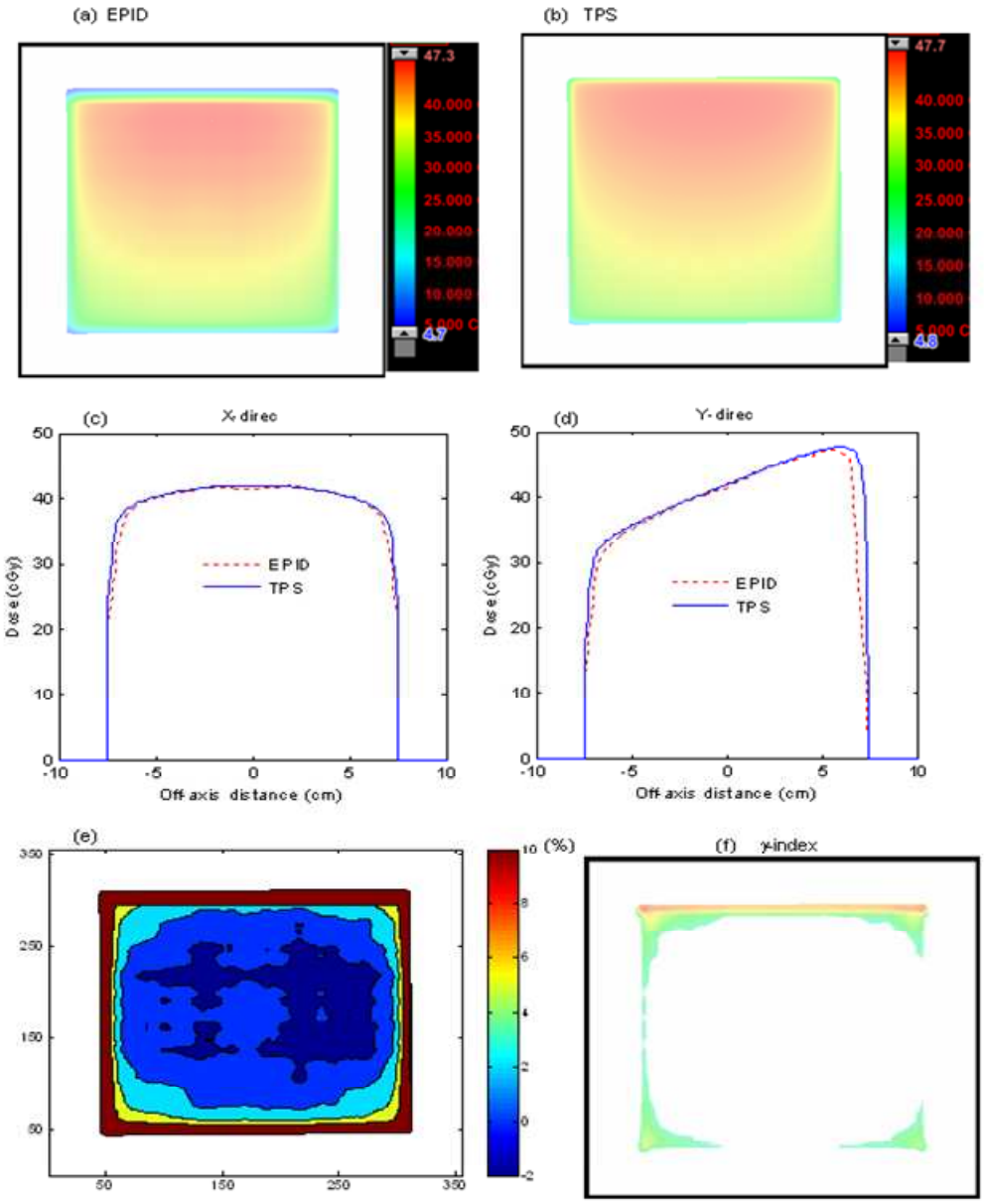

Figure 4- 39. Figures (a) and (b) are 2D colourwash exit dose distributions for EPD and TPS respectively for a 30^0 EDW with 15x15 cm^2. Figures (c) and (d) show their corresponding exit dose cross plane profiles in the X and Y direction respectively. Figures (e) and (f) show the percentage dose difference map and gamma index (3% DD and 3mm DTA) respectively.

Figures 4-40 (a) and (b) show EPID and TPS dose distributions respectively, for images obtained for the same setup as in figure 4-39 above, but images acquired at 200 MU. The calibration fitting parameters were all obtained for images at 100 MU. The purpose of this figure is to reaffirm that the same parameters can be used to predict EPL for EDW and hence dose, for any other non-reference MU. Figures 4-40 (c) and (d) also show the profiles dose difference. Discrepancies are

noted at the field edges where there are highest dose gradients, with largest differences at the level where the Y1 jaw stops.

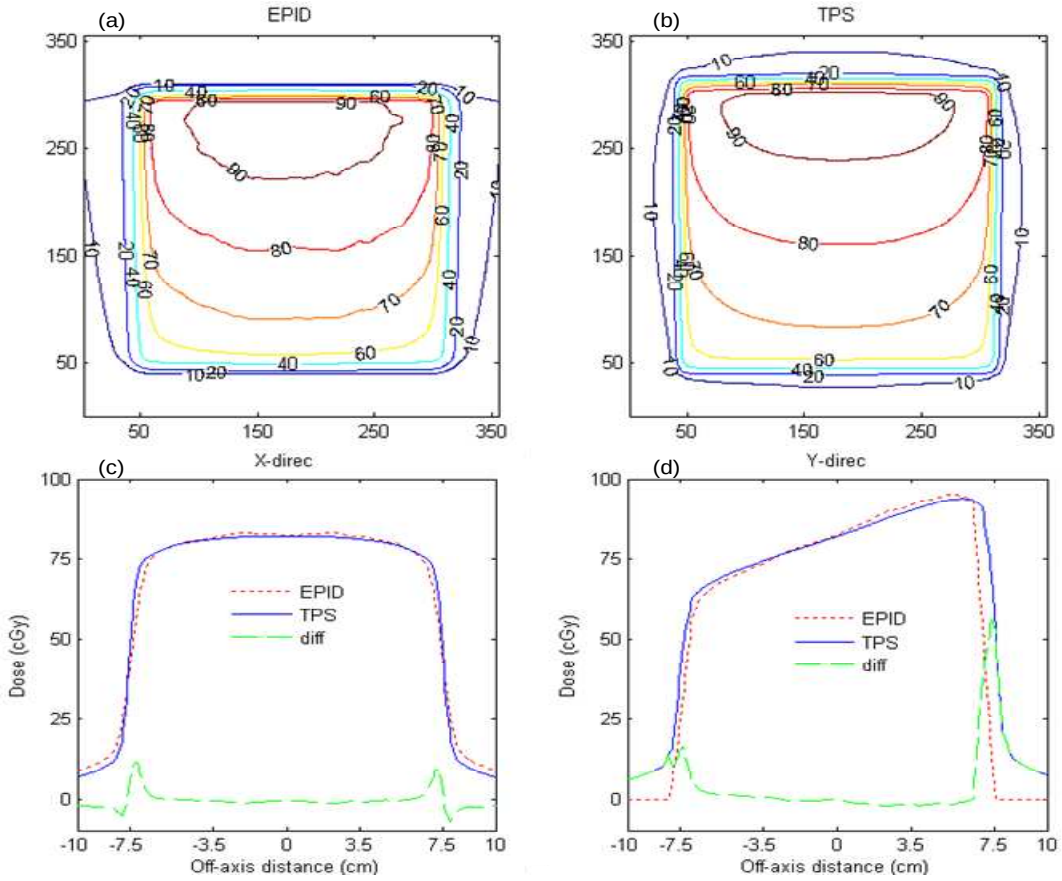

Figure 4- 40. Figures (a) and (b) are 2D exit dose distributions for EPD and TPS respectively for a 30^0 EDW with 15x15 cm^2 and 200 MU. Figures (c) and (d) show their corresponding exit dose cross plane profiles and dose differences (dashed lines) in the X and Y direction respectively.

Figures 4-41 (a) and (b) illustrate 2D exit dose distributions for EPD and TPS respectively for a 45^0 EDW with 10x10 cm^2 (X = 10.0 cm, Y1 = 5.0 cm, Y2 = 5 cm) field size. Figures 4-41 (c) and (d) are their corresponding exit dose cross plane profiles in the X and Y direction respectively. Figure 4-41 (e) shows a 2D pixel-by-pixel percentage dose difference between the EPID and TPS exit dose distributions while figure 4-41 (f) shows the gamma index map, calculated at 3% dose difference and 3 mm distance to agreement criteria. The percentage area (points) that failed gamma criteria was 7.6%.

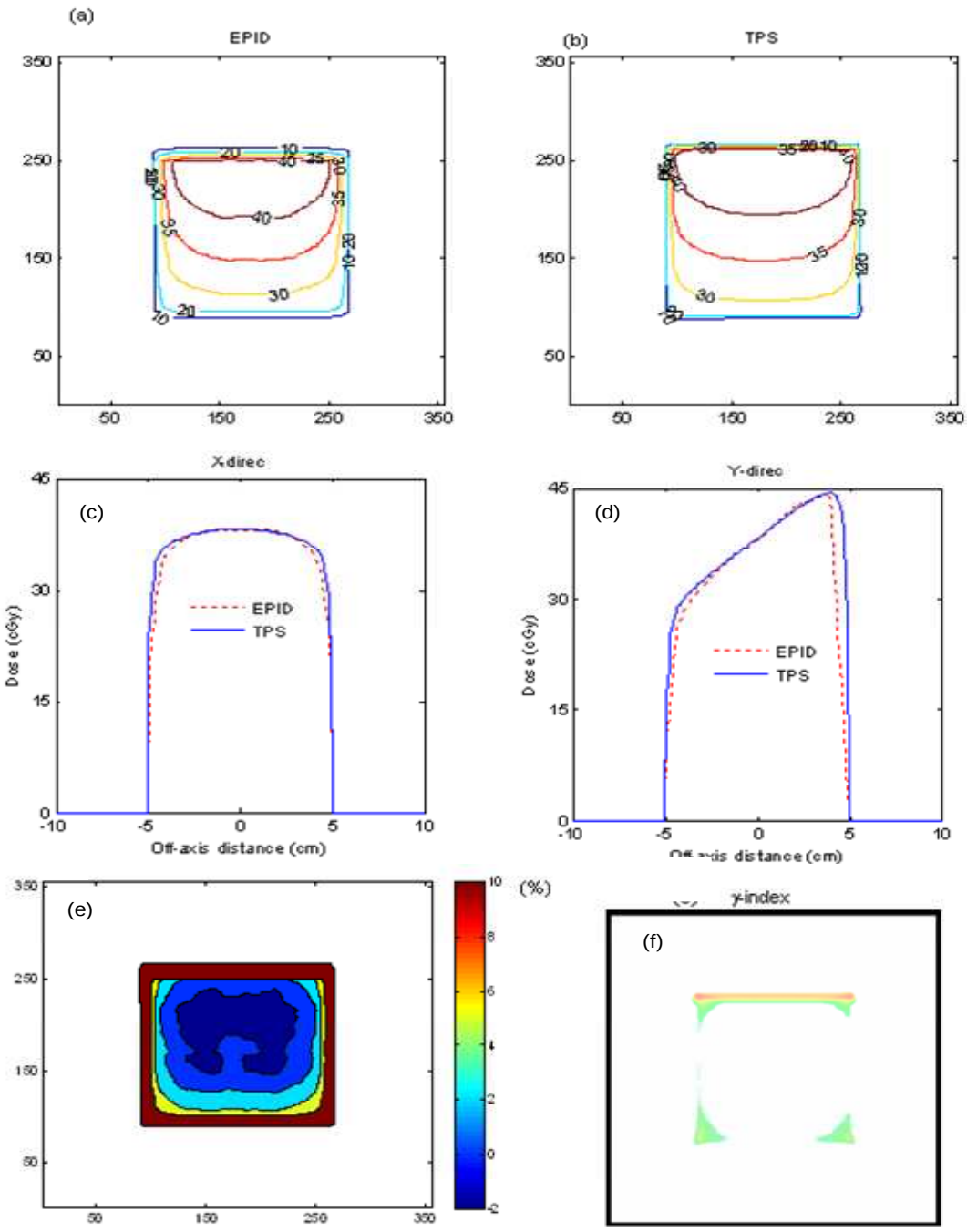

Figure 4- 41. Figures (a) and (b) are 2D exit dose distributions for EPD and TPS respectively for a 45^0 EDW with 10x10 cm^2. Figures (c) and (d) show their corresponding exit dose cross plane profiles in the X and Y direction respectively. Figures (e) and (f) show the percentage dose difference map and gamma index (3% DD and 3mm DTA) respectively.

Figures 4-42 (a) and (b) illustrate 2D exit dose distributions for EPD and TPS respectively for a 60^0 EDW with 20x20 cm^2 (X = 20.0 cm, Y1 = 10.0 cm, Y2 = 10 cm) field size. Figures 4-42 (c) and (d) are their corresponding exit dose cross plane profiles in the X and Y direction respectively. Figure 4-42 (e) shows a 2D

pixel-by-pixel percentage dose difference between the EPID and TPS exit dose distributions.

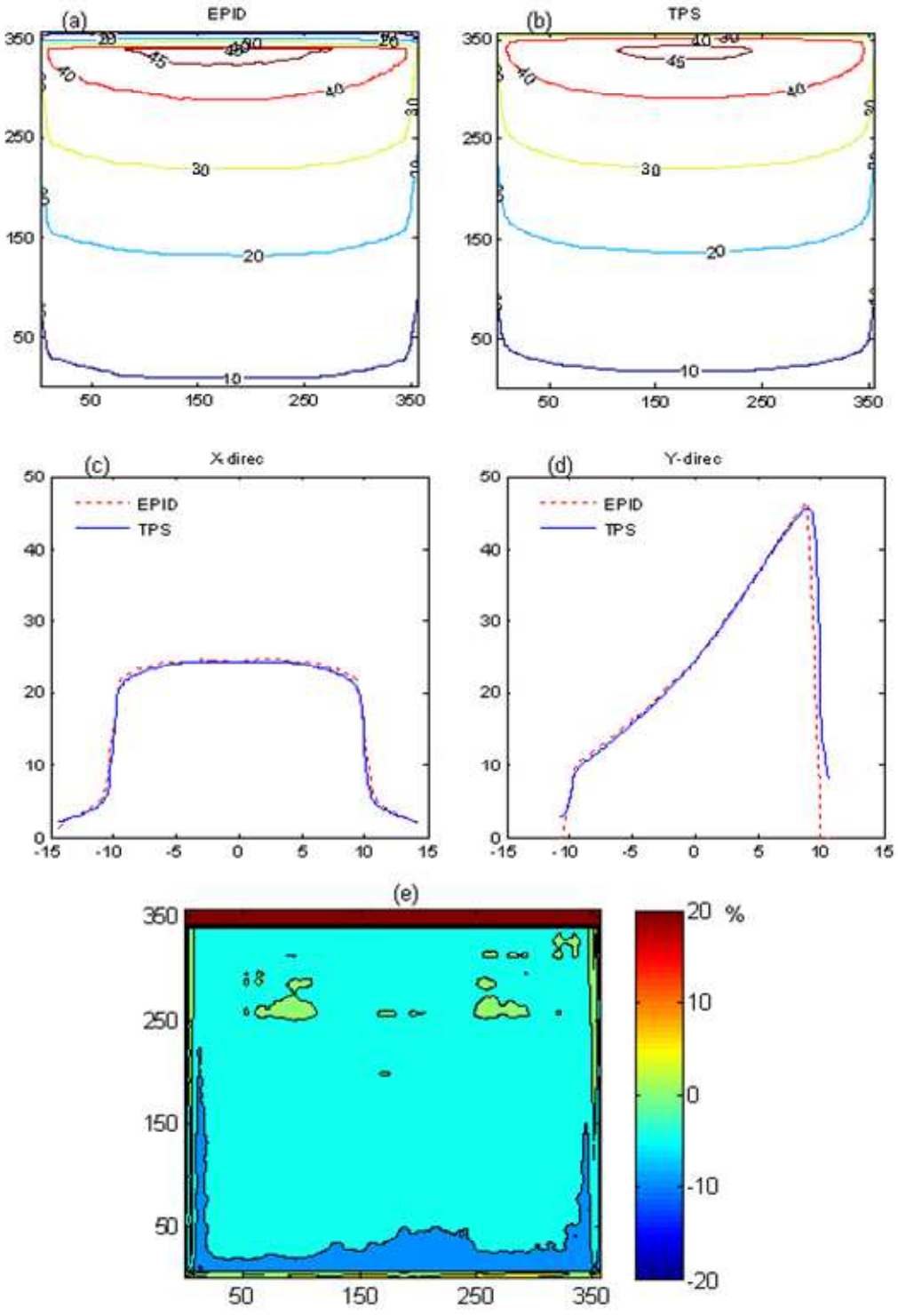

Figure 4- 42. Figures (a) and (b) are 2D exit dose distributions for EPD and TPS respectively for a 60^0 EDW with 20x20 cm^2. Figures (c) and (d) show their corresponding exit dose cross plane profiles in the X and Y direction respectively. Figure (e) shows the percentage dose difference map.

The profiles for all the test cases described in figures 4-38 to 4-42 are practically superimposed within 70% of the irradiated field. The largest deviations are towards the field edges (regions of steep dose gradients). Results in figures comparing exit doses in cross plane and 2D dose distribution for EDW show a good matching between the EPID and TPS for different EDW angles and field sizes. The cross plane dose comparisons for EDW indicate that the EPID had slightly lower doses of 1-2% at the field edges compared to TPS. This could be linked to the $M_o^{\theta}(i,j), B_{w\theta}(i,j) \quad and \quad A_{w\theta}(i,j)$ data matrices in figures 4-36, 4-37 (a) and 4-37 (b) respectively, which compare cross plane profiles of derived and measured coefficients. Towards the edges, both the derived $M_o^{\theta}(i,j) \quad and \quad B_{w\theta}(i,j)$ are lower than the measured, while $A_{w\theta}(i,j)$ is higher. An interplay between these factors results in an increase in EPL and hence a decrease in dose towards the field edges. Another possible reason for the failure at the edges is the utility of the GSTT described in equation 3.20. It tends to break down for large fields and deviations of 2-4% between measurement and calculated values have been reported (Gibbons 1998, Prado et al 2002 and Kuperman 2005). The variations in dose-rates during EDW dose delivery could be another factor that can affect EPID dose distribution, causing discrepancies. The readout of the a-Si array are synchronized with the beam pulses, hence EPIDs are calibrated at each accelerator dose-rate. The dark and flood field images are different at each doserate due to variation in image acquisition timing. Doserate variations that occur during EDW treatments could potentially affect the EPID signal, where the system is calibrated at a fixed accelerator dose-rate. Lastly, the disagreements are at the field edges (regions of steep dose gradients) where dose predictions may be inaccurate (Vieira et al 2003).

Figures 4-43 (a) and (c) compare typical profiles from EPID images acquired for the YI-IN and Y2-OUT for 30^o and 45^o EDW respectively. Figures 4-43 (b) and (d) show the same data superimposed onto each other by flipping the Y1-IN data. The images were acquired for 20x20 cm^2 with moving jaw Y1=10 cm, fixed jaw Y2=10 cm and X=20 cm at same SDD and 200 MU. The profiles were extracted from the centres of the images in the EDW motion direction. The results show that EPID pixel value responses for Y1-IN and Y2-OUT are practically symmetrical, implying that data for Y2-OUT jaw orientation can be created from

that of Y1-IN jaw orientation by data mirroring, saving valuable re-measurement time.

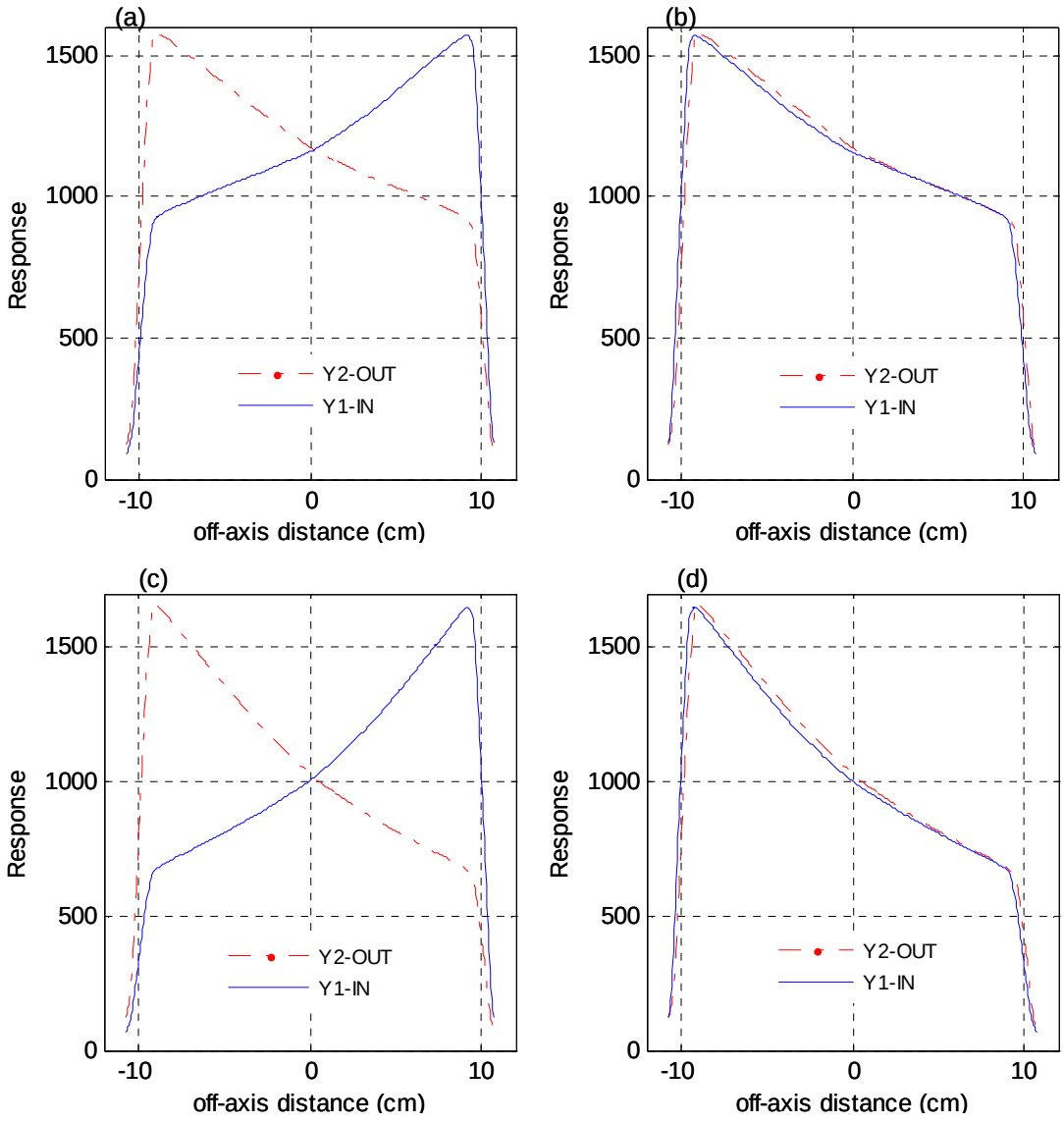

Figure 4- 43. Figures (a) and (c) compare EPID image profiles for Y1-IN (solid lines) and Y2-OUT (dash lines) for 30° and 45° EDW respectively. Figures (b) and (d) show the same data superimposed onto each other by flipping the Y1-IN data.

All the EDW coefficients data and test cases in this study were acquired with Y1-IN jaw orientations. Results from figure 4-43 which is also in agreement with Greer et al (2007), indicate that EPID pixel value response for Y1-IN and Y2-OUT for the same radiation field settings are practically symmetrical. Hence the data fitting coefficients for Y2-OUT can be created from the Y1-IN by data mirroring, saving valuable time of re-measurements.

Figure 4-44 compares EDW dose distributions for 15x15 cm^2 symmetric field size, Y2-OUT jaw motion and 100 MU. The EPID data used for dose calculation were obtained by data mirroring as described above. The difference between the TPS and EPID dose was calculated for each point within the 2D data matrix. The cross plane dose differences in figure 4-44 (c) (displayed as a dashed line) illustrates that most of the discrepancies are at the edges, similar to the Y1-IN jaw orientation. Figure 4-44 (d) shows the gamma index map, where the percentage of area (3% DD and 3mm DTA) failed was 6.9.

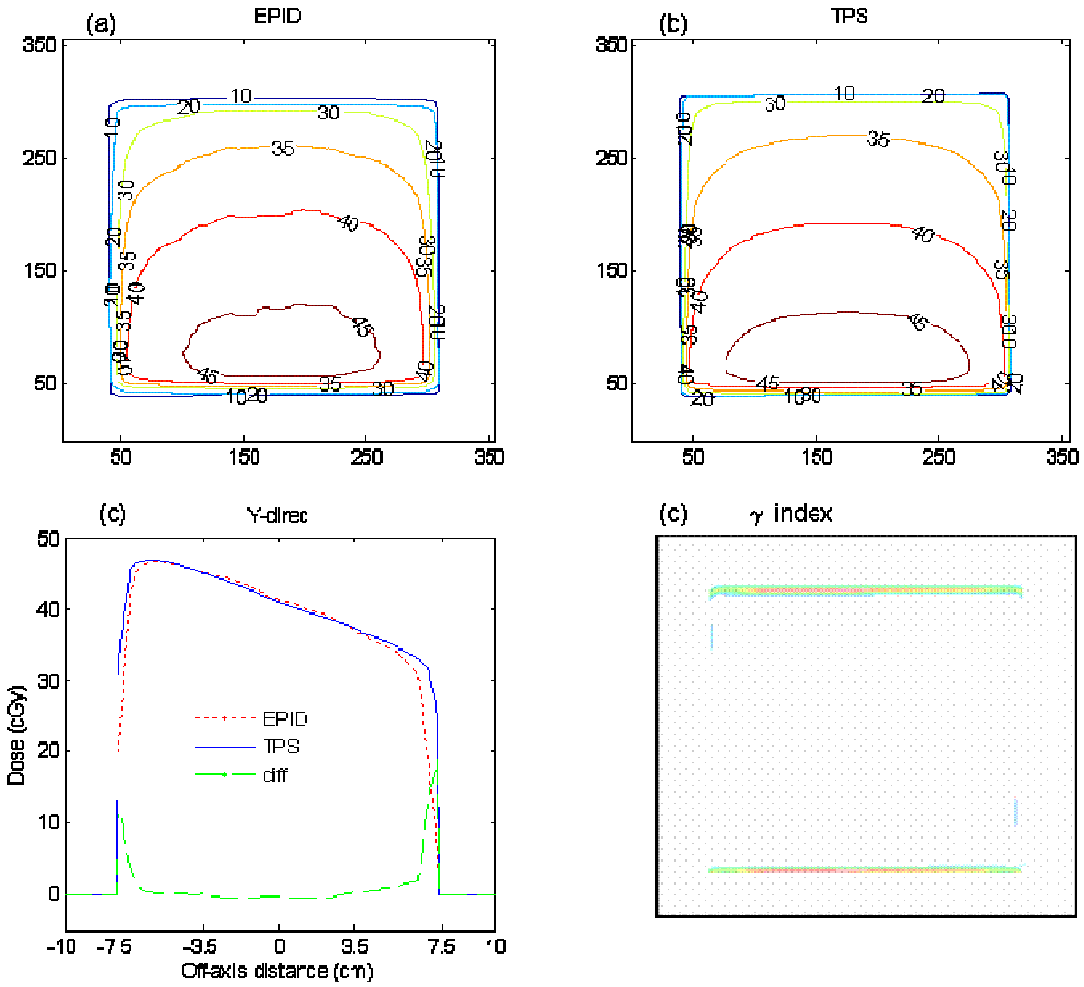

Figure 4- 44. Figures (a) and (b) are 2D exit dose distributions for EPD and TPS respectively for a 30^0, Y2- OUT, EDW with 15x15 cm^2. Figure (c) shows their corresponding exit dose cross plane profiles and dose differences (dashed lines) in the Y direction. Figure (d) is the gamma map (3% DD and 3mm DTA) computed from figures (a) and (b).

Figure 4-45 shows another case were the Y1-IN data were used to calculate the exit dose for an EPID acquired image. The results in this figure compare MapCHECK (a), TPS (b) and EPID image (c) dose distributions, acquired with 45^0

EDW, 15x15 cm^2 symmetric field size, Y2-OUT jaw motion, collimator angle 90^0 and 200 MU. The EPID data used for exit dose calculation was obtained by mirroring the Y1-IN data as described above. We used a rotated collimator angle in this example to show that the fitting data coefficients can be used at various beam orientation. The percentage of area in figure 4-45 where the gamma index (3% DD and 3mm DTA) failed were 5.5, 7.2 and 7.8 for the TPS vs MapCHECK, EPID vs MapCHECK and TPS vs EPID respectively. Reasonably large differences are at the field edges as illustrated by the EPID vs MapCHECK dose-difference profile in figure 4-45 (d). However this is not due to using the Y1-IN data to compute dose for Y2-OUT, as results in figures 4-38 and 4-42 also show a similar effect at the edges.

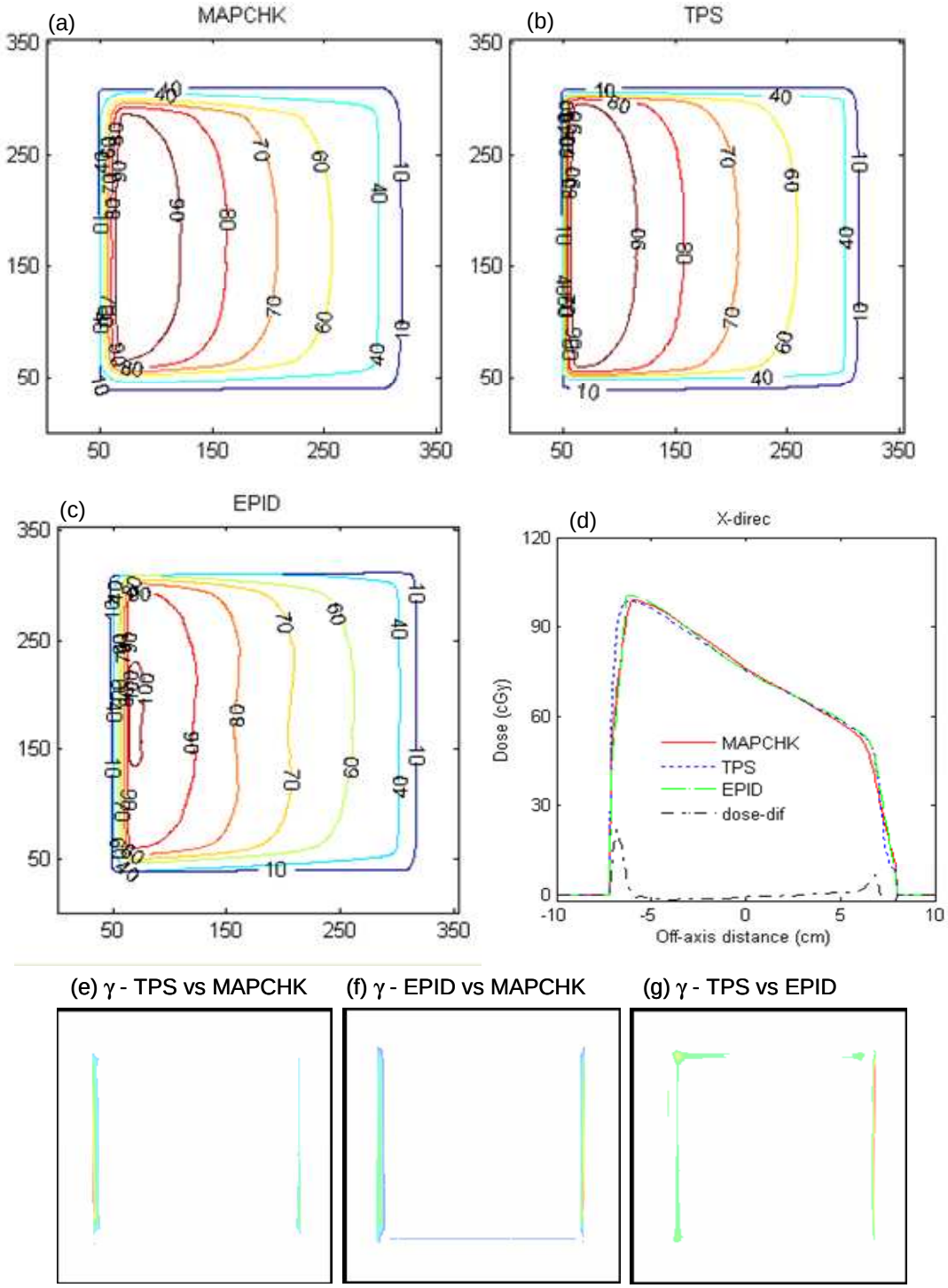

Figure 4- 45. Figures (a), (b) and (c) show 2D absolute exit dose (cGy) distributions measured with the MapCHECK device, calculated with TPS and those from EPID images respectively, for a 45^0, Y2- OUT, EDW with 15x15 cm^2. The image was acquired with 200 MU at collimator angle 90^0. Figure (d) shows the corresponding exit dose cross plane profiles and dose differences between EPID and MapCHECK profiles (dot-dashed line) in the X direction. Figures (e), (f) and (g) demonstrate the respective 2D gamma maps, evaluated at 3% DD and 3 mm DTA.Figure (d) is the gamma map (3% DD and 3mm DTA) computed from figures (a) and (b).

Figures 4-46 and 4-47 show exit dose comparisons for the anthropomorphic phantom case in figure 3-7(c) as described in section 3.2.6, irradiated with 30^0 (Y1- IN, collimator angle 0^0) and 45^0 (Y2- OUT, collimator angle 90^0) EDW fields respectively. The EPID images were acquired and TPS calculations were done with 100 MU and with 15x15 cm^2 symmetric field. Figures 4-46/4-47(a) and (b) compare 2D TPS and EPID dose contours respectively. Figures 4-46/4-47(c) and (d) compare TPS and EPID cross plane profiles in the X and Y directions respectively. Figures 4-46(e) and 4-47(e) are the respective percentage dose difference maps between the TPS and EPID. Figures 4-46(f) and 4-47(f) show the acquired EPID images from which the dose distributions in figures 4-46(b) and 4-47(b) respectively, were calculated. The EPID and TPS dose distributions illustrated in the two examples above, compare favourably well in low dose regions, but significant deviations are noticed in high dose areas (towards the end position of the moving jaw).

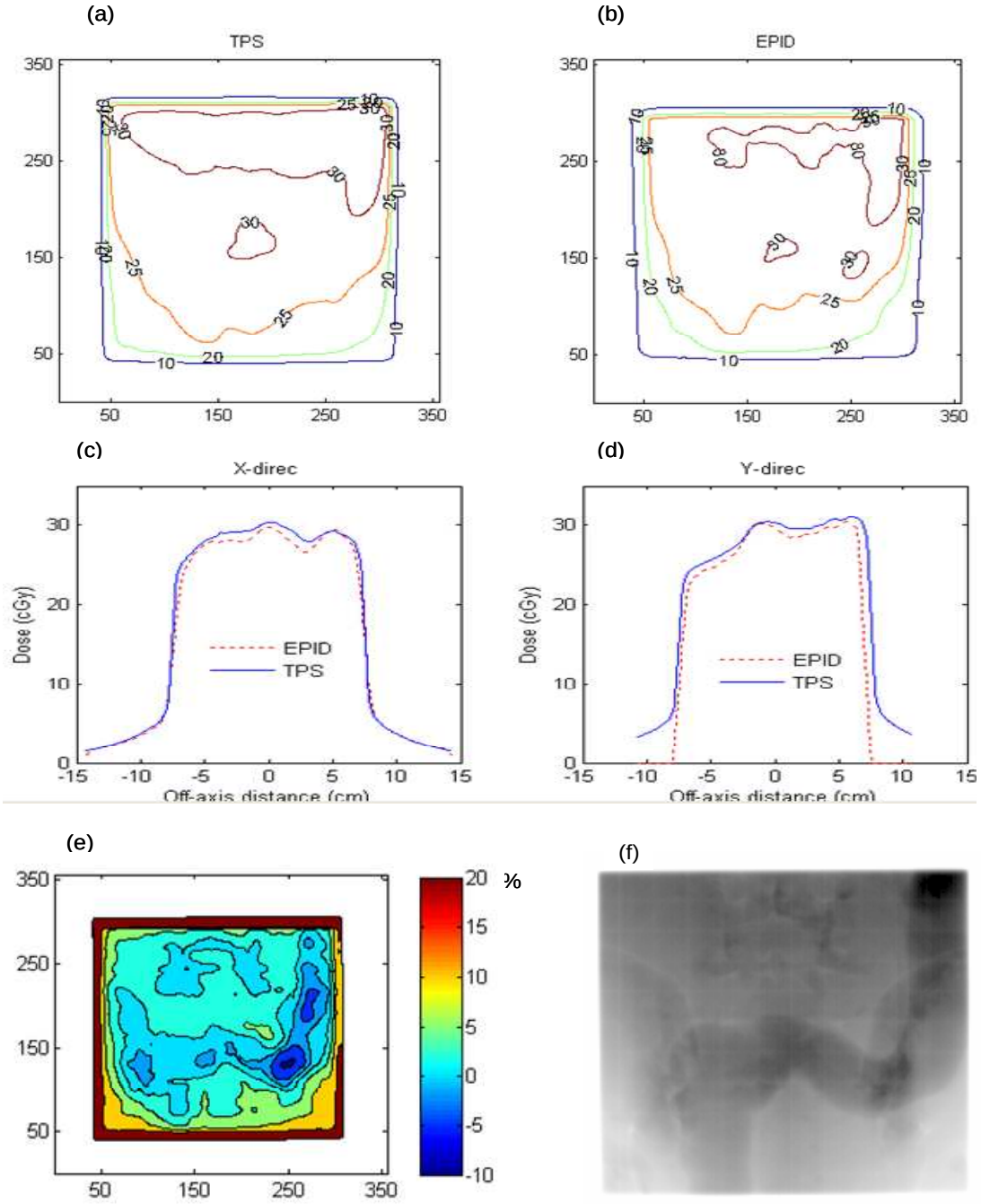

Figure 4- 46. Exit dose comparison for the anthropomorphic phantom case in figure 3-7 as described in section 3.2.4.4, irradiated with 100 MU, 30^0 EDW, Y1- IN, collimator angle 0^0, with 15x15 cm^2 symmetric field. Figures (a) and (b) compare 2D TPS and EPID dose contours respectively. Figures (c) and (d) compare cross plane profiles in the X and Y respectively. Figure (e) shows the percentage dose difference map between the TPS and EPID doses. Figure (f) is the acquired EPID image from which the dose distribution in figure (b) was calculated.

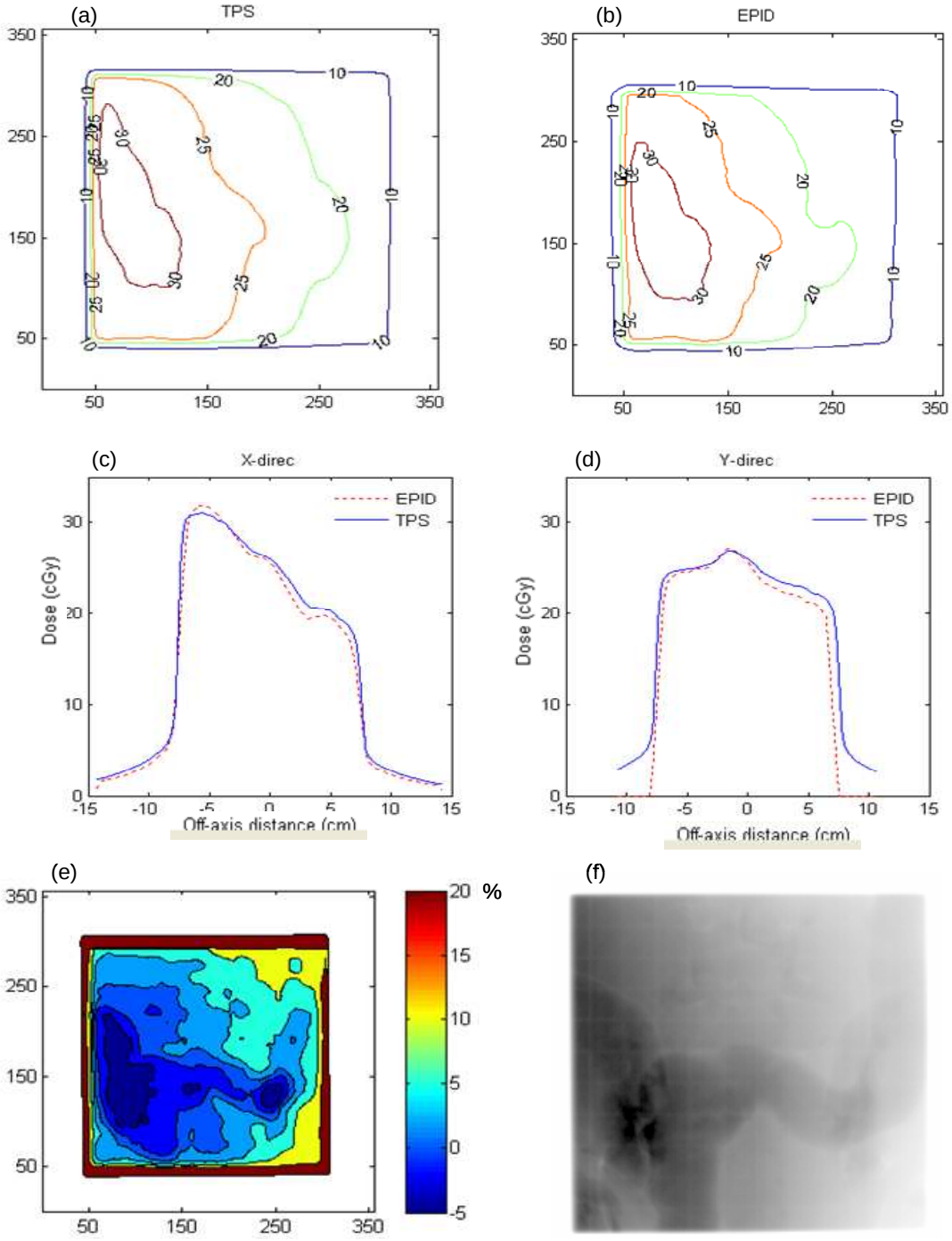

Figure 4- 47. Exit dose comparison for the anthropomorphic phantom case in figure 3-7 as described in section 3.2.4.4, irradiated with 100 MU, 45^0 EDW, Y2- OUT, collimator angle 90^0, with 15x15 cm^2 symmetric field. Figures (a) and (b) compare 2D TPS and EPID dose contours respectively. Figures (c) and (d) compare cross plane profiles in the X and Y respectively. Figure (e) shows the percentage dose difference map between the TPS and EPID doses. Figure (f) is the acquired EPID image from which the dose distribution in figure (b) was calculated.

4.3.4 Comparison of exit dose results with other literature

The present exit dose results for open and MLC shield fields can be compared to the work done by Parsaeia and El-Khatib (1998), Pasma et al (2002) and Chen et al (2006). Parsaeia and El-Khatib (1998) investigated the dosimetric characteristics of a scanning liquid-filled ionization chamber (SLIC) EPID. To assess the system's response in relation to incident radiation beam intensity, a series of characteristic curves were obtained for various field sizes and nominal energies of 6 and 10 MV photons. This study indicated that the response of the imaging system was dependent on incident radiation intensity and could be described to within 1% accuracy on central axis using a square root function. They used attenuating homogeneous phantom materials with thicknesses ranging from 0 – 22.5 cm and field sizes 5x5 cm^2 and 10x10 cm^2. This study compared relative transmission dosimetry with ionisation chamber measurements. Portal dose measurements at the plane of the detector, on central axis of the beam showed that the imaging system was capable of measuring the portal transmission dose to within 3% of the ionisation chamber results for homogeneous material. For 2D dosimetry applications, the system was calibrated with a 10 cm Perspex block used as beam flattening material on the detector cassette to correct for variations in individual ion chamber sensitivity and the effect of non-uniform beam profiles produced by the flattening filter. Open and wedged dose profiles measured agreed with ion chamber measured profiles to within 3.5% accuracy. The main limitation of this study was the requirement of additional material (10 cm Perspex block) to be placed on top of detector, which can be an obstacle in lateral fields. The profile agreements are comparable with results from our study.

Pasma et al (2002) used a fluoroscopic CCD camera based EPID for evaluating portal dosimetry of static wedged fields, an extension of the method they had published for open fields Pasma et al (1998). Their methods are based on calculation of 2D functions, describing the transmission of a photon beam through a patient for both open and wedged fields. The transmission functions are used for the prediction of portal dose images (dose distribution behind the patient) in a plane normal to the beam axis, which are compared with PDIs measured with an EPID. The calculations are based on the planning CT scan of the patient and on the irradiation geometry as determined in the treatment

planning process. Similar to work by Parsaeia and El-Khatib (1998), these studies were evaluated by computing percentage transmissions (main distinction between these studies and our study were we compare dose directly), measured with an ionisation chamber. The results indicated that for low and high energy photon beams of 6 and 23 MV, good agreement of approximately 1.2% (excluding points at steep dose gradient) were found between calculated and measured transmissions for homogeneous Perspex slabs (thicknesses of 10-30 cm) and a thorax phantom. The agreement in profiles for both open and wedged fields, shows noticeable large deviations at field edges, comparable to our results.

The Chen et al (2006) group slightly modified a convolution calibration method that has previously been used to calibrate liquid-filled ion and camera-based EPIDs, to calibrate a Siemens Perkin-Elmer EPID detector for exit dosimetry. The modified model utilised two convolution kernels: one to describe the flat panel detector and one to describe the water dose. They also represented the effects of the EPID energy response and the variations in the beam energy spectrum using a tabulated conversion function. The study limited itself to solid water phantoms less than 11 cm in thickness and the anthropomorphic (head) phantom. This is in contrast with the present study, where exit doses for thicknesses in the range of 5 to 32 cm and a pelvis anthropomorphic phantom have been calculated. For the centred fields excluding the smallest, the Chen et al (2006) EPID profiles fell within 3.1% of the ionisation chamber measured dose. This is very much in agreement with the our results where, within the irradiated regions, the average dose differences (computed for all cases and for 80% of the irradiated field) between the EPID and TPS is within 3%. The Chen et al (2006) study also indicated that, out of the field, the percent difference between the calibrated EPID and ion chamber measured signals was much greater due to the low signal level in this region. They observed percent differences ranging from −10% to as much as 65%; which is not much different from what we measured in the MLC shielded regions. The Chen et al (2006) exit dose verification study did not include wedged or EDW fields. The main limitation in the Chen et al (2006) study was the frame acquisition / calibration capabilities of their EPID detector, which restricted their analysis to single frame images of 2–4 MUs. The study concluded that to acquire clinical exit-beam measurements, suitable multi-frame acquisition mode would need to be implemented.

In all the studies discussed above, the authors used static wedged fields, rather than EDW used in our study. There is scanty information in literature about portal dosimetry of EDW using EPID. The work done by Greer and Barnes (2007) only assessed the dosimetric performance of an a-Si EPID for measurement and quality assurance of enhanced dynamic wedge profile and wedge factor. Similar work was done by Al Kattar (2009), and also addressed only quality assurance of enhanced dynamic wedge using the a-Si500 EPID. This work therefore, provides a novel assessment of the use of EPID to predict EPL and exit dose in routine clinical treatments, including EDW fields.

CHAPTER 5: CONCLUSIONS AND FUTURE WORK

5.1 Conclusions

The dosimetric properties of eleven accelerators in clinical use were examined. The EPID age and image acquisition system showed influence on the results with the system-II giving better data reproducibility and linearity fit than system-I. Uniformity was within 95% and independent of detector. Dose-rates and EPID field size factors have similar curves, thus can be described by analytical functions. Memory effects are system and age independent. System-II performance data are in agreement with other Varian a-Si500 EPID reports. Deviations are seen with the system-I which are attributed to detector age and acquisition software. Generally the results confirm the suitability of all the EPIDs for quantitative dosimetry, though there is a significant improvement in uniformity of response in those devices using software/hardware versions IAS3/IDU-20 over the older IAS2/IDU-II.

The objective of radiotherapy is to deliver an absolute dose to a reference point with an uncertainty of ± 3%. The results obtained in this work show that detectors with software/hardware versions IAS3/IDU-20 have a degree of accuracy well in excess of that required to allow their use in routine verification of delivered dose within this tolerance. However limitations in reproducibility and linearity mean that detectors with software/hardware versions IAS2/IDU-II are less suitable for routine quantitative IMRT dosimetric verification.

Various authors have approached portal dosimetry by radiological thickness / EPL calculations to verify treatment delivery when correcting EPID-image-derived dose data. This work has proposed a simple means to convert EPL to estimated dose, using an analytical method for the accurate prediction of in vivo dose using an EPID. The PETD data, boundary and envelope profiles have been used to convert the EPL into dose information at the exit. The developed tool is capable of converting EPID images into 2D dose maps, thus giving a real-time measure of the actual patient dose delivered during each treatment

fraction. Following some simple commissioning measurements, the tool may be implemented on almost any radiotherapy unit with an EPID. This will allow *in vivo* dosimetry to become a routine part of radiotherapy quality assurance, thus improving patient safety in radiotherapy centres. The method takes into account inhomogeneities at each pixel in the process of establishing the EPL. The determined EPL by the QCM method for homogeneous water and non-water equivalent materials are within ± 3mm. Furthermore, the evaluation of the method at two different beam energies provides a significant extension to previous work.

It has been shown that the QCM, applied to EPID images of homogeneous solid water phantoms, can be used to accurately predict 2D exit doses for conformal and EDW fields. The inclusion of MU correction improved the EPL determination and hence exit dose for various field sizes and thicknesses. The irradiated field areas can be accurately determined from EPID images to within ± 1% uncertainty. Good agreement between the EPID predicted, MapCHECK measured and TPS calculated dose distributions were obtained for conformal and EDW test cases, with more than 90% of pixels within the irradiated field meeting a gamma index criteria of 3% DD and 3mm DTA. But it should be emphasised that, for practical in vivo dosimetry, these areas of reduced accuracy at the field edges are less important.

The method requires the acquired EPID image, the delivered number of monitor units and angle of EDW (if used) as clinical input parameters to predict the equivalent path length (EPL) and exit dose. It is the author's belief that the algorithm developed here provides a clinically effective high resolution 2D in vivo dosimetry system for radiotherapy. It is concluded that the EPID QCM is an accurate and convenient method for online *in vivo* dosimetry and may therefore replace existing techniques.

The pixel sensitivity reproducibility of the Varian EPID has been reported to be within 1% (Greer et al 2003, Menon et al 2004, Kavuma et al 2008). It was established that the fitting coefficients were reproducible to within 2% (section 4.2.1) and also the EPL is reproducible to within ± 2mm (section 4.2.5.1). This consistency in response gives a high level of confidence in the sensitivity of the system for its intended in vivo dosimetry use. Grattan et al (2010) investigated the positional stability of the Varian EPID R-arm and Exact-arm support systems and concluded that the latter, which also is used in this study, provided more

reproducible positions than the former. This study indicated that the mean misalignment error for the Exact-arm was approximately 2.0 mm, which may not cause adverse dosimetric effects.

It is indicated in the materials and methods (section 3.2.1) that test plans with desired field settings were created using the Varian RT chart software and that these were scheduled in the time planner, exported to the accelerator and treatments executed in the clinical mode, acquiring single integrated images at the end of each treatment. The acquired images were then opened using the Varian portal dosimetry software and exported as ASCII files for analysis in Matlab. This means that our transit dosimetry algorithm should require only minimal work to be integrated into the existing commercial Varian portal dose image prediction (PDIP) and other operating / clinical software.

In the current study, we used the Varian a-Si 500 with IAS3 (pixel format 384x512 and pixel pitch in each dimension of 0.784 mm x 0.784 mm). The developed method can easily be adapted to the Varian's imager system (a-Si 1000 with pixel format 768x1024 and pixel pitch in each dimension of 0.392 mm x 0.392 mm) that comes with TrueBeam (Varian's new brand of linear accelerators). It will require image acquisitions on linac with these new imagers to determine the correction coefficient matrices A(i,j), B(i,j) and the open field matrix $M_0(i,j)$. The rest of the algorithm will remain unchanged. A change in beam characteristics has a significant effect on fitting coefficients and as indicated in section 4.2.1, the flattening filter has a significant influence on the shape of the fitting matrices. For TrueBeam that has the option of producing flattened and unflattened beams, two sets of data will be required for dose verification. Alternatively, the effect of the flattening filter on matrices A(i,j), B(i,j) and $M_0(i,j)$ can be characterised, but this needs further investigation.

5.2 Possible future direction

Despite the promising Gamma-Dose analysis, there is still work that needs to be done on developing the procedure. Often it is not straightforward to interpret the compared 2D dose deviations in terms of clinical implications for the patient. Therefore a method to derive 3D patient dose, based on EPL measured with an EPID needs to be established, that is the 2D EPID dose must be translated to a patient dose. Several authors have investigated the translation of EPID dose to patient dose at points along the central axis (Chang et al, 2000);

the patient dose at the midplane (Boellaard et al, 1998) and the full 3D patient dose distribution (Patridge et al, 2002 and Louwe et al, 2003). For an accurate dose determination in the target area, tissue density data of the patient during the actual treatment fraction is essential. These data can be obtained by performing an additional cone-beam CT scan just before the fraction in which the dose measurement is performed. By extending the current procedure to incorporate Cone- Beam CT (CBCT) images of the patient, taken before treatment, the calculated exit dose from EPID can be back projected into the CT data, and this will permit volumetric (3D) verification. Since the current algorithm has been verified extensively, particularly for the EDW, it would be expected that the 3D result will be more generally applicable to a wider range of clinical situations, comparable to the work done by:

1) McDermott et al (2008), who use CBCT images to reconstruct a phantom for in-vivo calculation. They use the EPID for transit dosimetry and then assumed that the CBCT-based phantom is homogeneous and water-like.
2) Chen et al (2006), whereby in their procedure they reconstructed the dose delivered to the patient based on treatment-time portal images and pre-treatment MV CBCT images of the patient. They calibrated the MV CBCT in terms of electron density and used this information together with dosimetric calibration of the portal imager for dose calculation.

Predicting the transmitted dose based on cone-Beam CT data acquired at treatment should ideally be performed in the future and this would improve the effectiveness and reliability of transit in vivo dosimetry techniques.

Further work needs to be done to assess the algorithm in situations not involving normal beam incidence on the phantom / patient. More investigation is needed to extend the scope of the algorithm to model doses in asymmetric EDW fields. Gibbons (1998) and Prado et al (2002) indicated that although simple in approach, the MU fraction model's prediction of EDW factors accurately, is limited in large or asymmetric fields. They suggested various means of modifying the MU fraction model to generalise it for both symmetric and asymmetric beams, based on beam-segmentation superposition. These beam summation methods are however, difficult to implement in routine clinical MU calculation schemes. Critical parameters and factors that may result in discrepancies between predicted and measured doses during clinical application may include

SDD variations, patient target volume variations, etc. These need to be well characterised.

Once the 3D verification is complete, the QCM will then be applicable for all static, conformal and EDW delivery techniques. Further development of the procedure will be necessary to extend verification to techniques that involve dynamic motion of MLCs during treatment, e.g. IMRT and Rapidarc. To use the QCM for dynamic treatment verification will require further testing. First, the linearity of the EPID panel response with respect to irradiation time, as determined by the moving MLCs, should be investigated. The fitting coefficients ($A(i,j)$, $B(i,j)$, $M_o(i,j)$) which are the pillars in the conversion of the EPID signal to EPL, need to be re-examined for the case of dynamic MLCs.

It may be possible to increase the EPID signal strength by changing the time between reset frames and imaging frames, and by decreasing the number of frames per sync pulse. Although the EPID dosimetric response will be raised, it may introduce more noise into the image. Hence this was not investigated as we attempted to keep the image acquisition set-up conditions as close as possible to the clinical imaging conditions.

Investigation in clinical situations is the subject of our continued work in order to demonstrate the usefulness, strengths and limitations of the current algorithm on actual patients.

Appendix A: Solving Quadratic Equations

The solutions of the quadratic equation

$$ax^2 + bx + c = 0 \qquad A1$$

where a, b and c are real fixed numbers, are given in exact form by the well known quadratic formula given by

$$x = \frac{-b \pm \sqrt{(b^2 - 4ac)}}{2a} \qquad A2$$

However if a, b and c are optimised values as in the case for the derivation of A(i,j) and B(i,j) in section 3.2, giving rise to unreasonable roots, then continued fractionation (iteration) is used to approximate the solution. The idea is that a function is found that, given an approximation of the solution as input (x_{old}), outputs a more precise approximation (x_{new}). If this function is used iteratively by recycling the values produced on each iteration, better and better solutions will be reached. This process can be continued until the required level of precision is reached.

The iterative scheme given in section 3.2 comes from rearrangement of equation (1) obtained as follows.

Starting with: $ax^2 + bx + c = 0$

Taking *c* to the right side of the equation gives: $ax^2 + bx = -c$ *A3*

Adding ax^2 to both sides gives: $2ax^2 + bx = ax^2 - c$ *A4*

Take out a common factor: $x(2ax + b) = ax^2 - c$ *A5*

Divide through

$$x = \frac{ax^2 - c}{2ax + b} \qquad A6$$

Set up the iterative scheme as

$$x_{n+1} = \frac{ax_n^2 - c}{2ax_n + b} \qquad A7$$

where x_n is the old solution (x_{old}) and x_{n+1} is the new solution (x_{new}), which is the second order iterative method scheme and converges quickly to the roots of the quadratic.

MATLAB ALGORITHM FOR DETERMINING THE EPL

```
%Using Matlab we read EPID image and Open image data (EPID_data and OPEN)
TRANS = -log(EPID_data./OPEN);

% From equation 3.8
Xn = (-B + sqrt(B.^2+4*A.*TRANS))./(2*B); % Xn is the initial solution
Xn_c = mean(mean(Th_un(186:198,250:262))); %Xn_c is initial mean pixel value
% in a 1cm ROI (first No in each coloum of Table 4-6)

% Effect of MU correction
MUs = [20 50 100 200 500];
MU_factor = [0.970 0.990 1.000 1.004 1.009];
SMUR = interp1(MUs,MU_factor,MU); % 1D Interpolation to get MU factor which
%the image was acquired

Thickness = [0 5 10 15 20 26 32 50];
FieldSize = [4.9 10 15 20 21.5];

% Table of correction factor
CF = [1.216   1.281   1.368   1.447   1.523   1.640   1.739   1.840
     1.097   1.152   1.218   1.268   1.325   1.393   1.445   1.550
     1.046   1.076   1.116   1.138   1.178   1.206   1.249   1.350
     1.009   1.016   1.033   1.037   1.043   1.048   1.060   1.070
     1.000   1.000   1.000   1.000   1.000   1.000   1.000   1.000];

for i = 1:n % n is total number of times we want to iterate
  corr = interp2(Thickness, FieldSize,CF, Xn, FieldArea*ones(384,512))/SMUR;
  % 2D interpolation to find scatter correction (corr) due to thickness Xn,
  % and field size (FieldArea). FieldArea is determined from EPID image
  % using equation 3.18
  Xn+1 = (A.*Xn.^2 -log(corr.*data./OPEN))./(2*A.*Xn + B); % equation 3.12
    Xn+1(find(isnan(Xn+1))) = 0.0; % Any value in data which is not a number
  %(NAN) is replaced by 0
  EPL_c = mean(mean(Xn+1(186:198,250:262)));%EPL_c is mean pixel value in
  %1cm ROI

end
```

Note1: A, B and C are fixed, but the correction (corr) keep on changing, meaning that the coefficient of C keeps on changing, which enable the Xn+1 values to change at each iteration.

Note 2: corr is also a 384x512 matrix (i.e correction is applied for each pixel depending on the previously calculated value or EPL). corr is evaluated at the same area (FieldArea) of the irradiated EPID image.

Proof of the Convergence of the iteration

According to Newton's Method, a function $x_{n+1} = g(x_n)$, converges quadratically to r if g'(r)=0, where r is a fixed point of g, (that is g(r)=r).

If we let f(x) = $ax^2 + bx + c = 0$, *A8*

Then the first derivative of f(x) is given by $f'(x) = 2ax + b$ A9

From equation A7, let g(x) = $x_{n+1} = \dfrac{ax_n^{\,2} - c}{2ax_n + b}$ A10

The derivative of g, $g'(x) = \dfrac{-2a(ax_n^{\,2} - c) + 2ax_n(2ax_n + b)}{(2ax_n + b)^2}$ A11

$$= \frac{2a(ax_n^{\,2} + bx_n + c)}{(2ax_n + b)^2} \quad \text{A12}$$

$$= \frac{2af(x)}{[f'(x)]^2} = 0 \quad \text{A13}$$

APPENDIX B: Relation between TPR and PETD

Consider the diagram below that relates the TPR and PETD for the same field area and phantom depth z.

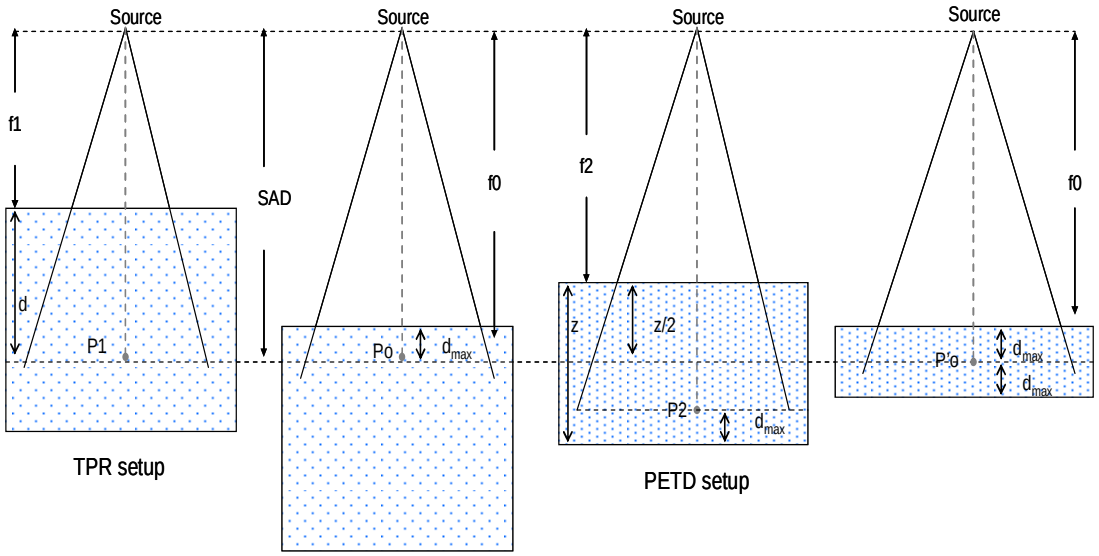

The TPR at a point P_1 located at an effective depth, $d = z - d_{\max}$, is related to doses $D(P_1)$ and $D(P_o)$ at P_1 and at d_{max} respectively by `

$$TPR(P_1) = \frac{D(P_1)}{D(P_o)} \qquad \text{B1}$$

The PETD for a depth d measured at point P_2 is given by

$$PETD(P_2) = \frac{D(P_2)}{D(P_o')} \qquad \text{B2}$$

Where $D(P_2)$ and $D(P'_o)$ are doses at P_2 and at d_{max} respectively. The dose $D(P_1)$ is

given by $$D(P_1) = \frac{PDD(P_1, f_1)}{100} D(P_o)\left(\frac{f_o}{f_1 + d_{\max}}\right)^2 \qquad \text{B3}$$

and dose $$D(P_2) = \frac{PDD(P_2, f_2)}{100} D(P_o')\left(\frac{f_o}{f_2 + d_{\max}}\right)^2 \qquad \text{B4}$$

neglecting the effect of appropriate back scatter at P'_o and at P_2.

Combining equations B1- B4,

$$PETD(P_2) = \frac{D(P_2)D(P_o)}{D(P_1)D(P_o')}TPR(P_1) = \frac{PDD(P_2, f_2)}{PDD(P_1, f_1)}\left[\frac{f_1 + d_{\max}}{f_2 + d_{\max}}\right]^2 TPR(P_1) \quad \text{B5}$$

Where f_1, f_o and f_2 are respective SSDs as shown in the figure above.

Using the Mayneord factor that relates PDDs measured at different SSDs, then

$$PETD(P_2) = \left(\frac{\frac{f_2 + d_{\max}}{f_2 + d}}{\frac{f_1 + d_{\max}}{f_1 + d}}\right)^2 \left[\frac{f_1 + d_{\max}}{f_2 + d_{\max}}\right]^2 TPR(P_1) = \left[\frac{f_1 + d}{f_2 + d}\right]^2 TPR(P_1) \quad \text{B6}$$

Thus $$PETD(z) = \left(\frac{SAD - (z - d_{\max}) + (z - d_{\max})}{SAD - (z/2) + (z - d_{\max})}\right)^2 TPR(z - d_{\max}) \quad \text{B7}$$

$$= \left(\frac{SAD}{SAD + z/2 - d_{\max}}\right)^2 TPR(z - d_{\max}) \quad \text{B8}$$

Equation B8 implies that PETD is TPR, corrected for inverse square law, i.e taking into account the shift in the calculation point away from the isocenter.

List of References

Al Kattar EZ, Foulquir JN, El balaa H, Orthuon A and Touboul E 2009 Quality assurance of enhanced dynamic wedge using the a-Si500 EPID *Cancer Radiother* **13(8)** 731-739

Allen XL 1999 Peak scatter factors for high energy photon beams *Med.Phys* **26(6)** 962-966 **E**

Amerio S, Boriano A, Bourhaleb F 2004 Dosimetric characterization of a large area pixel-segmented ionization chamber *Med Phys* **31** 414–20.

Antonuk LE 2002 Electronic portal imaging devices: a review and historical perspective of contemporary technologies and research *Phys. Med. Biol*. **47**

Antonuk L, El-Mohri Y, Huang W 1998 Initial performance evaluation of an indirect-detection, active matrix flat-panel imager (AMFPI) prototype for megavoltage imaging *Int J Radiat Oncol Biol Phys* **42** 437–54.

Beck JA, Budgell GJ, Roberts DA, Evans PM (2009) Electron beam quality control using an a-Si EPID *Med Phys* **36(5)** 1859-1866.

Berger L, François P, Gaboriaud G, and Rosenwald JC 2006 Performance optimization of the Varian a-Si500 electronic portal imaging device system *J Appl Clin Med Phys*. **7(1)** 105-14

Beyer WH 1987 CRC Standard Mathematical Tables, 28th ed, *CRC Press,* Baca Raton, FL pg 123-124

Bloemen-van Gurp EJ, Mijnheer BJ, Verschueren TA 2007 Total body irradiation, toward optimal individual delivery: dose evaluation with metal oxide field effect transistors, thermoluminescence detectors, and a treatment planning system. *Int J Radiat Oncol Biol Phys* **69** 1297-1304.

Boellaard R, Essers M, Van Herk M, Mijnheer BJ 1998 New method to obtain the midplane dose using portal in vivo dosimetry *Int J Rad Oncol Biol Phys* **41** 465-474

Boellaard R, Van Herk M, Mijnheer BJ 1997 A convolution model to convert transmission dose images to exit dose distributions *Med Phys*. **24(2)** 189-199

Boesecke R, Hartmann GH, Scharfenberg H, Schlegel W 1985 Dose calculations for irregular fields using 3-D first scatter integration *Phys.Med.Biol*. **31** 291-298

Boyer AL**,** Antonuk L, Fenster A, van Herk, Meertens H, Munro P, Reinstein LE Wong J 1992 A review of electronic portal imaging devices *Med Phys*. **19(1)** 1-16

Broggi S, Fiorino C, Calandrino R 2001 A simple and robust method for in vivo midline dose map estimations using diodes and portal detectors *Radiother Oncol* **58** 169-178

Chang J, Ling CC 2003 Using the frame averaging of a-Si500 electronic portal imaging device for IMRT verification J Appl Clin Med Phys **4(4)** 287-299

Chang J, Mageras GS, Chui CS, Ling CC, Lutz W 2000 Relative profile and dose verification of intensity-modulated radiation therapy *Int J Rad Oncol Biol Phys* **47** 231–40

Chang J, Mageras GS, Ling CC 2003 Evaluation of rapid dose map acquisition of a scanning liquid-filled ionization chamber electronic portal imaging device *Int J Rad Oncol Biol Phys* **55(5)** 1432–1445

Chen J, Chuang CF, Morin O, Aubi M and Pouliot J 2006 Calibration of an a-Si flat panel portal imager for exit-beam dosimetry *Med Phys.* **33(3)** 584-594

Chen J, Morin O, Aubi M, Bucci MK, Chuang CF, and Pouliot J 2006b Dose-guided radiation therapy with megavoltage cone-beam CT *Br. J. Radiol.* **33(3)** S87-S98

Chen M, Lu W, Chen Q, Ruchala K, Olivera G 2009 Efficient gamma index calculation using fast Euclidean distance transformation *Phys.Med.Biol.* **54(7)** 2037-2047

Cherry P, Duxbury A 1998 Practical Radiotherapy: Physics and equipment *Oxford University Press* pp 39-50

Chin PW, Spezi E, Lewis DG 2003 Monte Carlo simulation of portal dosimetry on a rectilinear voxel geometry: a variable gantry angle solution *Phys Med Biol* **48** N231–238

Cilla S, Fidanzio A, Greco F, Sabatino D, Russo A, Gargiulo L, Azario L and Piermattei A 2011 Calibration of Elekta aSi EPIDs Used as Transit Dosimeter *Technol Cancer Res Treat* **10(1)** 39-48

Clarke MF and Budgell 2008 Use of an amorphous silicon electronic portal imaging device for measuring MLC calibration at varying gantry angle *Phys.Med.Biol.* **53** 473-485

Dam JV, Vaerman C, Blanckaert N, Leunens G, Dutriex A, Van der Schueren E 1992 Are port films reliable for invivo exit dose measurements *Radiother Oncol* **45**:67-72.

De Boer JCJ, Heijmen BJM, Pasma KL, Visser AG 2000 Characterization of a high-elbow, fluoroscopic electronic portal imaging device for portal dosimetry *Phys.Med.Biol.* **45** 197-216

El-Mohri Y, Antonuk LE, Yorston J 1999 Relative dosimetry using active matrix flat-panel imager (AMFPI) technology *Med.Phys.* **26(8)** 1530-1541

Ezzell GA, Galvin JM, Low D, Palta JR, Rosen I, Sharpe MB, Xia P, Xiao Y, Xing L, and Yu CU 2003 Guidance document on delivery, treatment planning, and clinical implementation of IMRT: Report of IMRT subcommittee of the AAPM radiation therapy committee *Med. Phys.* **30 (8)** 2089-2115

Ferreira IH, Dutreix A, Bridier A *2000* The ESTRO-QUALity assurance network (EQUAL) *Radiother Oncol* **55**:273-284.

Fidanzio A, Cilla S, Greco F, Gargiulo L, Azario L, Sabatino D, Piermattei A 2010 Generalized EPID calibration for in vivo transit dosimetry Med Biol Eng Comp **49(3)** 373-383

Fielding AL, Evans PM, Clark CH 2002 The use of electronic portal imaging device to verify positioning during IMRT delivered by the dynamic MLC technique *Int J Radiat Oncol Bio Physl.* **54(4)** 1225-1234

Fiorino C, Corletto D, Manggilli P, Broggi S, Bonini A, Cattaneo GM, Parisi R, Rosso A, Signorotto P, Villa E, Calandrino R 2000 Quality assurance by systematic in vivo dosimetry: results on a large cohort of patients *J Radiother Oncol.* **56(1)** 85-95

Fippel M, Haryanto F, Dohm O, Nusslin F, Kriesen S 2003 A virtual photon energy fluence model for Monto Carlo dose calculation *Med.Phys.* **30(3)** 301-311

Fowler JF and Attix FH 1966 Solid state integrating dosimeters in Radiation Dosimetry **Vol 2** (*NewYork: Academic*) 241-90

Gibbons JP 1998 Calculation of Enhanced dynamic wedge factors for symmetric and asymmetric fields *Med Phys* **25** 1411-1418

Grattan MWD, McGaryy CK 2010 Mechanical characterization of the Varian Exact-arm and R-arm support systems for eight aSi500 EPID *Med Phys.* **37(4)** 1707-1713

Greer PB 2007 Off-axis dose response characteristics of an a-Si electronic portal imaging device *Med Phys.* **34(10)** 3815-24

Greer PB and Barnes MP 2007 Investigation of an a-Si electronic portal imaging device for measurement and quality assurance of enhanced dynamic wedge *Phys. Med. Biol.* **52** 1075-1087

Greer PB and Popescu CC 2003 Dosimetric properties of an a-Si electronic portal imaging device for verification of dynamic IMRT *Med Phys* **30 (7)** 1618-1627

Hee J K, Gyuseong C, Tae H L and Young S K 2002 Comparative study on the radiation damage of a-Si:H p-i-n diodes made by PECVD and ion shower doping *Nucl. Sci. IEEE.* **49 (5)** 2244-2249

Heijmen BJ, Pasma KL, Kroonwijk M 1995 Portal dose measurement in radiotherapy using an electronic portal imaging device (EPID) *Phys Med Biol* **40** 1943–1955

Herman M G, Balter J M, Jaffray D A, McGee K P, Shalev S, Van Herk M and Wong J W 2001 Clinical use of electronic portal imaging: Report of AAPM radiation therapy committee task group 58 *Med.Phys.* **28 (5)** 712-737

Heukelom S, Lanson JH and Mijnheer BJ 1991 Comparison of entrance and exit dose measurements using ionization chambers and silicon diodes *Phys. Med. Biol*. **36** 47-59

Huyskens DP, Bogaerts R, Verstraete J, Loof M, Nystrom H, Fiorino C, Broggi S, Jornet N, Ribas M, Thwaites DI 2001 Practical guidelines for the implementation of in vivo dosimetry with diodes in external radiotherapy with photon beams (entrance dose) ESTRO Brussels Belgium

ICRU report 24 1976 Determination of absorbed dose in a patient irradiated by beams of x-rays or γ-rays in radiotherapy procedures *International Commission on Radiation Units and Measurements* Bethesda USA

ICRU report 62 1999 Prescribing, recording and reporting Photon Beam Therapy (Supplement to ICRU Report 50 1993) International Commission on Radiation Units and Measurements Bethesda USA

Janaki MG, Kadam AR, Mukesh S, Nirmala, Ponni A, Ramesh BS, Rajeev AG 2010 Magnitude of fatigue in cancer patients receiving radiotherapy and its short term effect on quality of life *J Cancer Res Ther*. **6 (1)** 22-26

Kairn T, Cassidy D, Fielding AL, Sandford PM 2007 Electronic portal imaging devices for radiotherapy dosimetry: The thickness gauge *Radiother Oncol* **84**(Suppl.1)**:** S226-S226

Kairn T, Cassidy D, Sandford PM, Fielding AL 2008 Radiotherapy treatment verification using radiological thickness measured with an a-Si electronic portal imaging device: Monte Carlo simulation and experiment *Phys.Med.Biol*. **53** 3903-3919

Kavuma A, Glegg M, Currie G, Elliott A 2008 Assessment of dosimetrical performance in 11 Varian a-Si500 electronic portal imaging devices *Phys.Med.Biol*. **53** 6893-6909

Kavuma A, Glegg M, Metwaly M, Currie G, Elliott A 2010 A novel method for patient exit and entrance dose prediction based on water equivalent path length measured with an amorphous silicon electronic portal imaging device *Phys. Med. Biol*. **55** 435–452

Khan FM 2003 The physics of radiation therapy, Part 1: Basic physics – Interactions of ionizing radiation *Lippincott Williams & Wilkins* 3rd edition Philadelphia. 59 – 77

Kirby MC and Glendinning AG 2006 Developments in electronic portal imaging devices *Br J Radiol* **79** S50-S65

Kirby MC and Williams P 1994 The use of an electronic portal imaging device for exit dosimetry and quality control measurements *Int.J.Radiat. Oncol. Biol Phys* **31** 593-603

Ko L, Kim JO, Siebers JV 2004 Investigation of the optimal backscatter for an a-Si electronic portal imaging device *Phys Med Biol* **49(9)** 1723-1738

Krengil M, Gaiano S, Mones E, Ballare A, Beldi D Bolchini C, Loi G 2009 Reproducibility of patient setup by surface image registration system in conformal radiotherapy of prostate cancer *Radiat Oncol* **4** 4-9

Kuperman VY 2005 Analytical representation for Varian Enhanced dynamic wedge factors at off-axis points *Med Phys* **32(5)** 1256-1261

Kutcher GJ, Coia L, Gillin M 1999 Comprehensive QA for radiation oncology: Report of AAPM Radiation Therapy Committee Task Group 40 *Med Phys.* **21 (4)** 581-618

Lavalle MC, Gingras L, Beaulieu L 2006 Energy and integrated dose dependence of MOSFET dosimeter sensitivity for irradiation energies between 30 kV and 60Co. *Med Phys* **33**:3683-3689

Leunens G, Dam JV, Dutreix A, Van der Schueren 1990 Quality assurance in radiotherapy by in vivo dosimetry: Entrance dose measurements, a reliable procedure *Radiother Oncol **17(2)*** 141-151

Lorenz F, Nalichowski A, Rosca F, Kung J, Wenz F and Zygmanski P 2007 Spatial dependence of MLC transmission in IMRT delivery *Phys Med Biol* **52 (19)** 5985 – 5999

Louwe RJW, Damen EMF, Van Herk M, Minken AWH, Torzsok O and Mijnheer BJ 2003 Three-dimensional dose reconstruction of breast cancer treatment using portal imaging *Med Phys* **30(9)**:2376-2389

Low DA, Harms WB, Mutic S, Purdy JA 1998 A technique for the quantitative evaluation of dose distributions *Med Phys* **25** 656–661

Mayles P, Nahum AE, Rosenled JC 2007 Handbook of Radiotherapy Physics: Theory and practice. Chapter 40: Quality control of treatment delivery *Taylor and Francis*

McCurdy BMC, Luchka K, and Pistorious S 2001 Dosimetric investigation and portal dose image prediction using an a-Si electronic portal imaging device *Med Phys.* **28** 911-924

McDermott LN, Wendling M, Nijkamp J, Mans A, Sonke JJ, Mijnheer BJ, van Herk M 2008 Three-dimensional in vivo dose verification of entire hypo-fractionated IMRT

treatments using an electronic portal imaging device and cone-beam CT *Radiother Oncol*, **86(1)** 35-42

McDermott LN, Wendling M, Sonke J, Van Herk M, Mijnheer BJ 2007 Replacing pretreatment verification with in vivo electronic portal imaging device dosimetry for prostate IMRT *Int J Radiat Oncol Bio Physl*. **67(5)** 1568-1577

McDermott LN, Louwe RJ, Sonke JJ, van Herk MB and Mijnheer BJ 2004 Dose-response and ghosting effects of an a-Si electronic portal imaging device *Med Phys*. **31(2)** 285-295

McDermott LN, Nijsten SM, Sonke JJ, Partridge M, Herk M and Mijnheer BJ 2006 Comparison of ghosting effects for three commercial a-Si electronic portal imaging devices *Med Phys*. **33(7)** 2448-2451

McDonough J, Xiao Y, Bjarngard E 1999 Comparing two methods for calculating phantom scatter *Phys.Med.Biol*. **44** N9-N14

McGarry C K, Grattan M W D and Cosgrove V P 2007 Optimization of image quality and dose for Varian a-Si500 electronic portal imaging devices *Phys. Med. Biol*. **52** 6865-6877

Menon G V and Sloboda R S 2004 Quality assurance measurements of a-Si electronic portal imaging device performance *Medical dosimetry*. **29(1)** 11-17

Metcalfe P, Kron T and Hoban P 1997 The physics of Radiotherapy X-rays from Linear Accelerators (Madison: Medical Physics publishing)

Mohammadi M and Bezak E 2006 Two-dimensional transmitted dose measurements using scanning liquid ionisation chambers electronic portal imaging device Phys Med Biol **51** 2971 – 2985

Mohammadi M, Bezak E, Reich P 2007 The use of extended dose range film for dosimetric calibration of a scanning liquid ionisation chambers electronic portal imaging device J Appl Clin Med Phys. **8(1)** 69-84

Moore JA and Siebers JV 2005 Verification of the optimal backscatter for an a-Si electronic portal imaging device Phys Med Biol. **50** 2341-2350

Morton EJ, Swindell W, Lewis DG, Evans PM 1991 A linear array scintillation crystal-photodiode detector for megavoltage imaging *Med.Phys*. **18(4)** 681-691

Munro P, Bouius DC, Moseley J 1998 Glaring errors in transit dosimetry. Proceedings of the 5th International Workshop on Electronic Portal Imaging, Phoenix AZ 128-29

Munro P and Bouius DC 1998b X-ray quantum limited portal imaging using a-Si flat panel array *Med.Phys*. **25(5)** 689-702

Murthy KK, Al-Rahbi Z, Sivakumar SS, Davis CA, Ravichandran R, El Ghamrawy K 2008 Verification of setup errors in external beam radiation therapy using electronic portal imaging *J Med Phys.* **33(2)** 49-53

Nelms BE, Rasmussen KH and Tome WA 2010 Evaluation of a fast method of EPID-based dosimetry for intensity-modulated radiation therapy J Appl Clin *Med Phys* **10(2)** 140-157

Nichol LEA, Sankar AP, Macleod A 2010 Initial experience on the evaluation of "Dosimetry Check" at Edinburgh Cancer Center, Western General Hospital; Scottish + Radiotherapy physics meeting, 12th June 2010 Old Course Hotel, St Andrews, Scotland

Nicolini G and Fogliata A 2006 GLAaS: An absolute dose calibration algorithm for an amorphous silicon portal imager. Applications to IMRT verifications *Med. Phys* **33(8)** 2839-2851

Nijsten SMJJG, Mijnheer BJ, Dekker ALAJ, Lambin P and Minken AWH 2007 Routine individualized patient dosimetry using electronic portal imaging device *Radiother Oncol*. **83** 67-75

Nijsten SMJJG, van Elmpt WJC, Jacobs M, Mijnheer BJ, Dekker AL AJ, Lambin P, Minken AWH 2007b A global calibration model for *a*-Si electronic portal imaging devices used for transit dosimetry *Med.Phys.* **34(10)** 3872-3884

Ozard SR, Grein EE 2001 Analytical calculation of portal scatter to primary dose ratio: an EGS4 Monte Carlo and experimental validation at large air gaps *Phys.Med.Biol*. **46** 1719-1736

Papatheodorou S, Zefkili S and Rosenwald J 1999 The equivalent wedge implementation of the Varian Enhanced Dynamic Wedge (EDW) into a treatment planning system Phys. Med. Biol. **44** 509–524.

Pardo J, Franco L, Gomez F, Iglesias A, Pazoz A, Pena J, Mosquera J, Pombar M and Sendon J 2005 Development and operation of a pixel segmented liquid-filled linear array for radiotherapy quality assurance *Phys Med Biol*. **50** 1703-1716

Parent L, Fielding A, Dance DR, Seco J and Evans PM 2007 a-Si electronic portal imaging device calibration for dosimetric applications: comparison of a method based on Monte Carlo prediction of response with existing techniques *Phys Med Biol*. **52** 3351-3368

Parent L, Seco J, Evans PM, Dance DR and Fielding A 2006 Evaluation of two methods of predicting MLC leaf positions using electronic portal imaging device measurements *Med Phys*. **33(9)** 3174-3182

Parsaeia H and El-Khatib E 1998 The use of an electronic portal imaging system to measure portal dose and portal dose profiles *Med Phys*. **25(10)** 1903-1909

Pasma KL, Heijmen BJ, Kroonwijk M and Visser AG 1998 Portal dose image (PDI) prediction for dosimetric treatment verification in radiotherapy. An algorithm for open beams *Med Phys*. **25(6)** 830-840.

Pasma KL, Kroonwijk M, de Boer JC, Visser AG, Heijmen BJ 1998 Accurate portal dose measurement with a fluoroscopic electronic portal imaging device (EPID) for open and wedged beams and dynamic multileaf collimation *Phys Med Biol*. **43** 2047–2060

Pasma KL, Maarten LP, Kroonwijk D 1999 Dosimetric verification of IMRT *Int.J.Radiat.Oncol.Biol.Phys* **21(4)** 581-618

Pasma KL, Vieira SC, and Heijmen BJM Portal dose image prediction for dosimetric treatment verification in radiotherapy. An algorithm for wedged beams *Med Phys* 29(6) 925-931

Pasquino M, Borca VC, Tofani S, Ozzello F 2009 Verification of Varian enhanced dynamic wedge implementation in MasterPlan treatment planning system J App Clin Med Phys **10(2)** 11-20

Patridge M, Ebert M, Hesse BM 2002 IMRT verification by 3D dose reconstruction from portal beam measurements *Med Phys*. **29** 1847-1858.

Patridge M, Evans PM, Symonds T 1999 Optical scattering in camera based electronic portal imaging *Phys. Med. Biol*. **44** 2381-2396

Petti PL, Goodman MS, Gabriel TS, Mohan R 1983 Investigation of buildup dose from electron contamination of clinical photons *Med Phys*. 10(1) 18-24

Piermattei A, Fidanzio A, Cilla S, Greco F, Gargiulo L, Azario L, Sabatino D 2007 Application of a practical method for the isocenter point *in vivo* dosimetry by a transit signal *Phys. Med. Biol*. **52** 5101-5117

Piermattei A, Fidanzio A, Stimato G, Azario L, Grimaldi L, D'Onofrio G 2006 *In vivo* dosimetry by an aSi-based electronic portal imaging device *Med Phys* 2006 **33** 4414-4422.

Podgorsak E.B 2005 Radiation Dosimeters (71-99), External photon beams-Physical aspects (161-216), Basic radiobiology (485-504) Radiation Oncology Physics: Handbook for teachers & students, *Vienna- IAEA*

Prado KL, Kirsner SM, Kudchadker J, Steadham RE and Lane RG 2002 Enhanced dynamic wedge factors at off-axis points in asymmetric fields *J App Clin Med Phys* **4(1)** 75-84

Ramaseshan R, Kohli KS, Zhang TJ 2004 Performance characteristics of a microMOSFET as an in vivo dosimeter in radiation therapy. *Phys Med Biol* **49**:4031-4048.

Renner WD, Norton K and Holmes T 2005 A method for deconvolution of integrated electronic portal images to obtain fluence for dose reconstruction *J Appl Clin Med Phys*. **6(4)** 22 – 39

Royal College of Radiologists, Society and college of Radiographers, Institute of Physics and Engineering in Medicine, National Patients safety Agency, and British Institute of Radiology (2008) Towards Safer Radiotherapy. London: *The Royal College of Radiologists*

Sabet M, Menk FW, Greer PB 2010 Evaluation of an a-Si electronic portal imaging device in direct configuration as a water-equivalent dosimeter for transit dosimetry *Med Phys* **37(4)** 1459-1467

Sanz DE, Romaguera AL, Acosta NB 2001 Irregular field calculation on the central beam axis of photon beams using sector-integration *Med.phys* **28(7)** 1344-51

Siebers JV, Kim JO, Ko L, Keall PJ, Mohan R 2004 Monte Carlo computation of dosimetric a-Si electronic portal images *Med.Phys* **31(7)** 2135-2146

Spezi E, Angelini AL, Romani F, Ferri A 2005 Characterization of a 2D ion chamber array for the verification of radiotherapy treatments *Phys Med Biol* **50** 3361–73

Steciw S, Warkentin B, Rathee S and Fallone BG 2005 Three-dimensional IMRT verification with a flat-panel electronic portal imaging device *Med Phys*. **32(2)** 600-612

Storchi P, Woudstra E 1995 Calculation models for determining the absorbed dose in water phantoms in off-axis planes of rectangular fields of open and wedged photon beams *Phys Med Biol*. **40** 511-527

Storchi PRM, van Battum LJ, Woudstra E 1999 Calculation of a pencil beam kernel from measured photon beam data *Phys. Med. Biol*. **44** 2917-2928

Swindell W, Evans PM 1996 Scattered radiation in portal images: A Monte Carlo simulation and a simple physical model *Med.Phys* **23(1)** 63-73

Terron JA, Sanchez-Doblado F, Arrans R, Sanchez-Nieto, Errazquim L 1994 Midline dose algorithm for in vivo dosimetry *Med Dosim*. **19(4)** 263-267

Topolnjak R, Sonke JJ, Nijkamp J, Rasch C, Minkema D, Remeijer P, van Vliet-Vroengindeweij C 2001 Breast Patient Setup Error Assessment: Comparison of Electronic Portal Image Devices and Cone-Beam Computed Tomography Matching Results *Int J Radiat Oncol Biol Phys (In press)*

Van Dyk J 2005 The modern technology of radiation oncology *Medical physics publishing Madison WI USA* ***Vol 2***.

Van Elmpt W, McDermott L, Nijsten S, Wendling M, Lambin P, Mijnheer B 2008 A literature review of electronic portal imaging for radiotherapy *Radiother Oncol* **88** 289-309

Van Elmpt WJC, Nijsten SMJJG, Schiffeleers RFH, Dekker ALAJ, Mijnheer BJ, Lambin P and Minken AWH 2006 A Monte Carlo based 3D dose reconstruction method derived from portal dose images *Med Phys.* **33(7)** 2426-2434

Van Esch A, Depuydt T and Huyskes DP 2004 The use of an aSi-based electronic portal imaging device for routine absolute dosimetry pre-treatment verification of dynamic IMRT fields *Radiother Oncol*. **71** 223-234

Van Herk M 1991 Physical aspects of a liquid-filled ionization chamber with pulsed polarizing voltage *Med Phys* **18** 692–702

Van Zijtveld M, Dirkx M, Breuers M, de Boer H, Heijmen B 2009 Portal dose image prediction for in vivo treatment verification completely based on electronic portal imaging device measurements *Med.Phys* **36 (3)** 946-952

Vanetti de Palma E, Conte L, Nicolini G, Stucchi P, Mordacchini C, Cassani E, Novario R 2005 Experimental method to obtain scattering contribution in portal dose images *Physica Medica* **21(1)** 31-40

Varatharaj C, Moretti E, Ravikumar M, Malisan MR, Supe SS, Padovani R 2010 Implementation and validation of a commercial portal dosimetry software for intensity-modulated radiation therapy pre-treatment verification *J Med Phys* **35(4)** 189-196

Varian Medical Systems 1996 C-Series Clinac Enhanced Dynamic Wedge™ Implementation Guide

Varian Medical Systems 2001 Portalvision™ a-Si500 electronic portal imaging device

Vetterli D, Riem H, Aebersold DM, Greiner RH, Manser P, Cossmann P, Kemmerling L, Born EJ and Mini R 2004 Introduction of a novel dose saving acquisition mode for the PortalVision a-Si500 electronic portal imaging device to facilitate on-line patient setup verification *Med Phys.* **31(4)** 828-831

Vial P, Greer PB, Baldock C 2006 An experimental investigation into the radiation field offset of a dynamic multileaf collimator *Phys Med Biol*. **51(21)** 5517-5538

Vial P, Greer PB, hunt P, Oliver L and Baldock C 2008 The impact of MLC transmitted radiation on electronic portal imaging device dosimetry for dMLC beams *Med Phys*. **35(4)** 1267-1277

Vieira SC, Dirkx MLP, Pasma KL, Heijmen BJM 2003 Dosimetric verification of x-ray fields with steep dose gradients using an electronic portal imaging device *Phys. Med. Biol*. **48** 157-166

Wambersie A, Gahbauer R A 2001 Hadrons (protons, neutrons, heavy ions) in radiation therapy: rationale, achievements and expectations *Radiochim. Acta* **89** 245–53

Warkentin B, Steciw S, Rathee S and Fallone BG 2003 Dosimetric IMRT verification with a flat-panel electronic portal imaging device *Med. Phys* **30**, 3143 – 3155.

Wendling M, Louwe RJW, McDermott LN, Sonke JJ, Herk MV and Mijnheer BJ 2006 Accurate 2D IMRT verification using a back-projection electronic portal imaging device dosimetry method *Med Phys.* **33(2)** 259-273

Williams JR, Thwaites DI 2004 Treatment planning for external beam therapy: Principles and basic techniques, Radiotherapy Physics in Practice, 2nd ed. *Oxfor d Univer. Press* 150-178

Winkler P and George D 2006 An intercomparison of 11 a-Si electronic portal imaging devices of the same type: implications for portal dosimetry *Phys Med Biol*. **51(17)** 4189-200

Winkler P, Hefner A and George D 2005 Dose-response characteristic of an a-Si electronic portal imaging device *Med.Phys.* **32** 3095-3105

Zijtveld MV, Dirkx MLP, DeBoer HCJ and Heijmen BJM (2007) 3D dose reconstruction for clinical evaluation of IMRT pre-treatment verification with an electronic portal imaging device *Radiother Oncol* **81** 201-207

APPENDIX C: Peer reviewed publications arising from thesis

1) Awusi Kavuma, Martin Glegg, Garry Currie and Alex Elliott (2008) Assessment of dosimetrical performance in 11 Varian a-Si500 electronic portal imaging devices *Phys. Med. Biol*. **53** pg 6893–6909

2) Awusi Kavuma, Martin Glegg, Mohamed Metwaly, Garry Currie and Alex Elliott (2010) A novel method for patient exit and entrance dose prediction based on water equivalent path length measured with an amorphous silicon electronic portal imaging device *Phys. Med. Biol*. **55** 435–452

3) Awusi Kavuma, Martin Glegg, Mohamed Metwaly, Garry Currie and Alex Elliott (2010) Calculation of exit dose for conformal and dynamically wedged fields, based on water equivalent path length measured with an amorphous silicon electronic portal imaging device (In press - JACMP)

Presentations at conferences

1) Awusi Kavuma, Martin Glegg and Mohamed Metwaly (12 June 2008) Development of an algorithm to predict entrance and exit dose to a phantom from EPID. *Scottish + Radiotherapy physics meeting Glasgow*

2) Awusi Kavuma, Martin Glegg, Mohamed Metwaly, Garry Currie and Alex Elliott (Dec 2- 4, 2009) Patient exit and entrance dose prediction based on water equivalent path length measured with an amorphous silicon electronic portal imaging device. *International conference on modern radiotherapy: Advances and challenges in radiation protection of patients. Versailles - France*